

MECHANICS AND SUBCRITICAL CRACKING OF FRP-CONCRETE INTERFACE

by

CHAO ZHANG

JIALAI WANG, COMMITTEE CHAIR

JAMES A. RICHARDSON

JAMES P. HUBNER

KENNETH J. FRIDLEY

SAMIT ROY

A DISSERTATION

Submitted in partial fulfillment of the requirements
for the degree of Doctor of Philosophy
in the Department of Civil, Construction and Environmental Engineering
in the Graduate School of
The University of Alabama

TUSCALOOSA, ALABAMA

2011

Copyright Chao Zhang 2011
ALL RIGHTS RESERVED

ABSTRACT

The need for safe, effective, and efficient methods to strengthen and upgrade our nation's infrastructures is clear. Strengthening Reinforced Concrete (RC) members using Fiber Reinforced Polymer (FRP) composites through external bonding has emerged as a viable technique to retrofit/repair deteriorated infrastructures. The interface between the FRP and concrete plays a critical role in this technique.

This study proposes a life-cycle analytical framework on the integrity and long-term durability of the FRP-concrete interface through a combined analytical, numerical, and experimental approach. A novel three-parameter elastic foundation model (3PEF) is first established to provide a general tool to analyze and evaluate the design of the FRP strengthening system. This model correctly predicts the location where debonding can occur. To simulate the interface stress redistribution and creep deformations accumulated during service life due to the strong time dependent features of the adhesive layer, linear viscoelastic analytical solutions are then developed for the FRP-strengthened RC beams. Small cracks usually exist within the FRP-concrete interface, making fracture mechanics a more appropriate tool to evaluate the integrity of the FRP-concrete interface. Analytical solutions of energy release rate (ERR) and its phase angle at the tip of a crack along the FRP-concrete interface are obtained. Under the synergistic effects of the service loads and environments species, these small cracks can grow slowly even if the ERR at the crack tip is lower than the critical value. This slow-crack growth process is known as environment-assisted subcritical cracking. A series of subcritical cracking testing are conducted

using a wedge-driven testing to gain the ability to accurately predict the long-term durability of the FRP-concrete interface. It has been found that water, deicing salt and alkaline solutions can substantially reduce the ERR at the crack tip needed to drive the subcritical crack growth along the epoxy-concrete interface. Once the small cracks grow to the critical length, critical debonding will occur, leading to the premature failure of the structure. A nonlinear fracture mechanics model using a Cohesive Zone Model (CZM) is finally developed to simulate this final failure phase of the FRP-concrete interface.

DEDICATION

I dedicate this dissertation to my Lord, Jesus Christ; for without Him, I could do nothing and achieve nothing. I also dedicate this dissertation to my wonderful family. Particularly to my wife, Leina, who has supported me through these years of research, and to our precious my unborn baby, for he or she was with me for the last period of my writing process. I was blessed to have him or her for the time I did. I must also thank my loving parents who have given me their fullest support.

LIST OF ABBREVIATIONS AND SYMBOLS

a_c	Effective crack length
$A_{i,k}$	Dimensionless cross section areas of the arm i for case k
B_i	Shear stiffness of beam i
b_i	Width of beam i
CA	Concrete-Adhesive
$CFHO$	Closed Form High Order
$CFRP$	Carbon Fiber Reinforced Polymer
C_i	Axial stiffness of beam i
C_{ni}	Interface compliances in the normal direction
$CPS8$	Eight-node biquadratic element in ABAQUS
CSD	Crack Surface Displacement
$CSDE$	Crack Surface Displacement Extrapolation
C_{si}	Interface compliances in the shear direction
CZM	Cohesive Zone Model
d	Distance from the neutral axis of beam I to the interface
da/dN	Crack growth rate with respect to cyclic number N
da/dt	Debond growth rate with respect to time
D_c	Bending stiffness of the FRP-epoxy composite layer
DCB	Double Cantilever Beam

D_i	Bending stiffness of beam i
DIC	Digital Image Correlation
e	Volumetric strain component of the stress
E_a	Young's modulus of the adhesive
E_c	Modulus of elasticity of the concrete
E_i	Longitudinal Young's modulus of beam i
e_{ij}	Deviatoric components of the strain tensors
ERR	Energy Release Rate
f_c'	Specific 28-day compressive strength
FEA	Finite Element Analysis
FRP	Fiber Reinforced Polymer
G	Energy Release Rate
G_I	Component 1 of the total ERR
G_{II}	Component 2 of the total ERR
G_0	Initial shear modulus
G_a	Shear modulus of the adhesive
G_c	Critical ERR or fracture toughness
G_∞	Ultimate shear modulus
G_i	Shear modulus of beam i
GR	Goland and Reissner
G_{th}	Threshold ERR
H	Thickness of the whole beam model
$H(t)$	Heaviside step function

H_{11} and H_{22}	Bi-material constants
h_i	Thickness of beam i
IC	Intermediate crack induced
$I_{i,k}$	Dimensionless moment of inertias of the arm i for case k
K	Bulk modulus of the adhesive
K	Stress intensity factor
K_c	Critical stress intensity factor
L	Length of the uncracked region
L_a	Total crack length from the edge of the specimen to the crack tip
<i>LEFM</i>	Linear Elastic Fracture Mechanics
M_i	Bending moments in beam i
M_T	Resulting moment with respect to the neutral axis of the FRP plate
N_0	Pretension force applied to the FRP plate
N_c	Concentrated longitudinal force acting at the crack tip
N_i	Resulting axial force in beam i
N_T	Resulting axial forces with respect to the neutral axis of the FRP plate
<i>PA</i>	FRP plate-Adhesive
P_i and Q_i	Differential operators
q	Magnitude of uniform load
Q	Apparent activation energy of the interface
Q_a	Shear force of the adhesive layer
Q_c	Concentrated peel force acting at the crack tip
Q_i	Transverse shear forces in beam i

Q_T	Resulting shear forces with respect to the neutral axis of the FRP plate
R	Gas constant
R_0	Radius of adhesive layer
RC	Reinforced Concrete
RH	Relative Humidity
R_i	Radius of beam i
s	Volumetric hydrostatic component of the stress,
s_{ij}	Deviatoric components of the stress tensors
$\tan\delta_r$	Viscoelastic loss factor
U	Elastic strain energy
u_0	Initial displacement of the FRP plate before the pretension is released
U_i	Axial displacements of beam i
u_i	Axial displacements at the neutral axis of beam i
$VCCT$	Virtual Crack Closure Technique
VCE	Virtual Crack Extension
w_a	Deflection at the mid-plane of the adhesive layer
W_d	Work done by external forces
W_i	Transverse displacements of beam i
w_i	Transverse displacements at the neutral axis of beam i
α and β	Mismatch parameters in bi-material system
γ_{0i}	Shear strains along the neutral-axis of the beam i
γ_i	Shear strains of the beam i
Δ	Thickness of the wedge

δ_I	Crack surface displacement of the interface crack tip in shear direction
δ_I	Slip corresponding to the maximum shear bond strength
δ_2	Crack surface displacement of the interface crack tip in normal direction
δ_f	Slip corresponding to the complete debonding
ΔG	Strain energy release range
δ_{nf}	Maximum open displacement of the FRP-concrete interface
δ_x	Shearing relative displacements of the crack flanks
δ_y	Opening relative displacements of the crack flanks
ε_{0i}	Axial strains along the neutral-axis of the beam i
ε_i	Axial strains of the beam i
κ_{0i}	Curvatures along the neutral-axis of the beam i
κ_i	Curvatures of the beam i
Π	Energy potential of the system
σ_I	Normal stresses along the CA interface
σ_{12}	Shear traction ahead of the interface crack tip
σ_2	Normal stress along the PA interface
σ_{22}	Normal traction ahead of the interface crack tip
σ_f	Maximum normal stress of the FRP-concrete interface
τ	Shear stresses in the adhesive
τ_f	Maximum shear bond strength
ω	Mode mix angle
Ω	Mode mix parameter
μ_i	Shear modulus

ε	Bi-material constant
ν_i	Poisson's ratio
ϕ_i	Rotation at the neutral axis of beam i
ψ	Phase angle
∂A	Increased crack surface
∂a	Increment length of crack
$2PEF$	Two-Parameter Elastic Foundation
$3PEF$	Three-Parameter elastic Foundation

ACKNOWLEDGMENTS

I would like to thank all of those people who helped make this dissertation possible.

First, I wish to thank my advisor, Dr. Jialai Wang for all his guidance, encouragement, support, and patience. Also, I would like to thank my committee members Dr. Kenneth J. Fridley, Dr. James A. Richardson, Dr. Samit Roy, and Dr. James P. Hubner for their very helpful insights, comments and suggestions. Additionally, I would like to acknowledge all of those people who provided technical support and assistance with running the experiments: Tim Ryan and Bob Fanning, for assisting me with the process of running the experiments. Many thanks also go to Darlene Burkhalter, Ekandrea Tarver, and Liz Crawford for their great help during my whole process of studying in the University of Alabama. Finally, I would like to thank my fellow graduate students, Shixin Zeng, Elaina Jennings, and Chen Chen, who provided me invaluable support and suggestions throughout this process. This work is supported by the National Science Foundation under Grant No. 0927938.

CONTENTS

ABSTRACT.....	ii
DEDICATION.....	iv
LIST OF ABBREVIATIONS AND SYMBOLS	v
ACKNOWLEDGMENTS	xi
LIST OF TABLES	xvii
LIST OF FIGURES	xviii
CHAPTER 1 INTRODUCTION	1
1.1 Application background.....	1
1.1.1 Statement of the problem.....	2
1.1.2 Failure modes of FRP-strengthened RC beams	3
1.2 Overview of existing studies on FRP-concrete interface.....	6
1.2.1 FRP-concrete interface stresses analysis	7
1.2.1.1 Interface stress analysis of adhesive joints	8
1.2.1.2 Interface stress analysis of FRP-concrete specimens.....	10
1.2.1.3 Numerical interfacial stresses analysis of FRP-concrete interface	14
1.2.1.4 Experimental study on FRP-strengthened RC beam	17
1.2.2 LEFM analysis of FRP-strengthened RC beams	19
1.2.2.1 Introduction of the LEFM.....	19
1.2.2.2 LEFM analysis for FRP-concrete interface	22
1.2.2.3 Numerical analysis of layered structures based on the LEFM	23

1.2.3	CZM approach for interface debonding in FRP-strengthened RC beams	27
1.2.3.1	Cohesive zone model FRP-concrete interface	29
1.2.3.2	Experimental studies on the bond-slip laws of FRP-concrete interface ..	33
1.2.4	Durability of FRP-concrete interface.....	35
1.2.4.1	Effect of moisture on FRP-concrete interface	36
1.2.4.2	Fatigue of FRP-concrete interface	39
1.2.4.3	Viscoelastic analysis of FRP-concrete interface.....	40
1.2.5	Environment-assisted subcritical crack growth	42
1.2.5.1	Subcritical crack growth in bulk glass	43
1.2.5.2	Subcritical crack growth in adhesive joints	47
1.3	Research needs and tasks	50
1.4	Organization of the dissertation	52
CHAPTER 2 A THREE-PARAMETER ELASTIC FOUNDATION MODEL FOR INTERFACE STRESSES IN THE FRP-STRENGTHENED BEAMS.....		55
2.1	Introduction.....	55
2.2	3PEF model for an FRP-strengthened straight beam	57
2.2.1	Adhesively bonded bi-layered beam system.....	57
2.2.2	3PEF model for a straight adhesive layer	59
2.2.3	Governing differential equation of an FRP-strengthened straight RC beam....	61
2.2.4	Interface stress of an FRP-strengthened straight RC beam	66
2.2.5	Boundary conditions of an FRP-strengthened straight RC beam	67
2.2.6	Verifications and comparisons of present analytical solution for an FRP- strengthened straight RC beams.....	70
2.3	3PEF model of an FRP-strengthened curved RC beam.....	78
2.3.1	Shear deformable curved beam theory	78

2.3.2	3PEF model of a curved adhesive layer.....	81
2.3.3	Governing differential equation of an FRP-strengthened curved RC beam	83
2.3.4	Interface stress of an FRP-strengthened curved RC beam.....	87
2.3.5	Boundary conditions of an FRP-strengthened curved RC beam	88
2.3.6	Verifications and comparisons of present analytical solution for an FRP-strengthened curved RC beam	90
2.4	Conclusions.....	96
CHAPTER 3 VISCOELASTIC ANALYSIS OF FRP-STRENGTHENED RC BEAMS.....		97
3.1	Introduction.....	97
3.2	Viscoelastic model of an FRP-strengthened RC beam based on 2PEF model	98
3.2.1	Shear deformable beam theory	99
3.2.2	Viscoelastic interface model	102
3.2.3	Governing Equation of viscoelastic 2PEF model	104
3.2.4	Numerical method for inverse Laplace transform	109
3.2.5	Deflections	109
3.2.6	Validation of the analytical solution.....	110
3.2.6.1	FRP-strengthened RC beam without pretension force.....	112
3.2.6.2	Prestressed FRP-strengthened RC beam.....	117
3.3	Viscoelastic model of an FRP-strengthened RC beam based on 3PEF model	120
3.3.1	Bi-layer beam model for a prestressed FRP-strengthened RC beam.....	120
3.3.2	3PEF viscoelastic interface model	121
3.3.3	Governing Equation based on 3PEF viscoelastic model	123
3.3.4	3PEF viscoelastic solution of an FRP-strengthened RC beam	131
3.3.5	3PEF viscoelastic solution of a prestressed FRP-strengthened RC beam	137

3.4	Conclusions.....	141
CHAPTER 4 LINEAR ELASTIC FRACTURE MECHANICS ANALYSIS OF THE FRP-STRENGTHEND CONCRETE BEAMS		
		143
4.1	Introduction.....	143
4.2	A tri-layer crack tip element	143
4.3	Shear deformable joint model.....	146
4.3.1	Semi-rigid joint model	147
4.3.2	Flexible joint model	149
4.4	Interfacial fracture parameters	153
4.5	Verifications of present LEFM solutions.....	157
4.6	Conclusions.....	162
CHAPTER 5 ENVIRONMENT-ASSISTED SUBCRITICAL DEBONDING OF EPOXY-CONCRETE INTERFACE		
		164
5.1	Introduction.....	164
5.2	Environment-assisted subcritical cracking at the FRP-concrete interface.....	165
5.3	Drawbacks of existing durability studies.....	167
5.4	Advantages of subcritical debonding test	169
5.5	Research Scopes and Organization.....	170
5.6	Materials and test specimens	170
5.6.1	Concrete substrates	172
5.6.2	CFRP plates and structural adhesive.....	173
5.6.3	Bonding CFRP plates onto the concrete substrates	173
5.7	Experimental set-up and research plan	175
5.7.1	Wedge driving tests.....	175
5.7.2	Research experimental plan	177

5.8	Testing Results and discussions.....	179
5.8.1	Effect of concrete substrate’s strength on subcritical debonding	181
5.8.2	Effect of aggressive environment on subcritical debonding.....	183
5.9	Conclusions.....	187
CHAPTER 6 NONLINEAR FRACTURE MECHANICS OF FLEXURAL-SHEAR CRACK INDUCED DEBONDING OF FRP STRENGTHENED CONCRETE BEAMS		189
6.1	Introduction.....	189
6.2	Mixed-mode CZM of the flexural-shear IC debonding.....	192
6.2.1	Bi-beam system.....	192
6.2.2	Mixed-mode nonlinear bond stress-slip model.....	194
6.2.3	Spring model of flexural-shear crack.....	197
6.2.4	Analysis of the FRP-concrete interface debonding process	198
6.2.4.1	Shear stress along the interface.....	200
6.2.4.2	Normal stress along the interface.....	203
6.3	Numerical verifications.....	208
6.4	Parameter study and discussion	214
6.5	Conclusions.....	221
CHAPTER 7 CONCLUSIONS		223
REFERENCES		227
APPENDIX A.....		245
APPENDIX B		247

LIST OF TABLES

1.1 Comparison of assumptions in analytical solutions for the FRP-strengthened RC beams (Smith and Teng, 2001)	11
1.2 Literature review of moisture effect on FRP-concrete interface	37
3.1 Set of Constants for α_i and K_i for the Zakian's Method	109
3.2 Material properties of the FRP-strengthened RC beam.....	110
5.1 Subcritical debonding test plan in different environmental exposures	178

LIST OF FIGURES

1.1. A RC beam strengthened with externally bonded FRP composite.....	3
1.2. Failure modes of FRP-strengthened RC beams.....	5
1.3 Layered structure model for different structures	8
1.4 CFHO, Finite-Element, and Elastic Foundation Models Results: (a) Shear Stresses, (b) Peeling Stresses (Rabinovich and Frostig, 2000).	12
1.5 3D finite element model of FRP-strengthened RC beam (Kotynia, 2008).....	16
1.6 Full scale experiment on the FRP-strengthened RC beam (Smith and Teng, 2002)	17
1.7 Classification of FRP-concrete bond tests (Chen et al., 2001)	18
1.8 Three fracture modes	20
1.9 The interface crack between two different materials	21
1.10 Quadtrilateral element with quarter-point nodes (Krueger, 2004).....	24
1.11 Crack tip opening geometry.....	25
1.12 CSDE method presented schematically (Berggren et al., 2006).....	26
1.13 Definition of the FRP-concrete interface.....	27
1.14 Regions of cohesive zone.....	28
1.15 Bilinear CZM for shear stress bond slip law	30
1.16 Intermediate crack induced interface debonding (Wang, 2006a)	32

1.17	A typical experimental set-up (Mazzotti et al., 2005) to measure bond-slip law: (a) Specimen transverse section, (b) Side view with instrument positions and CFRP plate clamping system, (c) Spacing between strain gauges along the CFRP plate	33
1.18	Rheological model for viscoelasticity of the adhesive layer (Diab and Wu, 2008)	42
1.19	Schematic of typical environment-assisted debond	44
1.20	Crack growth data in soda-lime-silica glass (Wiederhorn, 1967).....	45
1.21	Crack growth of the 26Na ₂ O -11Al ₂ O ₃ - 63SiO ₂ glass in different corrosive media (Gehrke et al., 1991).....	46
1.22	Soda-lime-silicate glass tested in water as a function of temperature (Wiederhorn and Bolz, 1970).....	47
1.23	ERR varies with crack growth rate along the epoxy-concrete interface (Park, 2004).....	49
1.24	Competition between epoxy and water for surface sites leading to displacement of the adhesive from the surface: (a) Adhesive adsorbed at surface sites (b) Adhesive displaced from the surface sites (Shimizu et al., 1999).....	50
1.25	Research plan of the dissertation	51
2.1	Simply supported FRP-strengthened RC beam under concentrated load.....	57
2.2	Free body diagram of the adhesively bonded bi-layered beam system	58
2.3	Extending (a, b) 2PEF model to (c, d) 3PEF model for the adhesive layer.....	60
2.4	Implement boundary conditions of the straight FRP-strengthened beam using the principle of superposition	68
2.5	Finite element model of the FRP-strengthened straight RC beam	70
2.6	Comparison of interface stresses obtained by different methods for the FRP-strengthened straight RC beam: (a) interface shear stresses, (b) interface normal stresses.....	72
2.7	Comparison of interface stresses from the 3PEF model and FEA ($h_0 = 0.5$ mm) for the FRP-strengthened straight RC beam: (a) interface shear stresses, (b) interface normal stresses ..	74
2.8	Comparison of interface stresses from the 3PEF model and FEA ($h_0 = 4.0$ mm) for the FRP-strengthened straight RC beam: (a) interface shear stresses, (b) interface normal stresses ..	75
2.9	Comparison of interface stresses from the 3PEF model and FEA ($h_2 = 0.5$ mm) for the FRP-strengthened straight RC beam: (a) interface shear stresses, (b) interface normal stresses ..	76

2.10	Comparison of interface stresses from the 3PEF model and FEA ($h_2 = 4.0\text{mm}$) for the FRP-strengthened straight RC beam: (a) interface shear stresses, (b) interface normal stresses	77
2.11	Free body diagram of a curved beam bonded with a thin plate	79
2.12	3PEF model for the curved adhesive layer	83
2.13	A simply supported curved beam externally bonded with a FRP plate	88
2.14	Implement boundary conditions using the principle of superposition.....	90
2.15	Finite element model of the FRP-strengthened curved beam (a) mesh of the half of the beam; and (b) close-up of the mesh near the FRP plate end	91
2.16	Interface stresses in a curved RC beam strengthened by FRP plate ($R_0 = 1.5\text{ m}$): (a) shear stress; and (b) normal stresses	93
2.17	Radius of curvature's effect on interface stresses: (a) shear stress; (b) normal stresses along CA interface; and (c) normal stresses along PA interface.....	94
2.18	Interface stresses in a straight concrete beam strengthened by FRP plate: (a) shear stress; and (b) normal stresses	95
3.1	An FRP-strengthened RC beam.....	99
3.2	Free body diagram of an FRP-strengthened RC beam	101
3.3	Standard Linear Solid Model	103
3.4	Finite element model of simply supported RC beam.....	112
3.5	Redistribution of interface shear stress with time (day)	113
3.6	Redistribution of interface normal stress with time (day)	113
3.7	Maximum interface shear stress reducing with time	114
3.8	Maximum interface normal stress reducing with time	114
3.9	Variation of axial force in FRP plate with time (day)	115
3.10	Variation of moment in RC beam with time (day)	115
3.11	Axial forces of the FRP plate at 25mm from the FRP plate end varying with time	116
3.12	Moments in the RC beam at 25mm from FRP plate end varying with time	116

3.13	Deflection at the mid-span increasing with time	117
3.14	Redistribution of interface shear stress with time (day) in the prestressed FRP-strengthened RC beam	118
3.15	Redistribution of interface normal stress with time (day) in the prestressed FRP plate strengthened RC beam	118
3.16	Variation of the axial force in the prestressed FRP plate with time (day).....	119
3.17	Variation of moment in RC beam with time (day)	119
3.18	Deflection at the mid-span with time in the prestressed FRP-strengthened RC beam with time for different thicknesses of adhesive layer.....	120
3.19	Free body diagram of prestressed FRP-strengthened RC beam	120
3.20	Three-parameter elastic foundation model of the adhesive layer	122
3.21	Redistribution of interface shear stress with time (day)	132
3.22	Redistribution of normal stress along the CA interface with time (day)	132
3.23	Comparison of normal stress along the PA interface with time (day).....	133
3.24	Variation of shear stress distribution with time (day).....	133
3.25	Variation of normal stress at CA interface distribution with time (day)	134
3.26	Variation of normal stress at PA interface distribution with time (day).....	134
3.27	Deflections at the mid-span for different thicknesses of adhesive layer	135
3.28	Change of axial force in the FRP plate with time (day)	135
3.29	Change of moment in RC beam with time (day)	136
3.30	Axial forces in FRP plate at 25mm away from plate end for different thicknesses of adhesive layer	136
3.31	Moments in RC beam at 25mm away from plate end for different thicknesses of adhesive layer	137
3.32	Variation of shear stress distribution of prestressed FRP plated RC beam (day).....	137
3.33	Variation of normal stress distribution of prestressed FRP plated RC beam along the CA interface.....	138

3.34	Variation of normal stress distribution of prestressed FRP plated RC beam along the PA interface.....	138
3.35	Variation of axial force in prestressed FRP plate with time (day).....	139
3.36	Variation of moment in prestressed FRP strengthened RC beam with time (day).....	139
3.37	Axial forces variation in the FRP plate for different thicknesses of adhesive layer of prestressed FRP plated RC beam (day).....	140
3.38	Change of moments in RC beam with time or different thicknesses of adhesive layer of prestressed FRP plated RC beam (day).....	140
3.39	Change of Deflection with time for different thicknesses of adhesive layer of prestressed FRP plated RC beam (day).....	141
4.1	Crack tip element of FRP-strengthened concrete beam.....	144
4.2	Free body diagram of the tri-layer beam model.....	145
4.3	Crack tip elements for different joint models	147
4.4	Calculation of energy release rate using the principle of superposition	153
4.5	Finite element model of the FRP-strengthened concrete DCB specimen.....	158
4.6	FRP-strengthened concrete DCB specimen.....	158
4.7	EERs versus crack lengths for a DCB specimen	160
4.8	Phase angles versus crack lengths for a DCB specimen.....	160
4.9	EERs versus thickness of the FRP plate for a DCB specimen	161
4.10	Phase angles versus thicknesses of the FRP plate for a DCB specimen.....	162
5.1	Reaction of water with a strained crack tip bond to propagate the crack at the driving forces below the critical fracture energy	166
5.2	Crack growth velocity as a function the strain energy release rate.....	167
5.3	Wedge driving test configuration.....	171
5.4	Wedge dimensions	171
5.5	Aluminum models for concrete specimen making	172

5.6	Concrete specimens and standard cylinder specimens prepared for experiment.....	173
5.7	Experimental apparatus for the wedge driving tests	175
5.8	Fixture of concrete specimen and test setup in ambient condition	176
5.9	Wedge driving test set up in a transparent glass vessel	177
5.10	Crack growth with time in the ambient condition	180
5.11	Variance of ERR with time in the ambient condition.....	180
5.12	Crack growth with time in tap water.....	180
5.13	Variance of ERR with time in the tap water	181
5.14	Comparison of subcritical crack growth velocity v (in log scale) as a function of the ERR in ambient condition for different concrete strength substrates	182
5.15	Comparison of subcritical crack growth velocity v (in log scale) as a function of the ERR in tap water for different concrete strength substrates	182
5.16	Comparison of subcritical crack growth velocity v (in log scale) as a function of the ERR in alkaline solution for different concrete strength substrates.....	183
5.17	Comparison of subcritical crack growth velocity v (in log scale) as a function of the ERR in deicing salt solution for different concrete strength substrates.....	183
5.18	Comparison of the subcritical crack growth velocity v (in log scale) as a function of the ERR at the crack tip of group 1	184
5.19	Comparison of the subcritical crack growth velocity v (in log scale) as a function of the ERR at the crack tip of group 2.....	185
5.20	Comparison of the subcritical crack growth velocity v (in log scale) as a function of the ERR at the crack tip of group 3.....	185
5.21	Interface fracture surfaces of wedge driving tests	187
6.1	Flexural-shear crack induced debonding of an FRP-strengthened RC beam	193
6.2	Free body diagram for equilibrium equation	194
6.3	Traction-separation law used in this study: (a) Shear traction-separation law, (b) Normal traction-separation law.	195
6.4	Spring model of the flexural-shear crack.....	197

6.5	Free body diagram of the debonded zone	205
6.6	Simply supported FRP-strengthened RC beam with a flexural-shear crack.....	208
6.7	FEA model for the FRP-strengthened RC beam with a flexure-shear crack	209
6.8	Interface stress distributions at different debonding stages: (a) interfacial shear stress, (b) interfacial normal stress.....	210
6.9	Stress distributions at different debonding stages for small crack length: (a) interfacial shear stress, (b) interfacial normal stress	212
6.10	Stress distributions at different debonding stages for a flexural crack: (a) interfacial shear stress; (b) interfacial normal stress	214
6.11	Debonding propagation characteristics: (a) fracture energy; (b) mode mixity; (c) debonding driving force; (d) maximum axial force of the FRP plate	217
6.12	Effect of the FRP thickness on debonding: (a) fracture energy; (b) maximum stress of the FRP plate; (c) debonding driving force	218
6.13	Effect of the angle of the crack on debonding: (a) debonding driving force; (b) maximum axial force of the FRP plate; (c) fracture energy; (d) mode mixity	221

CHAPTER 1

INTRODUCTION

1.1 Application background

The civil infrastructure in the U.S. is deteriorating due to aging, natural extreme events, excessive use, and intentional attacks. According to the 2009 report card released by ASCE, the overall GPA of American's infrastructure is "D" and a five-year investment of \$2.2 trillion is needed for repair and maintenance. According to the ASCE infrastructure scorecard, more than 26% of the bridges are either structurally deficient or functionally obsolete, which may result from lack of maintenance, increased load demand, aging, and degradation due to environment (ASCE report card, 2009). Moreover, the high cost of maintenance and delayed repairing actions seem to further exacerbate the condition. The tragic collapse of the interstate bridge in Minneapolis can be considered as a wake up call of the serious national crisis for the need to maintain and retrofit the existing highways, bridges, and transit systems. However, it is not realistic to repair or replace all of these infrastructures in the conventional way due to the staggering cost. There is an urgent need for innovative techniques, which can improve the bearing capacity and the durability of the existing infrastructure efficiently while minimizing the cost and the impact on the surrounding environment.

1.1.1 Statement of the problem

To meet the need of rehabilitating and retrofitting the existing infrastructure, various innovative construction techniques and new materials have been recently developed. Among them, the outstanding performance of the Fiber Reinforced Polymer (FRP) composites make them an excellent candidate for repairing or retrofitting existing civil infrastructures. The FRP composites are made of fibers (such as glass, aramid, and carbon) embedded in a resin matrix. The resin matrix is usually a sort of adhesive which can protect the fibers, maintain their alignment, and distribute loads among them. The FRP composites, which have been extensively implemented in the fields of aerospace, automotive, electronic, and sport equipments, are now becoming a mainstream technology to upgrade the existing reinforced concrete (RC) structures. The FRP laminates or sheets can be easily attached to the surface of RC structural members to increase their load bearing capacities and seismic resistance with minimum impact on the environment (Smith and Teng, 2001). Compared to conventional materials, such as concrete, steel, and timber, the FRP composites have higher specific strength, lighter weight, and better corrosion resistance. The FRP laminates or sheets can be either externally bonded (Seible et al., 1997; Lorenzis et al., 2001) as shown in Fig. 1.1, or near-surface mounted (Hassan and Rizkalla, 2003; Parretti and Nanni, 2004; Lorenzis and Teng, 2006) onto the RC structures through structural adhesives. In addition, by applying a prestress to the FRP laminates or sheets, the strengthening efficiency can be improved significantly (El-Hacha et al., 2001). This strengthening method has evolved into one of the primary techniques to solve the deterioration problem of the nation's infrastructure system. Compared to traditional repairing methods,

retrofitting/rehabilitating the infrastructures with the FRP composites is a more reasonable solution because it provides not only better material properties, but also entails lower indirect cost through shorter road closures and traffic detours.

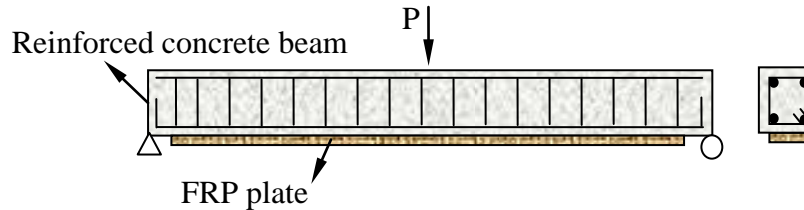


Fig.1.1. A RC beam strengthened with externally bonded FRP composite.

However, the failure mechanism of the FRP-strengthened RC structures is more complicated than those of conventional RC structures. Because the interface between the FRP laminates and the concrete substrate plays a critical role in maintaining the integrity of the FRP-concrete hybrid beam, interface debonding can lead to fatally premature failure. Even though extensive research has been done on this technique, a better understanding on the short-term interface bonding behavior of the FRP-concrete hybrid beam is needed. Moreover, many field applications of this FRP bonding technique are in hostile environments and are intended for long-term usage. However, there is still a lack of sound understanding on the long term behavior and durability of the FRP-concrete interface up to now. The important role of interface bonding in the integrity of the FRP-strengthened RC beam will be demonstrated when the failure modes are discussed in details in the next section.

1.1.2 Failure modes of FRP-strengthened RC beams

The FRP-strengthened RC beams can fail in more modes than conventional RC beams due to the existence of bonding interface between the FRP plate and the concrete substrate. The

reported possible failure modes for the FRP-strengthened RC beams can be classified into two main categories: material failure modes and premature interface debonding failure modes, as shown in Fig.1.2 (Smith and Teng, 2001; Chen and Teng, 2001; Teng et. al., 2002). If the interface bond between the concrete and the FRP composite is strong enough, the failure modes will depend on the material strengths of the concrete and the FRP composite, as shown in Figs.1.2 (a) - (c). These kinds of failure modes are referred to as material failure modes, and are similar to those of conventional RC beams. However, when the strength of the bond is not sufficient, interface debonding can occur between the FRP plate and the concrete beam (Figs.1.2 (d) - (f)), often leading to a brittle and sudden failure of the beam. These modes are often referred to as interface debonding failure modes, and are unique to the FRP-strengthened RC beams.

As for the first category, the bond between the concrete and the FRP composite remains intact when the FRP-strengthened RC beam fails. The failure of the strengthened beam has three modes: rupture of the FRP composite (Fig.1.2(a)), crush of concrete within the compressive zone of the RC beam (Fig.1.2(b)), and shear failure of the RC beam (Fig.1.2(c)). The first failure mode may occur for relatively low ratios of internal steel reinforcement or externally bonded FRP composite to the area of the concrete cross section. This failure mode can be prevented by increasing the amount of the FRP composite attached onto the RC structure by using a higher strength FRP composite. The second failure mode can be avoided by using higher strength concrete, less FRP composites, and smaller steel reinforcement embedded in the RC structure. The third failure mode can be eliminated by adding more shear reinforcement or by attaching

more FRP composite on the surfaces of the RC beams. However, all of these fixes simply shifts the failure to the next relative weakness.

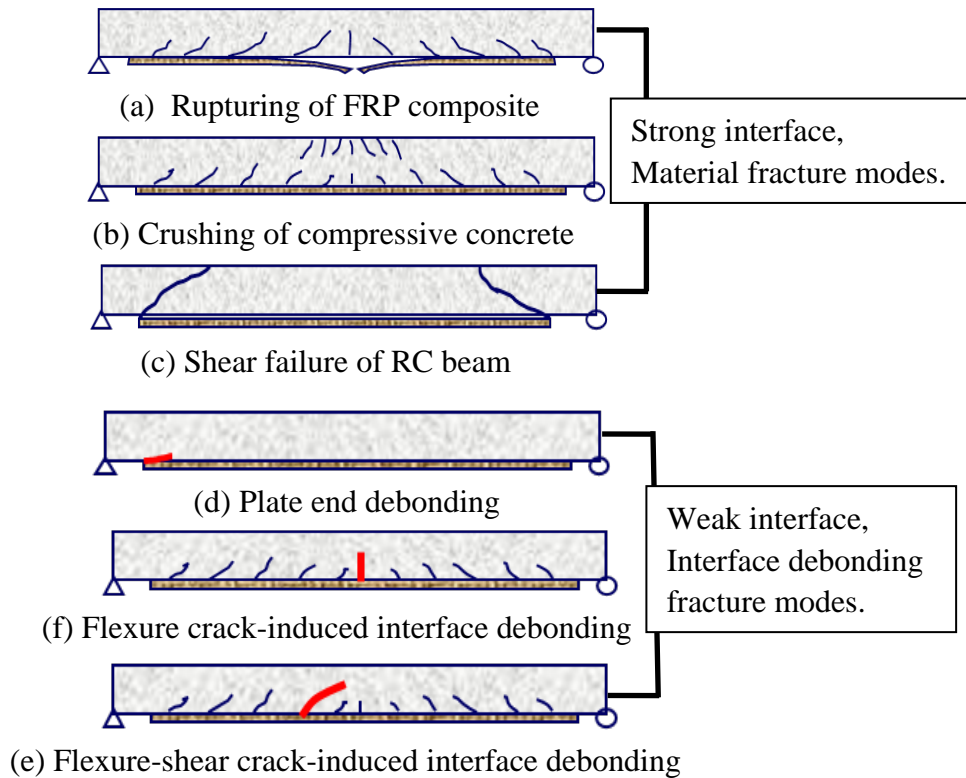


Fig.1.2. Failure modes of FRP-strengthened RC beams.

A large body of testing results show that the interface debonding (Figs.1.2 (d) - (f)) is more dangerous to the FRP-strengthened RC structures (Sharif et al., 1994; Büyüköztürk and Hearing, 1998; Teng et al., 2003). The interface debonding failure modes can be broadly classified into two types according to the starting point of the debonding: plate end debonding and intermediate crack induced interface debonding. In the first case, the interface debonding initiates from the plate end and propagates towards the mid-span as shown in Fig.1.2 (d). In the second case, the debonding occurs in the vicinity of an intermediate flexure or a flexure-shear crack within the RC beam as shown in Figs.1.2 (e) and (f). The intermediate crack induced

interface debonding can be further classified into flexure crack induced interface debonding (Fig. 1.2(e)) and flexure-shear crack induced interface debonding (Fig. 1.2(f)). Even though the intermediate crack induced interface debonding modes are less reported and studied, these modes are likely to control the strength of FRP-strengthened RC beams (Teng et al., 2003). The interface between the FRP and concrete plays a critical role in this technique. Therefore, to prevent the interface debonding induced premature failure of the FRP-strengthened structures, extensive studies have been conducted on the interface strength and durability of the FRP-concrete interface.

1.2 Overview of existing studies on FRP-concrete interface

FRP composites have been introduced in the field of civil engineering at a rapid rate in the past two decades because of their superior properties (Ritche et al., 1991; Täljsten, 1997a; Seible et al., 1997; Lorenzis et al., 2001). To have a better understanding on the mechanism of FRP-concrete interface, extensive studies have been conducted on both the short-term and long-term behavior of FRP-strengthened RC beams. Various advantages of this strengthening technique have been demonstrated by numerous laboratory studies and field applications. The interface bond between the FRP plate and the concrete substrate plays a critical role in this strengthening technique through transferring the load from the RC beam to the FRP plate. The debonding of the FRP-concrete interface can cause the failure of this strengthening technique, or even the fatal premature failure of the strengthened RC beams before the ultimate strength can be attained.

In this section, a comprehensive review on the existing studies of the FRP-concrete interface is presented. For the RC beams “perfectly” bonded with the FRP laminates or plates, the strength based criteria can be applied once the interface stresses can be predicted accurately. The research related to the interface stress of the FRP-strengthened RC beam will be discussed in detail and compared in terms of analytical method, numerical simulation, and experimental study. If the interface bond is not “perfect” and has some small cracks, the Linear Elastic Fracture Mechanics (LEFM) method is usually used to study the integrity of the FRP-concrete interface. Some relevant analytical solutions regarding the FRP-concrete interface based on the LEFM will first be reviewed, followed by the review of numerical methods and other relevant experimental studies. The FRP-concrete interface debonding will propagate with the increase of loads. The research associated with the FRP-concrete interface based on Cohesive Zone Models (CZMs) will be summarized in details. Furthermore, to study the long-term behavior of the FRP-strengthened RC structures, tremendous efforts have been made to examine the durability characteristics of the FRP-concrete interface in the aggressive environments and under fatigue loads. Finally a literature survey will be conducted on the environment-assisted subcritical debonding of adhesive bonded joints.

1.2.1 FRP-concrete interface stress analysis

Structurally, an FRP-strengthened RC beam is similar to an adhesive joint as shown in Fig.1.3. The major differences between these two structures are the geometric and the material properties. For this reason, all of the existing analytical solutions of the FRP-concrete interface stress have been derived from existing interface stress solutions of adhesive joints.

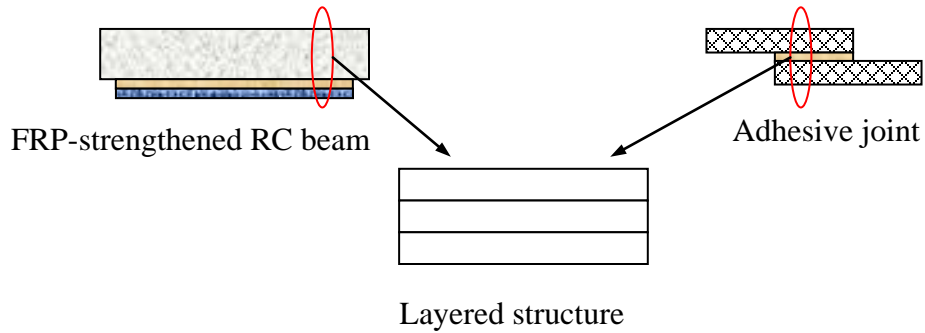


Fig.1.3. Layered structure model for different structures.

1.2.1.1 Interface stress analysis of adhesive joints

The adhesive bonding technique has been widely used in the field of aerospace and automotive industries due to its many advantages, such as ease of application, time and cost saving, and good corrosion resistance. Even though numerical methods, such as the finite difference method and the finite element method, can be used to analyze the interfacial stresses, closed-form solutions are more effective for the preliminary design and the parametric study. Over decades, many researchers have studied the adhesive joints and proposed a number of analytical models for the stresses in the adhesive layer (Goland and Reissner, 1944; Hart-Smith, 1973; Chen and Cheng, 1983; Oplinger, 1991; Tsai and Morton, 1994; Oplinger, 1994; Frostig et.al., 1999; Wu et.al., 2002; Luo and Tong, 2004). As the first attempt, a simple shear lag model of the adhesive joints was proposed by Volkersen in 1938 (Tsai et.al., 1998). In this simple model, two adherends were modeled as perfect rigid one-dimensional bars connected with an adhesive layer. The adhesive layer was modeled as a series of continuously distributed shear springs. The deflections of the adherends and the transverse normal strain in the adhesive layer were all ignored. Several years later, Goland and Reissner (1944) (subsequently referred to as

“GR’s model”) postulated a refined model to analyze a single-lap joint. The major improvements of the GR’s model are: 1) the adherends are treated as beams, and 2) both the shear and the transverse normal deformations of the adhesive layer are taken into consideration. In this model, Goland and Reissner (1944) assumed that the shear and normal stresses within the adhesive layer were uniformly distributed through the thickness of the adhesive layer. In this way, the adhesive layer was modeled as continuously distributed shear and vertical springs. No interactions between the shear and vertical springs were considered, and the force equilibrium of the adhesive layer was ignored. The adhesive layer is essentially modeled as a two-parameter elastic foundation (2PEF) in this model. Therefore, the GR’s model is also referred to as the 2PEF model in this dissertation. The GR’s model has been widely adopted and modified by many authors (Lubkin and Reissner, 1958; Hart-Smith, 1973; Delale et al., 1981; Tong, 1996; Smith and Teng, 2002; Wang and Qiao, 2004a; Taheri and Zou, 2004; Zou et.al., 2004; Lee and Kim, 2005). Hart and Smith (1973) improved the GR’s model by considering the individual deformations of the upper and lower adherends respectively, which was more reasonable than the lumped overlap used in the GR’s model. In this modified model, Hart and Smith (1973) also treated the edge moments as unknowns, which were solved together with the shear stress and normal stress in the adhesive layer. This model also took the large deflections of the outer adherends into account, but disregarded the large deflection in the overlap sections. More recently, Luo and Tong (2004) extended the GR’s method by assuming that the displacements of the adhesive layer were linear or even higher order. With this model, some parametric studies were performed on the single lap joints and the piezoelectric smart plates. Even though the

governing equations were much more complicated than that of the GR's model, no significant improvements were observed for the interfacial stresses. Recently, a comprehensive survey on the analytical solutions of adhesively bonded joints was presented by Lucas et al. (2009a, b).

1.2.1.2 Interface stress analysis of FRP-concrete specimens

Due to the simplicity and intuitiveness of the 2PEF model, it was widely employed to analyze the FRP-strengthened RC beams in the last two decades (Vilnay, 1988; Roberts, 1989; Roberts and Haji-Kazami, 1989; Liu and Zhu, 1994; Täljsten, 1997b; Malek et al., 1998; Smith and Teng, 2001; Lau et al., 2001; Wang and Qiao, 2004b; Yang et al., 2004a). The major assumptions of these existing solutions are identical to the GR's model, assuming that the shear and normal stresses within the adhesive layer are constant through the thickness of the adhesive layer. A comprehensive review on these models of the interfacial stresses in the FRP-strengthened RC beams was provided by Smith and Teng (2001), as shown in Table 1.1. The closed-form solutions shown in Table 1.1 did not consider the effect of shear deformations. Smith and Teng (2001) proposed an FRP-concrete interface stress model considering the shear deformation of the FRP-strengthened RC beams. Smith and Teng (2001)'s model was recently improved by Abdelouahed (2006). Compared with experiment results (Jones et al., 1988), the Abdelouahed's solutions attained better accuracy than those based on the Smith and Teng's model. However, in both methods, the curvatures of the beams and the thin plates were assumed as the same. This assumption has been shown unnecessary by Wang (2003).

Table 1.1 Comparison of assumptions in analytical solutions for the FRP-strengthened RC beams (Smith and Teng, 2001).

	Theory	Vilnay [2]	Roberts [3]	Roberts and Haji-Kazemi [4]	Liu and Zhu [9]	Taljsten [14]	Malek et al. [16]
Shear and normal stresses	Load cases	Point load at mid-span	General	UDL	UDL, point load at mid-span, two symmetric point loads	Single point load	General with some limitations
Shear stress	Axial deformations of beam	No	Partially considered*	Yes	No	Yes	Partially considered*
	Bending deformations of plate	No	Partially considered*	Yes	No	No	Partially considered*
	Shear deformations	No	No	No	Yes but incorrectly	No	No
	Boundary/continuity conditions at point load	Zero shear stress	-	-	Continuity in shear stress and its first derivative	Zero shear stress	Zero shear stress
	Other remarks	-	*Considered in stage 1 analysis which is for a fully composite section	-	Only general solutions are given with boundary conditions	-	*Stress at base of the original beam based on fully composite action
Normal stress	Bending deformations of beam	No	No	No	Yes	Yes	Yes
	Shear deformations	No	No	No	Yes but incorrectly	No	No
	Additional plate bending deformations due to interfacial shear	Yes	No	Yes	Yes	Yes	No

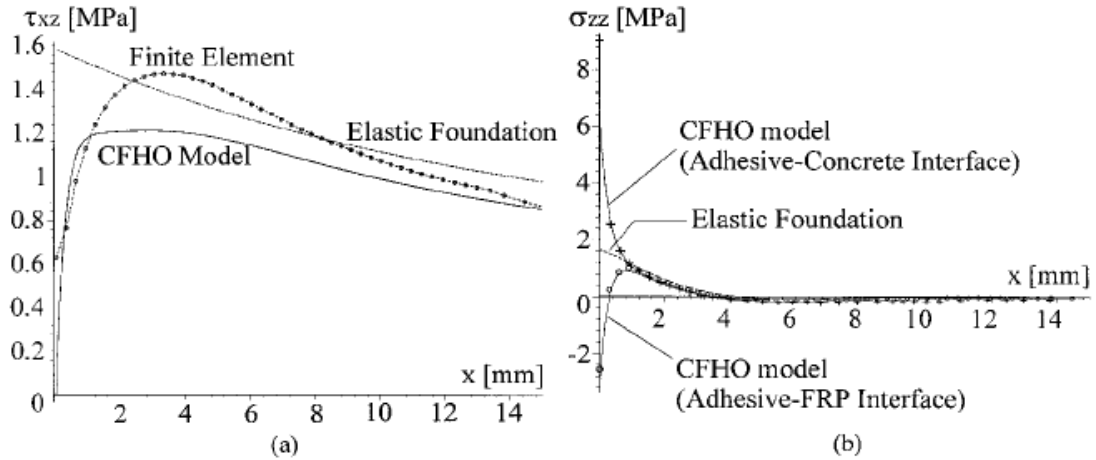


Fig.1.4. CFHO, Finite-Element, and Elastic Foundation Models Results: (a) Shear Stresses, (b) Peeling Stresses (Rabinovich and Frostig, 2000).

Although the 2PEF model can yield simple explicit closed-form solution, it has a few inherent drawbacks. First, it cannot satisfy all boundary conditions. As illustrated by Delale et al. (1981), the governing differential equation of the 2PEF model is sixth order, which requires only six boundary conditions; while there are eight boundary conditions available, including six force and two zero-shear stress boundary conditions. The zero shear stress conditions at two free edges of the adhesive layer have to be ignored in the 2PEF model. As a result, the shear stress at the edge of the adhesive layer reaches its maximum in the 2PEF model; while in reality it is zero (Fig.1.4 (a)). Second, the stress equilibrium condition of the adhesive layer is not satisfied due to the assumption of constant interfacial normal stress through the thickness of adhesive layer. A continuum analysis of the FRP-strengthened RC beams based on the Closed-form High-order (CFHO) theory (Rabinovich and Frostig, 2000) revealed that the normal stress along the concrete-adhesive (CA) interface was different from that along the FRP plate-adhesive (PA) interface, as shown in Fig. 1.4(b). The normal stress along the CA interface was tensile while the

one along the PA interface was compressive near the end of the FRP plate. Obviously, debond will occur along the interface where the normal interfacial stress is tensile, i.e., along the CA interface, not along the PA interface. This phenomenon has been verified by experimental study (Yuan et al., 2004).

One approach to overcome these drawbacks is to model the adhesive layer as a continuum. For instance, in an adhesive joint model presented by Allman (1977), the effect of bending, stretching, and shearing of the adherends and shearing and tearing of the adhesive layer were all taken into account. This continuum model provided a unified approach for various materials and satisfied all the boundary conditions of lap joints. Chen and Cheng (1983) presented another unified theory applicable to all kinds of lap joints with different adhesive layer stiffnesses that strictly satisfy all of the boundary conditions. They assumed that the interfacial shear stress remained constant through the thickness of adhesive layer, and the interfacial normal stresses varied linearly in the thickness direction. By minimizing the energy functional, two coupled fourth order ordinary differential equations were derived to solve for the interfacial stresses. Similarly, the CFHO theory, proposed by Frostig and Baruch (1990) for sandwich panels with transversely flexible core, also modeled the adhesive layer as a continuous medium. These continuum models (Frostig, 1993; Frostig and Shenhar, 1995; Frostig and Baruch, 1996; Frostig et.al., 1999) have distinct advantages over the 2PEF model such as: a) they satisfy the zero shear stress boundary conditions at the free edges of the adhesive layer; and b) they reveal the difference of the normal stresses along two interfaces. However, no explicit expression or

complicated explicit solutions were provided by these continuum models, making them difficult to be employed in engineering design (Teng et al., 2002).

Moreover, due to the wide application of the curved members, such as arch beams made of various materials and bridges in the form of arch, there is potential need to extend the existing analytical solutions for the straight beams to the curved ones. Recently, Lorenzis et. al. (2006) extended the Smith and Teng (2001)'s solution to analyze the curved members strengthened with thin plates. However, the assumption of the same curvature for the beam and the thin plate was also employed, which was unnecessary and could be removed. Until now, there are still very few analytical solutions of the FRP-strengthened curved structures, which can satisfy the zero shear stresses at free edges and give the different normal stresses at the two interfaces of the strengthened beams.

1.2.1.3 Numerical interfacial stresses analysis of FRP-concrete interface

Although the closed-form solutions are desirable for design, they are limited to simple geometry and boundary conditions. For the FRP-strengthened RC structures with complicated geometries and material properties, various numerical methods, such as the finite element method and the finite difference method, need to be employed. In addition, the numerical results can be used as the baseline to verify the analytical solutions (Wooley and Carver, 1971; Harris and Adams, 1984; Frostig et al., 1999; Taheri and Zou, 2004; Luo and Tong, 2004; Lee and Kim, 2005; Luo and Tong, 2007). Cooper and Sawyer (1979) conducted the FEA using fine meshes in the adhesive layer to study the variation of stresses in the adhesive layer. Their models also considered the nonlinear effect for higher magnitude loads. Similarly a nonlinear finite element

model (Li and Pearl, 2001) was established to compare with the experimental results and analytical solutions. Furthermore, to explore the three dimensional nature of the stress concentrations at the edge of the interface, Gonçalves et al. (2002) established a three dimensional finite element model using solid brick elements and specially developed interface elements.

The finite element analyses mentioned above mainly focus on the interface stresses in the adhesive joints. The complex configurations of the RC beam with embedded steel bars and the complicated mechanical behaviors of FRP composite and concrete make the modeling more difficult than the adhesive joints. Various modeling methods have been attempted to achieve better estimation for the response of the FRP-strengthened RC beams. There are mainly three types of elements widely used in the finite element models:

(1) Frame elements. A two-node displacement-based RC beam model was adopted by Aprile et al. (2001) to study the FRP-strengthened RC beams. The bond slip between the concrete and the strengthening plate was simulated by a triangle model. This simplified model was only suitable for shallow beams whose shear deformations were negligible. Recently an FRP force-based element model (Barbato, 2009) was developed based on the classical Euler - Bernoulli assumptions to study the load bearing capacity and deflection of the FRP-strengthened RC beams.

(2) Two-dimensional plate/shell elements. The finite element 2D models were widely adopted by many researchers (Jerome and Ross, 1997; Rahimi and Hutchinson, 2001; Camata et al, 2007). Since the early 2D finite element models only considered the materials as linear elastic,

these models only provided certain indications of the stress distributions along the interface at low loading levels (Malek et al., 1998). Recently nonlinear finite element models were widely adopted and the research focus shifted from the material properties to the interface debonding failure mechanisms between the concrete substrate and the adhesive layer (Rahimi and Hutchinson, 2001; Moller et al., 2005; Camata et al, 2007). In an experimental-analytical combined study (Camata et al, 2007), the actual crack patterns were considered in establishing the nonlinear finite element model using the smear crack model and an interface element. The numerical results matched up well with the experimental results. Both results showed that the crack propagation inside the concrete would cause interface debonding and concrete cover splitting failure.

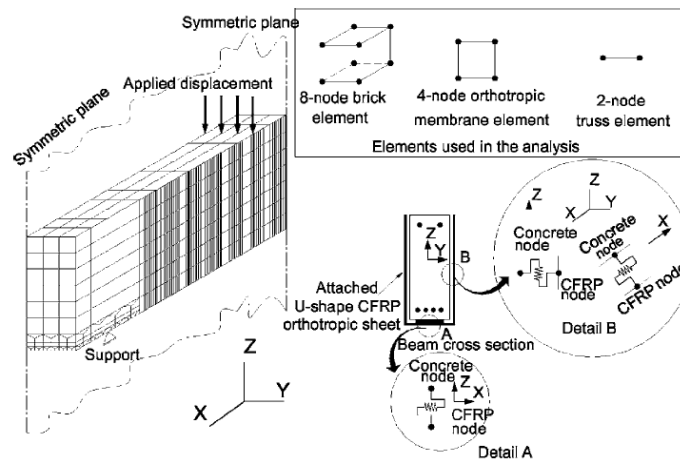


Fig.1.5. 3D finite element model of FRP-strengthened RC beam (Kotynia, 2008).

(3) Three-dimensional solid elements. The 3D finite element model can simulate the mechanical behavior of the FRP-strengthened RC beam in every phase (Neale et al., 2005; Kotynia, 2008). As shown in Fig.1.5, to establish a comprehensive 3D model, various elements have to be employed and different interface connections should be considered in detail. In such a

complex finite element model, the convergence and the high cost of computation would be prohibitive. In addition, it is difficult to implement very fine meshes and complex material models in such a compute intensive model.

1.2.1.4 Experimental study on FRP-strengthened RC beam

Considering the complexity of the material properties and the interface behavior of the FRP-strengthened RC beams, experimental methods are still the most reliable testimony to verify the analytical or numerical methods. At the early stage, many full scale experiments as shown in Fig.1.6 were conducted to explore the failure modes, the enhancement of the flexure strength, and the effect of different FRP composites (Saadatmanesh and Ehsani,1991; Ritchie et al., 1991; Sharif et al., 1994; Bonacci, 1996; Spadea et al., 1998; Buyle-Bodin et al., 2002; Smith and Teng, 2002). According to these experiments, the FRP composite materials can significantly improve the stiffness and strength of the specimens. The different failure modes shown in Fig. 1.2 were observed.

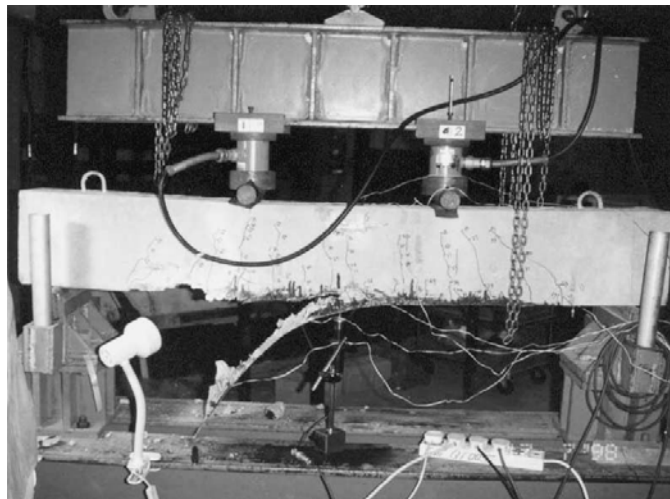


Fig.1.6. Full scale experiment on the FRP-strengthened RC beam (Smith and Teng, 2002).

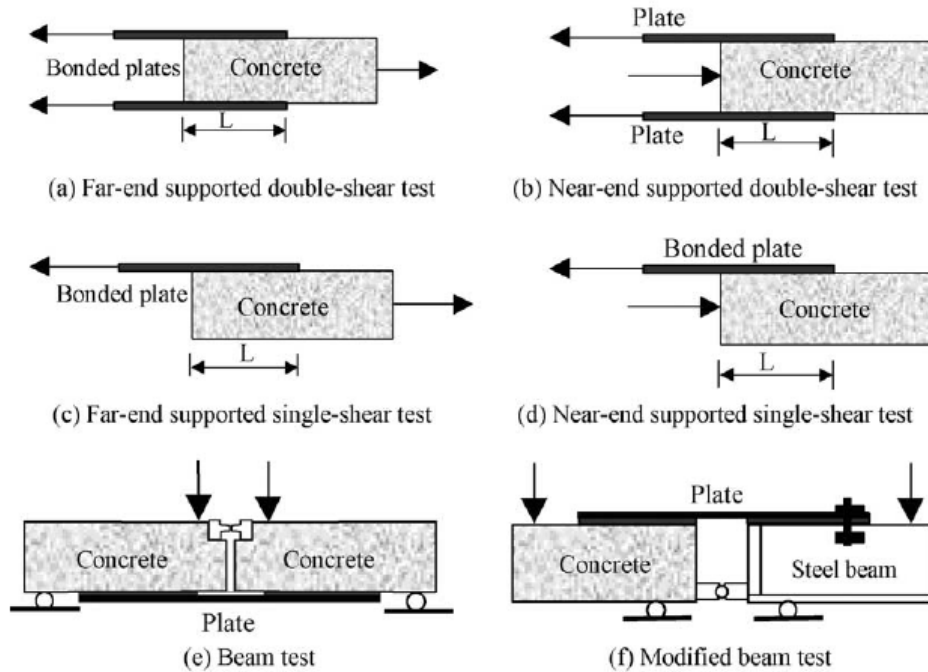


Fig.1.7. Classification of FRP-concrete bond tests (Chen et al., 2001).

The important role of the FRP-concrete interface is recognized from the failure modes of the full scale experiments. Hence, more attention has been focused on investigating the force transfer mechanism of the FRP-concrete interface. Many different test set-ups have been proposed to determine the bond strength and its major controlling factors. The most commonly used set-ups include: single shear test (Chajes et al., 1995a; Bizindavyi and Neale, 1999; Täljsten, 1997a), double shear test (Swamy et al., 1986; Kobatake et al., 1993; Brosens and van Gemert, 1997; Maeda et al., 1997), and modified beam test (Ziraba et al. 1995). Chen et al. (2001) classified the existing test set-ups into the following five types: (a) Far-end supported double-shear test, (b) Near-end supported double-shear test, (c) Far-end supported single-shear test, (d) Near-end supported single-shear test, (e) Beam test, and (f) Modified beam test (Fig. 1.7). A review on these FRP-concrete interface tests has been conducted by Chen and Teng (2001).

These experiments systematically studied the failure modes along the interface (Yao et al., 2005), the interface stress transfer mechanism (Täljsten, 1997a), and the effect of geometry and material properties on the failure modes (Yao et al., 2005).

1.2.2 LEFM analysis of FRP-strengthened RC beams

In the studies reviewed above, the material strength based methods have been used. To evaluate the integrity of the FRP-strengthened RC beam, the maximum interface stresses are compared with the corresponding ultimate interface bond strength. As demonstrated by Rabinovitch and Frostig (2001), the material strength based methods are only valid for ductile elasto-plastic materials. At the end of the FRP plate, a stress singularity exists, making it impossible to determine the interface stresses accurately. In such a case, the LEFM is a better tool to study the cracking mechanism along the FRP-concrete interface.

1.2.2.1 Introduction of the LEFM

Two types of LEFM methods are widely used: the stress intensity factor approach and the fracture energy method. These two approaches are equivalent or related to each other in certain cases. The stress intensity factor approach was proposed by Irwin (1957), in which the stress field around crack tips was described by the stress intensity factor. The stress intensity factor, K , is a function of the sample geometry, size and location of the crack, and the magnitude and modal distribution of the loads on the specimen. There is a unique critical stress intensity factor, K_c , for each material, which can be measured by experimental methods. Cracks will initiate when the actual K is greater than the critical stress intensity factor, K_c . There are three different fracture modes as shown in the Fig.1.8.

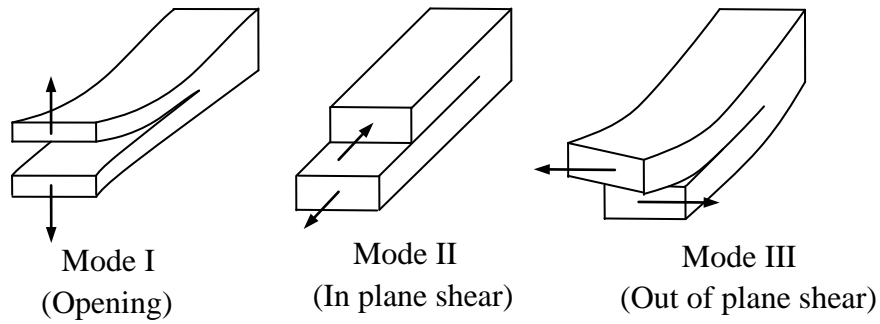


Fig.1.8. Three fracture modes.

However, since the stress intensity factor approach is not convenient in practice, many researchers prefer another LEFM method - the fracture energy method. This method is based on the Griffith's theory (Kaplan 1961), who proposed the energy-balance concept of fracture based on the principle of energy conservation laws of mechanics and thermodynamics. When the fracture energy applied at the crack tip is greater than the required fracture energy to create new surface area, the crack will propagate. The energy release rate, G , needs to be introduced to describe the energy dissipation near the crack tip in a manner independent of applied forces and specimen geometry. G is calculated by,

$$G = -\frac{\partial \Pi}{\partial A} = \frac{1}{b} \frac{\partial (W_d - U)}{\partial a}, \quad (1.1)$$

where U is the elastic strain energy; W_d is the work done by external forces; $\Pi = W_d - U$ is the potential energy of the system; ∂A is the increased crack surface; and ∂a is the increment length of the crack; b is the width. Therefore, the ERR is the amount of energy that will be released if the crack advanced a unit length. The crack will propagate if the actual G is greater than the critical energy release rate, G_c . The G_c can be measured through a variety of experimental

methods, such as the direct pull-off test (Mullins et. al.,1998), the four-point bending test (Kurtz, 2000), and the peel test (Karbhari and Engineer, 1996a).

The LEFM methods mentioned above only applies to the cracks in one material. However, for the layered structures such as FRP-strengthened RC beams, the cracks may lie at the interface between two materials. In this case, interface fracture mechanics accounting for the material mismatch across the bi-material interface should be used. Considering a crack lying along the interface between two different materials as shown in Fig.1.9, the elastic dependence of the bi-material system can be expressed by two non-dimensional moduli mismatch parameters α and β (Dundurs, 1969).

$$\alpha = \frac{\mu_2(\kappa_1 + 1) - \mu_1(\kappa_2 + 1)}{\mu_1(\kappa_2 + 1) + \mu_2(\kappa_1 + 1)}, \quad (1.2)$$

$$\beta = \frac{\mu_2(\kappa_1 - 1) - \mu_1(\kappa_2 - 1)}{\mu_1(\kappa_2 + 1) + \mu_2(\kappa_1 + 1)}, \quad (1.3)$$

where $\kappa_i = 3 - 4\nu_i$ for plane strain and $\kappa_i = \frac{3 - \nu_i}{1 + \nu_i}$ for plane stress. μ_i and ν_i are the shear modulus and Poisson's ratio of the material i .

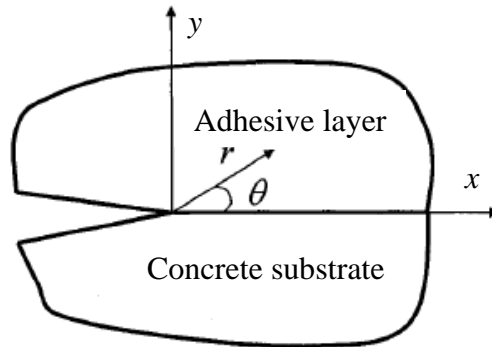


Fig.1.9. Interface crack between two different materials.

To describe the stress and displacement fields ahead of the interface crack tip, a term, bi-material constant ε , is defined as,

$$\varepsilon = \frac{1}{2\pi} \ln \left(\frac{1-\beta}{1+\beta} \right). \quad (1.4)$$

The stresses and the crack surface displacements at a distance r ahead of the interface crack tip can be expressed as (Rice, 1988; Hutchinson et. al., 1987),

$$\sigma_{22} + i\sigma_{12} = \frac{K}{\sqrt{2\pi r}} r^{i\varepsilon}, \quad (1.5)$$

$$\delta_2 + i\delta_1 = \frac{c_1 + c_2}{2\sqrt{2\pi}(1+2i\varepsilon)\cosh(\pi\varepsilon)} K \sqrt{r} r^{i\varepsilon}, \quad (1.6)$$

where $K = K_1 + iK_2$, $i = \sqrt{-1}$, $c_1 = \frac{\kappa_1 + 1}{\mu_1}$ and $c_2 = \frac{\kappa_2 + 1}{\mu_2}$.

1.2.2.2 LEFM analysis of FRP-concrete interface

Interface cracking is one of the most common failure modes in layered structures. The most classical solution on the interface crack in a layered structure was proposed by Suo and Hutchinson (1990). By using elementary beam theory, they obtained the closed-form solution of the ERR in an asymptotic approximation. The mode mix is obtained by solving a 2D continuum problem. Another classical solution was developed by Davidson et al. (1995) for the layered elastic structures using a crack-tip element (Schapery and Davidson, 1990). The analytical solutions of total ERRs and mode mixities were expressed in terms of the concentrate forces and the moments at the crack tip. These solutions were applicable to the cracks within or between isotropic or orthotropic materials. A mode mix parameter, Ω , was defined to conduct mode decomposition. This parameter had similar function as the angle ω (Suo and Hutchinson, 1990),

but it was obtained by the finite element analysis (FEA). The major drawback of these two existing solutions is that the transverse shear is ignored. By using the Suo and Hutchinson's solution (1990), Au and Büyüköztürk (2006a) obtained the ERR expressions of interface debonding in a FRP-strengthened RC beam through a tri-layer model. However, they failed to obtain the phase angles of the debondings, which required an auxiliary continuum analysis.

1.2.2.3 Numerical analysis of layered structures based on the LEFM

Besides the analytical solutions reviewed above, numerical methods based on finite element method are widely used to analyze interface fractures. To capture the ERRs and mode mixities, four methods have been developed: the Virtual Crack Closure Technique (VCCT), the crack surface displacement (CSD) method, the Virtual Crack Extension (VCE) method, and the Crack Surface Displacement Extrapolation (CSDE) method.

The VCCT method (Rybicki and Kanninen, 1977) is one of the most widely used numerical methods to calculate ERR due to its reliability and efficiency. The VCCT method can easily capture the total ERRs using the nodes' forces and displacements near the crack tip. It is also very stable in various situations since it is independent of element size. Only a moderate mesh is sufficient for this method. Beuth (1996) proposed a more general VCCT method to extract the ERRs within the orthotropic materials. More details of VCCT can be found in a review paper by Krueger (2004). Consider a quadrilateral element shown in Fig. 1.10. The equations to calculate the ERR components for the cracks in the homogeneous material could be expressed as (Krueger, 2004),

$$G_I = -\frac{1}{2\Delta a} \left(Z_i \{t_{11}(w_l - w_{l^*}) + t_{12}(w_m - w_{m^*})\} + Z_j \{t_{21}(w_l - w_{l^*}) + t_{22}(w_m - w_{m^*})\} \right), \quad (1.7)$$

$$G_{II} = -\frac{1}{2\Delta a} \left(X_i \{t_{11}(u_l - u_{l^*}) + t_{12}(u_m - u_{m^*})\} + X_j \{t_{21}(u_l - u_{l^*}) + t_{22}(u_m - u_{m^*})\} \right), \quad (1.8)$$

where

$$t_{11} = 6 - \frac{3\pi}{2}, \quad t_{12} = 6\pi - 20, \quad t_{21} = \frac{1}{2}, \quad t_{22} = 1. \quad (1.9)$$

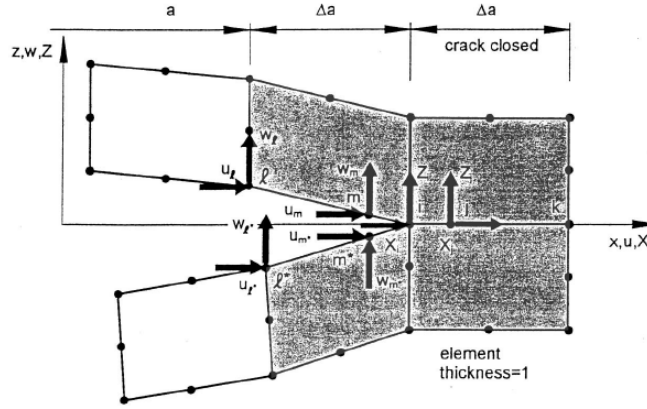


Fig.1.10. Quadrilateral element with quarter-point nodes (Krueger, 2004).

The major limitation of the VCCT is that it cannot predict accurate mode mixities for the bi-material interface cracks, as pointed out by Raju et al. (1988) and Raju and Fichter (1989). In their studies, the convergence of the ERR components for an interface crack was studied through a quasi three dimensional FEA on the edge-delamination at the 35/90 interface of an eight ply $[0/\pm 35/90]_s$ composite laminate under uniform axial loads. To overcome this drawback of the VCCT, Agrawal and Karlsson (2006) proposed a new method to calculate the mode mixity for a bimaterial interface crack through introducing a “normalizing length parameter” and defining a Δ -independent strain energy release based mode mixity. The accuracy of the mode mixities obtained by this method was proven to be acceptable as compared to other methods.

The second method to extract the ERRs and mode mixities is the cracked surface displacement (CSD) method (Matos et al., 1989). According to the Griffith's theory (Kaplan, 1961), the mode mixity and total ERR can be written as:

$$\psi = \arctan\left(\sqrt{\frac{H_{22}}{H_{11}}}\frac{\delta_x}{\delta_y}\right) - \varepsilon \ln\left(\frac{|x|}{h}\right) + \arctan(2\varepsilon), \quad (1.10)$$

$$G = \frac{\pi(1+4\varepsilon^2)}{8H_{11}|x|}\left(\frac{H_{11}}{H_{22}}\delta_y^2 + \delta_x^2\right), \quad (1.11)$$

where δ_y and δ_x are the opening and shearing relative displacements of the crack flanks as shown in Fig. 1.11. H_{11} , H_{22} , and ε are the bi-material constants, depending on the material compliances.

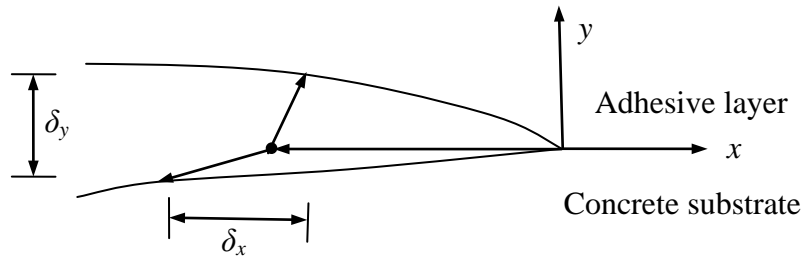


Fig.1.11. Crack tip opening geometry.

Based on the the relative nodal displacements obtained from the FEA, the mode mixities and total ERRs can be calculated by Eqs. (1.10) and (1.11). However, this method may be difficult to be implement if the crack surfaces are not straight. Moreover, due to the oscillations of the displacements near the crack tip (Fig.1.12), the total ERRs and mode mixities calculated using this method may be inaccurate (Berggren et al., 2006). A number of methods have been proposed to improve the accuracy of mode mixity. Davidson et al. (1995) proposed a modified CSD method by combining the CSD method and the VCCT method. Østergaard and Sørensen (2007) developed another CSD-based method, which was known as the Crack Surface

Displacement Extrapolation (CSDE) method. As demonstrated by Berggreen (2004), the CSDE method was stable in most cases. However, the linear extrapolation of the transition zone could lead to poor fitting in some cases. The CSDE method was used by Berggren et al. (2007) to study debonding of foam-cored beams. The accuracy of the CSDE method was verified through comparing the FEA results with the experimental results. The CSDE method was also used to obtain the interface fracture toughness of the sandwich structures under different mixed-mode loadings.

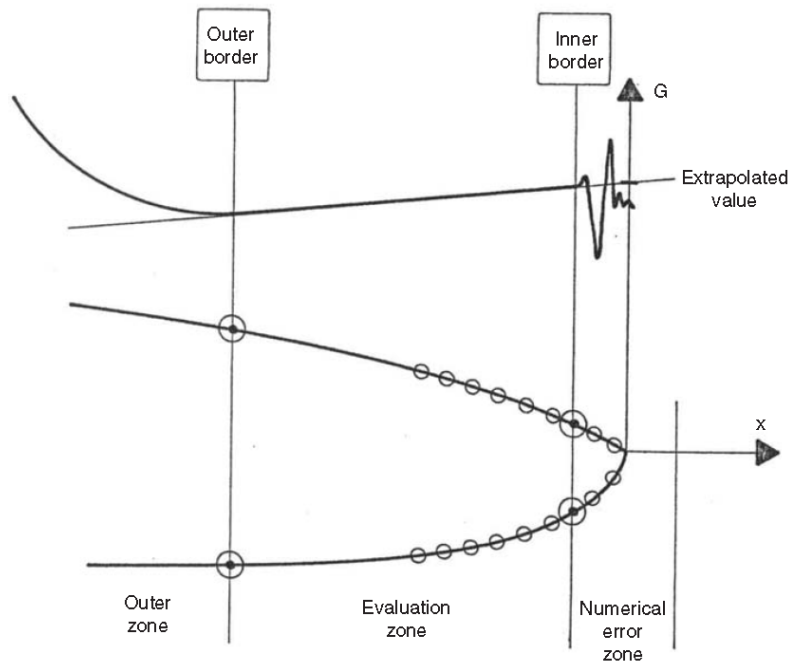


Fig.1.12. CSDE method presented schematically (Berggren et al., 2006).

Another finite element method is called the Virtual Crack Extension (VCE) method, which is an energy-based method proposed by Parks (Suo and Valeta, 1998). In order to compute the ERRs of the cracks in the linear or nonlinear materials, the VCE method calculates the variation of the total potential energy due to a virtual infinitesimal change in crack length.

Charalambides and Zhang (1995) further extended this method to the orthotropic bi-materials. Based on the J-integral method, the VCE method could determine the mode mixity of the crack using the displacement and stress fields far away from the crack tip. However, this method included a large matrix multiplication and needed a superelement representation to achieve the stiffness matrix for an element ring, which could significantly increase the CPU expense. Li and Carlsson (2001) employed the VCE method to analyze the tilted sandwich specimens with different configurations. The stress intensity factors and the mode mixities were obtained using various mesh refinements over a range of tilt angles. Au and Büyüköztürk (2006) also employed the VCE method to verify the accuracy of their tri-layer interface fracture model.

1.2.3 CZM approach for interface debonding in FRP-strengthened RC beams

It is necessary to clarify the term of “FRP-concrete interface” before discussing the delamination problems of the FRP-strengthened RC beams. According to many experiments (Kobatake et al., 1993; Chajes et al., 1995; Bizindavyi and Neale, 1999; Dai et al., 2005a), most of the interface debonding failures in FRP-strengthened RC beams occurred within a thin layer inside the concrete substrates. Therefore the FRP-concrete interface refers to the combination of the adhesive layer and a very thin concrete layer adjacent to it as shown in Fig. 1.13.



Fig.1.13. Definition of the FRP-concrete interface.

Numerous experimental studies have shown that the real stress-deformation relationship of the FRP-concrete interface is nonlinear (Karbhari and Engineer, 1996; Giurguitiu et al., 2001,

Lyons et al., 2002; Wan et al., 2004), rather than linear as assumed in the LEFM methods. Moreover, as illustrated by Suo and Hutchinson (1990), all of the interface fractures in nature are mixed-mode. Mathematically, the total energy release rate of an interface crack can be decomposed into two parts corresponding to the real and imaginary parts of its complex stress intensity factor. But these two parts do not bear the same physical meaning as those of a crack in the homogenous materials. Therefore, it is difficult to obtain the mode mixity of the FRP-concrete interface debonding if LEFM is used. As a matter of fact, no rigorous analytical solution of the mode decomposition has been conducted in all of the existing studies aforementioned. For these reasons, nonlinear fracture mechanics has gained more attentions and has been adopted by more and more researchers. Here, the nonlinear fracture mechanics refers to the use of a nonlinear bond stress-slip law, rather than the linear one as assumed in the LEFM, to describe the stress-deformation relationship of the FRP-concrete interface. By using a non-linear bond stress-slip law in the analytical model, the debonding process is essentially approached through the cohesive zone model (CZM).

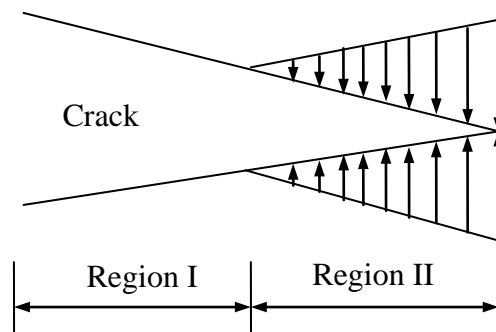


Fig.1.14. Regions of cohesive zone.

The CZM was introduced by Dugdale (1960) and Barenblatt (1962), who stated that the crack region can be divided into two parts as shown in Fig. 1.14. One part is stress free (region I) and the other part (region II) is subjected to certain cohesive stress. The cohesive stress is yield stress as demonstrated by Dugdale (1960). Barenblatt (1962) made several assumptions: 1) the extension of the cohesive zone was a constant for a given material, and 2) the stresses in the cohesive zone followed a certain distribution along the ligament coordinate, which was unique for a given material but independent of global loading situations. In a CZM, the locally damaged materials forming a narrow band of localized deformation may be modeled by nonlinear springs which represent the major physical variables. Compared with the single-parameter fracture approach of LEFM, the CZM considers the behavior of fracture processing zone and provides a method to achieve better understanding, characterizing, and modeling failure processes.

Moreover, the CZM unifies the crack initiation and growth into one model and can be easily formulated and implemented in numerical simulation, such as the “interface element” method in finite element code. Therefore the CZM has emerged as one of the most powerful tools to study the debonding of the FRP-concrete interface (Chajes et al., 1995; Bizindavyi and Neale, 1999; Dai et al., 2006; Wang, 2006a, b; Wang, 2007a, b; Wang and Zhang, 2007b; Rabinovitch, 2008).

1.2.3.1 Cohesive zone model of FRP-concrete interface

The CZM describes the relationships between the interfacial stresses and the relative displacements along the interface at the crack tip, which are also known as bond-slip laws.

Different CZMs have been developed to explore the delamination propagation in metals, ceramics, polymers, and other composites (Needleman, 1987; Rice and Wang, 1989; Chandra et

al., 2002). It has been shown in experiments (Wu and Yin, 2003; Nakaba et al., 2001) that a bi-linear bond-slip relationship (Fig.1.15) is a good approximation for the FRP-concrete interface behavior. This bond-slip law has three segments: (1) elastic stage when $\tau \leq \tau_f$ or $\delta \leq \delta_1$: stress increases linearly with slip; (2) softening stage when $\delta_1 < \delta \leq \delta_f$: stress decreases linearly with slip; and (3) debonding stage when $\delta_f \geq \delta$: stress is zero and FRP is separated from the concrete beam. Three fundamental parameters are critical to define the CZMs: 1) maximum bond strength, τ_f ; 2) slip corresponding to maximum bond strength, δ_1 ; 3) slip corresponding to ultimate bond strength, δ_f . The area underneath the bond-slip curve represents the mode II interfacial fracture toughness, G_c , which is the ERR required for complete debonding. A number of modifications of this bi-linear law have also been proposed for the FRP-concrete interface (Täljsten, 1996; Yuan et al., 2001; Wu et al., 2002; Yuan et al., 2004; Fallah et al., 2008).

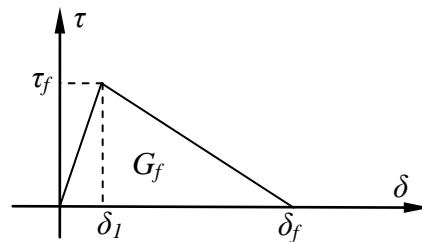


Fig.1.15. Bilinear CZM for shear stress bond-slip law.

Täljsten (1996) analyzed a plate bonded concrete prism using nonlinear bond-slip laws. He stated that only simple bond-slip laws could be used in deriving the analytical solutions for interface bonding and the general nonlinear bond-slip laws could only be employed in the numerical analysis. Yuan et al. (2001) investigated the interfacial stress transfer behavior and debonding process with various CZMs for the FRP-concrete interface. The closed-form solutions

of the interfacial shear stress were derived. Wu et al. (2002) studied the stress transfer and fracture propagation process in different adhesive joints using two nonlinear bond-slip laws. Similarly, Yuan et al. (2004) obtained analytical solutions for the interfacial shear stress and the load-displacement curve at different loading stages of a simple shear FRP-concrete specimen.

Intermediate crack induced debonding is still an ongoing research topic which attracts many researchers (Wu et al., 1997; Sebastian, 2001; Teng et al., 2003; Wang, 2006a, b; Liu et al., 2007; Smith and Gravina, 2007; Lu et al., 2007). Wu and Niu (2000) studied the intermediate flexure-cracks-induced interface debonding for different load cases using a linear shear stress-slip model. An energy-based methodology was developed to predict the initiation and debonding failure of a plate bonded concrete beam. Wang (2006a) used a bilinear CZM to study the whole failure process of an intermediate flexure-crack-induced debonding of an FRP-strengthened RC beam. Three different failure stages were compared and closed-form solutions for the interfacial stresses were obtained for the whole debonding process, as shown in Fig.1.16. Using similar analytical method, Wang (2006b) conducted parametric studies and compared the closed-form solutions with numerical solutions (Wu and Yin, 2003). Wang focused his analysis (Wang, 2006a, b) on FRP-strengthened RC beams with only one intermediate crack. Later, Liu et al. (2007), Smith and Gravina (2007), and Chen et al. (2007) extended the CZM method to multiple flexural cracks induced debonding of FRP-strengthened RC beams using iteration approaches. Chen et al. (2007) simplified the bi-linear bond-slip law by ignoring the linearly ascending branch to study the FRP bonded concrete joint with multiple intermediate cracks. Simple

expressions were obtained for the ultimate strength of the FRP bonded concrete joint with little loss of accuracy compared with those obtained by the bilinear CZM.

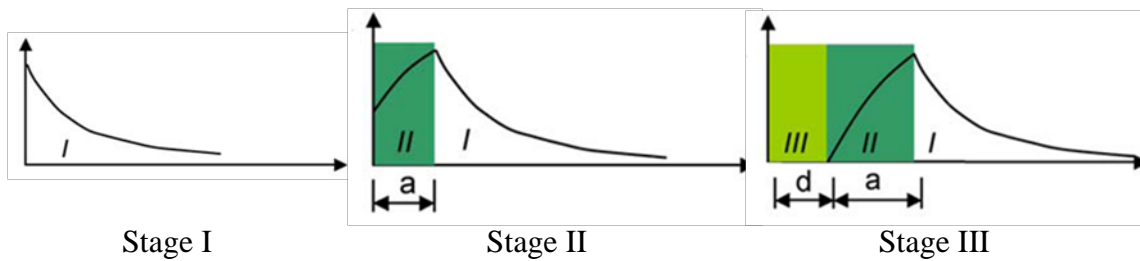


Fig.1.16. Intermediate crack induced interface debonding (Wang, 2006a).

All the studies mentioned above are mainly limited to the pure mode II interface debonding. The pure mode II interface debonding can only be induced at the locations of the flexure-cracks in the FRP-strengthened RC beams. As demonstrated by many researchers (Jones et al., 1988; Roberts and Haji-Kazemi, 1989; Malek et al., 1998) for the plate end debonding or the flexure-shear cracks induced interface debonding, both shear and peel stress concentrations exist along the interface. Therefore, neglecting the peeling stress can lead to discrepancies in the fracture parameters measured by different specimens (Chen and Teng, 2001). Until now very few studies have been conducted on the flexural-shear crack induced interface debonding because of its nature of complexity. Besides a displacement jump in the axial direction, a transverse displacement jump is also induced by the flexural-shear crack, which causes the interface debonding under peeling and shear loadings. Teng et al. (2003b) noted this and believed that the peeling effect was a secondary factor in interface debonding. Wang (2007a) developed a more general mixed-mode CZM for the debonding of a FRP-concrete adhesive joint. So far, no rigorous analytical solution was provided on the flexure-shear crack induced interface

debonding process using CZM. Recently, only a few numerical and experimental analyses have been conducted on the mixed mode debonding process (Niu et al., 2006; Pan and Leung, 2007). Niu et al. (2006) presented a finite element simulation of the diagonal-crack induced debonding along the FRP-concrete interface. Pan and Leung (2007) conducted a series of experimental studies on FRP-concrete interface debonding under pulling and peeling effects.

1.2.3.2 Experimental studies on the bond-slip laws of FRP-concrete interface

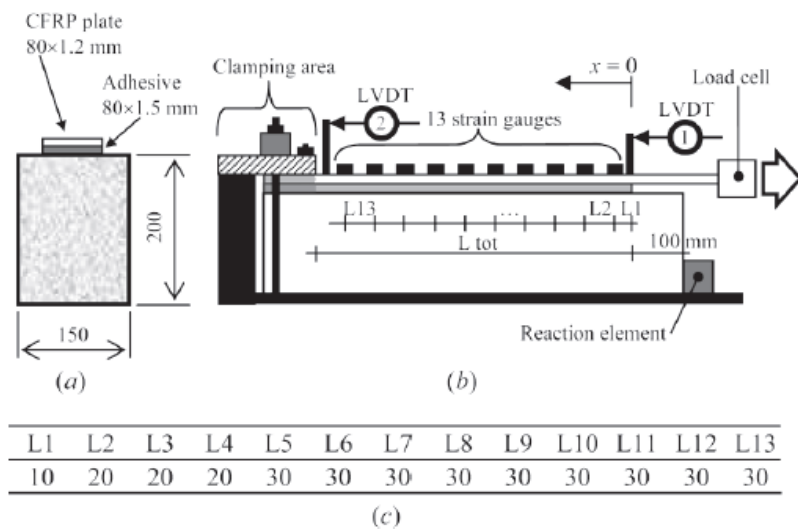


Fig.1.17. A typical experimental set-up (Mazzotti et al., 2008) to measure bond-slip law: (a) Specimen transverse section, (b) Side view with instrument positions and CFRP plate clamping system, (c) Spacing between strain gauges along the CFRP plate.

Many FRP-concrete bond specimens, such as single lap pull out tests (Chajes et al., 1996; Täljsten, 1997; Bizindavyi and Neale, 1999), double lap pullout bond tests (Gemert, 1980; Swamy et al., 1986; Sharif et al., 1994; Wu et al., 2002), and shear bending tests (Leung, 2001; Lorenzis et al., 2001) have been developed to investigate the mechanical behavior of the FRP-concrete interface. Fig. 1.17 shows a typical experimental setup to measure the nonlinear bond-slip law along the Carbon Fiber Reinforced Polymer (CFRP)-concrete interface.

As shown in Fig. 1.16, stress transfer along the FRP-concrete interface mainly focuses on the softening zone, not the whole bond length. Outside of this zone, the stress level is fairly low. Consequently, the stress transfer capacity in this zone is not mobilized. As a result, there exists an effective bond length beyond which load transfer capacity of the FRP-concrete interface bond keeps constant even though the bond length increase (Chen and Teng, 2001). The effective bond length was measured by many researchers (Horiguchi and Saeki, 1997; Maeda et al., 1997; Brosens and Gemert, 1997; Bizindavyi and Neale, 1999; Lorenzis and Nanni, 2001; Yuan et al., 2001; Pellegrino et al., 2008). The measured effective length ranged from 45mm to 275mm due to the differences of effective length definition and test configurations.

Recently a new technique named Digital Image Correlation (DIC) has been widely used as a tool to study the fracture mechanics of interface cracks. DIC is a computer aided vision technique to track the surface displacements of specimens and can be used as a non-destructive and non-contact measurement tool. Corr et al. (2007) and Moutrille et al. (2008) showed that the DIC technique was suitable to measure the displacement field and shear strain through the thickness of the adhesive layer. Ahmad et al. (2006) successfully determined the interfacial material behavior for FRP-concrete interface and fracture energy using the data obtained from the DIC system.

1.2.4 Durability of FRP-concrete interface

The term “durability” is used widely in many engineering fields. Its meaning and implications change frequently. It is necessary to clarify its definition in the field of civil engineering. According to Karbhari et al. (2003), “durability of a material or structure is defined

as its ability to resist cracking, oxidation, chemical degradation, delamination, wear, and/or the effects of foreign object damage for a specified period of time, under the appropriate load conditions, under specified environmental conditions”. Durability is often difficult to assess and requires a keen judgment of what constitutes sufficient duration and adequate performance. Many accelerated tests have been undertaken to provide information on the durability behavior of the FRP-concrete interface. The deterioration of the FRP-strengthened structures can be caused by various factors, among which seven are considered as major effects (Karbhari et al., 2003): moisture/solution, alkali, thermal (including temperature cycling and freeze-thaw), creep and relaxation, fatigue, ultraviolet, and fire. Experimental studies show that the long term physical, chemical, and mechanical properties of the FRP-strengthened RC specimens change gradually due to temperature, moisture, biological degradation, ultra-violet rays, chemical reactions, erosion, fatigue, and other natural phenomena (Toutanji and Gomez, 1997; Grace and Singh, 2005; Moutrille et al., 2008; Shahawy and Beitelman, 1999; Heffernan and Erki, 2004; Masoud et al., 2005; Dutta and Hui, 1996; Nairn, 2006). In the following sections, the effect of moisture, cyclic loading, and time-dependence of the adhesive on the long-term durability of the FRP-concrete interface will be reviewed.

1.2.4.1 Effect of moisture on FRP-concrete interface

Moisture attack is one of the most common and harmful imperilments for civil infrastructure. Extensive experimental studies have been carried out to explore the effect of moisture on the FRP-concrete interface (Chajes et al., 1995; Karbhari and Engineer, 1997; Toutanji and Gomez, 1997; Karbhari et al., 1998; Mukhopadhyaya et al., 1998; Green et al.,

2000; Myers et al., 2001; Davalos et al., 2008; Qiao and Xu, 2004; Grace and Singh, 2005; Chen et al., 2007; Wan et al., 2006; Au and Büyüköztürk, 2006; Ouyang and Wan, 2008a). Most of these studies focused on moisture's effect on the ultimate load bearing capacity, stiffness, and deformation of the specimens. Moisture effects on the fracture behavior of the FRP-concrete interface has also been explored by various experiments, such as the four-point bending test, the peel test, the three-point bending test, the modified DCB test, the shear test, etc. Literature related to moisture effects on FRP-concrete interface is summarized in Table 1.2.

It has been observed that ultimate strength of the FRP-concrete interface decreased dramatically after a period of exposure to different environmental conditions. The CFRP composites have better environmental resistance than the GFRP and AFRP composites. Similarly, the fracture toughness and flexure stiffness also reduced with time when exposing to various moisture conditions.

Table 1.2 Literature review of moisture effect on FRP-concrete interface.

Researchers	Test setup	Environmental conditions	Main research objects	Main conclusions about moisture effect
Chajes et al.,1995	(a)	(5) and (6)	Strength parameters	Ultimate strength of GFRP and CFRP bonded concrete specimen reduced about 36% and 19%, respectively
Karbhari and Engineer, 1996b	(b)	(1) - (5)	Strength parameters and Fracture toughness	More reduction in GFRP strengthened concrete specimen than that of CFRP bonded specimens.
Toutanji and Gomez ,1997	(a)	(1) and (6)	Strength parameters	Strength reductions ranged from 3% to 33% after 300 wet-dry cycles.
Karbhari and Zhao, 1998	(a)	(1) - (5)	Strength parameters	40% reduction in the flexure strength after 120 days exposure of moisture.
Mukhopadhyaya et al., 1998	(c)	(5) and (6)	Strength parameters	After wet/dry cyclings, the debonding took place near the FRP-concrete interface.
Myers et al., 2001	(a)	Combine (5) and (7)	Strength parameters	After 20 wet/dry cyclings test, flexure stiffness of GFRP and CFRP bonded specimens reduced about 85% and 55%, respectively.
Leung et al., 2004	(a)	(2), (6), and (7)	Strength parameters	The specimens exposed to water had lower strength than those subjected to heating-cooling cycling.
Murthy et al., 2002	(a)	(5), (7),(8), (9), and some combinations	Strength parameters	The CFRP sheets have better environmental resistance than GFRP and AFRP.
Lyons et al., 2002	(g)	(10) and (11)	Fracture toughness	No significant reduction at elevated temperature in 50% humidity. Severe degradation at 100°C in 95% humidity.

Continue on Table 1.2

Researchers	Test setup	Environmental conditions	Main research objects	Main conclusions about moisture effect
Qiao and Xu, 2004	(d)	(5) and (6)	Fracture toughness	With the increase of the number of cycles, both environmental conditions decrease the fracture toughness of the specimens.
Grace and Singh, 2005	(d)	(2), (3), (5), (6), and (12)	Strength parameters	Up to 87% reduction in the strength of the CFRP bonded specimens when exposed to moist environment.
Davalos et al., 2008	(i)	(5) and (6)	Fracture toughness	The fracture toughness reduced 72% at the end of 30 cycles of wet-dry conditions.
Wan et al., 2006	(g)	(2)	Fracture toughness	The bond mechanism degrades with time of exposure to water.
Au and Büyüköztürk, 2006	(b) and (h)	(2) and (10)	Fracture toughness	Bond interface failure observed after exposure to water conditions.
Ouyang and Wan, 2008a	(g)	(2)	Fracture toughness	Local bond interface region relative humidity can be correlated with deterioration of fracture energy.

Note: Test setups: (a) Four-point bending test; (b) Peel test; (c) Double lap shear test; (d) Three-point bending test; (f) Lap joint test; (g) Modified DCB test; (h) Shear test; (i) Single contoured cantilever beam test.

Environmental conditions: (1) Ambient condition; (2) In water; (3) In sea water or salt water; (4) Frozen; (5) Freeze-thaw cycling; (6) Wet-dry cycling; (7) Heating-cooling cycling; (8) Relative humidity cycling; (9) Chloride with indirect UV exposure; (10) Temperature effect; (11) Humidity effect; (12) Alkaline solution.

1.2.4.2 Fatigue of FRP-concrete interface

Generally the FRP composites have better fatigue performance than the conventional construction materials, like concrete, steel, and wood (Conolly, 1992). As the FRP composites are widely applied to upgrade or repair existing functionally obsolete structures, significant amounts of research have been conducted on the fatigue behavior of structures strengthened with the FRP composites. One of the earliest fatigue experiments was performed by Meier et al. (1992). In this study, the improvement of the fatigue performance due to the application of the FRP sheet was demonstrated by two fatigue tests of RC beams strengthened with a glass/carbon-hybrid sheet. Shahawy and Beitelman (1999) presented a study on both static and fatigue performances of the CFRP-strengthened RC beam. Accelerated fatigue experiments were performed on several specimens strengthened with CFRP lamination. It was observed that the stiffness of the FRP-strengthened RC beam was equal to or greater than that of the bare control RC beams. Recently, notable enhancements of fatigue life of RC beams strengthened with CFRP laminates have been observed by many researchers (Barnes and Mays, 1999; Papakonstantinou et al., 2001; Heffernan and Erki, 2004; Masoud et al., 2005).

As aforementioned, the FRP-concrete interface plays a very important role in the mechanical performance of the FRP-strengthened RC beams. An experimental study was conducted by Bizindavyi et al. (2003) to investigate the effect of cyclic loads on the bond stress-slip law. They used a power-law expression of the “*S-N*” curve to represent the effect of cyclic loading on the interface slip, the crack opening, and the strain profile of the FRP bonded joints. Similarly, Ko and Sato (2004) proposed another fatigue model for the FRP-concrete interface based on the tests of 54 specimens under cyclic loading. Recently, a comprehensive review on the fatigue behavior of FRP-strengthened RC beams was provided by Kim and Heffernan (2008).

1.2.4.3 Viscoelastic analysis of FRP-concrete interface

Epoxy, the most widely used adhesive in bonding FRP, exhibits viscoelastic properties (Brinson, 1982; Mirman and Knecht, 1990; Ferrier and Hamelin, 1999; Dean, 2007). Its material properties vary with time under different situations, especially in the regions of high stress concentrations. Such variation of material properties can induce redistributions of stresses and additional deformations, which can be significant during the service life of the structure and cause potential failure of the strengthening technique. Meshgin et al. (2009) found that the creep of epoxy could result in failure at the interface due to the combined effect of a relatively high ratio of shear stress to ultimate shear strength and a thick layer of epoxy. For this reason, the time-dependent behavior of FRP-strengthened concrete structures has become the focus of a number of recent studies both experimentally and numerically (Savoia et al., 2005; Diab and Wu, 2007a, b; Choi et al, 2007; Ascione et al., 2008; Meshgin et al., 2009; Ferrier et al., 2010; Choi et al., 2010). All of these studies showed that the FRP- concrete interface exhibited significant time-dependent behavior, and the shear stress to the shear strength ratio within the adhesive layer was a primary factor affecting the long-term behavior of the FRP-concrete interface.

Several rheological models were proposed to simulate the creep behaviors observed in the tests (Savoia et al., 2005; Diab and Wu, 2007a; Meshgin et al., 2009; Ferrier et al., 2010; Choi et al., 2010). Based on these rheological models, numerical methods including the finite difference method (Savoia et al, 2005) and the finite element analysis (Diab and Wu, 2007a, Choi et al., 2010) have been proposed to simulate the time-dependent behavior of the FRP-concrete interface. Numerical methods are usually very time-consuming in simulating the time-dependent behavior of structures because sufficient small step must be used to avoid error accumulation. Analytical solutions are much more efficient.

Based on the existing analytical solutions of the interface stresses (Roberts, 1989; Malek et al., 1998; Smith and Teng, 2001; Wang, 2003), a few viscoelastic analytical solutions were developed (Delale and Erdogan, 1981; Brinson, 1982; Mirman and Knecht, 1990). Delale and Erdogan (1981) proposed a viscoelastic solution for a symmetric adhesive joint by treating two adherends as elastic simple beams and the adhesive as a linearly viscoelastic spring. Due to the complexity of the mathematic manipulation, only one specific joint with two identical adherends was solved by the Laplace transform technique. The stress distributions in the adhesive layer were presented for three loading conditions, but no deformation solution was provided. Brinson (1982) correlated the bulk adhesive properties with the long term mechanical characteristics. A viscoelastic model was developed based on a modified Bingham's model, but no significant difference was observed. Mirman and Knecht (1990) proposed another simple viscoelastic model to study the creep behavior of the adhesive joint, in which the peeling stress and the creep deformation of the adhesive layer were ignored. Even though the formulas seemed to be simplified, numerical method was still required to solve the problem. Good agreement with the FEA result was achieved in a time-dependent "lead foot" example.

For the FRP-concrete interface, an analytical solution was presented by Plevris and Triantafillou (1994) to study the time-dependent behavior of an FRP-strengthened RC beam. To simulate the stress relaxation process, the concrete was modeled based on an age-adjusted effective modulus method and the FRP laminates were simulated using the Findley's model. The analytical results were confirmed by the experimental results by comparing the deflection at the mid span. However, in this model the adhesive layer was ignored, which turned out to be a crucial part of the structure. A fine incremental model was presented by Savoia et al. (2005) to study a FRP-strengthened RC tensile member considering concrete cracking, creep deformation

of the concrete, and viscous interface between concrete, steel bars, and FRP plates. Numerical examples were presented to show the improvement in both short term and long term behaviors due to the use of the FRP composites. Diab and Wu (2007a, b) and Diab et al., (2009) conducted a series of experiments to establish the time-dependent constitutive models of the FRP-concrete interface. Based on these experiments, Diab and Wu (2008) developed a finite element model to study the long term behavior of the FRP-concrete interface using an interface element modeled by the generalized Maxwell constitutive law as shown in Fig.1.18. In this model, several parameters had to be identified experimentally. Recently, Meshgin et al. (2009) investigated the creep of the epoxy adhesive at the FRP-concrete interface by conducting the double shear tests on nine specimens. Several rheological models such as the Burger's model, the Findley's model, and the modified Maxwell model, were evaluated based on the experimental results. It was also demonstrated that most of the creep deformation of the adhesive layer developed within a relatively shorter period compared to that of concrete. And the shear creep behavior of the adhesive at the interface depended on the ratio of shear stress to the ultimate shear strength and the time before loading.

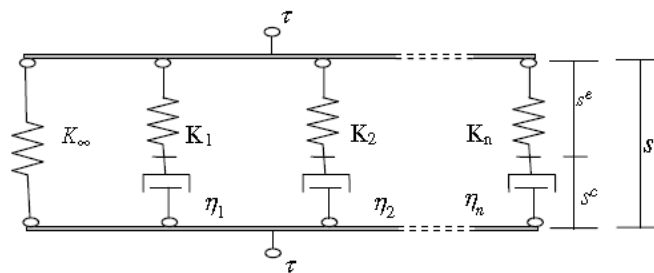


Fig.1.18. Rheological model for viscoelasticity of the adhesive layer (Diab and Wu, 2008).

1.2.5 Environment-assisted subcritical crack growth

An inherent problem of all the studies reviewed previous is that only the loads at the time of catastrophic failure are measured. However, the debonding is, as pointed out by RILEM

(Technical Committee FRP, 2003), “a gradual process where slow growth of cracks occurs at the interface.” The most distinct feature of these cracks is that they grow very slowly at an ERR that is only a fraction of the critical energy release rate G_c if environmental species exist. This slow crack growth is a long-term process involving synergistic action of environments and mechanical loads. The catastrophic interface debond (critical crack) is only the ending point of this process. For any structure which requires long-term stability, a resistance to this slow crack growth would be needed. To understand the degradation mechanism of the interface, and to gain the ability to accurately predict the long-term durability requires quantifying and analysis of the slow-debond growth process. The slow crack growth in adhesive joints in aggressive environments is referred to as environment-assisted subcritical cracking (Wiederhorn, 1968; Williams, 1973; Maugis, 1985; Ritter and Conley, 1992; Dauskardt et al., 1998; Gurumurthy et al., 2001; O’Brien et al., 2005; Singh et al., 2008) in corresponding to critical cracking when the catastrophic failure occurs. Sometimes it is also known as static fatigue or stress corrosion cracking in the literature (Krausz, 1978, 1979; Wiederhorn and Bolz, 1970; Ripling et al., 1971; Mostovoy and Ripling, 1971, 1972).

1.2.5.1 Subcritical crack growth in bulk glass

The subcritical crack growth may be driven by mechanical loads, residual stresses, elevated temperature, and moisture. It has been observed that the subcritical crack growth can reduce the strength of bulk materials like glasses (Wiederhorn, 1968; Freiman, 1974; Wiederhorn et al. 1982; Crichton et al. 1999; Suratwala and Steele, 2003; Etter et al. 2008), and polymers (Chan and Williams, 1983; Tonyali and Brown, 1986; Kook and Dauskardt, 2002; Korenberg et al., 2004; Kinloch et al., 2007).

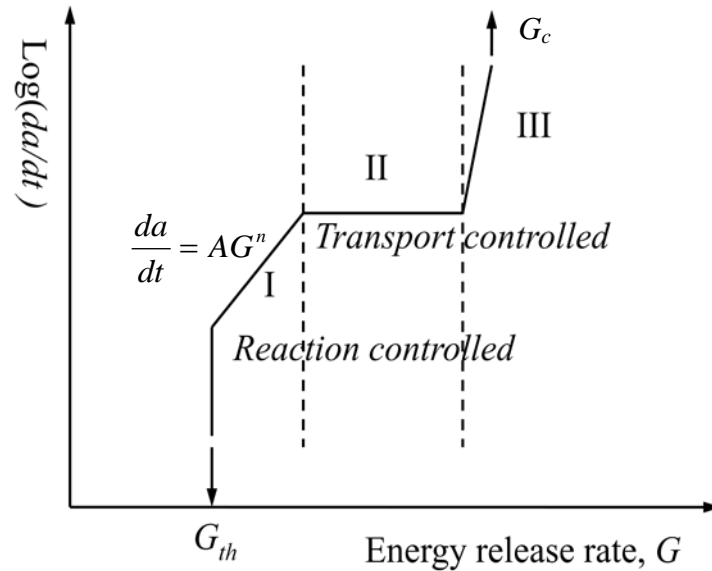


Fig.1.19. Schematic of typical environment-assisted debond.

Following the classic work of Wiederhorn et al. (1968), the environment-assisted subcritical crack growth can be treated as a synergistic interaction between strained adhesion bonds and environmental species. A schematic illustration of debond growth rate (da/dt) vs. driving ERR at the crack tip (G) is shown in Fig.1.19. This curve consists of three crack growth regions and a threshold “ G_{th} ”. If the driving ERR “ G ” is less than G_{th} , subcritical cracking will not initiate. In Region I, crack growth is so slow that the environmental species have enough time to transport to the crack tip to enable the environmental attack mechanism to occur readily. As a result, the crack growth rate depends on both the reaction rate and the mechanical load “ G ”. In Region II, crack growth is faster so that the debond growth is controlled by the availability of the environmental species. As a result, the crack growth rate is almost independent of the mechanical load “ G ”. In Region III, crack growth is much faster than the transportation rate of environmental species so that the environmental species cannot reach the crack tip. Consequently, the crack growth rate is only dependent on the mechanical load “ G ”. Measurements in this region do not provide any information about the interaction of environmental species at the crack

tip. Clearly, Region III describes the critical crack growth in the material and the corresponding G is the critical ERR “ G_c ”. It was believed that the mechanism of crack growth in Region III is independent of the environment species (Wiederhorn, 1968). However, it was found that the environment also can affect Region III (Wiederhorn et al., 1982).

As one of the first attempts, Wiederhorn (1967) used the DCB specimens to study the crack growth mechanism in glass by measuring the crack growth rates as a function of applied forces, using an optical microscope to follow the crack growth. The data in Fig.1.20 first showed the crack growth process, in which the crack velocity was plotted as a function of stress intensity factor in water vapor with different humidity levels. Similar curves were observed for other brittle inorganic materials (Freiman, 1974; Wiederhorn et al., 1982; Crichton et al., 1999).

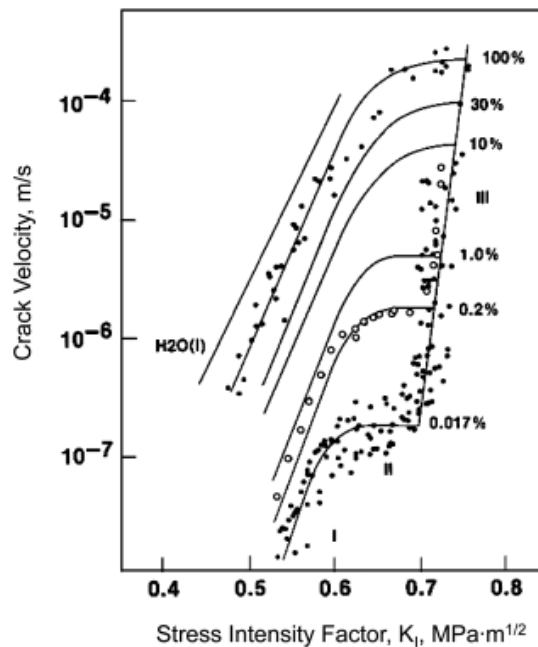


Fig.1.20. Crack growth data in soda-lime-silica glass (Wiederhorn, 1967).

The PH value effect of the solution on crack growth velocity was examined by some researchers (Simmons and Freiman, 1981; Michalske and Bunker, 1989; Gehrke et al., 1991). According to the experimental results (Gehrke et al., 1991), there was slight difference among

the water, the *NaOH* solution, and the *HCl* solution when the crack velocity was above 10^{-6} $\text{m}\cdot\text{sec}^{-1}$, as shown in Fig. 1.21. A plateau was observed at stress intensity factors less than 0.45 in the *NaCl* solution. Similar results were obtained by Simmons and Freiman (1981), and Michalske and Bunker (1989).

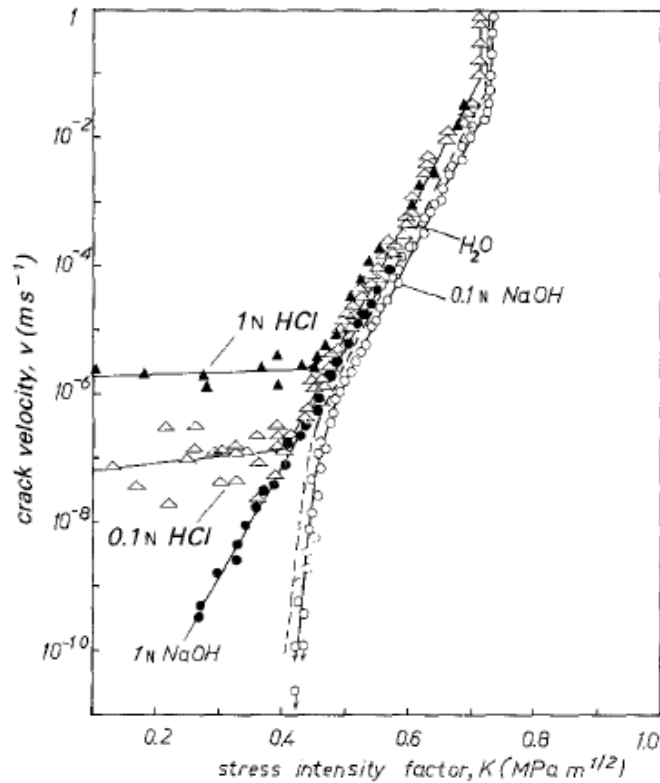


Fig.1.21. Crack growth of the $26\text{Na}_2\text{O} - 11\text{Al}_2\text{O}_3 - 63\text{SiO}_2$ glass in different corrosive media (Gehrke et al., 1991).

In addition, the effect of temperature on crack growth was also studied by many researchers (Wiederhorn and Bolz, 1970; Suratwala and Steele, 2003; Wiederhorn et al., 1978; Hibino et al. 1984). As shown in Fig. 1.22, the cracks within the soda lime silicate glass in water grew faster with temperature increasing (Wiederhorn and Bolz, 1970). This phenomenon was also observed by Hibino et al. (1984). However, Suratwala and Steele (2003) and Hibino et al (1984) found the crack growth rate decreased with increasing temperature for the silica glass in nitrogen gas with controlled concentration of water vapor.

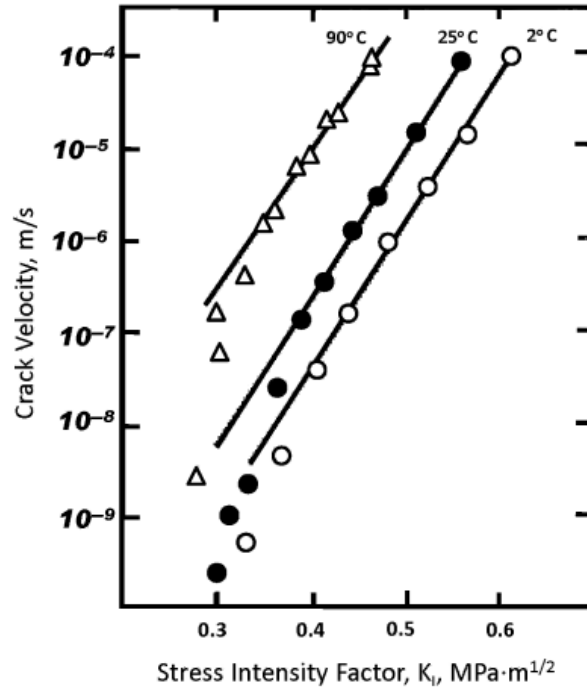


Fig.1.22. Soda-lime-silicate glass tested in water as a function of temperature (Wiederhorn and Bolz, 1970).

1.2.5.2 Subcritical crack growth in adhesive joints

Mostovoy, Ripling and co-workers (Ripling et al., 1971; Mostovoy and Ripling, 1971 and 1972) studied the aluminum/epoxy adhesive joints in the presence of water. During the tests, a tapered DCB specimen was studied under long time static loading. Mostovoy and Ripling (1971) observed that there existed a threshold value G_{th} , below which the subcritical crack would not occur in aqueous environments. However, Kinloch (1979) raised the doubt on the existence of such a threshold (Kinloch, 1979). In two recent studies conducted by Kinloch et al. (Korenberg et al., 2004; Kinloch et al., 2007) on crack growth in metallic joints bonded with a rubber-toughened epoxy adhesive, the three regions shown in Fig.1.19 were identified on the crack growth rate vs. G curves. Their studies have shown that different mechanisms of environmental attacks can be identified through the measured crack growth rate vs. G curves (Kinloch et al., 2007).

All the existing studies on the environment-assisted subcritical crack growth in adhesive joints are related to metallic joints. To date, no study has been published on the environment-assisted subcritical crack along the FRP-concrete interface. It seems that researchers of FRP-strengthened structures are not aware of the subcritical cracking even though some of their studies clearly show the slow growth of cracks. Meshgin et al. (2009) found that the FRP-concrete interface debonded 65 days after the specimen was subjected to a sustained load. This “delayed failure” is the result of subcritical cracking. The author thought this failure was “unexpected” and suggested further study on this “delayed failure” due to creep since it is not considered in the current design guidelines. The delayed failure due to creep was investigated by Diab and Wu (2007). In their study, the authors observed the debond growing slowly along the FRP-concrete interface until full debond occurred. An interesting phenomenon observed by Diab and Wu (2007) is that the debond locus can shift from within concrete to the epoxy-concrete interface if the debond speed is slow enough. Using the wedge driving tests, Park (2004) found that the debond growth rate along the epoxy-concrete interface depended on the driving energy release rate “ G ”, as shown in Fig.1.23. From this figure, it can be found that even with G as low as 20 J/m^2 , interface debond can still grow at a very low speed. This debond growth is “unexpected” according to the current critical-crack based fracture mechanics approach since the critical ERR measured are between 1000 to 3200 J/m (Dai and Ueda, 2006). Fig.1.23 provides the best evidence of the existence of subcritical cracking along the FRP-concrete interface. However, all of these existing studies tried to use the viscosity of the adhesive to explain the observed phenomenon, but this has been shown to be not sufficient by recent study of Kinloch et al. (2007). Their study suggested that the reaction with environmental species should be considered. More importantly, studies on other adhesive bonded joints showed that the

subcritical debond were more determined by the interphase zone of the adhesive/substrate, rather than by the adhesive layer.

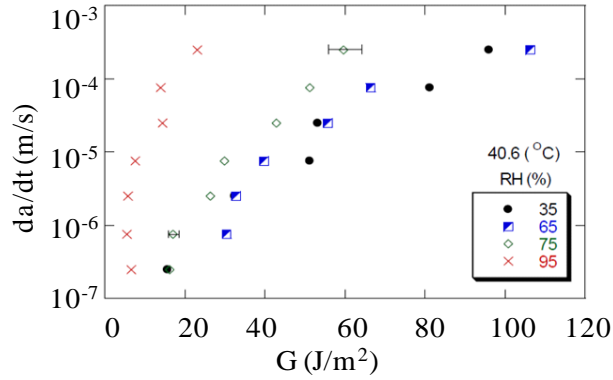


Fig.1.23. ERR varies with crack growth rate along the epoxy-concrete interface (Park, 2004).

Water has been identified as the primary agent in the degradation process of adhesive bonds (Leung et al., 2004; Grace and Grace, 2005). Water molecules can permeate the adhesive or concrete and preferentially migrate to the interfacial region. These water molecules can reduce the bonding strength of the adhesive/concrete interface through the displacement mechanism illustrated in Fig. 1.24 (Shimizu et al., 1999). To understand and quantify the role of moisture on the degradation of the adhesive-concrete interface, subcritical debond testing needs to be carried out in a large range of relative humidity and in water. For subcritical crack growth in Region I, existing studies on adhesive joints suggested that the G and da/dt could be fitted into a power-law expression (Johnsen et al., 2003),

$$da/dt = KG^n \exp(-Q/RT), \quad (1.13)$$

where K is a constant dependent on the materials and relative humidity; n is crack growth exponent.

Because the subcritical debond is thermally activated, a temperature term also appears in Eq. (1.13), where Q is the apparent activation energy of the interface; and R is the gas constant. It should be pointed out that Eq. (1.13) is not only valid for moisture-assisted subcritical debond

growth, but also for creep-induced (Park et al., 2006) and cyclic fatigue load-induced (He and Hutchinson, 1989) subcritical crack growth. The crack growth exponent n is an important kinetic parameter of the environment-assisted debonding because its value reflects the reaction mechanism at the crack tip (Kinloch et al., 2007). If the viscoelasticity process occurring at the crack tip controls the debond, the n should satisfy (Korenberg, et al., 2004),

$$\tan \frac{n\pi}{2} = \tan \delta_r, \quad (1.14)$$

where $\tan \delta_r$ is the viscoelastic loss factor. If the dominating mechanism of debond is moisture corrosion, n value should be much higher than that given by Eq. (1.14) (Kinloch et al. 2007).

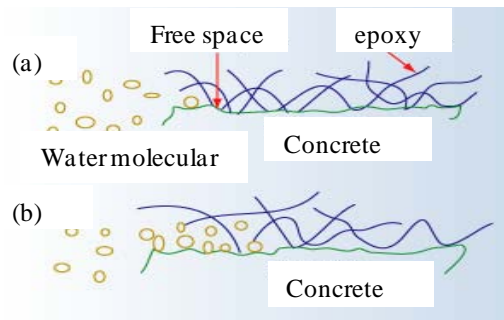


Fig.1.24. Competition between epoxy and water for surface sites leading to displacement of the adhesive from the surface: (a) Adhesive adsorbed at surface sites (b) Adhesive displaced from the surface sites (Shimizu et al., 1999).

1.3 Research needs and tasks

Since the interface debonding induced failure modes are the major failure modes of FRP-strengthened RC beams, it is of great importance to understand the mechanics, fracture, and long-term behavior of the FRP-concrete interface. Although extensive studies have been conducted on the strength and durability of the FRP-concrete interface, a number of research gaps still exist, which prevent the wide acceptance of FRP strengthening/repair in civil infrastructure. To fill these research gaps, this study proposes a life-cycle analytical framework

on the integrity and long-term durability of the FRP-concrete interface through a combined analytical, numerical, and experimental approach, as shown in Fig. 1.25.

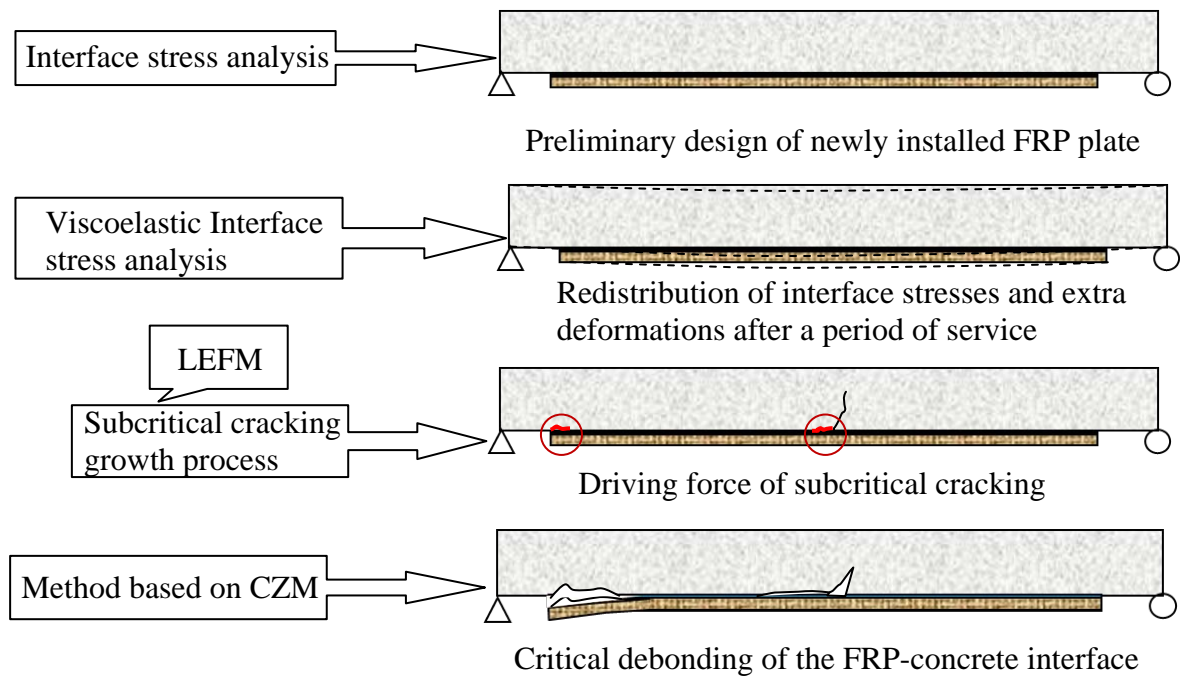


Fig.1.25. Research plan of the dissertation.

First of all, more accurate closed-form solutions of interface stresses along the FRP-concrete interface are needed for preliminary design and choice of materials. With the elapse of time, the interface stresses along the FRP-concrete interface will redistribute due to the strong time-dependent properties of the adhesive layer. Therefore, the interface stress based on an elastic solution needs to be modified to consider this feature of the adhesive layer so that it can be used to study the long term behavior of FRP-strengthened RC beams. Under service loads, a small delamination crack may develop along the FRP-concrete interface. These small cracks can grow slowly driven by service loads and environments during the whole service life of the strengthened structure. This process can be best described by environment-assisted subcritical cracking. To study this process, LEFM is needed to calculate the ERR at the crack tip. A systematic experimental program is also needed to relate ERR with crack growth rate under

different environment exposures. Once the small cracks reach the critical lengths, critical debonding will occur, leading to the premature failure of the strengthened structures. Nonlinear fracture mechanics based on CZM is needed to analyze this critical crack growth stage, as suggested by numerous experimental studies reviewed in the previous section. To address the above research needs, the following tasks were finished in this study:

- a) Develop a three parameter elastic foundation (3PEF) model to calculate the short-term interface stresses of FRP-strengthened RC beams.
- b) Develop a viscoelastic analytical solution of the interface stresses to study the long-term behavior of FRP-strengthened RC beams.
- c) Develop a LEFM solution to calculate the ERRs and mode mixities for the interface debonding in FRP-strengthened RC beams.
- d) Conduct subcritical cracking tests to relate the environment and mechanical loads to the crack growth rates along the epoxy-concrete.
- e) Simulate the critical interface debonding process induced by an intermediate crack in an FRP-strengthened RC beam using a bilinear CZM.

1.4 Organization of the dissertation

Background knowledge, research motivation and the specific tasks of this study have been discussed in the previous sections. The rest of the dissertation will be organized as follows:

Chapter 2 describes the details of the 3PEF model to predict accurate stresses along the FRP-concrete interface for preliminary design. The 3PEF model, which is an extension of the classic 2PEF model, assumes that the shear stress in the adhesive layer is constant through the thickness, and the interface normal stresses along two interfaces, concrete-adhesive and adhesive-FRP interfaces, are different. The validations of the solutions are confirmed by FEA.

In Chapter 3, to simulate the interface stress redistributions and creep deformations accumulated during service life due to the strong time-dependent feature of the adhesive layer, two viscoelastic solutions are developed for FRP-strengthened RC beams. In this solution, the RC beam and the FRP plate are modeled as isotropic elastic materials, whereas the adhesive layer is modeled with the 2PEF and the 3PEF models considering the viscoelastic material properties using the Standard Linear Solid (SLS) model. Closed-form solutions of the interface stresses and the deflections of FRP-strengthened RC beams are obtained using the Laplace transform technique and Zakian's method. The validation of this solution is verified by the FEA using the commercial software ABAQUS through a subroutine UMAT based on the SLS model.

Considering the small cracks that usually exist within the FRP-concrete interface, Chapter 4 develops the LEFM analytical solutions of the FRP-concrete interface debonding. A small segment at the vicinity of an interface crack tip is analyzed by two shear deformable bi-layered beam models. Closed-form solution of the total ERRs and mode mixities of the interface crack are obtained. The closed-form solutions are then verified by FEA using the modified CSD method.

Chapter 5 describes the details of wedge driving tests conducted on the environment-assisted subcritical debond growth within the FRP-concrete interface to clarify the slow crack growth process of the small cracks,. It has been found that water can substantially increase the crack growth rate along the epoxy-concrete interface. Fracture surface analysis suggests that the debonding mode can change from the cohesive failure within the concrete in critical crack growth to the adhesive failure along the epoxy-concrete interface in subcritical crack growth. The proposed subcritical debond testing can closely simulate the failure occurring during the service-life of the FRP-concrete interface. It also can allow interaction with environmental

species during testing and reduce the ambiguity associated with fracture energy due to the competitive effects of concrete curing, long-term concrete strength gaining.

Eventually, the small cracks will grow to the critical length, critical debonding will occur, leading to the premature failure of the structure. In chapter 6, the FRP-concrete interface debonding induced by a flexural-shear crack is analyzed using CZM. A bilinear bond-slip model is adopted to simulate the shear traction- separation law of the FRP-concrete interface, while the normal traction-separation law of the interface is approximated by a triangular model. Closed-form solutions of interfacial stresses and the axial force of the FRP plate are obtained for the whole debonding process and verified with FEA results. The peeling effect induced by the flexural-shear crack is accounted for and its effect on interface debonding is examined in detail. Parametric studies are conducted to provide a better understanding of the mode-dependent debonding process induced by the flexural-shear crack. This model provides a unified description of the debonding initiation and propagation, which can be used to analyze mixed-mode debonding of the FRP-concrete interface.

CHAPTER 2

A THREE-PARAMETER ELASTIC FOUNDATION MODEL FOR INTERFACE STRESSES IN FRP-STRENGTHENED BEAMS

2.1 Introduction

As discussed in chapter one, FRP-concrete interface are of great importance for the success of this type of strengthening technique. As the first stage of the life-cycle of the FRP-strengthening system, proper preliminary design is important. As for the newly installed FRP plate, it can be assumed the bonding is “perfect”. Since high interface stress concentrations at plate ends can induce premature failure of the strengthened beams, more accurate closed-form solutions of interface stresses along the FRP-concrete interface are needed.

Even though simple closed-form solution can be obtained by the classical GR’s model or other similar models (Roberts, 1989; Smith and Teng, 2001; Wang, 2003; Yang et al., 2004a), this kind of model has two major drawbacks. First, this model cannot predict that the normal stresses along the CA interface and the PA interface are significantly different. This feature is important because compressive stress does not contribute to the debonding of the interface, tensile normal stress along the CA interface suggests that debonding should occur along the CA interface, instead of the PA interface. Another shortcoming of the 2PEF model is that it cannot satisfy all the boundary conditions, because the governing differential equation of the 2PEF model is sixth order, which requires only six boundary conditions; while there are eight boundary conditions available, including six force and two zero-shear-stress boundary

conditions at two free edges of the adhesive layer. Those two zero shear stress boundary conditions have to be ignored in the 2PEF model. As a result, the shear stress at the free edge of the adhesive layer reaches its maximum in the 2PEF model; while it actually vanishes there.

To overcome the shortcomings of the 2PEF model, a new solution is developed for the FRP-strengthened beams by directly extending the 2PEF model to an innovative 3PEF model. This new model is made possible by introducing a new term related to the deflection of the adhesive layer, which is usually ignored in the 2PEF model, to express the shear strain in the adhesive layer. By considering the equilibrium condition of the adhesive layer, an eighth order governing differential equation of the FRP-strengthened RC beam is obtained in terms of the axial force of the RC beam. Therefore all the eight boundary conditions can be satisfied in this model. Explicit closed-form expressions of interface normal stresses along CA and PA interface and the interface shear stress are obtained by this new model. Since the formulation of this study is in the similar fashion of the 2PEF model (Delale et al. 1981, Wang 2003) and the solutions are in explicit closed-forms, the present model can be followed and implemented conveniently by other researchers.

The interfaces stresses of the FRP-strengthened straight beam will be first presented based on the 3PEF model. Even though the straight FRP-strengthened RC beams have been studied extensively, there are few studies published for the curved FRP-strengthened RC beams, which are also commonly used in practice. Elmalich and Rabinovitch (2009) conducted an FEA on the circular arches strengthened with composite materials. De Lorezis et al. (2006) developed an analytical solution of interfacial stresses between a curved beam and a bonded thin plate. This solution is based on the 2PEF model and therefore bears the aforementioned shortcomings of the 2PEF model. To remove the drawbacks in the existing analytical solution, this study extends the

3PEF model for straight beams bonded with thin plates to curved beams bonded with a thin plate. Closed-form solutions are obtained for the interface normal stresses along the CA and PA interfaces, and the shear stress within the adhesive layer in a thin plate strengthened straight and curved beam. The validation of these solutions is then verified by FEA results.

2.2 3PEF model for an FRP-strengthened straight beam

Consider a RC beam (adherend 1) strengthened by an FRP plate (adherend 2) through a thin adhesive layer as shown in Fig.2.1. Both the adherends and adhesive layer are the linear elastic and orthotropic materials to account for the most general situation. The adherends are modeled as two beams with the thicknesses of h_1 and h_2 , respectively, and are connected by an interface of thin adhesive layer with the thickness of h_0 . A simply support beam is considered (Fig.2.1) in this chapter for simplicity. Other boundary and loading conditions can also be solved by this model with very little modification.

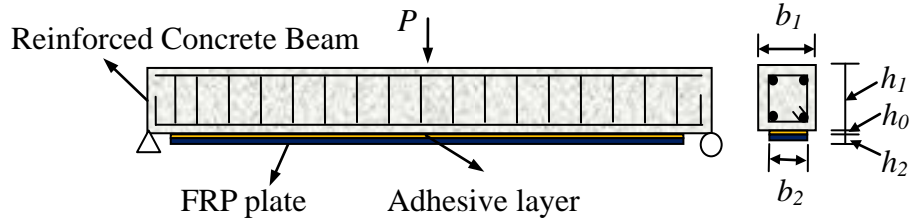


Fig.2.1. Simply supported FRP-strengthened RC beam under concentrated load.

2.2.1. Adhesively bonded bi-layered beam system

Considering a typical infinitesimal isolated body of the bi-layered beam system (Fig. 2.2). The deformations of in the FRP plate and RC beam can be written as:

$$U_i(x_i, z_i) = u_i(x_i) + z_i \phi_i(x_i), \quad W_i(x_i, z_i) = w_i(x_i), \quad (2.1)$$

where subscript $i = 1, 2$, represent the beam 1 (RC beam) and 2 (FRP plate) in Fig. 2.2, respectively; x_i and z_i are the local coordinates of beam i with x axis along the neutral axes of the

beam i . u_i , w_i , and ϕ_i ($i = 1, 2$) are the axial, transverse displacements, and rotation at the neutral axis of beam i , respectively; U_i and W_i ($i = 1, 2$) are the axial and transverse displacements of beam i , respectively.

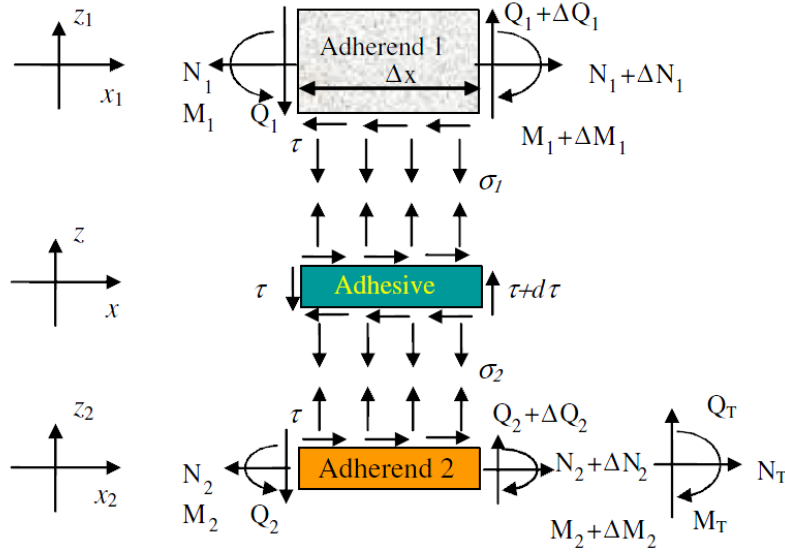


Fig.2.2. Free body diagram of the adhesively bonded bi-layered beam system.

By making use of the constitutive equations of individual layers, we can relate the forces and displacements of the beams as,

$$\frac{du_1}{dx} = \frac{N_1}{C_1}, \quad \frac{du_2}{dx} = \frac{N_2}{C_2}, \quad (2.2a)$$

$$\frac{dw_1}{dx} + \phi_1 = \frac{Q_1}{B_1}, \quad \frac{dw_2}{dx} + \phi_2 = \frac{Q_2}{B_2}, \quad (2.2b)$$

$$\frac{d\phi_1}{dx} = \frac{M_1}{D_1}, \quad \frac{d\phi_2}{dx} = \frac{M_2}{D_2}, \quad (2.2c)$$

where N_i , M_i and Q_i ($i = 1, 2$) are the resulting axial force, bending moments, and transverse shear forces in beam i ; C_i , D_i , and B_i ($i = 1, 2$) are the axial, bending, and shear stiffness, respectively, which are defined as,

$$C_i = E_i b_i h_i, \quad D_i = E_i \frac{b_i h_i^3}{12}, \quad \text{and} \quad B_i = \frac{5}{6} G_i b_i h_i, \quad (i = 1, 2),$$

where E_i and G_i are the longitudinal Young's modulus and shear modulus; b_i and h_i are the width and thickness of beam i .

Assuming that the shear stress is constant through the thickness of the adhesive layer, the following equilibrium equations can be established according to the free body diagram as shown in Fig. 2.2:

$$\frac{dN_1}{dx} = b_2 \tau, \quad \frac{dN_2}{dx} = -b_2 \tau, \quad (2.3a)$$

$$\frac{dQ_1}{dx} = b_2 \sigma_1, \quad \frac{dQ_2}{dx} = -b_2 \sigma_2, \quad (2.3b)$$

$$\frac{dM_1(x)}{dx} = Q_1(x) - \frac{h_1}{2} b_2 \tau(x), \quad \frac{dM_2(x)}{dx} = Q_2(x) - \frac{h_2}{2} b_2 \tau(x), \quad (2.3c)$$

where σ_1, σ_2 are the normal stresses along the CA interface and the normal stress along the PA interface, respectively; τ is the shear stresses in the adhesive.

Note that the overall equilibrium condition requires,

$$N_1 + N_2 = N_T, \quad (2.4a)$$

$$Q_1 + Q_2 + Q_a = Q_T, \quad (2.4b)$$

$$M_2 + M_3 + N_2 \left(\frac{h_1 + h_2}{2} + h_0 \right) = M_T, \quad (2.4c)$$

where N_T, Q_T , and M_T are the corresponding resulting forces with respect to the neutral axis of the FRP plate; Q_a is the shear force of the adhesive layer, which is given by $\tau b_2 h_0$.

2.2.2. 3PEF model for a straight adhesive layer

As shown in Fig.2.2, adherends 1 and 2 are connected together through a thin adhesive layer. The adhesive layer usually has a much lower extensional and bending stiffness than those

of the adherends. Therefore, the axial force and bending moment of the adhesive layer can be ignored. In the classical 2PEF model of the adhesive layer, the peel stresses acting on the top and bottom surfaces of the adhesive layer are assumed identical (Fig. 2.3a), i.e., $\sigma_1 = \sigma_2$. Then the equilibrium condition of the adhesive layer gives,

$$\frac{d\tau}{dx} = 0. \quad (2.5a)$$

Eq. (2.5a) suggests that the shear stress is a constant along the x -direction, which contradicts the shear stress distribution predicted by the 2PEF model. To remove this contradiction, we can assume that the peel stresses along these two surfaces have different values, as shown in Fig. 2.3(c). Then, we have,

$$\frac{d\tau}{dx} = \frac{\sigma_1 - \sigma_2}{h_0}. \quad (2.5b)$$

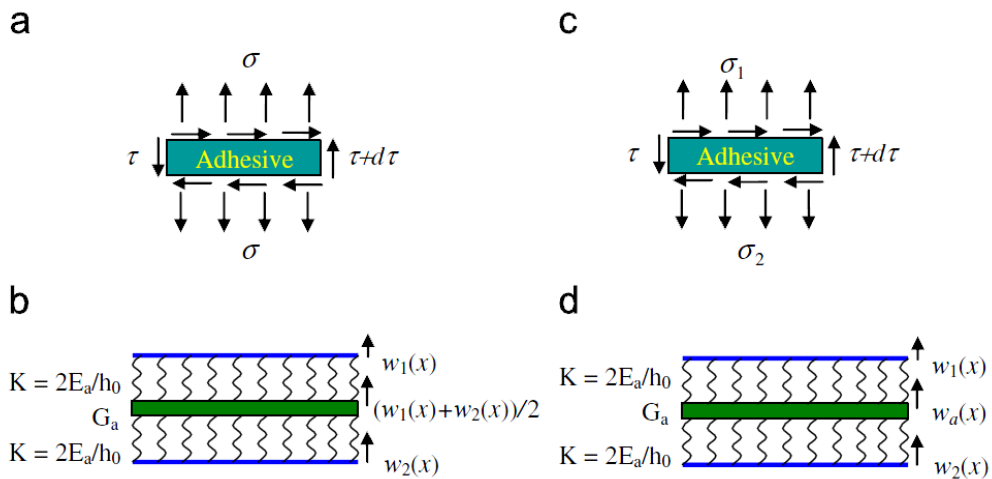


Fig.2.3. Extending (a, b) 2PEF model to (c, d) 3PEF model for the adhesive layer.

To accommodate Eq. (2.5b), the adhesive layer cannot be represented by the classical 2PEF model, so a 3PEF model should be used. As shown in Fig. 2.3(d), the adhesive layer in this new model is treated as two linear-normal spring layers with the stiffness of $K = 2E_a/h_0$

interconnected by a shear layer with the shear constant of G_a . Then, the strain-stress relations of the adhesive layer can be written as,

$$\sigma_1 = \frac{2E_a}{h_0}(w_1 - w_a), \quad \sigma_2 = \frac{2E_a}{h_0}(w_a - w_2), \quad (2.6a)$$

$$\tau = \frac{G_a}{h_0} \left(u_1 - \frac{h_1}{2} \phi_1 - u_2 - \frac{h_2}{2} \phi_2 \right) + \frac{dw_a}{dx}, \quad (2.6b)$$

where E_a and G_a are the Young's modulus and the shear modulus of the adhesive, respectively. w_a is the deflection at the mid-plane of the adhesive layer. Stress-strain relations given by Eq. (2.6) have the same shapes as those of the 3PEF model (Kerr, 1965; Avramidis and Morfidis, 2006). The stiffness of the normal spring, K , is chosen following the same reasoning used in the 2PEF model. Eq.2.6 (a) is equivalent to assuming that the peel strain is constant through the upper and lower halves of the adhesive layer. It also can be found that Eq.(2.6) is not the exact two-dimensional, elastic equilibrium equation of the adhesive layer in the thickness direction. Therefore, the present model is not a continuum model.

The 2PEF model is a special case of the current model. As illustrated in Fig. 2.3(b), the 3PEF model would be equivalent to the 2PEF model if the deflection of the mid-plane of the adhesive layer were assumed to be $(w_1 + w_2)/2$, instead of an independent new parameter, w_a , in the present 3PEF model.

2.2.3. Governing differential equation of an FRP-strengthened straight RC beam

Substituting the first equation in Eq. (2.3a) into Eq. (2.6b) and differentiating the above equation with respect to x yields,

$$\frac{d^2 N_1}{dx^2} = \frac{b_2 G_a}{h_0} \left(\frac{N_1}{C_1} - \frac{h_1}{2} \frac{M_1}{D_1} - \frac{N_2}{C_2} - \frac{h_2}{2} \frac{M_2}{D_2} \right) + b_2 G_a \frac{d^2 w_a}{dx^2}. \quad (2.7)$$

Differentiating Eq. (2.6a) twice, we have,

$$\frac{d^2 w_a}{dx^2} = \frac{d^2 w_1}{dx^2} - \frac{h_o}{2E_a} \frac{d^2 \sigma_1}{dx^2}. \quad (2.8)$$

Differentiating the constitutive equation Eq. (2.2b) and considering the Eqs. (2.3c) and (2.2c) yeild,

$$\frac{d^2 w_1}{dx^2} = \frac{1}{B_1} \frac{dQ_1}{dx} - \frac{d\phi_1}{dx} = \frac{1}{B_1} \left(\frac{d^2 M_1}{dx^2} + \frac{h_1}{2} \frac{d^2 N_1}{dx^2} \right) - \frac{M_1}{D_1}. \quad (2.9)$$

Differentiating the first equation of equilibrium equation Eq. (2.3b) twice and considering the Eq. (2.3c) lead to,

$$\frac{d^2 \sigma_1}{dx^2} = \frac{1}{b_2} \frac{d^3 Q_1}{dx^3} = \frac{1}{b_2} \left(\frac{d^4 M_1}{dx^4} + \frac{h_1}{2} \frac{d^4 N_1}{dx^4} \right). \quad (2.10)$$

Substituting Eqs. (2.8) to (2.10) into Eq. (2.7) yields,

$$\frac{d^4 M_1}{dx^4} + A_{11} \frac{d^4 N_1}{dx^4} + A_{12} \frac{d^2 N_1}{dx^2} + A_{13} \frac{d^2 M_1}{dx^2} + A_{14} N_1 + A_{15} M_1 = A_{16} N_T + A_{17} M_T, \quad (2.11)$$

where

$$\begin{aligned} \xi &= \frac{h_1}{2D_1} - \frac{h_2}{2D_2}, \quad \eta = \frac{1}{C_1} + \frac{1}{C_2} + \frac{(h_1 + h_2)h_2}{4D_2}, \quad A_{11} = \frac{h_1}{2}, \quad A_{12} = \frac{2E_a}{G_a h_o} \left(1 - \frac{bG_a h_1}{2B_1} \right), \quad A_{13} = -\frac{2b_2 E_a}{h_o B_1}, \\ A_{14} &= -\frac{2b_2 E_a}{h_o^2} \eta, \quad A_{15} = \frac{2b_2 E_a}{h_o} \left(\frac{1}{D_1} + \frac{\xi}{h_o} \right), \quad A_{16} = -\frac{2b_2 E_a}{h_o} \frac{1}{C_2}, \quad A_{17} = -\frac{2b_2 E_a}{h_o^2} \frac{h_2}{2D_2}. \end{aligned} \quad (2.12)$$

Based on Eq. (2.6a), we have,

$$\sigma_1 + \sigma_2 = \frac{2E_a}{h_o} (w_1 - w_2). \quad (2.13)$$

Differentiating the above equation twice and considering Eq. (2.2b) yield,

$$\frac{d^2 \sigma_1(x)}{dx^2} + \frac{d^2 \sigma_2(x)}{dx^2} = \frac{2E_a}{h_o} \left(\frac{1}{B_1} \frac{dQ_1(x)}{dx} - \frac{d\phi_1(x)}{dx} - \frac{1}{B_2} \frac{dQ_2(x)}{dx} + \frac{d\phi_2(x)}{dx} \right). \quad (2.14)$$

Differentiating Eq. (2.5b) twice and considering Eq. (2.3a) give,

$$\frac{d^2\sigma_2(x)}{dx^2} - \frac{d^2\sigma_1(x)}{dx^2} = \frac{h_0}{b_2} \frac{d^4N_1(x)}{dx^4}. \quad (2.15)$$

Eq. (2.3b) can also be rewritten as,

$$\frac{dQ_2(x)}{dx} = -b_2\sigma_2(x) = h_0 \frac{dN_1^2(x)}{dx^2} - \frac{dQ_1(x)}{dx}. \quad (2.16)$$

Substituting Eqs. (2.15) and (2.16) into Eq. (2.14) and considering the constitutive Eq.

(2.3) and (2.4), we have,

$$\frac{d^4M_1}{dx^4} + B_{11} \frac{d^4N_1}{dx^4} + B_{12} \frac{d^2N_1}{dx^2} + B_{13} \frac{d^2M_1}{dx^2} + B_{14}N_1 + B_{15}M_1 = B_{17}M_T, \quad (2.17)$$

where

$$B_{11} = \frac{h_1 + h_0}{2}, B_{12} = -\frac{b_2E_a}{h_0} \left(\frac{h_1}{2} \left(\frac{1}{B_1} + \frac{1}{B_2} \right) + \frac{h_0}{B_2} \right), B_{13} = -\frac{b_2E_a}{h_0} \left(\frac{1}{B_1} + \frac{1}{B_2} \right),$$

$$B_{14} = \frac{b_2E_a}{h_0} \frac{h_1 + h_2}{2D_2}, B_{15} = \frac{b_2E_a}{h_0} \left(\frac{1}{D_1} + \frac{1}{D_2} \right), B_{17} = \frac{b_2E_a}{h_0} \frac{1}{D_2}. \quad (2.18)$$

Subtracting Eq. (2.11) from Eq. (2.17) and rearranging give,

$$\frac{d^2M_1}{dx^2} = C_{11} \frac{d^4N_1}{dx^4} + C_{12} \frac{d^2N_1}{dx^2} + C_{13}N_1 + C_{14}M_1 + C_{15}N_T + C_{16}M_T, \quad (2.19)$$

where

$$C_{11} = -\frac{B_{11} - A_{11}}{B_{13} - A_{13}}, C_{12} = -\frac{B_{12} - A_{12}}{B_{13} - A_{13}}, C_{13} = -\frac{B_{14} - A_{14}}{B_{13} - A_{13}},$$

$$C_{14} = -\frac{B_{15} - A_{15}}{B_{13} - A_{13}}, C_{15} = -\frac{A_{16}}{B_{13} - A_{13}}, C_{16} = \frac{B_{17} - A_{17}}{B_{13} - A_{13}}. \quad (2.20)$$

Subtracting Eq. (2.17) multiplied by A_{13} from Eq. (2.11) multiplied by B_{13} and after rearranging, we have,

$$\frac{d^4 M_1}{dx^4} = D_{11} \frac{d^4 N_1}{dx^4} + D_{12} \frac{d^2 N_1}{dx^2} + D_{13} N_1 + D_{14} M_1 + D_{15} N_T + D_{16} M_T, \quad (2.21)$$

where

$$D_{11} = -\frac{A_{11}B_{13} - A_{13}B_{11}}{B_{13} - A_{13}}, D_{12} = -\frac{A_{12}B_{13} - A_{13}B_{12}}{B_{13} - A_{13}}, D_{13} = -\frac{A_{14}B_{13} - A_{13}B_{14}}{B_{13} - A_{13}},$$

$$D_{14} = -\frac{A_{15}B_{13} - A_{13}B_{15}}{B_{13} - A_{13}}, D_{15} = \frac{A_{16}B_{13}}{B_{13} - A_{13}}, D_{16} = \frac{A_{17}B_{13} - A_{13}B_{17}}{B_{13} - A_{13}}. \quad (2.22)$$

Differentiating Eq. (2.19) twice and substituting into Eq. (2.21) give,

$$M_1 = E_{11} \frac{d^6 N_1}{dx^6} + E_{12} \frac{d^4 N_1}{dx^4} + E_{13} \frac{d^2 N_1}{dx^2} + E_{14} N_1 + E_{15} N_T + E_{16} M_T, \quad (2.23)$$

where

$$E_{11} = \frac{C_{11}}{D_{14} - C_{14}^2}, E_{12} = \frac{C_{12} + C_{14}C_{11} - D_{11}}{D_{14} - C_{14}^2}, E_{13} = \frac{C_{13} + C_{14}C_{12} - D_{12}}{D_{14} - C_{14}^2},$$

$$E_{14} = \frac{C_{14}C_{13} - D_{13}}{D_{14} - C_{14}^2}, E_{15} = \frac{C_{14}C_{15} - D_{15}}{D_{14} - C_{14}^2}, E_{16} = \frac{C_{14}C_{16} - D_{16}}{D_{14} - C_{14}^2}. \quad (2.24)$$

Substituting Eq. (2.23) back into Eq. (2.19) yields the governing equation as,

$$F_{11} \frac{d^8 N_1}{dx^8} + F_{12} \frac{d^6 N_1}{dx^6} + F_{13} \frac{d^4 N_1}{dx^4} + F_{14} \frac{d^2 N_1}{dx^2} + F_{15} N_1 + F_{16} N_T + F_{17} M_T = 0, \quad (2.25)$$

where

$$F_{11} = E_{11}, F_{12} = E_{12} - C_{14}E_{11}, F_{13} = E_{13} - C_{11} - C_{14}E_{12}, F_{14} = E_{14} - C_{12} - C_{14}E_{13},$$

$$F_{15} = -C_{13} - C_{14}E_{14}, F_{16} = -C_{15} - C_{14}E_{15}, F_{17} = -C_{16} - C_{14}E_{16}. \quad (2.26)$$

Eq. (2.25) is the governing equation of the adhesively bonded bi-beam system shown in Fig. 2.2 based on the 3PEF model. Compared with that based on the 2PEF model (Wang 2003), Eq. (2.25) is two orders higher and allows for implementing all the boundary conditions. If the

widely accepted assumption which states the normal stress is uniform within the adhesive layer is adopted, Eq. (2.16) becomes,

$$\frac{dQ_1}{dx} = b_2\sigma = \frac{b_2E_a(w_1 - w_2)}{h_0}. \quad (2.27)$$

Differentiating the above equation twice more results in,

$$\frac{d^3Q_1}{dx^3} = \frac{b_2E_a}{h_0} \left(\left(\frac{1}{B_1} + \frac{1}{B_2} \right) \frac{dQ_1}{dx} - \frac{M_1}{D_1} + \frac{M_2}{D_2} \right). \quad (2.28)$$

Substituting equilibrium equation Eq. (2.3c) into the above equation and considering Eq. (2.4), we can find that two coefficients in Eq. (2.17) should be changed to account for this assumption:

$$B_{11} = \frac{h_1}{2}, \quad B_{12} = -\frac{b_2E_a}{h_0} \left(\frac{h_1}{2} \left(\frac{1}{B_1} + \frac{1}{B_2} \right) \right). \quad (2.29)$$

As a result, F_{11} becomes zero and the governing equation reduces to sixth order. In this case, the 3PEF model degrades to the classical 2PEF model. Furthermore, if the second term of Eq. (2.6) is ignored, as did in the existing 2PEF model, the shear strain in the adhesive layer is written as:

$$\gamma_{xz} = \frac{1}{h_0} \left(u_1 - \frac{h_1}{2} \phi_1 - u_2 - \frac{h_2}{2} \phi_2 \right). \quad (2.30)$$

Following the similar procedures to obtained Eq. (2.14), we have:

$$\frac{d^2N_1}{dx^2} - \frac{G_a}{h_0} \eta N_1 + \frac{G_a}{h_0} \xi M_1 = -\frac{G_a}{h_0} \left(\frac{N_T}{C_2} + \frac{h_2}{2D_2} M_T \right). \quad (2.31)$$

The 2PEF model governing equation of adhesively bonded bi-layer beam system is then obtained as (Wang 2003),

$$\frac{d^6N_1}{dx^6} + a_4 \frac{d^4N_1}{dx^4} + a_2 \frac{d^2N_1}{dx^2} + a_0N_1 + a_M M_T + a_N N_T = 0, \quad (2.32)$$

where

$$a_4 = -b_2 \left(\frac{G_a}{h_0} \left(\frac{\xi h_1}{2} + \eta \right) + \frac{E_a}{h_0} \left(\frac{1}{B_1} + \frac{1}{B_2} \right) \right), \quad a_2 = \frac{b_2 G_a}{h_0} \left(\frac{b_2 G_a}{h_0} \left(\frac{1}{B_1} + \frac{1}{B_2} \right) \left(\frac{\xi h_1}{2} + \eta \right) + \left(\frac{1}{D_1} + \frac{1}{D_2} \right) \right),$$

$$a_0 = -\frac{b_2 E_a G_a}{h_0^2} \left(\frac{\xi (h_1 + h_2)}{2D_2} + \left(\frac{1}{D_1} + \frac{1}{D_2} \right) \eta \right), \quad a_M = \frac{b_2^2 E_a G_a}{h_0^2} \left(\frac{\xi}{D_2} + \frac{h_2}{2D_2} \left(\frac{1}{D_1} + \frac{1}{D_2} \right) \right),$$

$$a_M = \frac{b_2^2 E_a G_a}{C_2 h_0^2} \left(\frac{1}{D_1} + \frac{1}{D_2} \right).$$

2.2.4. Interface stress of an FRP-strengthened straight RC beam

The governing equations Eq. (2.25) can be solved through the characteristic equation, and they are expressed by the forces in beam 1:

$$N_1 = \Delta N_1 + N_{1c}, \quad M_1 = \Delta M_1 + M_{1c}, \quad Q_1 = \Delta Q_1 + Q_{1c}, \quad (2.33)$$

where

$$\Delta N_1 = \sum_{i=1}^8 c_i e^{R_i x}, \quad \Delta M_1 = \sum_{i=1}^8 c_i S_i e^{R_i x}, \quad \Delta Q_1 = \sum_{i=1}^8 c_i T_i e^{R_i x}, \quad (2.34)$$

and

$$N_{1c} = -\frac{F_{16}}{F_{15}} N_T, \quad M_{1c} = \left(E_{15} - \frac{E_{14} F_{16}}{F_{15}} \right) N_T + \left(E_{16} - \frac{E_{14} F_{17}}{F_{15}} \right) M_T, \quad Q_{1c} = \frac{dM_{1c}}{dx} + \frac{h_1}{2} \frac{dN_{1c}}{dx}. \quad (2.35)$$

S_i and T_i are given by,

$$S_i = E_{11} R_i^6 + E_{12} R_i^4 + E_{13} R_i^2 + E_{14}, \quad T_i = S_i R_i + h_2 R_i / 2, \quad (2.36)$$

where R_i ($i = 1, \dots, 8$) are the eight roots of the characteristic equation of Eq. (2.25). c_i ($i = 1, \dots, 8$) are the eight coefficients to be determined by the boundary conditions. N_{1c} , M_{1c} , and Q_{1c} are the particular solutions of Eq. (2.25) which are the internal forces of beam 1 if the whole adhesively bonded beam is treated as a composite beam (Wang and Qiao 2004a). Eq. (2.33) shows that the internal forces of the beam consist of two parts: the exponential terms (ΔN_1 , ΔM_1 ,

and ΔQ_I) which is the local disturbance of the relative soft adhesive layer, and steady terms (N_{1c} , M_{1c} , and Q_{1c}) which are the internal forces of the beam based on composite beam theory.

By using Eq. (2.3), the interface stresses are obtained as,

$$\sigma_1 = \Delta\sigma_1 + \sigma_{1c}, \quad \sigma_2 = \Delta\sigma_2 + \sigma_{2c}, \quad \tau = \Delta\tau + \tau_c, \quad (2.37)$$

where

$$\Delta\sigma_1 = \sum_{i=1}^8 \frac{c_i T_i R_i}{b_2} e^{R_i x}, \quad \Delta\sigma_2 = \sum_{i=1}^8 \left(\frac{c_i T_i R_i}{b_2} + \frac{h_0 c_i R_i^2}{b_2} \right) e^{R_i x}, \quad \Delta\tau = \sum_{i=1}^8 \frac{c_i R_i}{b_2} e^{R_i x}, \quad (2.38)$$

and

$$\sigma_{1c} = \frac{1}{b_2} \frac{dQ_{1c}}{dx}, \quad \sigma_{2c} = -\frac{1}{b_2} \frac{dQ_{2c}}{dx}, \quad \tau_c = \frac{1}{b_2} \frac{dN_{1c}}{dx}. \quad (2.39)$$

Similar to the internal forces, the interface stresses are also composed of two parts, the exponential terms representing the local stresses concentration near the plate ends, and the steady terms representing the composite beam solutions.

2.2.5. Boundary conditions of an FRP-strengthened straight RC beam

To determine the coefficients c_i in the above solutions, necessary boundary conditions are needed. Consider the three-point bending test shown in Fig. 2.1, in which a concentrated force P is applied to the beam at a distance x_P from the left end of the FRP plate. To simplify the calculation, we can only take the bonded zone as shown in Fig. 2.4(a) for analysis. The external forces applied to the concrete beam (N_L , M_L , Q_L , N_R , M_R , and Q_R) can be easily determined by equilibrium analysis. In the conventional way (Rabinovitch and Frostig, 2000; Smith and Teng, 2001), this beam is divided into two segments, I and II, as shown in Fig. 2.4(a). For each segment, individual solutions are written as:

$$N_1^{I,II} = \sum_{i=1}^8 c_i^{I,II} e^{R_i x} + N_{1c}^{I,II}, \quad M_1^{I,II} = \sum_{i=1}^8 c_i^{I,II} S_i e^{R_i x} + M_{1c}^{I,II},$$

$$Q_1^{I,II} = \sum_{i=1}^8 c_i^{I,II} T_i e^{R_i x} + N_{1c}^{I,II}, \quad \tau^{I,II} = \frac{1}{b_2} \sum_{i=1}^8 c_i^{I,II} e^{R_i x} + \tau_{1c}^{I,II}. \quad (2.40)$$

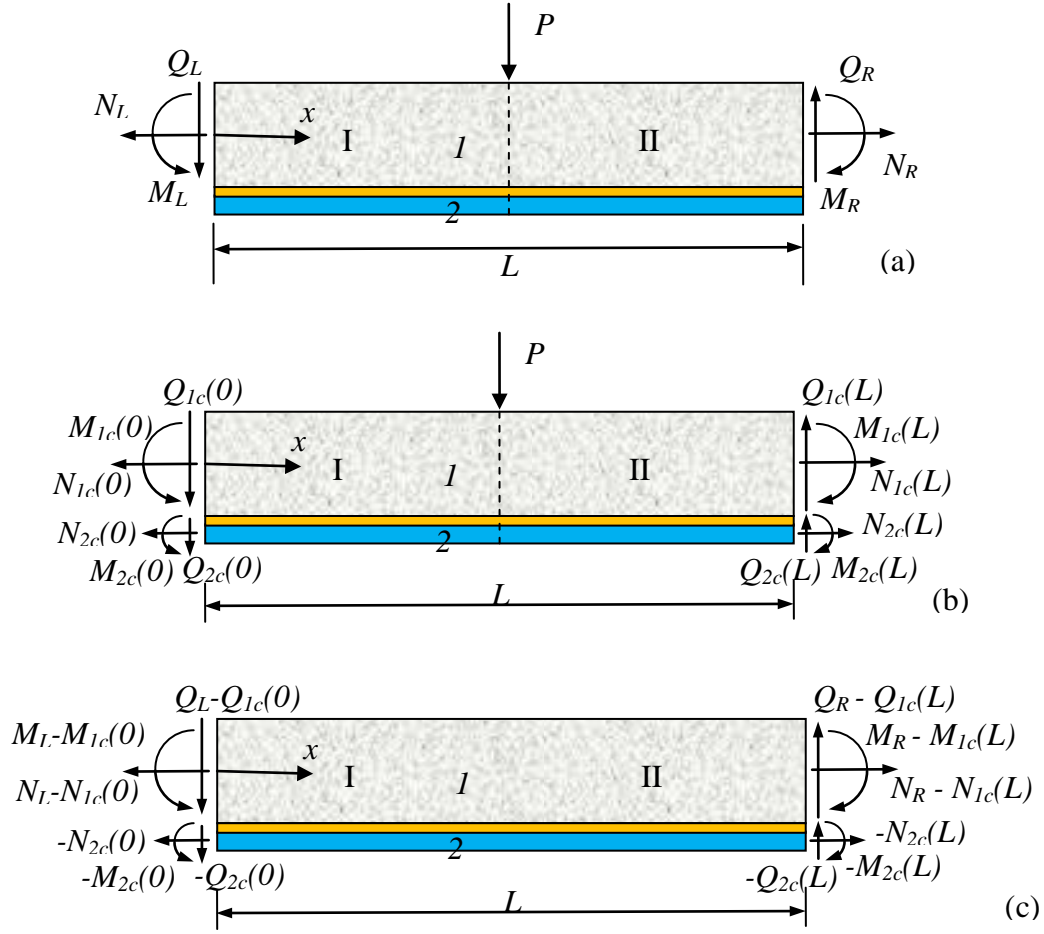


Fig.2.4. Implement boundary conditions of the straight FRP-strengthened beam using the principle of superposition.

To determine sixteen coefficients in Eq. (2.40), eight boundary conditions and eight continuity conditions at the loading point are used:

$$N_1^I(0) = N_L, M_1^I(0) = M_L, Q_1^I(0) = Q_L, \tau^I(0) = 0. \quad (2.41)$$

$$N_1^I(L) = N_R, M_1^I(L) = M_R, Q_1^I(L) = Q_R, \tau^I(L) = 0. \quad (2.42)$$

$$N_1^I(x_p) = N_1^{II}(x_p), M_1^I(x_p) = M_1^{II}(x_p), Q_1^I(x_p) = Q_1^{II}(x_p) + P, \tau^I(x_p) = \tau^{II}(x_p),$$

$$\sigma_1^I(x_p) = \sigma_1^{II}(x_p), \sigma_2^I(x_p) = \sigma_2^{II}(x_p), \frac{d^2\sigma_1^I(x_p)}{dx^2} = \frac{d^2\sigma_1^{II}(x_p)}{dx^2}, \frac{d^2\sigma_2^I(x_p)}{dx^2} = \frac{d^2\sigma_2^{II}(x_p)}{dx^2}. \quad (2.43)$$

where superscript *I* and *II* represent segment *I* and *II*, respectively. Clearly, the above approach is very tedious, especially when more than one discontinuities of loading exists in the bonded zone. To eliminate this tedious procedure used in the existing studies, a new approach is proposed to implement boundary conditions using the principle of superposition. As shown in Eqs. (2.33) and (2.37), the beam forces and interface stresses (Fig. 2.4a) can be obtained by superposing the composite beam solutions (Fig. 2.4b) and the local disturbance (Fig. 2.4c).

In Fig. 2.4(b), the boundary forces with subscript “c” at the left and right ends of the beam are given by Eq. (2.35). Besides the forces applied at two ends, there is no external force applied to the beam within the bonded region in Fig. 2.4(c). Therefore, there is no need to divide the bonded zone into two segments, and thus, the complex calculation induced by implementing continuity conditions is avoided. In this case, the eight coefficients can be determined using the following boundary conditions:

$$\Delta N_1^I(0) = N_L - N_{1c}(0), \Delta M_1^I(0) = M_L - M_{1c}(0), \Delta Q_1^I(0) = Q_L - Q_{1c}(0), \tau^I(0) = 0. \quad (2.44)$$

$$\Delta N_1^I(0) = N_R - N_{1c}(0), \Delta M_1^I(0) = M_R - M_{1c}(0), \Delta Q_1^I(0) = Q_R - Q_{1c}(0), \tau^I(L) = 0. \quad (2.45)$$

The above procedures are applicable to general loading conditions and are particularly efficient when more than one external loading discontinuities existing within the bonded zone. It should be pointed out the interface stress obtained by this method shows some difference from those obtained by the conventional method described by Eqs. (2.41) - (2.43) at the loading point. However, stress concentration at loading point is much smaller than that at the FRP plate end and, therefore, not critical to the debonding analysis.

2.2.6. Verifications and comparisons of FRP-strengthened straight RC beams

As verifications, a straight RC beam strengthened by a thin FRP plate under three-point bending (Fig. 2.1) studied by Smith and Teng (2001) is examined. A simply supported RC beam

with the span of 3000 mm is subjected to a mid-span load of $P = 150$ kN. The distance from the support to the end of FRP plate is 300 mm. Material properties are given as: Adherends, $E_1 = 30000$ MPa, $\nu_1 = 0.28$ (concrete), $E_2 = 100000$ MPa, $\nu_2 = 0.3$ (FRP); Adhesive, $E_a = 2000$ MPa, $\nu_a = 0.35$. The geometries of the beam are given by: $h_1 = 300$ mm, $h_2 = 4$ mm, $h_0 = 1$ mm, and $b_1 = b_2 = 200$ mm.

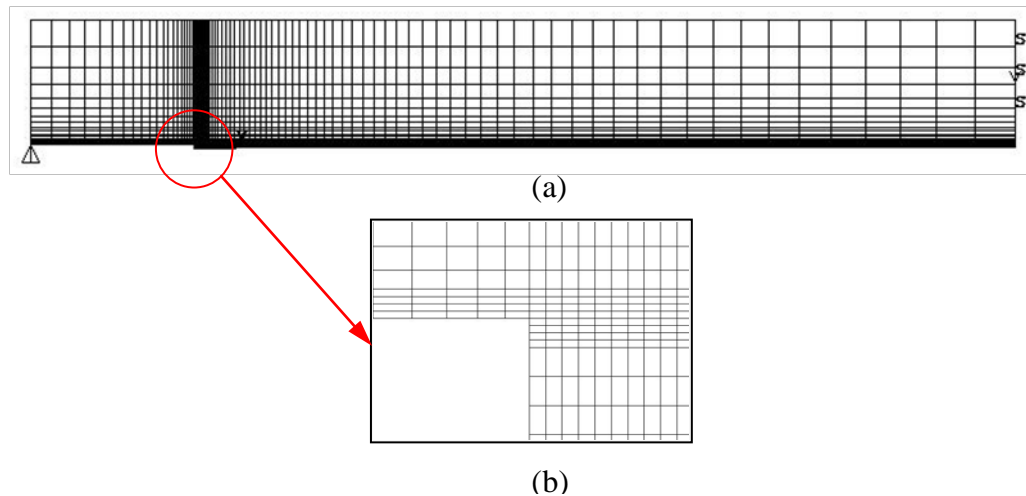


Fig.2.5. Finite element model of the FRP-strengthened straight RC beam.

Numerical solutions by FEA are computed as the baseline for comparison with the commercial finite element package ANSYS. Isoparametric eight-node quadrilateral elements are used to generate the mesh. This type of element can provide more accurate results than the mixed automatic meshes and can tolerate irregular shapes without too much loss of accuracy. It has compatible displacement interpolation function and good curved boundary fitting ability. Due to symmetric characteristics, only half of the beam is modeled as shown in Fig. 2.5 (a). The elements near the edge corner are finely meshed, as shown in Fig. 2.5 (b). The finest element size at the plate end is 0.125mm.

Shear and normal stresses obtained by the present method and FEA are presented in Fig. 2.6. As comparison, stresses predicted by the 2PEF model (Smith and Teng, 2001; Wang, 2003)

are also presented in the figure. Fig. 2.6 (a) shows the shear stress distribution near the end of the FRP plate. FEA provides three shear stress distributions, i.e., the shear stress distribution along the CA interface, PA interface, and center plane of the adhesive layer, as shown in Fig.2.6 (a). These three shear stress distributions are almost identical except a very small region at the edge of the adhesive layer due to the stress singularity at the corner edge. This suggests that it is reasonable to assume the shear stress is uniform through the thickness of the adhesive layer. Shear stress along the center plane reaches its maximum at a small distance to the edge and reduces to zero at the edge of the adhesive layer as anticipated. This feature is captured successfully by the present 3PEF model, as demonstrated by the solid line in Fig. 2.6 (a). The results of 2PEF model (Wang, 2003, Smith and Teng, 2001) are very close to those of the 3PEF model except that they cannot satisfy the zero shear stress boundary condition at the edge of the adhesive layer (Fig. 2.6 (a)). Compared with FEA results, all the three analytical models overestimate the shear stress near the edge of the adhesive layer. This is because that the interface stresses' effects on the deformation of the bottom of the concrete beam and top of the FRP plate are negligible (Qiao and Wang, 2005a). As a result, the FRP-strengthened beam is stiffer in the analytical model than in the FEA model, which causes more severe shear stress concentration near the edge of the adhesive layer in the analytical model. To reduce this difference between the analytical model and FEA solution, two interface compliances can be induced as illustrated in details by Qiao and Wang (2005a) to account for the effect of interface stresses on the deformation of concrete beam and FRP plate.

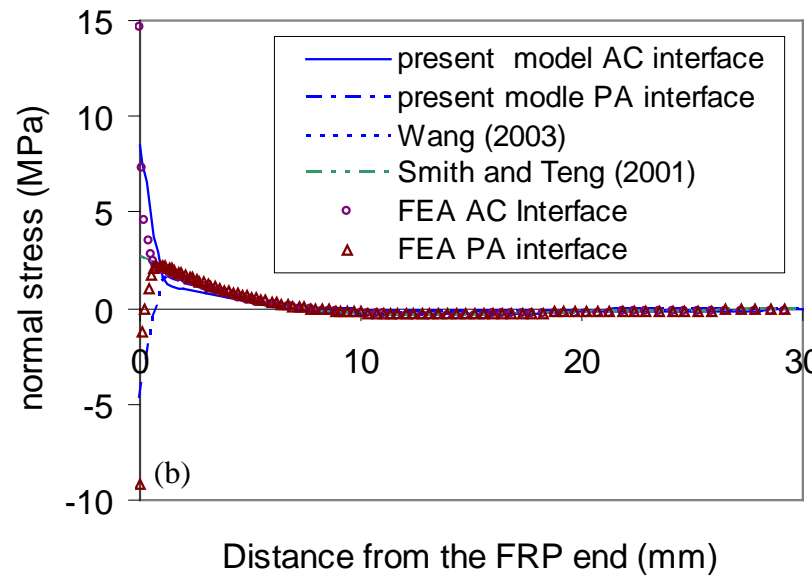
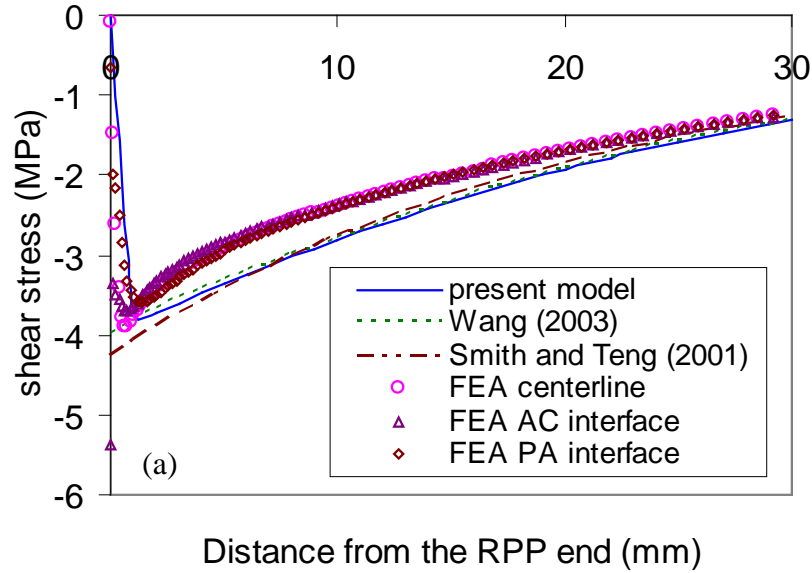


Fig.2.6. Comparison of interface stresses obtained by different methods for the FRP strengthened straight RC beam: (a) interface shear stresses, (b) interface normal stresses.

Fig. 2.6 (b) compares the normal stresses distributions obtained by different methods. As illustrated by FEA predictions, the normal stress distribution along the CA interface is different from that along the PA interface. The normal stress along the CA interface is tensile while the one along the PA interface is compressive at the end of the FRP plate. This feature is important because it explains why debonding usually occurs along the CA interface (with a thin layer of

concrete), not along the PA interface. As demonstrated by Fig. 2.6 (b), the present 3PEF model captures this feature very well; while the 2PEF model only predicts one value for both interfaces. Nevertheless, all the solutions converge to one value if the distance from the edge is large.

Fig. 2.6 verifies that the present 3PEF model overcomes the drawbacks of the well-known 2PEF model successfully and captures two important features of the interface stress of the FRP strengthened concrete beam. Excellent agreement with FEA prediction has been achieved by the present model except a very small region at the end of the FRP plate caused by the stress singularities existing at the edge corners.

Figs. 2.7 and 2.8 compare interface stresses predicted by the present solution and FEA for different adhesive thicknesses. The same geometries of concretes and FRP plate and loading conditions used in Fig. 2.6 are considered in the calculation. It can be observed that when the adhesive layer is thin (Fig. 2.7 (b) $h_0 = 0.5$ mm), the present 3PEF model reaches a better agreement with FEA in predicting normal stresses. In the case of thicker adhesive layer (Fig. 2.8 (b) $h_0 = 4$ mm), the present analytical model tends to underestimate the normal stress along the CA interface, but overestimate the normal stress along the PA interface, as shown in Fig. 2.8 (b). Figs. 2.7 and 2.8 also suggest that the present model overestimates the shear stress more if the adhesive layer is thinner, which is caused by the same reason aforementioned. Comparing Figs. 2.7 and 2.8, we can find that the location of the maximum shear stress is closer to the edge of the adhesive layer if the adhesive layer is thinner. Figs. 2.7 and 2.8 also confirm that higher stress concentration is induced by thinner adhesive layer.

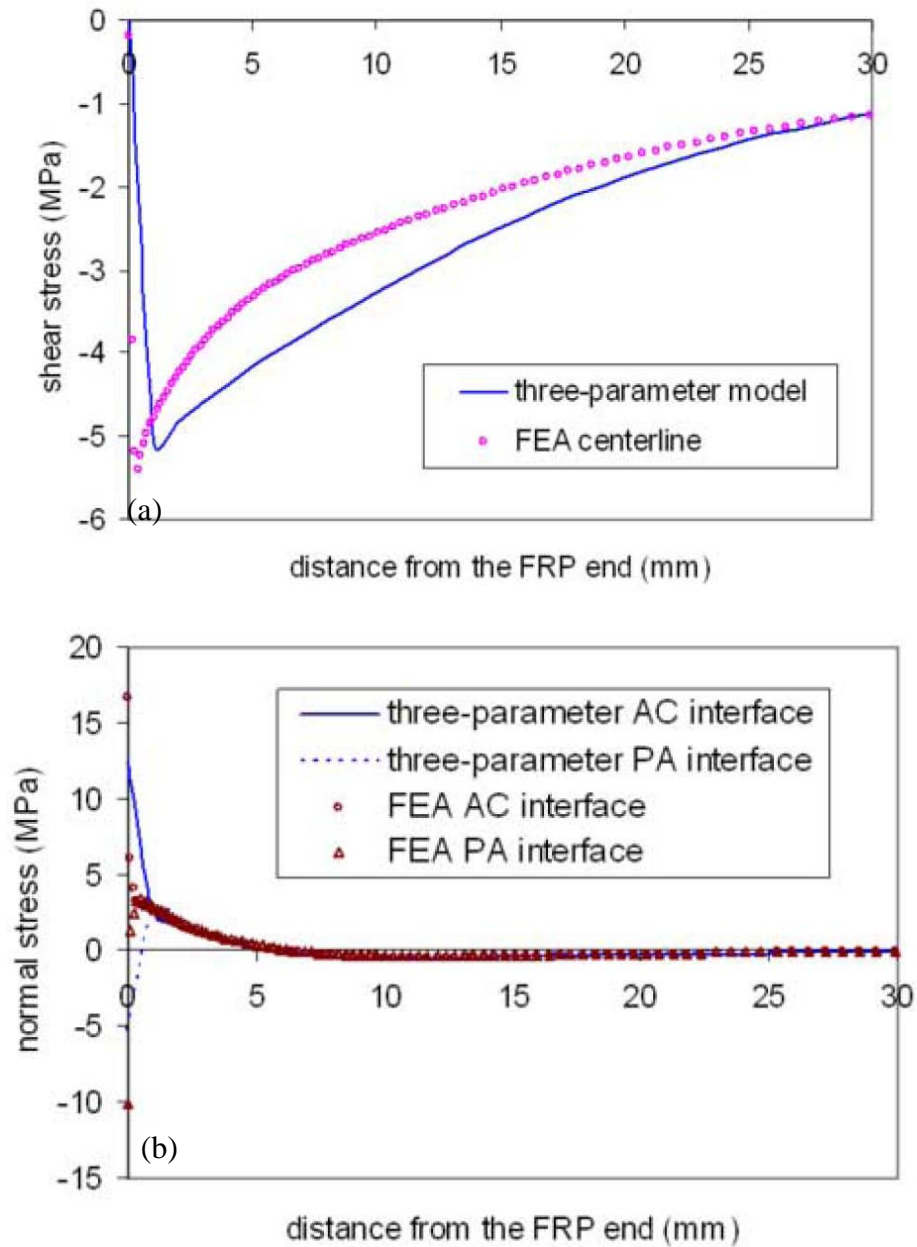


Fig.2.7 Comparison of interface stresses from the 3PEF model and FEA ($h_0 = 0.5$ mm) for the FRP-strengthened straight RC beam: (a) interface shear stresses, (b) interface normal stresses.

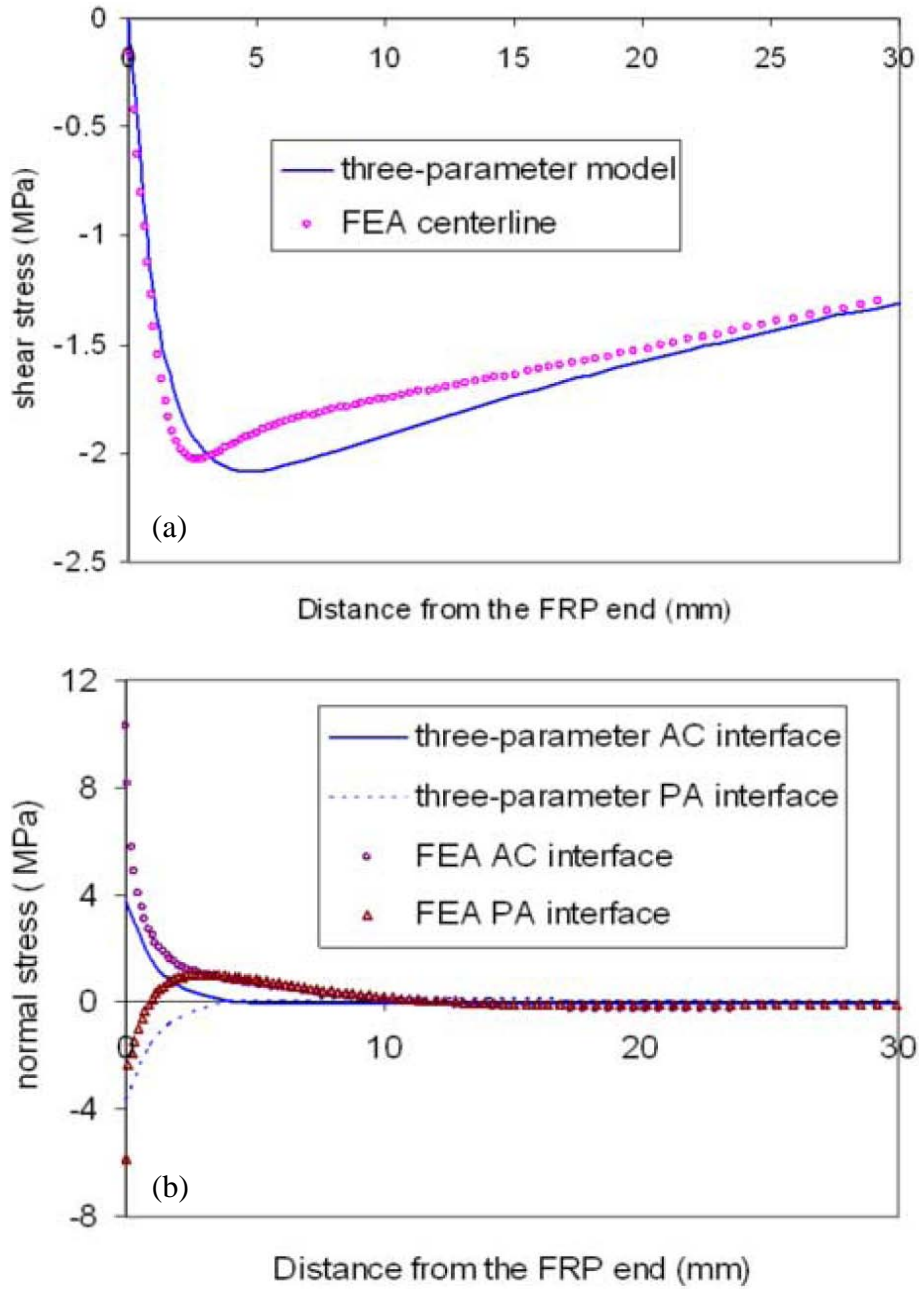


Fig.2.8 Comparison of interface stresses from the 3PEF model and FEA ($h_0 = 2.0$ mm) for the FRP-strengthened straight RC beam: (a) interface shear stresses, (b) interface normal stresses.

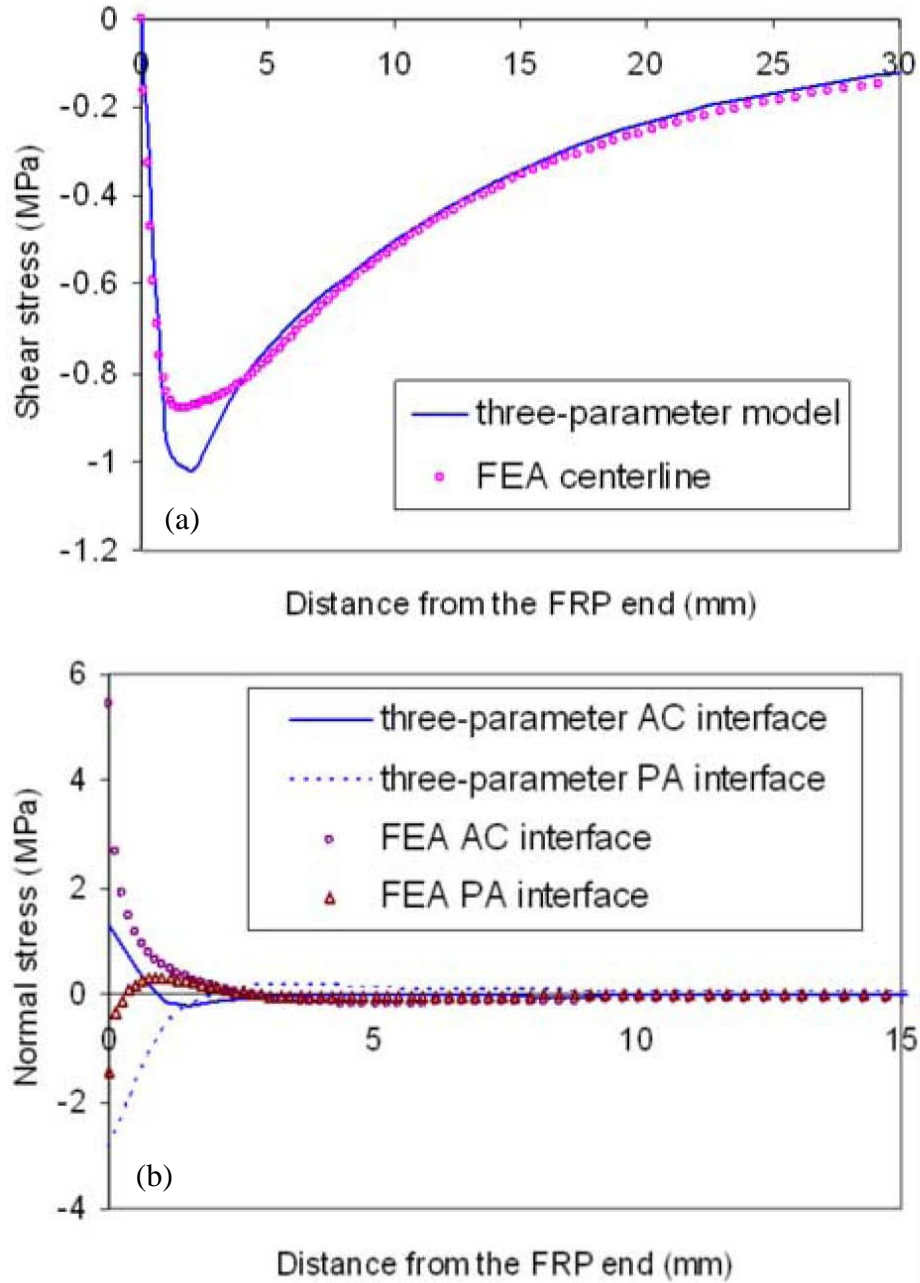


Fig.2.9 Comparison of interface stresses from the 3PEF model and FEA ($h_2 = 0.5\text{mm}$) for the FRP-strengthened straight RC beam: (a) interface shear stresses, (b) interface normal stresses.

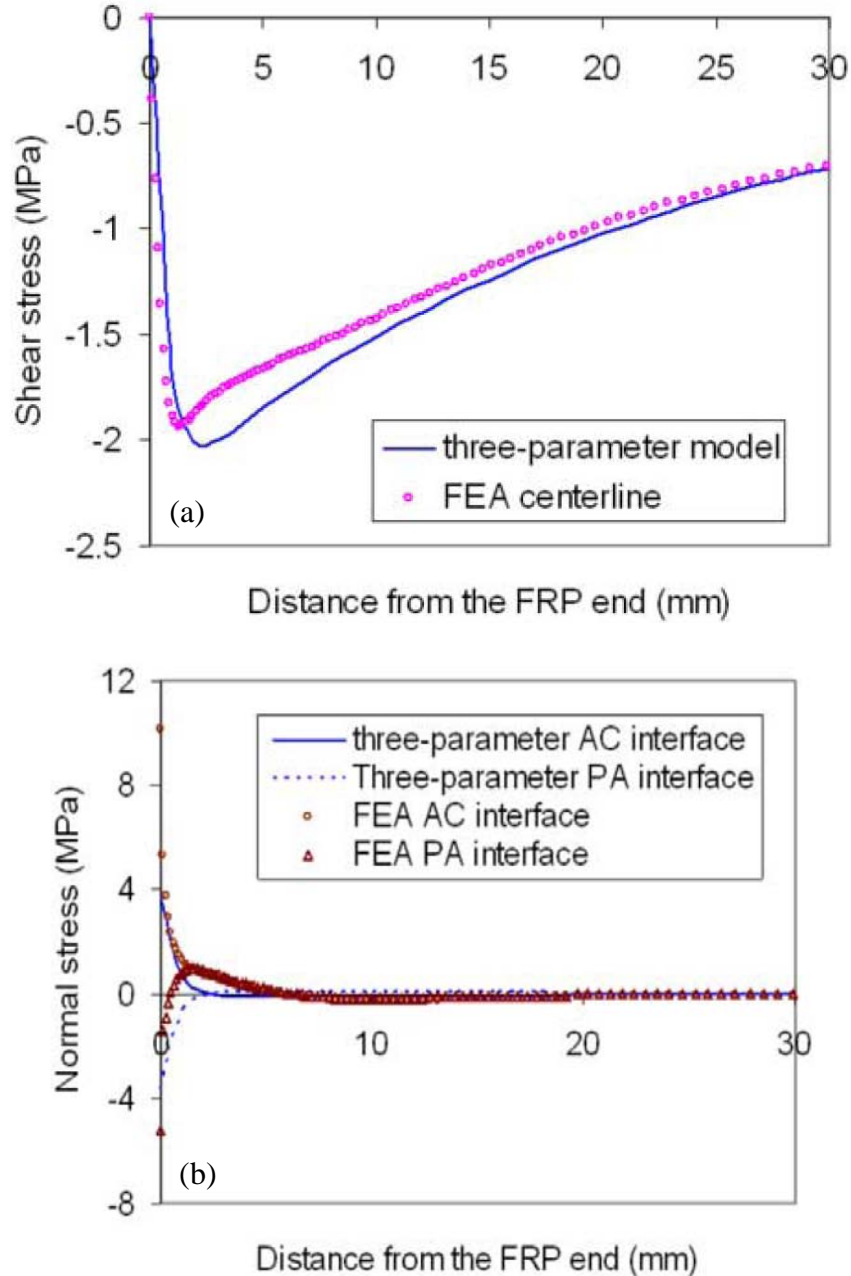


Fig.2.10 Comparison of interface stresses from the 3PEF model and FEA ($h_2 = 2.0\text{mm}$) for the FRP-strengthened straight RC beam: (a) interface shear stresses, (b) interface normal stresses.

Figs. 2.9 and 2.10 examine the sensitivity of the present model to the thickness of the FRP plate. To obtain these two figures, FRP thickness h_2 are chosen as 0.5 mm (Fig. 2.9) and 2 mm (Fig. 2.10), and the thickness of adhesive layer $h_0 = 2$ mm for both figures. All the other parameters are the same as in Fig. 2.6. Compared with FEA result, the present analytical

solutions seem to underestimate the normal stress along the CA interface and overestimate the compressive normal stress along the PA interface, especially when the FRP plate is thin (Fig. 2.9 (b) $h_2 = 0.5$ mm). The shear stress distribution predicted by the present model agrees with the FEA result very well when the FRP plate is thin (Fig. 2.9 (a)), and is higher than the FEA prediction if the FRP plate gets thicker (Fig. 2.10 (a)).

All the above results show that the 3PEF model predicts two different normal stress distributions along the CA interface and PA interface correctly. The zero shear stress at the edge of the adhesive layer is also satisfied by the new model. The parametric studies shown in Figs. 2.7 to 2.10 suggest that higher accuracy of the present model is expected for the normal stress if the FRP plate is thicker or the adhesive layer is thinner. The present model tends to overestimate the shear stress if the adhesive is thinner or the FRP plate is thicker. This overestimation can be reduced if interface shear compliance is used to account for the effect of interface shear stress on the deformation of two adherends (Qiao and Wang 2005).

2.3 3PEF model of an FRP-strengthened curved RC beam

Since the curved members are also commonly used in practice, the 3PEF model of the straight FRP-strengthened RC beam need to be extended to the FRP-strengthened curved RC beam in this section. Closed-form solutions are obtained for the interface normal stresses along the CA and PA interfaces, and the shear stress within the adhesive layer in a thin plate strengthened curved beam. The validation of these solutions is then verified by FEA results.

2.3.1. Shear deformable curved beam theory

Consider a structural (RC) beam (adherend 1) strengthened by a thin (FRP) plate (adherend 2) through a thin adhesive layer (Fig. 2.11). Both the adherends and the adhesive layer are assumed linearly elastic and orthotropic materials to account for the most general situation.

The adherends are modeled as two curved beams with the thicknesses of h_1 and h_2 , respectively, connected by an interface of thin adhesive layer with the thickness of h_0 .

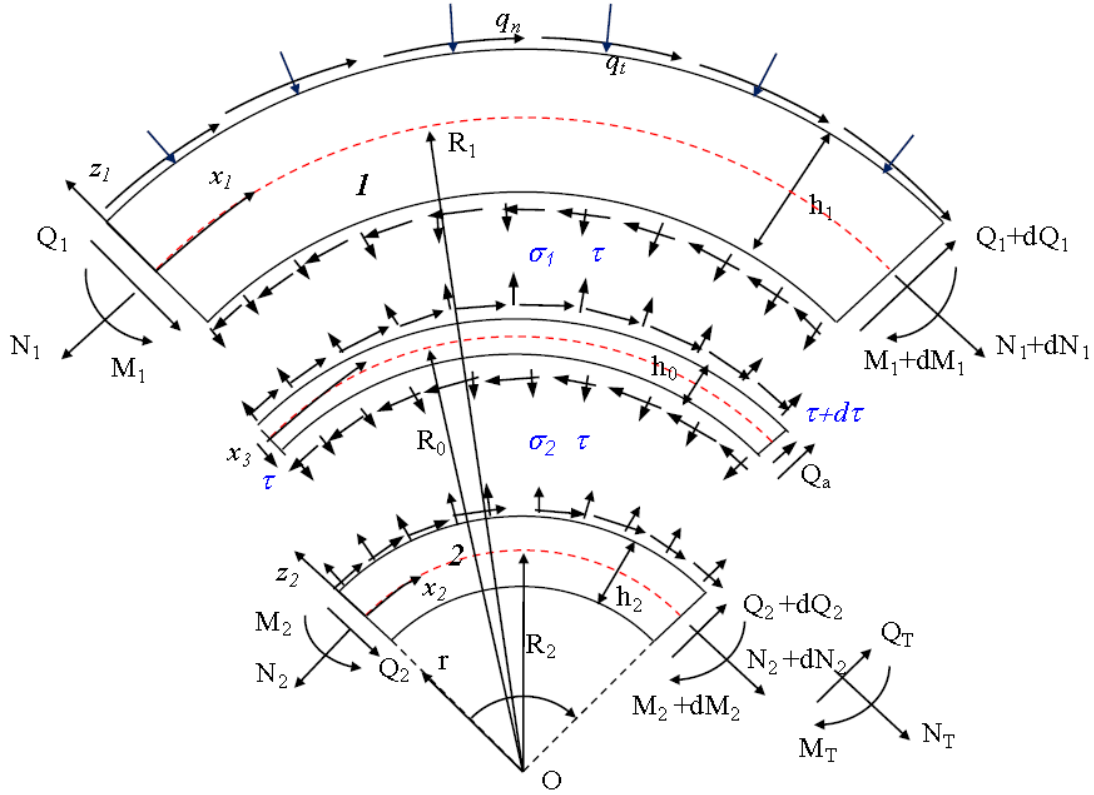


Fig.2.11. Free body diagram of a curved beam bonded with a thin plate.

According to the shear-deformable beam theory, the deformations of two curved beams have the form,

$$U_i(x_i, z_i) = u_i(x_i) + z_i \phi_i(x_i), \quad W_i(x_i, z_i) = w_i(x_i). \quad (2.46)$$

where subscript $i = 1, 2$, represent the beams 1 and 2 in Fig. 2.11, respectively. x_i and z_i are the curvilinear coordinates of the local coordinates in beam i . u_i and w_i are the tangential, rotational, and radial displacements of the mid-axis of curved beam i , respectively. The strains along the mid-axis of the curved beams can be written in term of curvilinear coordinate systems as,

$$\varepsilon_{0i} = \frac{du_i}{dx_i} + \frac{w_i}{R_i}, \quad \kappa_{0i} = \frac{d\phi_i}{dx_i}, \quad \gamma_{0i} = \frac{dw_i}{dx_i} + \phi_i - \frac{u_i}{R_i}. \quad (2.47)$$

The normal and shear strains in curved beam i are given by,

$$\varepsilon_i = \frac{R_i}{R_i + z_i} (\varepsilon_{0i} + z_i \kappa_{0i}), \quad \gamma_i = \frac{R_i}{R_i + z_i} \gamma_{0i}. \quad (2.48)$$

The constitutive equations for these two curved beams can be written in the conventional way as (Wang and Zhang, 2007a),

$$\begin{Bmatrix} \varepsilon_{0i} \\ \kappa_{0i} \\ \gamma_{0i} \end{Bmatrix} = \begin{bmatrix} \frac{1}{C_i} & \frac{1}{C_i R_i} & 0 \\ \frac{1}{C_i R_i} & \frac{\beta_i}{C_i R_i^2 (\beta_i - 1)} & 0 \\ 0 & 0 & \frac{1}{\kappa G_i A_i \beta_i} \end{bmatrix} \begin{Bmatrix} N_i \\ M_i \\ Q_i \end{Bmatrix}, \quad (2.49)$$

where $\beta_i = \frac{R_i}{h_i} \ln \left(\frac{2R_i + h_i}{2R_i - h_i} \right)$; $C_i = E_i b_i h_i$ (plane stress) or $C_i = \frac{E_i b_i h_i}{1 - \nu_{xzi} \nu_{zxi}}$ (plane strain) is the

axial stiffness of the curved beam i ; b_i and h_i are the width and thickness of the curved beam i , respectively; E_i , G_i , ν_{xzi} , ν_{zxi} are, respectively, the longitudinal modulus, transverse shear modulus, and Poisson's ratios of plate i . κ is the shear correction coefficient chosen as 5/6 in this study; N_i , Q_i , and M_i are, respectively, the resultant axial force, transverse shear force, and bending moment per unit width of beam i .

Considering a typical infinitesimal isolated body of the bonded curved bi-beam system (Fig. 2.11), the following equilibrium equations can be established,

$$\begin{aligned} \frac{dN_1}{dx_1} &= \frac{R + h_0/2}{R_1} b\tau - \frac{Q_1}{R_1} - \frac{R_1 + h_1/2}{R_1} bq_t, & \frac{dQ_1}{dx_1} &= \frac{R + h_0/2}{R_1} b\sigma_1 + \frac{N_1}{R_1} + \frac{R_1 + h_1/2}{R_1} bq_n, \\ \frac{dM_1}{dx_1} &= -\frac{h_1 + h_0}{2} \frac{R + h_0/2}{R_1} b\tau + Q_1, & & \\ \frac{dN_2}{dx_2} &= -\frac{R - h_0/2}{R_2} b\tau - \frac{Q_2}{R_2}, & \frac{dQ_2}{dx_2} &= -\frac{R - h_0/2}{R_2} b\sigma_2 + \frac{N_2}{R_2}, \end{aligned} \quad (2.50)$$

$$\frac{dM_2}{dx_2} = -\frac{h_2 + h_0}{2} \frac{R - h_0/2}{R_2} b\tau + Q_2, \quad (2.51)$$

where τ and σ_1, σ_2 are the shear stress in the adhesive layer, the normal stress along the CA interface, and the normal stress along the PA interface, respectively. q_t and q_n are the external loads applied to beam I .

Combing the first and third equations of Eqs. (2.50) and (2.51) yields,

$$Q_1 = \frac{R_1}{R_0} \left(\frac{dM_1}{dx_1} + \frac{h_1 + h_0}{2} \frac{dN_1}{dx_1} \right) + \frac{(h_1 + h_0)(R_1 + h_1/2)}{2R_0} bq_t, \quad Q_2 = \frac{R_2}{R_0} \left(\frac{dM_2}{dx_2} - \frac{h_2 + h_0}{2} \frac{dN_2}{dx_2} \right). \quad (2.52)$$

Global equilibrium conditions read,

$$N_T = N_1 + N_2, \quad (2.53a)$$

$$Q_T = Q_1 + Q_2 + Q_a, \quad (2.53b)$$

$$M_T = M_1 + M_2 + \left(\frac{h_1 + h_2}{2} + h_0 \right) N_1, \quad (2.53c)$$

where N_T , Q_T , and M_T are the resulting forces of the whole bi-layered beam with respect to the axis of FRP plate (Fig. 2.11); Q_a is the shear force in adhesive layer.

2.3.2. 3PEF model of a curved adhesive layer

In this study, the 3PEF model proposed by Wang (2007) is used to model the adhesive layer. Similar to the classical 2PEF model of Goland and Reissner (1944), this new model also assumes that the shear stress is constant through the thickness of the adhesive layer. The normal stress, which is assumed uniformly distributed through the thickness of the whole adhesive layer in 2PEF model, is assumed as constant only through the half of the adhesive layer. The normal stresses in the upper and lower halves, σ_1 and σ_2 shown in Fig. 2.11, have different values. In this way, the adhesive layer can be viewed as an assembly of two linear normal spring layers with stiffness of K interconnected by a shear layer with constants of G_a as shown in Fig. 2.12. Since

the normal stress is assumed uniformly distributed through the thickness of the upper and lower half of the adhesive layer, the stiffnesses of these two normal springs can be estimated as $K = 2E_a/h_0$. Then the strain–stress relations of the adhesive layer can be written as:

$$\sigma_1(x) = K(w_1 - w_a) = \frac{2E_a}{h_0}(w_1 - w_a), \quad (2.54a)$$

$$\sigma_2(x) = K(w_a - w_2) = \frac{2E_a}{h_0}(w_a - w_2), \quad (2.54b)$$

$$\tau(x) = \frac{G_a}{h_0} \left(\frac{du_a}{dz} - \frac{u_a}{R_0} + \frac{1}{R_0} \frac{dw}{d\theta} \right) \approx \frac{G_a}{h_0} \left(u_1 - \frac{h_1}{2} \phi_1 - u_2 - \frac{h_2}{2} \phi_2 \right) + G_a \frac{dw_a}{dx}, \quad (2.54c)$$

where E_a and G_a are the Young's modulus and the shear modulus of the adhesive, respectively; u_a and w_a are the tangential and radial displacements of adhesive layer, respectively. u/R_0 is ignored in Eq.(2.54c) since it is much smaller than other two terms. Eq. (2.54) is similar to the 3PEF model used by Kerr (1965) and Avramidis and Morfidis (2006). Therefore, the adhesive layer model described by Eq. (2.54) is referred to as 3PEF by Wang (2007). It can be found that Eq. (2.54) is a straight extension of the classical 2PEF model (Goland and Reissner, 1944) by breaking the one layer normal spring in the 2PEF model into two layers. Consequently, the number of independent parameters is changed from two (σ and τ) in the 2PEF model to three (σ_1 , σ_2 , and τ) in the 3PEF model. Introducing two different normal stresses not only makes all boundary conditions be satisfied, but also reveals different nature of normal stresses along the PA and CA interfaces, which cannot be obtained through the 2PEF model.

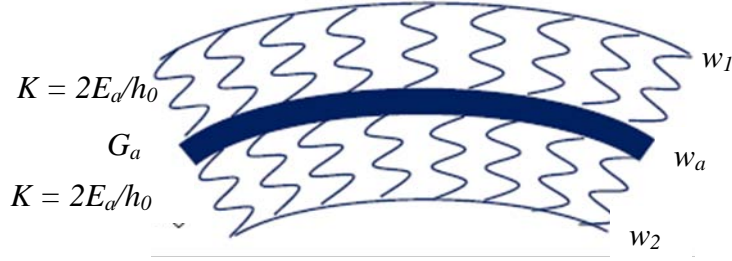


Fig. 2.12. 3PEF model for the curved adhesive layer.

Ignoring the axial and bending moment of the adhesive layer, equilibrium condition of the adhesive layer requires (Fig. 2.11),

$$\frac{d\tau}{dx} = \frac{(R_0 - h_0/2)\sigma_2 - (R_0 + h_0/2)\sigma_1}{R_0 h_0}. \quad (2.55)$$

Eq. (2.55) describes the interaction between the normal and shear stresses within the adhesive layer. Noting that τ changes drastically at the vicinity of the thin plate end, Eq. (2.55) suggests that σ_1 and σ_2 are significantly different in this region. In the 2PEF model (De Lorezis et al., 2006), σ_1 is equal to σ_2 even though the left-hand side of Eq. (2.55) is not zero. Clearly, the force equilibrium condition of the adhesive layer is violated in the 2PEF model.

2.3.3. Governing differential equation of an FRP-strengthened curved RC beam

Substituting the first equation in Eq. (2.50) into Eq. (2.54c) and differentiating both sides and considering Eq. (2.49), we have,

$$\begin{aligned} \frac{R_1 h_0}{b G_a (R_0 + h_0/2) R_0} \left(R_1 \frac{d^2 N_1}{dx_1^2} + \frac{dQ_1}{dx_1} + b \left(R_1 + \frac{h_1}{2} \right) \frac{dq_t}{dx_1} \right) &= h_0 \frac{d^2 w_a(x)}{dx^2} + \frac{R_1}{R_0} \left(\frac{N_1}{C_1} + \frac{M_1}{C_1 R_1} \right) \\ - \frac{R_2}{R_0} \left(\frac{N_2}{C_2} + \frac{M_2}{C_2 R_2} \right) - \frac{h_1 R_1}{2 R_0} \left(\frac{N_1}{C_1 R_1} + \frac{M_1 \beta_1}{C_1 R_1^2 (\beta_1 - 1)} \right) - \frac{h_2 R_2}{2 R_0} \left(\frac{N_2}{C_2 R_2} + \frac{M_2 \beta_2}{C_2 R_2^2 (\beta_2 - 1)} \right). \end{aligned} \quad (2.56)$$

Differentiating the Eq. (2.54a) twice yields,

$$\frac{d^2 w_a}{dx^2} = \left(\frac{R_1}{R_0} \right)^2 \frac{d^2 w_1}{dx_1^2} - \frac{h_0}{R_0} \frac{d^2 \sigma_1}{dx^2}. \quad (2.57)$$

Considering the constitutive equation (2.49), we can write,

$$\frac{d^2 w_1}{dx_1^2} = \frac{1}{B_1 \beta_1} \frac{dQ_1}{dx_1} - \frac{d\phi_1}{dx_1} + \frac{1}{R_1} \frac{du_1}{dx_1} = \frac{R_1}{R_0 B_1 \beta_1} \frac{d^2 M_1}{dx_1^2} + \frac{R_1(h_1 + h_0)}{2R_0 B_1 \beta_1} \frac{d^2 N_1}{dx_1^2} - \frac{M_1}{C_1 R_1^2 (\beta_1 - 1)}. \quad (2.58)$$

Differentiating the Eq. (2.54b) twice leads to,

$$\begin{aligned} \frac{d^2 \sigma_1}{dx^2} &= \frac{1}{b(R_0 + h_0/2)} \left(\frac{R_1}{R_0} \right)^2 \frac{d^2}{dx_1^2} \left(\left(R_1 \frac{dQ_1}{dx_1} - N_1 \right) - \left(R_1 + \frac{h_1}{2} \right) b q_n \right) \\ &= \frac{R_1^4}{b(R_0 + h_0/2) R_0^3} \frac{d^4 M_1}{dx_1^4} + \frac{R_1^4 (h_1 + h_0)}{2b(R_0 + h_0/2) R_0^3} \frac{d^4 N_1}{dx_1^4} - \frac{R_1^2}{b(R_0 + h_0/2) R_0^2} \frac{d^2 N_1}{dx_1^2} - \frac{(R_1 + h_1/2)}{(R_0 + h_0/2)} \frac{d^2 q_n}{dx^2}. \end{aligned} \quad (2.59)$$

Substituting Eqs. (2.57) - (2.59) into Eq. (2.56) and considering Eq. (2.53), we obtain,

$$C_{11} \frac{d^4 M_1}{dx_1^4} + C_{12} \frac{d^4 N_1}{dx_1^4} + C_{13} \frac{d^2 M_1}{dx_1^2} + C_{14} \frac{d^2 N_1}{dx_1^2} + C_{15} M_1 + C_{16} N_1 + F_1(x) = 0, \quad (2.60)$$

where

$$\begin{aligned} C_{11} &= -\frac{h_0^2 R_1^4}{2bE_a (R_0 + h_0/2) R_0^3}, \quad C_{12} = -\frac{h_0^2 (h_1 + h_0) R_1^4}{4bE_a (R_0 + h_0/2) R_0^3}, \quad C_{13} = \frac{h_0 R_1^3}{B_1 \beta_1 R_0^3} - \frac{h_0 R_1^2}{bG_a (R_0 + h_0/2) R_0^2}, \\ C_{14} &= \frac{h_0^2 R_1^2}{2E_a (R_0 + h_0/2) b R_0^2} + \frac{h_0 (h_1 + h_0) R_1^2}{2B_1 \beta_1 R_0^3} - \frac{h_0 (2R_0 + h_1 + h_0) R_1^2}{2bG_a (R_0 + h_0/2) R_0^2}, \\ C_{15} &= -\frac{h_0}{C_1 R_0^2 (\beta_1 - 1)} + \frac{1}{R_0} \left(\frac{1}{C_1} + \frac{1}{C_2} - \frac{h_1 \beta_1}{2C_1 R_1 (\beta_1 - 1)} + \frac{h_2 \beta_2}{2C_2 R_2 (\beta_2 - 1)} \right), \\ C_{16} &= \frac{1}{R_0} \left(\frac{R_1}{C_1} + \frac{R_2}{C_2} - \frac{1}{2} \left(\frac{h_1}{C_1} - \frac{h_2}{C_2} \right) + \frac{h_1 + h_2 + 2h_0}{2} \left(\frac{1}{C_2} + \frac{h_2 \beta_2}{2R_2 (\beta_2 - 1)} \right) \right), \\ F_1(x) &= -\frac{1}{R_0} \left(\frac{1}{C_2} + \frac{h_2 \beta_2}{2R_2 (\beta_2 - 1)} \right) M_T - \frac{R_2 - h_2/2}{R_0 C_2} N_T - \frac{h_0^2}{2E_a} \frac{R_1 + h_1/2}{R_1 - h_1/2} \frac{d^2 q_n}{dx^2} - \frac{h_0}{G_a} \frac{R_1 + h_1/2}{R_1 - h_1/2} \frac{d^2 q_t}{dx^2}. \end{aligned} \quad (2.61)$$

Adding Eq. (2.54a) and Eq. (2.54b) gives,

$$\sigma_1 + \sigma_2 = \frac{2E_a (w_1 - w_2)}{h_0}. \quad (2.62)$$

Differentiating the above equation twice and considering Eq. (3.49), we have,

$$\begin{aligned} \frac{d^2\sigma_1}{dx^2} + \frac{d^2\sigma_2}{dx^2} &= \frac{2E_a}{h_0R_0^2} \left(R_1^2 \frac{d^2w_1}{dx_1^2} - R_2^2 \frac{d^2w_2}{dx_2^2} \right) \\ &= \frac{2E_a}{h_0R_0^2} \left(R_1^2 \left(\frac{1}{B_1} \frac{dQ_1}{dx_1} - \frac{d\phi_1}{dx_1} + \frac{1}{R_1} \frac{du_1}{dx_1} \right) - R_2^2 \left(\frac{1}{B_2} \frac{dQ_2}{dx_2} - \frac{d\phi_2}{dx_2} + \frac{1}{R_2} \frac{du_2}{dx_2} \right) \right). \end{aligned} \quad (2.63)$$

Differentiating Eq. (2.55) twice with respect to x yields,

$$\frac{d^2\sigma_2}{dx^2} = \frac{R_0 + h_0/2}{R_0 - h_0/2} \frac{d^2\sigma_1}{dx^2} + \frac{R_0h_0}{R_0 - h_0/2} \frac{d^3\tau}{dx^3}. \quad (2.64)$$

Substituting Eqs. (2.59), (2.64), (2.50) and (2.51) into Eq. (2.63), we have

$$C_{21} \frac{d^4M_1}{dx_1^4} + C_{22} \frac{d^4N_1}{dx_1^4} + C_{23} \frac{d^2M_1}{dx_1^2} + C_{24} \frac{d^2N_1}{dx_1^2} + C_{25}M_1 + C_{26}N_1 + F_2(x) = 0. \quad (2.65)$$

where

$$\begin{aligned} C_{21} &= \frac{R_1^4(2R_0 + h_0)}{bR_0^3(R_0 + h_0/2)(R_0 - h_0/2)}, \quad C_{22} = \frac{R_1^4(R_0(h_1 + 2h_0) + h_0(h_1 + h_0))}{bR_0^3(R_0 + h_0/2)(R_0 - h_0/2)}, \\ C_{23} &= -\frac{2E_aR_1^3}{h_0R_0^3} \left(\frac{1}{B_1} + \frac{R_2}{B_2R_1} \right), \quad C_{24} = -\frac{R_1^2}{b(R_0 + h_0/2)R_0^2} - \frac{E_aR_1^3(h_1 + h_0)}{h_0R_0^3} \left(\frac{1}{B_1} + \frac{R_2}{B_2R_1} \right), \\ C_{25} &= \frac{2E_a}{h_0R_0^3} \left(\frac{1}{B_1C_1(\beta_1 - 1)} + \frac{1}{B_2C_2(\beta_2 - 1)} \right), \quad C_{16} = \frac{E_a(h_1 + h_2 + 2h_0)}{h_0R_0^2C_2B_2}, \\ F_2(x) &= -\frac{2E_a}{h_0} \left(-\frac{R_2}{B_2R_0} \left(\frac{d^2M_T}{dx^2} - \frac{h_2}{2} \frac{d^2N_T}{dx^2} \right) - \frac{M_T}{B_2C_2R_0^2} \right) \\ &\quad - \frac{2R_0}{R_0 - h_0/2} \frac{R_1 + h_1/2}{R_1 - h_1/2} \frac{d^2q_n}{dx^2} + \frac{R_0h_0}{R_0 - h_0/2} \frac{R_1 + h_1/2}{R_1 - h_1/2} \frac{d^3q_t}{dx^3}. \end{aligned} \quad (2.66)$$

Subtracting Eq. (2.65) multiplied by C_{11} from Eq. (2.60) multiplied by C_{21} and after rearranging, we have,

$$\frac{d^2M_1}{dx_1^2} - D_{11} \frac{d^4N_1}{dx_1^4} + D_{12} \frac{d^2N_1}{dx_1^2} + D_{13}M_1 + D_{14}N_1 + F_3(x) = 0 \quad (2.67)$$

where

$$D_{11} = -\frac{C_{12}C_{21} - C_{22}C_{11}}{C_{13}C_{21} - C_{23}C_{11}}, D_{12} = -\frac{C_{14}C_{21} - C_{24}C_{11}}{C_{13}C_{21} - C_{23}C_{11}}, D_{13} = -\frac{C_{15}C_{21} - C_{25}C_{11}}{C_{13}C_{21} - C_{23}C_{11}},$$

$$D_{14} = -\frac{C_{16}C_{21} - C_{26}C_{11}}{C_{13}C_{21} - C_{23}C_{11}}, D_{11} = -\frac{C_{12}C_{21} - C_{22}C_{11}}{C_{13}C_{21} - C_{23}C_{11}}, F_3(x) = -\frac{C_{21}F_1(x) - C_{11}F_2(x)}{C_{13}C_{21} - C_{23}C_{11}}. \quad (2.68)$$

Subtracting Eq. (2.65) multiplied by C_{13} from Eq. (2.60) multiplied by C_{23} and after rearranging, we have

$$\frac{d^2M_1}{dx_1^2} - E_{11}\frac{d^4N_1}{dx_1^4} + E_{12}\frac{d^2N_1}{dx_1^2} + E_{13}M_1 + E_{14}N_1 + F_4(x) = 0, \quad (2.69)$$

where

$$E_{11} = -\frac{C_{12}C_{23} - C_{22}C_{13}}{C_{11}C_{23} - C_{21}C_{13}}, E_{12} = -\frac{C_{14}C_{23} - C_{24}C_{13}}{C_{11}C_{23} - C_{21}C_{13}}, E_{14} = -\frac{C_{15}C_{23} - C_{25}C_{13}}{C_{11}C_{23} - C_{21}C_{13}},$$

$$E_{14} = -\frac{C_{16}C_{23} - C_{26}C_{13}}{C_{11}C_{23} - C_{21}C_{13}}, F_4(x) = -\frac{C_{23}F_1(x) - C_{13}F_2(x)}{C_{11}C_{23} - C_{21}C_{13}}. \quad (2.70)$$

Differentiating Eq. (2.67) twice and substituting into Eq. (2.69) give,

$$M_1 = F_{11}\frac{d^6N_1}{dx_1^6} + F_{12}\frac{d^4N_1}{dx_1^4} + F_{13}\frac{d^2N_1}{dx_1^2} + F_{14}N_1 + F_5(x), \quad (2.71)$$

where

$$F_{11} = \frac{D_{11}}{E_{13} - D_{13}^2}, F_{12} = \frac{D_{12} + D_{13}D_{11} + E_{11}}{E_{13} - D_{13}^2}, F_{13} = \frac{D_{14} + D_{13}D_{12} - E_{12}}{E_{13} - D_{13}^2},$$

$$F_{14} = \frac{D_{13}D_{14} - E_{14}}{E_{13} - D_{13}^2}, F_5(x) = \frac{1}{E_{13} - D_{13}^2} \left(F_4(x) + D_{13} \left(\frac{R_0}{R_1} \right)^2 \frac{d^2F_3(x)}{dx^3} \right). \quad (2.72)$$

Substituting Eq. (2.71) back into Eq. (2.67), we have,

$$G_{11}\frac{d^8N_1}{dx_1^8} + G_{12}\frac{d^6N_1}{dx_1^6} + G_{13}\frac{d^4N_1}{dx_1^4} + G_{13}\frac{d^2N_1}{dx_1^2} + G_{15}N_1 + F_6(x) = 0, \quad (2.73)$$

where

$$G_{11} = F_{11}, G_{12} = F_{12} - D_{13}F_{11}, G_{13} = F_{13} - D_{11} - D_{13}F_{12}, G_{14} = F_{14} - D_{12} - D_{13}F_{13},$$

$$G_{15} = -D_{14} - D_{13}F_{14}, \quad F_6(x) = \left(\frac{R_0}{R_1}\right)^2 \frac{d^2 F_3(x)}{dx^3} - D_{13}F_5(x) - F_3(x). \quad (2.74)$$

Eq. (2.73) is the governing equation of a curved beam bonded with a thin plate shown in Fig. 2.11 based on the 3PEF model. Eq. (2.73) is of eighth-order which allows for implementing all the boundary conditions.

2.3.4. Interface stresses of an FRP-strengthened curved RC beam

The governing equation (2.73) can be solved through its characteristic equation. The forces in beam 1 can be obtained as

$$N_1 = \Delta N_1 + N_{1c}, \quad M_1 = \Delta M_1 + M_{1c}, \quad Q_1 = \Delta Q_1 + Q_{1c}, \quad (2.75)$$

where

$$\Delta N_1 = \sum_{i=1}^8 c_i e^{r_i x}, \quad \Delta M_1 = \sum_{i=1}^8 c_i S_i e^{r_i x}, \quad \Delta Q_1 = \sum_{i=1}^8 c_i T_i e^{r_i x}, \quad (2.76)$$

and S_i and T_i are given by,

$$S_i = F_{11}r_i^6 + F_{12}r_i^4 + F_{13}r_i^2 + F_{14}, \quad T_i = \frac{R_1}{R_0} \left(S_i r_i + \frac{h_1 + h_0}{2} r_i \right), \quad (2.77)$$

where r_i ($i = 1, \dots, 8$) are eight roots of the characteristic equation of Eq. (2.73). c_i ($i = 1, \dots, 8$) are eight coefficients to be determined by boundary conditions. N_{1c} , M_{1c} , and Q_{1c} are the particular solutions of Eq. (2.73) which are the resultant forces of the curved beam 1 if the curved beam and the thin plate bonded to it are treated as a composite bi-layer curved beam. Eq. (2.75) suggests that the resultant forces of the curved beam consist of two parts: the exponential terms (ΔN_1 , ΔM_1 , and ΔQ_1) which are the local disturbance of the relative soft adhesive layer, and the steady terms (N_{1c} , M_{1c} , and Q_{1c}) which are the internal forces of the beam based on the composite beam theory.

By using Eqs. (2.50) and (2.51), the interface stresses are obtained as,

$$\sigma_1 = \Delta\sigma_1 + \sigma_{1c}, \quad \sigma_2 = \Delta\sigma_2 + \sigma_{2c}, \quad \tau = \Delta\tau + \tau_c, \quad (2.78)$$

where

$$\begin{aligned} \Delta\sigma_1 &= \frac{R_1}{b(R_0 + h_0/2)} \sum_{i=1}^8 \left(T_i r_i - \frac{1}{R_1} \right) c_i e^{r_i x}, \\ \Delta\sigma_2 &= \frac{R_1}{b(R_0 - h_0/2)} \sum_{i=1}^8 \left(\frac{R_0 + h_0/2}{R_0 - h_0/2} \left(T_i r_i - \frac{1}{R_1} \right) + R_0 h_0 \left(r_i + \frac{T_i}{R_1} \right) \right) c_i e^{r_i x}, \\ \Delta\tau &= \frac{R_1}{bR_0} \sum_{i=1}^8 \left(r_i + \frac{T_i}{R_1} \right) c_i e^{r_i x}, \end{aligned} \quad (2.79)$$

and

$$\begin{aligned} \sigma_{1c} &= \frac{R_1}{b(R_0 + h_0/2)} \left(\frac{dQ_{1c}}{dx_1} - \frac{N_{1c}}{R_1} - \frac{R_1 + h_1/2}{R_1} q_n \right), \quad \sigma_{2c} = -\frac{R_2}{b(R_0 - h_0/2)} \left(\frac{dQ_{2c}}{dx_2} - \frac{N_{2c}}{R_2} \right), \\ \Delta\tau_c &= \frac{R_1}{bR_0} \left(\frac{dN_{1c}}{dx_1} + \frac{Q_{1c}}{R_1} + \frac{R_1 + h_1/2}{R_1} b q_t \right). \end{aligned} \quad (2.80)$$

Similar to the beam resultant forces, the interface stresses are also composed of two parts, the exponential terms representing the local stresses concentration near the plate ends, and the steady terms representing the composite beam solutions.

2.3.5. Boundary conditions of an FRP-strengthened curved RC beam

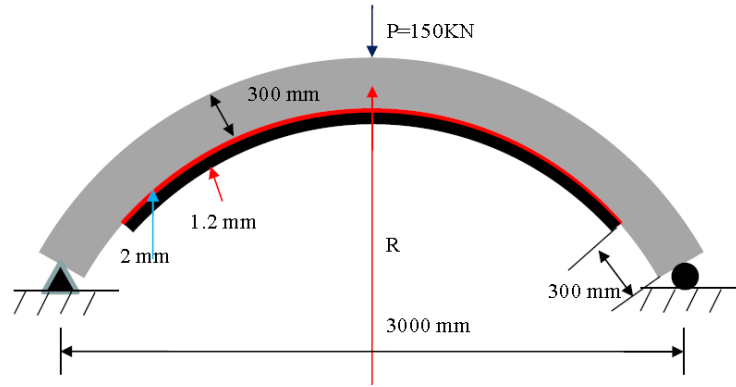


Fig.2.13. A simply supported curved beam externally bonded with a FRP plate.

To determine the coefficients c_i in the above solutions, necessary boundary conditions are needed. Consider a three-point bending test shown in Fig. 2.13, in which a concentrated force P is applied to the mid-span of the strengthened curved beam. For the sake of simplicity, we only take the bonded zone as shown in Fig. 2.14(a) for analysis. The external forces applied to the concrete beam (N_L , M_L , Q_L , N_R , M_R , and Q_R) can be easily determined by equilibrium analysis. In the conventional way (De Lorezis et al., 2006), this beam is divided into two segments, I and II, as shown in Fig. 2.14(a). Individual solutions are written for each segment and total eight boundary conditions and eight continuity conditions at the loading point are used to determine the coefficients in the solutions. Clearly, this approach is very tedious, especially when more than one loading discontinuity exists in the bonded zone. To eliminate this tedious procedure, a new approach is proposed to implement the boundary conditions using the principle of superposition. As shown in Eqs. (2.75) and (2.78), the beam forces and interface stresses can be obtained by superposing the composite beam solutions (Fig. 2.14b) and the local disturbance (Fig. 2.14c). In Fig. 2.14(b), the boundary forces with subscript “c” at the left and right ends of the beam are given by the particular solution of Eq. (2.73) or composite beam theory. Besides the forces applied at two ends, there is no other external force applied to the beam within the bonded region in Fig. 2.14(c). Therefore, there is no need to divide the bonded zone into two segments. Implementing continuity conditions is thus avoided. In this case, we only need to determine the eight coefficient c_i using the following boundary conditions:

$$\Delta N_{1L} = N_L + N_{1cL}, \Delta M_{1L} = M_{1L} + N_{1cL}, \Delta Q_{1L} = Q_L + Q_{1cL}, \tau_L = 0, \quad (2.81a)$$

$$\Delta N_{1R} = N_R + N_{1cR}, \Delta M_{1R} = M_{1R} + N_{1cR}, \Delta Q_{1R} = Q_R + Q_{1cR}, \tau_R = 0. \quad (2.81b)$$

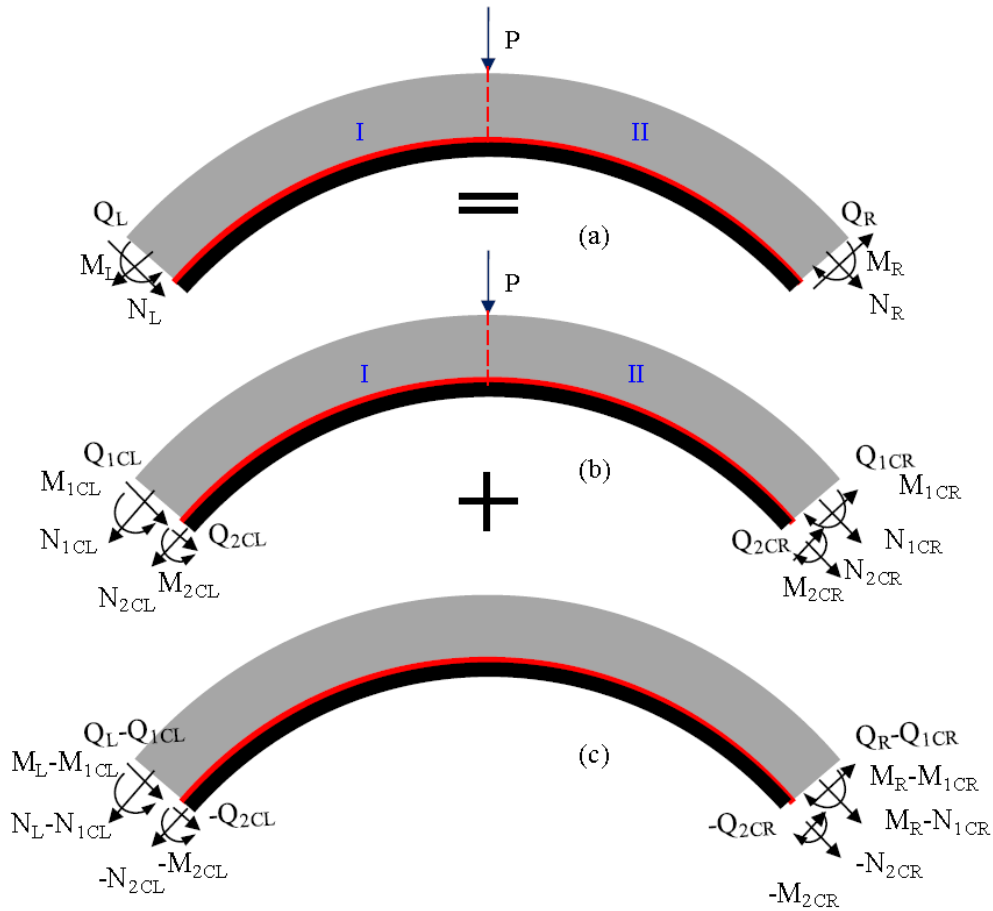


Fig.2.14. Implement boundary conditions using the principle of superposition.

The above procedure is applicable to general loading conditions, and is particularly efficient when more than one external loading discontinuity exists within the bonded zone. It should be pointed out that the interface stresses obtained by this method show some difference from those obtained by the conventional method at the loading point. However, the stress concentration at loading point is much smaller than that at the FRP plate end and therefore, is not critical to the debonding analysis.

2.3.6. Verifications and comparisons of present analytical solution for an FRP-strengthened curved RC beam

As verifications, a curved RC beam strengthened by a thin FRP plate under three-point bending (Fig. 2.13) studied by De Lorezis et al. (2006) is examined. The simply supported RC

beam with a span of 3000mm is subjected to a mid-span load of $P = 150$ kN. The curvilinear distance from the support to the end of FRP plate is 300 mm. Material properties are given as: Adherends, $E_1 = 30,000$ MPa, $\nu_1=0.28$; (concrete), $E_2 = 165,000$ MPa (FRP) $\nu_2=0.3$; Adhesive, $E_a = 4000$ MPa; $\nu_a = 0.35$. The geometries of the beam are given by: $h_1= 300$ mm, $h_2 = 1.2$ mm, $h_0 = 2$ mm, and $b_1 = b_2 = 200$ mm. Numerical solutions by FEA with ANSYS are obtained and used as the baseline for comparison. Isoparametric eight-node quadrilateral element is used to generate the mesh. It has compatible displacement interpolation function and good curved boundary fitting ability. This type of element can provide more accurate results than mixed automatic meshes and can tolerate irregular shapes without loss of too much accuracy. The detailed finite element mesh is shown in Fig. 2.15.

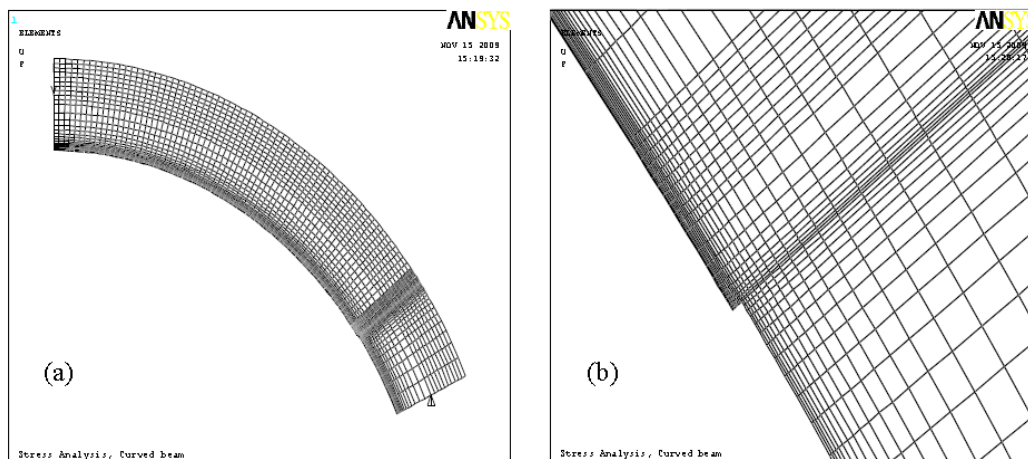


Fig.2.15. Finite element model of the FRP-strengthened curved beam: (a) mesh of the half of the beam; and (b) close-up of the mesh near the FRP plate end.

Fig. 2.16 shows the interface stresses predicted by present 3PEF model and the FEA for $R_0 = 1.5$ m. As comparison, stresses obtained from the 2PEF model (De Lorezis et al., 2006) are also presented in this figure. Fig. 2.16(a) shows the shear stress distribution near the end of the FRP plate. FEA results suggest that the shear stress along the mid-plane of the adhesive layer reaches its maximum at a small distance to the free edge and reduces to zero at the free edge of

the adhesive layer as anticipated. This feature is captured successfully by the 3PEF model, as demonstrated by the solid line in Fig. 2.16(a). This figure also shows that the 2PEF model fails to satisfy the zero-shear-stress boundary condition at the free edge. Fig. 2.16(b) compares the normal stresses distributions obtained through different methods. As illustrated by the FEA results, the normal stress distribution along the CA interface is different from that along the PA interface. The normal stress along the CA interface is tensile while the one along the PA interface is compressive near the end of the FRP plate. This feature suggests that debonding may initiate along the CA interface (within a thin layer of concrete), not along the PA interface for a curved RC beam strengthened by FRP plate. As demonstrated by Fig. 2.16(b), the present 3PEF captures this feature very well; while the 2PEF model only predicts one value for the both interfaces. Nevertheless, all the solutions converge to one value if the distance from the edge is large enough.

Fig. 2.16 confirms that the present 3PEF model successfully overcomes the drawbacks of the commonly used 2PEF model and captures two important features of the interface stress of the FRP strengthened curved concrete beam. Excellent agreement with FEA results has been achieved by the present model except a very small region near the end of the FRP plate. In this small boundary region, stress distribution is dominated by a rather complicated local stress field, which is singular and oscillatory along the CA and PA interfaces. The current analytical solutions based on the Timoshenko's beam theory are only valid out of this boundary region according to Saint Venant's Principle. Hogan and Knowles's (1983) estimation suggests that this small region is in proportion to the thickness of the beam. Therefore, the boundary zone for the normal stress along the CA interface is larger than that along the PA interface, as can be observed in Fig. 2.16(b).

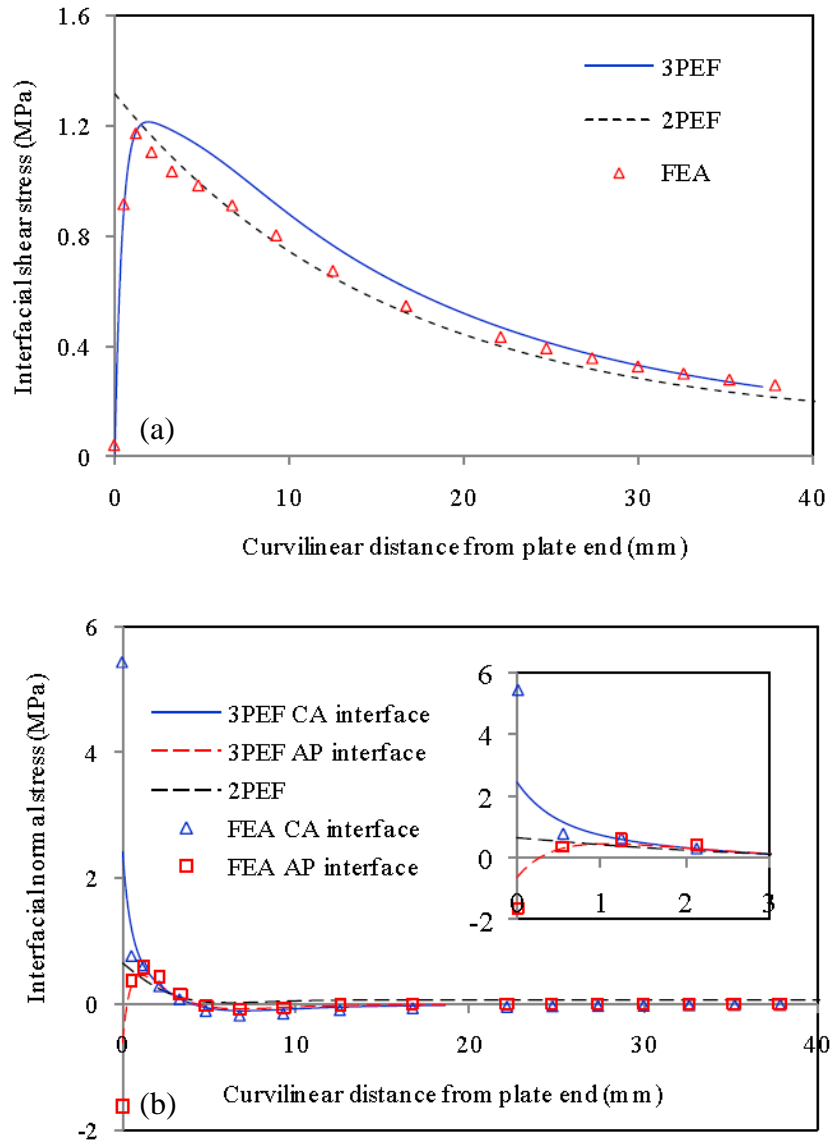


Fig.2.16. Interface stresses in a curved RC beam strengthened by FRP plate ($R_0 = 1.5$ m): (a) shear stress; and (b) normal stresses.

Fig. 2.17 demonstrates the effect of the radius of curvature of the beam on interface stress concentration near the edge of the FRP plate. Fig. 2.17(a) shows a clear trend of shear stress concentration increasing with the radius of curvature R_0 . Similar trend can be observed for normal stresses along the CA and PA interfaces, as shown in Fig. 2.17(b) and (c). This observation is in agreement with De Lorezis et al. (2006).

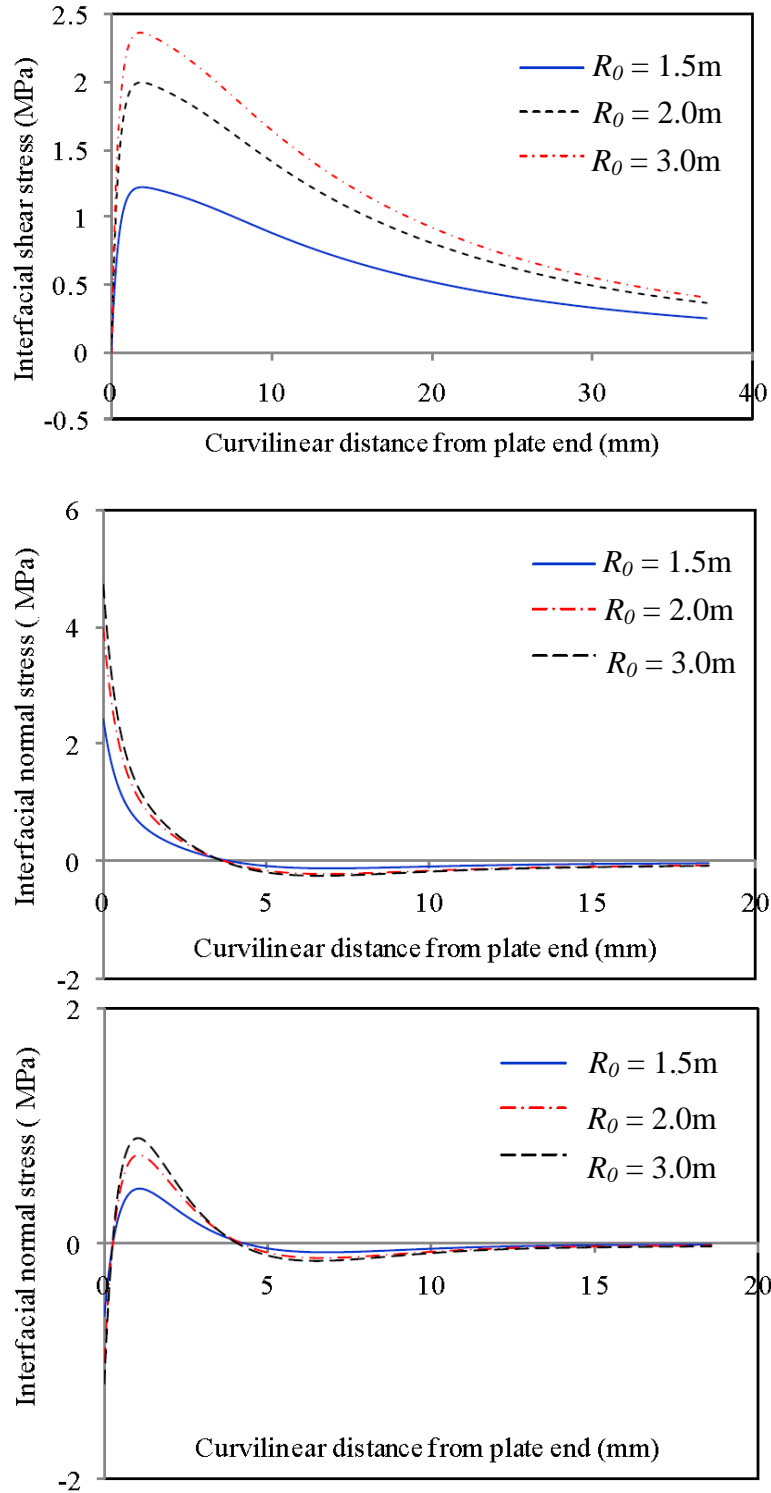


Fig.2.17. Radius of curvature's effect on interface stresses: (a) shear stress; (b) normal stresses along CA interface; and (c) normal stresses along PA interface.

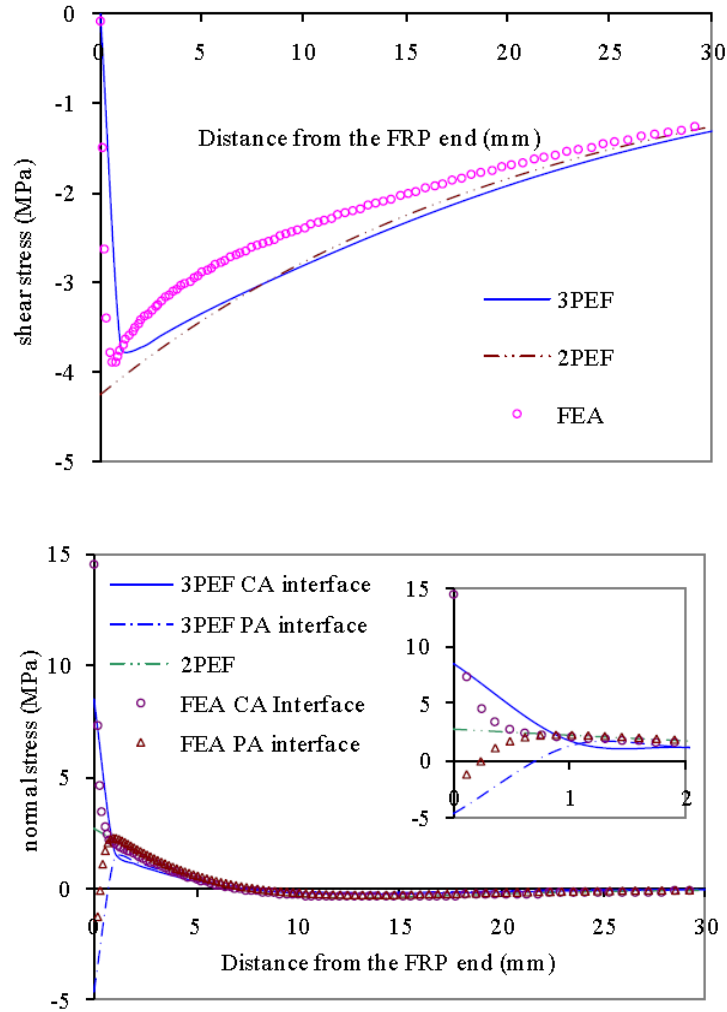


Fig.2.18. Interface stresses in a straight concrete beam strengthened by FRP plate: (a) shear stress; and (b) normal stresses.

When the radius of curvature R_0 goes to infinite, the curved RC beam becomes a straight beam. In such a case, the solution obtained in this study degrades to the solution for straight beams (Wang, 2007). Fig.2.18 compares the interface stresses in a straight reinforced concrete beam bonded with a FRP plate studied by Smith and Teng (2001). Similar conclusions can be draw on the straight beams: (a) the 3PEF model satisfies the zero-shear-stress boundary condition at the free edge of the adhesive layer, and (b) the 3PEF model can correctly predict two different normal stresses along the CA and PA interfaces.

2.4 Conclusions

In this study, an innovative three-parameter elastic foundation model is developed to better predict the interface stresses of the FRP strengthened concrete beam. This model is a direct extension of the 2PEF model used widely in adhesively bonded joint analysis. The new model considers the deflection of the adhesive layer, which is missing in 2PEF model. In addition, the 3PEF model is used to predict the interface stresses in a curved beam bonded with a thin plate. The 3PEF model considers the different normal stresses along the CA and PA interfaces, which are assumed the same along the two interfaces in the 2PEF model. The interaction between the normal and shear interface stress is also counted for through the equilibrium condition of the adhesive layer. In this way, an eighth-order governing differential equation is reached which makes it possible to implement all the eight available boundary conditions. The salient features of the are as follows: 1) it better predicts the tensile normal stress distribution along the CA interface and the compressive normal stress along the PA interface at the vicinity of the FRP plate end; 2) it satisfies all boundary conditions, including the zero shear stress at the edge of the adhesive layer; 3) its solutions are in explicit closed-form. Therefore, it can be easily implemented for analysis and design of FRP strengthened beams. The accuracy of the present model has been verified by its good agreements with FEA solutions. It should be pointed out that the present model can also be directly used to analyze general adhesively bonded joints (Wang and Zhang, 2009).

CHAPTER 3

VISCOELASTIC ANALYSIS OF FRP-STRENGTHENED RC BEAMS

3.1. Introduction

After a period of service, some extra deformations and interface stresses redistributions will become notable due to the strong time dependent feature of the adhesive layer. The FRP strengthening system enters its second stage, in which the viscoelastic behavior of the adhesive layer has to be taken into consideration. Epoxy, the most widely used adhesive in bonding FRP composite, exhibits viscoelastic properties (Brinson, 1982; Mirman and Knecht, 1990; Ferrier and Hamelin, 1999; Dean, 2006). Its material properties vary with time under different situations, especially in the regions of high stress concentration. Such variation of material properties can induce redistributions of stresses and additional deformations, which could be significant during the service life of the structure and cause potential failure of the strengthening, as demonstrated recently by Meshgin et al. (2009). Meshgin et al. (2009) found that the creep of epoxy could result in failure at the interfaces due to the combined effect of relatively high shear stress to ultimate shear strength and a thick layer of epoxy. For this reason, the time-dependent behavior of the FRP strengthened concrete structures has become the focus of a number of recent studies, both experimentally and numerically (Savoia et al., 2005; Diab and Wu, 2007a, b; Choi et al., 2007; Ascione et al., 2008; Chami et al., 2009; Meshgin et al., 2009; Ferrier et al., 2010; Choi et al., 2010). All of these studies showed that the FRP-concrete interface exhibited significant time-dependent behavior (Choi et al., 2010), and that the shear stress to the shear strength ratio

within the adhesive layer was a primary factor affecting the long-term behavior of the FRP-concrete interfaces (Choi et al., 2010).

Several rheological models were proposed to simulate the creep behaviors observed in the tests (Savoia et al., 2005; Diab and Wu, 2007a; Meshgin et al., 2009; Ferrier et al., 2010; Choi et al., 2010). Based on these rheological models, numerical methods including the finite difference method (Savoia et al., 2005) and the finite element method (Diab and Wu, 2007a; Choi et al., 2010) have been proposed to simulate the time-dependent behaviors of the FRP-strengthened RC structures. Numerical methods are usually time-consuming in simulating the time-dependent behavior of structures because sufficient small step must be used to avoid error accumulation. Analytical solutions are much more efficient.

So far no rigorous viscoelastic solution for the interface stresses and deflection for the FRP-strengthened RC beams is available. The major objective of this research is to fill this gap through developing viscoelastic solutions of the interface stresses and the deflection of a FRP-strengthened RC beam. These new solutions can be used as an efficient tool to evaluate the long-term behavior of the FRP-strengthened RC beams.

3.2. Viscoelastic model of an FRP-strengthened RC beam based on 2PEF model

Consider a simply supported RC beam (beam 1) with the thickness of h_1 strengthened by a thin FRP plate (beam 2) with the thickness of h_2 through external bonding with a thin adhesive layer with the thickness of h_0 , as shown in Fig. 3.1. A uniform load with magnitude of q is applied to the RC beam. Since the creep of the concrete and the FRP plate occurs within a much longer time period compared with the adhesive (Choi et al., 2007), only the adhesive layer is modeled as viscoelastic material in this study. The time-dependent properties of the FRP plate and the strengthened beam are ignored for the sake of simplicity.

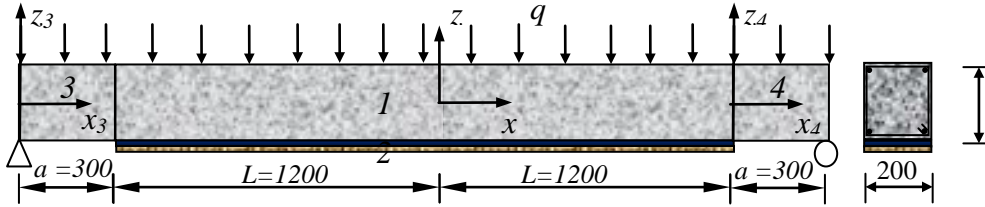


Fig.3.1. An FRP-strengthened RC beam.

A notable recent development in the FRP strengthening technique is that the FRP plate is prestressed before bonding to the RC beam. This technique can make better use of the tensile strength of the FRP plate (Wight et al., 2001) and reduce the crack development in the RC beam (Al-Emrani and Kligler, 2006). Although a number of experiments have been conducted to study the short-term behaviors of the RC beams strengthened by this technique (Xue et al., 2010; Nordin and Täljsten, 2006; Quantrill and Hollaway, 1998), the long-term behavior has not been addressed sufficiently, especially the prestress loss due to the creep of adhesive layer, which is critical to the success of the prestressing technique. To make this study also applicable to the prestressed FRP-strengthened RC beams, a prestress force N_0 is applied to the FRP plate in the formulation thereafter. This prestress is applied as following (Triantafillou and Deskovic, 1991). First the FRP plate is pretensioned; then the prestressed FRP plate is bonded to the tension side of the RC beam; finally, the FRP plate is cut at the two far ends once the adhesive achieves its full bonding strength.

3.2.1. Shear deformable beam theory

Both the RC beam and the FRP plate are modeled as the Timoshenko's beams, respectively. The displacement fields can then be written as:

$$\begin{aligned}
 U_1(x_1, z_1, t) &= u_1(x_1, t) + z_1 \phi_1(x_1, t), & U_2(x_2, z_2, t) &= u_2(x_2, t) + z_2 \phi_2(x_2, t) - u_0(x_2, t), \\
 W_i(x_i, z_i, t) &= w_i(x_i, t), & & (3.1)
 \end{aligned}$$

where subscripts, $i = 1, 2$, represent the beams 1 and 2 in Fig. 3.1. The x_i and z_i axels are the local coordinates and x_i is located at the neutral axis of beam i . $u_i(x, t)$, $\phi_i(x, t)$ and $w_i(x, t)$ are the axial displacement, rotation and deflection at the neutral axis of beam i . $u_0(x, t)$ is the initial displacement of the FRP plate before the pretension is released. $U_i(x_i, z_i, t)$ and $W_i(x_i, z_i, t)$ are the axial and transverse displacements of the beam i . The strains along the neutral axis in the two plates can be written as:

$$\begin{aligned}\varepsilon_{01}(x, t) &= \frac{\partial u_1(x, t)}{\partial x}, \quad \varepsilon_{02}(x, t) = \frac{\partial u_2(x, t)}{\partial x} - \frac{\partial u_0(x, t)}{\partial x}, \\ \kappa_{0i}(x, t) &= \frac{\partial \phi_i(x, t)}{\partial x}, \quad \gamma_{0i}(x, t) = \phi_i(x, t) + \frac{\partial w_i(x, t)}{\partial x}.\end{aligned}\quad (3.2)$$

The constitutive equations for beam i can be written as,

$$\begin{aligned}N_1(x, t) &= C_1 \frac{\partial u_1(x, t)}{\partial x}, \quad N_2(x, t) - N_0 H(t) = C_2 \left(\frac{\partial u_2(x, t)}{\partial x} - \frac{\partial u_0(x, t)}{\partial x} \right), \\ M_i(x, t) &= D_i \frac{\partial \phi_i(x, t)}{\partial x}, \quad Q_i(x, t) = B_i \left(\phi_i(x, t) + \frac{\partial w_i(x, t)}{\partial x} \right),\end{aligned}\quad (3.3)$$

where $N_i(x, t)$, $Q_i(x, t)$ and $M_i(x, t)$ are the resultant axial force, transverse shear force, and bending moment of beam i , respectively. $H(t)$ is the Heaviside step function. N_0 is the pretension force applied to the FRP plate. C_i , B_i and D_i are the axial, shear and bending stiffness coefficients of the beam i , respectively. For the plane stress condition,

$$C_i = E_i b h_i, \quad D_i = E_i b h_i^3 / 12, \quad B_i = \kappa G_i b h_i, \quad (3.4)$$

where E_i , G_i , are the longitude modulus, transverse shear modulus, respectively. κ is the shear correction coefficient chosen as 5/6 in this study and b is the width of the beam.

Considering an infinitesimal free body diagram of the FRP-strengthened RC beam shown in Fig. 3.2, the following equilibrium equations can be established as,

$$\frac{\partial N_1(x,t)}{\partial x} = b\tau(x,t), \quad \frac{\partial M_1(x,t)}{\partial x} = Q_1(x,t) - \frac{h_1}{2}b\tau(x,t), \quad \frac{\partial Q_1(x,t)}{\partial x} = b\sigma(x,t) + bqH(t), \quad (3.5a)$$

$$\frac{\partial N_2(x,t)}{\partial x} = -b\tau(x,t), \quad \frac{\partial M_2(x,t)}{\partial x} = Q_2(x,t) - \frac{h_2}{2}b\tau(x,t), \quad \frac{\partial Q_2(x,t)}{\partial x} = -b\sigma(x,t), \quad (3.5b)$$

where $\tau(x,t)$ and $\sigma(x,t)$ are the interface stress within the adhesive layer, which are assumed to be constant through the thickness of the adhesive layer.

Combining the first and third equation of (3.5a) and (3.5b) yields,

$$Q_1(x,t) = \frac{\partial M_1(x,t)}{\partial x} + \frac{h_1}{2} \frac{\partial N_1(x,t)}{\partial x}, \quad (3.6a)$$

$$Q_2(x,t) = \frac{\partial M_2(x,t)}{\partial x} - \frac{h_2}{2} \frac{\partial N_2(x,t)}{\partial x}. \quad (3.6b)$$

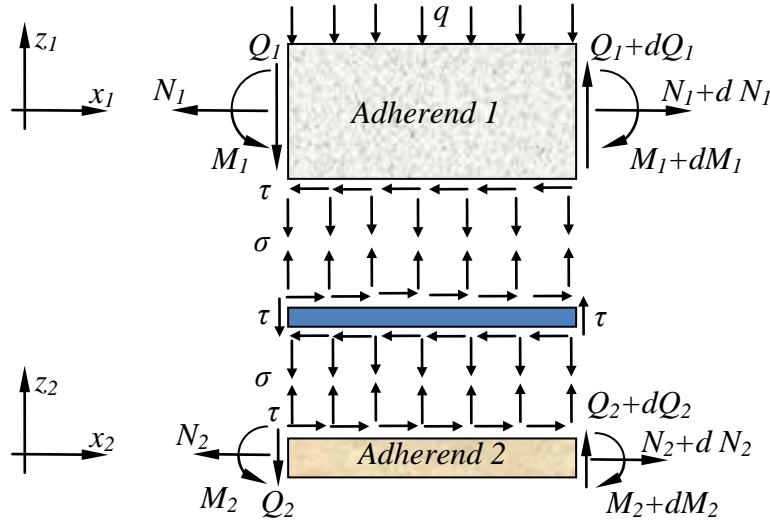


Fig.3.2. Free body diagram of an FRP-strengthened RC beam.

Global equilibrium of the bi-layer plate system requires,

$$N_T(x,t) = N_1(x,t) + N_2(x,t), \quad (3.7a)$$

$$Q_T(x,t) = Q_1(x,t) + Q_2(x,t), \quad (3.7b)$$

$$M_T(x,t) = M_1(x,t) + M_2(x,t) + N_1(x,t) \frac{h_1 + h_2}{2}, \quad (3.7c)$$

where $N_T(x,t)$, $Q_T(x,t)$, $M_T(x,t)$ are essentially the resulting forces of the bi-layer plate system with respect to the mid-plane of the FRP plate, as shown in Fig.3.2.

3.2.2. Viscoelastic interface model

Following the assumptions commonly used in the GR's model, the shear and normal stresses are assumed constant through the thickness of adhesive layer. Then the average strains within the adhesive layer can be established as (Delale and Erdogan, 1981),

$$\gamma_{xy}(x,t) = \left(u_0(x,t) + u_1(x,t) - \frac{h_1}{2} \phi_1(x,t) - u_2(x,t) - \frac{h_2}{2} \phi_2(x,t) \right) / h_0, \quad (3.8a)$$

$$\varepsilon_y(x,t) = (w_1(x,t) - w_2(x,t)) / h_0, \quad (3.8b)$$

$$\varepsilon_x(x,t) = \left(\frac{\partial u_1(x,t)}{\partial x} - \frac{h_1}{2} \frac{\partial \phi_1(x,t)}{\partial x} + \frac{\partial u_2(x,t)}{\partial x} + \frac{h_2}{2} \frac{\partial \phi_2(x,t)}{\partial x} - \frac{\partial u_0(x,t)}{\partial x} \right) / 2. \quad (3.8c)$$

The constitutive equation of a linear isotropic viscoelastic material can be expressed by means of differential operators in following forms,

$$P_1(s_{ij}) = Q_1(e_{ij}), \quad (i, j) = 1, 2, 3, \quad (3.9a)$$

$$P_2(s) = Q_2(e), \quad (3.9b)$$

where P_1 , Q_1 , P_2 and Q_2 are the differential operators; s_{ij} and e_{ij} ($i, j = 1, 2, 3$) are the deviatoric components of the stress and strain tensors, respectively; e and s are the volumetric strain and hydrostatic component of the stress, respectively. By considering the plane stress condition, the volumetric strain and hydrostatic stress are given by,

$$e = (\varepsilon_x + \varepsilon_y + \varepsilon_z) / 3, \quad (3.10a)$$

$$s = (\sigma_x + \sigma_y) / 3. \quad (3.10b)$$

Then the deviatoric strain tensor can be obtained as,

$$[e_{ij}] = \begin{bmatrix} \varepsilon_x & \gamma_{xy}/2 & 0 \\ \gamma_{xy}/2 & \varepsilon_y & 0 \\ 0 & 0 & \varepsilon_z \end{bmatrix} = \begin{bmatrix} e & 0 & 0 \\ 0 & e & 0 \\ 0 & 0 & e \end{bmatrix} + \begin{bmatrix} \varepsilon_x - e & \gamma_{xy}/2 & 0 \\ \gamma_{xy}/2 & \varepsilon_y - e & 0 \\ 0 & 0 & \varepsilon_z - e \end{bmatrix}. \quad (3.11a)$$

By defining $\sigma_y = \sigma$ and $\tau_{xy} = \tau$, we can obtain the deviatoric stress tensor as,

$$[s_{ij}] = \begin{bmatrix} \sigma_x & \tau & 0 \\ \tau & \sigma & 0 \\ 0 & 0 & 0 \end{bmatrix} = \begin{bmatrix} s & 0 & 0 \\ 0 & s & 0 \\ 0 & 0 & s \end{bmatrix} + \begin{bmatrix} \sigma_x - s & \tau & 0 \\ \tau & \sigma - s & 0 \\ 0 & 0 & -s \end{bmatrix}. \quad (3.11b)$$

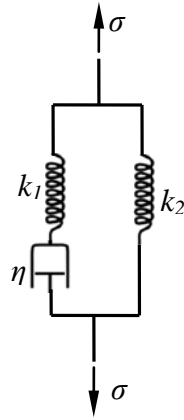


Fig. 3.3. Standard Linear Solid Model.

A number of visoelastic models have been proposed to simulate the adhesive layer (Brinson, 1982; Wu and Diab, 2007, Meshgin et al., 2009). Meshgin et al. (2009) found that a SLS Model can properly simulate the long-term creep behavior of the FRP concrete interface. Therefore, this model is employed in this study. As shown in Fig. 3.3, the SLS model consists of a Maxwell Model and a Hookean spring in parallel. The notations η and k_1 represent the coefficient of viscosity and the elastic stiffness for the Maxwell model, and k_2 is the elastic stiffness of the lone spring. Generally, these coefficients will change with environmental factors such as temperature, moisture, loading conditions, etc. These coefficients are assumed constants in this study for the sake of simplicity. Then the differential operator of the adhesive can be expressed as,

$$P_1 = a_1 + \frac{d}{dt}, \quad Q_1 = b_1 + b_2 \frac{d}{dt}, \quad (3.12)$$

where $a_1 = \frac{k_2}{\eta} = \frac{1}{t_0}$; $b_1 = \frac{k_1 k_2}{\eta} = \frac{k_1}{t_0}$; $b_2 = k_1 + k_2$; t_0 is the retardation time.

3.2.3. Governing Equation of viscoelastic 2PEF model

Inserting the deviatoric stress and strain components (Eqs. (3.10) and (3.11)) into the Eq. (3.9) yields,

$$P_1(2\sigma_x - \sigma) = Q_1(2\varepsilon_x - \varepsilon_y - \varepsilon_z), \quad (3.13a)$$

$$P_1(2\sigma - \sigma_x) = Q_1(2\varepsilon_y - \varepsilon_x - \varepsilon_z), \quad (3.13b)$$

$$-P_1(\sigma_x + \sigma) = Q_1(2\varepsilon_z - \varepsilon_x - \varepsilon_y), \quad (3.13c)$$

$$P_1(\tau) = \frac{1}{2}Q_1(\gamma_{xy}), \quad (3.13d)$$

$$P_2(\sigma_x + \sigma) = Q_2(\varepsilon_x + \varepsilon_y + \varepsilon_z). \quad (3.13e)$$

Noting that Eq. (3.13b) can be obtained by adding Eq. (3.13a) and (3.13c), it is neglected in the following derivation.

Since most viscoelastic materials behave elastically under a hydrostatic stress state, we can assume:

$$P_2 \equiv 1, \quad Q_2 \equiv 3K. \quad (3.14)$$

where K is the bulk modulus of the adhesive and $K = \frac{E_a G_a}{3(3G_a - E_a)}$.

By substituting Eq. (3.13e) into Eq. (3.13a) and Eq. (3.13c), we can eliminate ε_z ,

$$(2Q_1 + 3KP_1)(Q_1(2\varepsilon_x - \varepsilon_y) - P_1(6K(\varepsilon_x + \varepsilon_y) - 3\sigma)) - (6KP_1 + Q_1)(Q_1(\varepsilon_x + \varepsilon_y) - 3KP_1(\varepsilon_x + \varepsilon_y)) = 0. \quad (3.15)$$

Substituting the expression of the differential operator Eq. (3.12) into Eq. (3.15) and rearranging yield,

$$\left(a_{10} + a_{11} \frac{\partial}{\partial t} + a_{12} \frac{\partial^2}{\partial t^2} \right) \varepsilon_x + \left(b_{10} + b_{11} \frac{\partial}{\partial t} + b_{12} \frac{\partial^2}{\partial t^2} \right) \varepsilon_y + \left(c_{10} + c_{11} \frac{\partial}{\partial t} + c_{12} \frac{\partial^2}{\partial t^2} \right) \sigma = 0. \quad (3.16)$$

where $a_{10} = 3b_1^2 - 9a_1b_1K$, $a_{11} = 6b_1b_2 - 9b_1K - 9a_1b_2K$, $a_{12} = 3b_2^2 - 9b_2K$,

$b_{10} = -3b_1^2 - 18a_1b_1K$, $b_{11} = -6b_1b_2 - 18b_1K - 18a_1b_2K$, $b_{12} = -3b_2^2 - 18b_2K$,

$c_{10} = 6a_1b_1 + 9a_1^2K$, $c_{11} = 6b_1 + 6a_1b_2 + 18a_1K$, $c_{12} = 6b_2 + 9K$.

Substituting the strains equation (3.2) into (3.16),

$$\begin{aligned} & \left(a_{10} + a_{11} \frac{\partial}{\partial t} + a_{12} \frac{\partial^2}{\partial t^2} \right) \left(\frac{1}{2} \frac{\partial u_1(x,t)}{\partial x} - \frac{h_1}{4} \frac{\partial \phi_1(x,t)}{\partial x} + \frac{1}{2} \frac{\partial u_2(x,t)}{\partial x} + \frac{h_2}{4} \frac{\partial \phi_2(x,t)}{\partial x} - \frac{1}{2} \frac{\partial u_0(x,t)}{\partial x} \right) \\ & + \left(b_{10} + b_{11} \frac{\partial}{\partial t} + b_{12} \frac{\partial^2}{\partial t^2} \right) \left(\frac{w_1(x,t) - w_2(x,t)}{h_0} \right) + \left(c_{10} + c_{11} \frac{\partial}{\partial t} + c_{12} \frac{\partial^2}{\partial t^2} \right) \sigma(x,t) = 0. \end{aligned} \quad (3.17)$$

Differentiating both sides of Eq. (3.17) twice and inserting Eq. (3.3) into Eq. (3.17)

yields:

$$\begin{aligned} & \left(a_{10} + a_{11} \frac{\partial}{\partial t} + a_{12} \frac{\partial^2}{\partial t^2} \right) \left(\left(\frac{1}{2C_1} - \frac{1}{2C_2} - \frac{h_2(h_1+h_2)}{8D_2} \right) \frac{\partial^2 N_1(x)}{\partial x^2} \right. \\ & \left. - \left(\frac{h_1}{4D_1} + \frac{h_2}{4D_2} \right) \frac{\partial^2 M_1(x)}{\partial x^2} + bqH(t) \frac{h_2}{4D_2} \right) \\ & + \frac{1}{h_0} \left(b_{10} + b_{11} \frac{\partial}{\partial t} + b_{12} \frac{\partial^2}{\partial t^2} \right) \left(\left(\frac{1}{B_1} + \frac{1}{B_2} \right) \left(\frac{\partial^2 M_1(x)}{\partial x^2} + \frac{h_1}{2} \frac{\partial^2 N_1(x)}{\partial x^2} \right) - \frac{h_1+h_2}{2D_2} N_1(x) \right. \\ & \left. - \left(\frac{1}{D_1} + \frac{1}{D_2} \right) M_1(x) - \frac{1}{B_2} bqH(t) + \frac{1}{D_2} M_T(x) \right) \\ & + \frac{1}{b} \left(c_{10} + c_{11} \frac{\partial}{\partial t} + c_{12} \frac{\partial^2}{\partial t^2} \right) \left(\frac{\partial^4 M_1(x)}{\partial x^4} + \frac{h_1}{2} \frac{\partial^4 N_1(x)}{\partial x^4} \right) = 0. \end{aligned} \quad (3.18)$$

By inserting Eq. (3.8a) into Eq. (3.13d), we have

$$P_1(\tau, t) = \frac{1}{2} Q_1 \left\{ \left(u_1(x, t) - \frac{h_1}{2} \phi_1(x, t) - u_2(x, t) - \frac{h_2}{2} \phi_2(x, t) + u_0(x, t) \right) / h_0 \right\}. \quad (3.19)$$

Differentiating both sides of Eq. (3.19) twice and substituting Eq. (3.3) yields,

$$P_1 \left(\frac{1}{b} \frac{\partial^2 N_1(x,t)}{\partial x^2} \right) = \frac{1}{2} Q_1 \{ C_{11} N_1(x,t) + C_{12} M_1(x,t) + C_{13} N_T(x,t) + C_{14} M_T(x,t) + C_{15} N_0(x,t) \}, \quad (3.20)$$

where

$$C_{11} = \frac{1}{h_0} \left(\frac{1}{C_1} + \frac{1}{C_2} + \frac{h_2(h_1+h_2)}{4D_2} \right), \quad C_{12} = -\frac{1}{2h_0} \left(\frac{h_1}{D_1} - \frac{h_2}{D_2} \right),$$

$$C_{13} = -\frac{1}{C_2 h_0}, \quad C_{14} = -\frac{h_2}{2D_2 h_0}, \quad C_{15} = \frac{1}{C_2 h_0}.$$

Applying Laplace transform to Eq. (3.18) and rearranging give,

$$\begin{aligned} E_{11}(s) \frac{\partial^4 N_{1L}(x,s)}{\partial x^4} + E_{12}(s) \frac{\partial^4 M_{1L}(x,s)}{\partial x^4} + E_{13}(s) \frac{\partial^2 N_{1L}(x,s)}{\partial x^2} + E_{14}(s) \frac{\partial^2 M_{1L}(x,s)}{\partial x^2} \\ + E_{15}(s) N_{1L}(x,s) + E_{16}(s) M_{1L}(x,s) + E_{17}(s) M_{iL}(x,s) + E_{18}(s) q = 0. \end{aligned} \quad (3.21)$$

where

$$E_{11}(s) = \frac{h_1}{2b} (c_{10} + c_{11}s + c_{12}s^2), \quad E_{12}(s) = \frac{1}{b} (c_{10} + c_{11}s + c_{12}s^2),$$

$$E_{13}(s) = \frac{h_1}{2h_0} \left(\frac{1}{B_1} + \frac{1}{B_2} \right) (b_{10} + b_{11}s + b_{12}s^2) + \frac{1}{8} \left(\frac{4}{C_1} - \frac{4}{C_2} - \frac{h_2(h_1+h_2)}{D_2} \right) (a_{10} + a_{11}s + a_{12}s^2),$$

$$E_{14}(s) = \frac{1}{h_0} \left(\frac{1}{B_1} + \frac{1}{B_2} \right) (b_{10} + b_{11}s + b_{12}s^2) - \frac{1}{4} \left(\frac{h_1}{D_1} + \frac{h_2}{D_2} \right) (a_{10} + a_{11}s + a_{12}s^2),$$

$$E_{15}(s) = -\frac{1}{2D_2 h_0} (h_1 + h_2) (b_{10} + b_{11}s + b_{12}s^2), \quad E_{16}(s) = -\frac{1}{h_0} \left(\frac{1}{D_1} + \frac{1}{D_2} \right) (b_{10} + b_{11}s + b_{12}s^2),$$

$$E_{17}(s) = \frac{1}{D_2 h_0} (b_{10} + b_{11}s + b_{12}s^2), \quad E_{18}(s) = -\frac{b}{B_2 h_0 s} (b_{10} + b_{11}s + b_{12}s^2) + \frac{bh_2}{4D_2 s} (a_{10} + a_{11}s + a_{12}s^2).$$

Similarly, by applying Laplace transform to Eq. (3.20) and rearranging, we have,

$$M_{1L}(x,s) = \frac{D_{12}(s)}{D_{11}(s)} \frac{\partial^2 N_{1L}(x,s)}{\partial x^2} + \frac{D_{13}(s)}{D_{11}(s)} N_{1L}(x,s) + \frac{D_{14}(s)}{D_{11}(s)} N_{iL}(x,s) + \frac{D_{15}(s)}{D_{11}(s)} M_{iL}(x,s) + \frac{D_{16}(s)}{D_{11}(s)s} N_0. \quad (3.22)$$

where $N_{iL}(x,s)$ is the Laplace transform of $N_T(x,t)$, and

$$D_{11}(s) = \frac{1}{2}C_{12}(b_1 + b_2s), \quad D_{12}(s) = \frac{1}{2b}(a_1 + s), \quad D_{13}(s) = -\frac{1}{2}C_{11}(b_1 + b_2s),$$

$$D_{14}(s) = -\frac{1}{2}C_{13}(b_1 + b_2s), \quad D_{15}(s) = -\frac{1}{2}C_{14}(b_1 + b_2s), \quad D_{16}(s) = -\frac{1}{2}C_{15}(b_1 + b_2s).$$

By substituting Eq. (3.22) into Eq. (3.21), we can eliminate $M_{1L}(x,s)$ and obtain the governing equation in term of $N_{1L}(x, s)$ as:

$$\begin{aligned} & F_{11}(s) \frac{\partial^6 N_{1L}(x, s)}{\partial x^6} + F_{12}(s) \frac{\partial^4 N_{1L}(x, s)}{\partial x^4} + F_{13}(s) \frac{\partial^2 N_{1L}(x, s)}{\partial x^2} \\ & + F_{14}(s) N_{1L}(x, s) + F_{15}(s) N_{1L}(x, s) + F_{16}(s) M_{1L}(x, s) + F_{17}(s) N_0 / s + F_{18}(s) q = 0, \end{aligned} \quad (3.23)$$

where

$$F_{11}(s) = \frac{D_{12}(s)E_{12}(s)}{D_{11}(s)}, \quad F_{12}(s) = E_{11}(s) + \frac{D_{13}(s)E_{12}(s)}{D_{11}(s)} + \frac{D_{12}(s)E_{14}(s)}{D_{11}(s)},$$

$$F_{13}(s) = E_{13}(s) + \frac{D_{13}(s)E_{14}(s)}{D_{11}(s)} + \frac{D_{12}(s)E_{16}(s)}{D_{11}(s)}, \quad F_{14}(s) = E_{15}(s) + \frac{D_{13}(s)E_{16}(s)}{D_{11}(s)},$$

$$F_{15}(s) = \frac{D_{14}(s)E_{16}(s)}{D_{11}(s)}, \quad F_{16}(s) = E_{17}(s) + \frac{D_{15}(s)E_{16}(s)}{D_{11}(s)}, \quad F_{17}(s) = E_{18}(s) + \frac{bD_{15}(s)E_{14}(s)}{D_{11}(s)s},$$

$$F_{18}(s) = \frac{D_{16}(s)E_{16}(s)}{D_{11}(s)}.$$

By solving Eq. (3.23), we can obtain the axial force of the RC beam in the Laplace transform as,

$$N_{1L}(x, s) = \sum_{i=1}^6 c_i(s) e^{R_i(s)x} + N_{1CL}(x, s), \quad (3.24)$$

where $R_i(s)$ ($i = 1, 2, \dots, 6$) are the six roots of the characteristics equation of Eq. (3.23); $c_i(s)$ ($i = 1, 2, \dots, 6$) are the coefficients to be determined by the boundary conditions and

$$N_{1CL}(x, s) = -\frac{F_{15}(s)}{F_{14}(s)} N_{1L}(x, s) - \frac{F_{16}(s)}{F_{14}(s)} M_{1L}(x, s) - \frac{F_{17}(s)}{F_{14}(s)} q - \frac{F_{18}(s)}{F_{14}(s)s} N_0. \quad (3.25)$$

By inserting Eq. (3.24) into Eq. (3.22),

$$M_{1L}(x, s) = \sum_{i=1}^6 \frac{c_i(s)}{D_{11}(s)} \left(D_{12}(s) R_i^2(s) + D_{13}(s) \right) e^{R_i(s)x} + M_{1CL}(x, s), \quad (3.26)$$

where

$$M_{1CL}(x, s) = \frac{D_{12}(s)}{D_{11}(s)} \frac{\partial^2 N_{1CL}(x, s)}{\partial x^2} + \frac{D_{13}(s)}{D_{11}(s)} N_{1CL}(x, s) + \frac{D_{14}(s)}{D_{11}(s)} N_{1L}(x, s) + \frac{D_{15}(s)}{D_{11}(s)} M_{1L}(x, s) + \frac{D_{16}(s)}{D_{11}(s)} N_0. \quad (3.27)$$

Substituting Eqs. (3.24) and (3.26) into Eq. (3.6) gives

$$Q_{1L}(x, s) = \sum_{i=1}^6 \left(\frac{D_{12}(s)}{D_{11}(s)} R_i^3(s) + \frac{D_{13}(s)}{D_{11}(s)} R_i(s) + \frac{h_1}{2} R_i(s) \right) c_i(s) e^{R_i(s)x} + Q_{1CL}(x, s), \quad (3.28)$$

where

$$Q_{1CL}(x, s) = \frac{\partial M_{1CL}(x, s)}{\partial x} + \frac{h_1}{2} \frac{\partial N_{1CL}(x, s)}{\partial x}. \quad (3.29)$$

The Laplace transforms of interface shear and normal stresses are then obtained as:

$$\tau_L(x, s) = \frac{1}{b} \left(\sum_{i=1}^6 c_i(s) R_i(s) e^{R_i(s)x} + \frac{\partial N_{1CL}(x, s)}{\partial x} \right), \quad (3.30)$$

$$\sigma_L(x, s) = \frac{1}{b} \sum_{i=1}^6 \left(\frac{D_{12}(s)}{D_{11}(s)} R_i^4(s) + \frac{D_{13}(s)}{D_{11}(s)} R_i^2(s) + \frac{h_1}{2} R_i^2(s) \right) c_i(s) e^{R_i(s)x} + \frac{1}{b} \frac{\partial Q_{1CL}(x, s)}{\partial x} - \frac{q}{s}. \quad (3.31)$$

For a simply supported beam shown in Fig.3.1, the following boundary conditions can be used to determine $c_i(s)$,

$$(1) N_1(-L, t) = 0, \quad (2) Q_1(-L, t) = -\frac{bL}{2} qH(t), \quad (3) M_1(-L, t) = -\frac{bLa}{2} qH(t), \quad (3.32a)$$

$$(4) N_1(L, t) = 0, \quad (5) Q_1(L, t) = \frac{bL}{2} qH(t), \quad (6) M_1(L, t) = -\frac{bLa}{2} qH(t). \quad (3.32b)$$

Here it is assumed that the external forces are applied instantly and kept constant with time.

3.2.4. Numerical method for inverse Laplace transform

An explicit formula developed by Zakian (1969, 1970a, b) is used to evaluate the inverse Laplace transform numerically. According to the Zakian's algorithm, the inverse Laplace transverse of $F(s)$ can be written as,

$$f(t) = \sum_{i=1}^n K_i F(s_i), \quad (3.33)$$

where the values of K_i , s_i , and n are determined by a particular method. A simple implementation of Zakian's algorithm is given by,

$$f(t) = \frac{2}{t} \sum_{i=1}^5 \operatorname{Re} \left(K_i F \left(\frac{\alpha_i}{t} \right) \right), \quad (3.34)$$

where constants α_i and K_i are given by Zakian (1970a) as listed in Table 3.1.

Table 3.1 Set of Constants α_i and K_i for the Zakian's Method

i	α_i	K_i
1	$12.83767675 + j 1.666063445$	$-36902.08210 + j 196990.4257$
2	$12.22613209 + j 5.012718792$	$61277.02524 - j 95408.62551$
3	$10.93430308 + j 8.409673116$	$-28916.56288 + j 18169.18531$
4	$8.776434715 + j 11.92185389$	$4655.361138 - j 1.901528642$
5	$5.225453361 + j 15.72952905$	$-118.7414011 - j 141.3036911$

3.2.5. Deflections

Once the resultant forces and interface stresses are obtained, the deflection and rotation of the RC beam are calculated using the constitutive equation Eq. (3.3).

In the segment $x < -L$,

$$Q_1(x) = -bq(L + a - x), \quad M_1(x) = bqx(x/2 - (L + a)). \quad (3.35)$$

Then the rotation and the deflection of this segment are calculated by,

$$\phi_1(x, t) = \int_{-a-L}^x \frac{M_1(x)}{D_1} dx + \phi_1(-a-L, t), \quad w_1(x) = \int_{-a-L}^x \left(\frac{Q_1(x)}{B_1} - \phi_1(x) \right) dx + w_1(-L-a, t). \quad (3.36)$$

In the segment $-L < x < L$, $M_I(x, t)$ and $Q_I(x, t)$ are determined in the above sections.

$$\phi_1(x,t) = \int_{-L}^x \frac{M_1(x)}{D_1} dx + \phi_1(-L,t), \quad w_1(x) = \int_{-L}^x \left(\frac{Q_1(x)}{B_1} - \phi_1(x) \right) dx + w_1(-L,t). \quad (3.37)$$

The integration constants in Eqs. (3.35) and (3.36) can be determined by the boundary and continuity conditions. Considering the symmetry of the structure shown in Fig. 3.1, the following boundary and continuity conditions can be obtained,

$$w_1(-L-a,t) = 0, \quad \phi_1(0,t), \quad (3.38)$$

$$\phi_1(-L,t) = \int_{-a-L}^{-L} \frac{M_1(x)}{D_1} dx + \phi_1(-a-L,t), \quad w_1(-L,t) = \int_{-L-a}^{-L} \left(\frac{Q_1(x)}{B_1} - \phi_1(x) \right) dx. \quad (3.39)$$

3.2.6. Validation of the analytical solution

As verifications, a simply supported RC beam strengthened by an FRP plate shown in Fig.3.1 is studied using the present analytical method and the FEA. As shown in Fig.3.1, a uniformly distributed load $q = 0.1 \text{ N/mm}^2$ is applied to the RC beam. The geometry of the structure shown in Fig. 3.1 is given as: $a = 300 \text{ mm}$, $L = 1200 \text{ mm}$, $h_1 = 300 \text{ mm}$, $h_2 = 4\text{mm}$, $h_0 = 2 \text{ mm}$, and $b = 200 \text{ mm}$. The material properties of the RC beam, the FRP plate, and the adhesive layer are listed in Table 3.2.

Table 3.2 Material properties of the FRP-strengthened RC beam

Materials	RC beam	Adhesive layer	FRP plate
Young's modulus	30,000	2000	100,000
Poisson ratio	0.18	0.3	0.35

Following a procedure similar to Delale and Endogen (1981), we can relate the viscoelastic properties in SLS model to the conventional elastic material properties such as shear modulus. To this end, we can consider a shear stress $\tau = \tau_0 H(t)$ applied to SLS model shown in Fig. 3.3. Then

$$\left(a_1 + \frac{\partial}{\partial t}\right)\tau_0 H(t) = \frac{1}{2}\left(b_1 + b_2 \frac{\partial}{\partial t}\right)\gamma. \quad (3.40)$$

Applying the Laplace transform to both sides of Eq. (3.39) and rearranging yield,

$$\frac{1}{2}\gamma_L = \tau_0 \frac{1}{b_1 + b_2 s} \left(1 + \frac{a_1}{s}\right), \quad (3.41)$$

where γ_L is the Laplace transform of the shear strain γ . Applying the inverse Laplace transform to the both sides of Eq. (3.40) yields,

$$\frac{1}{2}\gamma = \frac{\tau_0}{b_1} \left(a_1 + \frac{b_1 - a_1 b_2}{b_2} e^{-\frac{b_1}{b_2} t} \right). \quad (3.42)$$

Considering two extreme cases, $t = 0$ and $t = \infty$ gives,

$$\frac{\tau_0}{\gamma(0^+)} = \frac{1}{2} \frac{b_1}{a_1 + \frac{b_1 - a_1 b_2}{b_2}} = \frac{b_2}{2}, \quad \frac{\tau_0}{\gamma(\infty)} = \frac{1}{2} \frac{b_1}{a_1 + 0} = \frac{b_1}{2a_1}. \quad (3.43)$$

Define the initial and ultimate shear moduli as,

$$G_0 = \frac{\tau_0}{\gamma(0^+)}, \quad G_\infty = \frac{\tau_0}{\gamma(\infty)}, \quad (3.44)$$

where G_0 and G_∞ are the initial and the ultimate shear modulus, respectively.

Rewrite Eq. (3.42) as

$$b_2 = 2G_0, \quad k_1 = 2G_\infty. \quad (3.45)$$

Then

$$k_2 = k_1 + k_2 - k_1 = b_2 - 2G_\infty = 2(G_0 - G_\infty) \quad (3.46)$$

In the following examples, the initial shear modulus G_0 is chosen as the elastic shear modulus of the adhesive shown in Table 3.2. The ultimate shear modulus and the retardation time are chosen as,

$$G_\infty = G_0/3, \quad t_0 = 5 \text{ days}. \quad (3.47)$$

High order plane stress element (8-node biquadratic element (CPS8)) is employed to mesh the structure in order to obtain accurate FEA solution. This element can be used where stress concentrations exist and provide the best resolution of the stress gradients at the lowest cost. Due to symmetry, only half of the beam is modeled as shown in Fig. 3.4. Very fine mesh is used at the plate end to accurately capture the stress concentrations at that location. The size of elements placed within the adhesive layer is 0.25mm, which is one fourth of the thickness of the adhesive layer. The viscoelastic behavior of the adhesive layer is implemented in a commercially available FEA software ABAQUS through a user subroutine UMAT. The user subroutine UMAT provides a way to program any mechanical constitutive model, which is not included in the ABAQUS's material library. For a particular mechanical constitutive model, the stress and strain tensors and material Jacobian matrix will be updated at the end of the time increment.

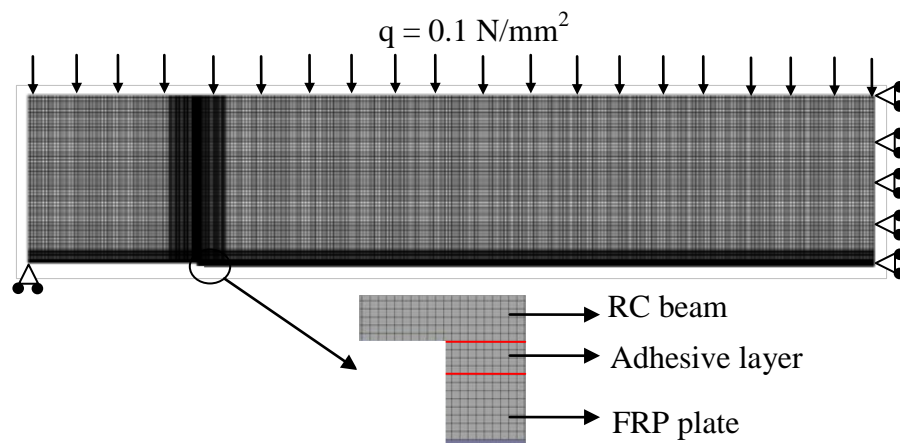


Fig. 3.4. Finite element model of simply supported RC beam.

3.2.6.1 FRP-strengthened RC beam without pretension force

Figs. 3.5 and 3.6 show the interface shear and normal stresses obtained by the present method and FEA for the FRP strengthened RC beams shown in Fig. 3.1. There is no prestress applied to the FRP plate. The stresses obtained by the FEA are extracted from the middle plane of the adhesive layer. It is observed that the present model agrees well with FEA except a small

zone near the free edge of the adhesive layer. In this small zone, FEA shows that shear stress reduces to zero at the free edge; while the present analytical model shows that the shear stress reaches its maximum at the free edge. This discrepancy is caused by the inherent shortcoming of the 2PEF model of the adhesive layer.

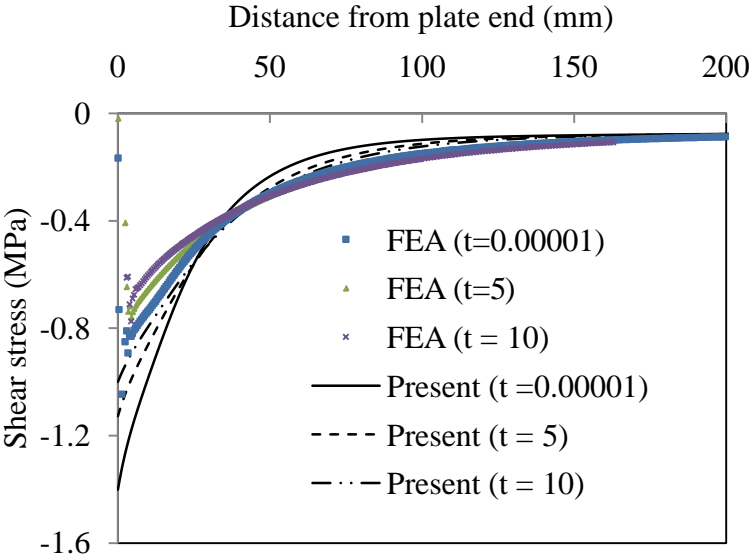


Fig.3.5. Redistribution of interface shear stress with time (day).

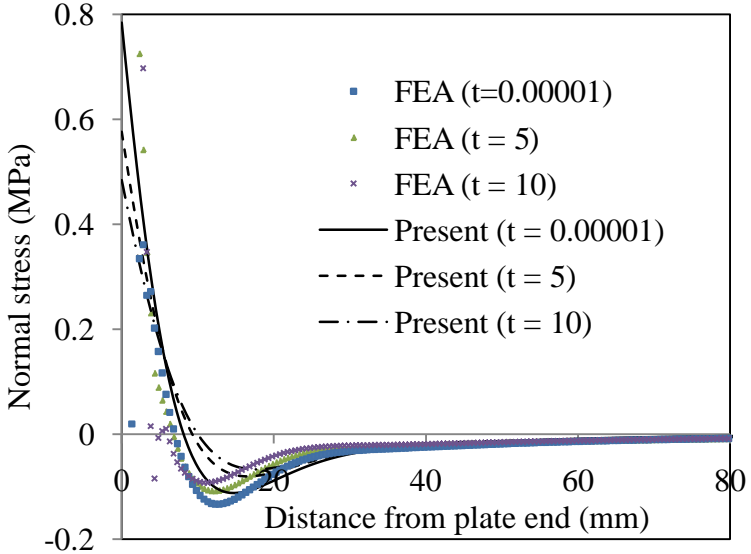


Fig.3.6. Redistribution of interface normal stress with time (day).

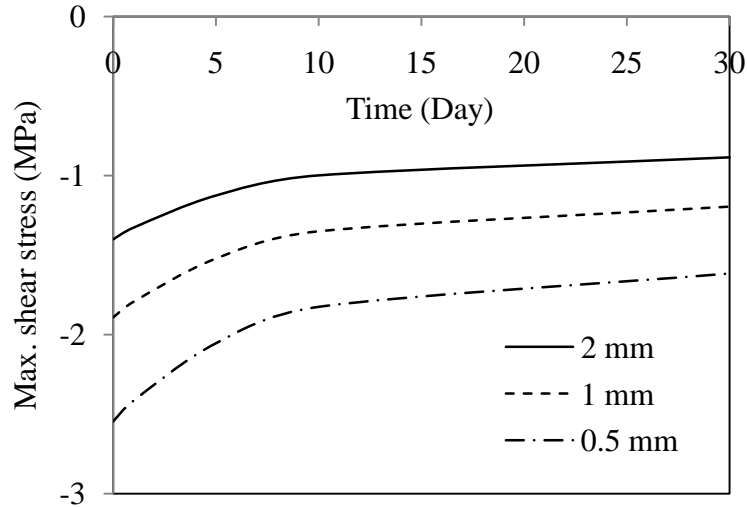


Fig.3.7. Maximum interface shear stress reducing with time.

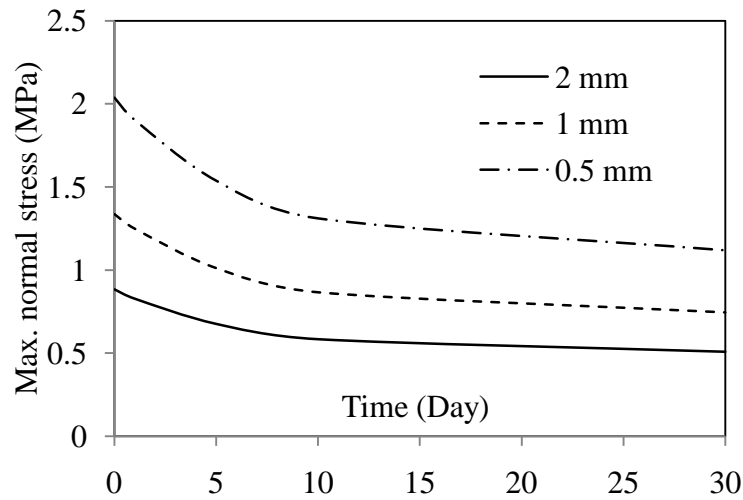


Fig.3.8. Maximum interface normal stress reducing with time.

As anticipated, significant interface stress redistributions with time are observed from both figures. Both the shear and normal interface stress concentrations are alleviated due to the creep deformation of the adhesive layer. Figs. 3.7 and 3.8 show that the maximum interface shear and normal stresses reduce with time. In these two figures, three thicknesses of the adhesive layer are considered. It can be seen that the maximum interface stresses are higher for thinner adhesive layer. The reducing in the maximum interface stresses with time is desirable for preventing the interface debonding. But it can reduce the efficiency of the interface layer in

transferring loading from the RC beam to the FRP plate. This is seen more clearly in Figs. 3.9 and 3.10.

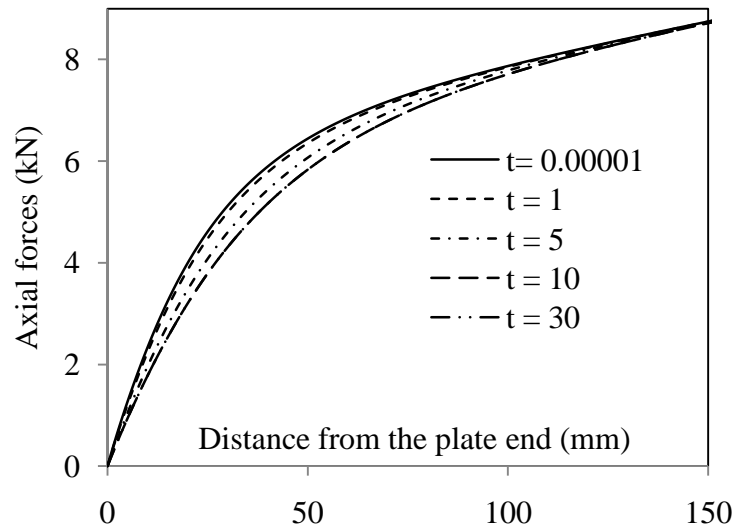


Fig.3.9. Variation of axial force in FRP plate with time (day).

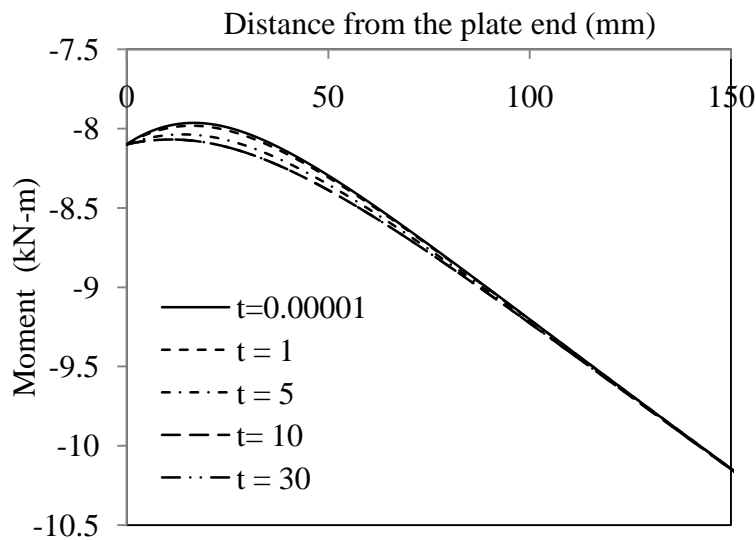


Fig.3.10. Variation of moment in RC beam with time (day).

Fig. 3.9 shows that the axial force transferred from the RC beam to the FRP plate reduces with time. As a result, the bending moment magnitude in the RC beam increases with time, as shown in Fig. 3.10. This trend is more clearly demonstrated in Figs. 3.11 and 3.12, in which the axial force of the FRP plate and the bending moment of the RC beam at a distance of 25 mm

from the FRP plate end are presented, respectively. This trend suggests that the strengthening effect of the FRP plate near the ends reduces with time due to the relaxation of the adhesive layer. Figs. 3.11 and 3.12 also show that more force can be transferred to the FRP plate if the thinner adhesive layer is used. However, this could increase the interface stress significantly, as shown in Figs. 3.7 and 3.8.

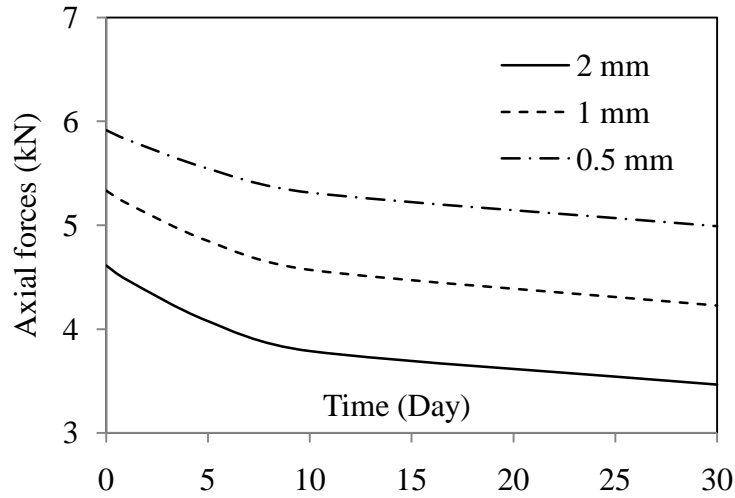


Fig.3.11. Axial forces of the FRP plate at 25mm from the FRP plate end varying with time.

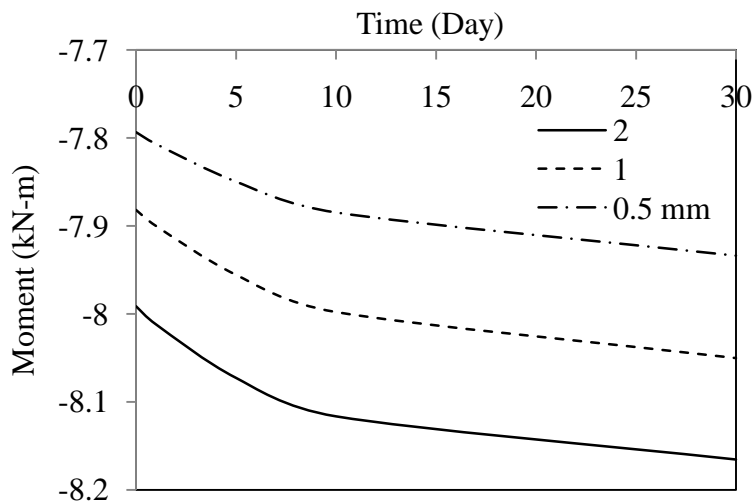


Fig.3.12. Moments in the RC beam at 25mm from FRP plate end varying with time.

Fig. 3.13 shows the creep deflection at the middle span of the beam. As shown in this figure, the creep deflection increases more quickly in the first several days and slows down after a certain time. The thickness of the adhesive layer plays an important role in the deflection of the beam. When thicker adhesive layer is used, the instant deflection due to the elastic deformation and the creep deflection due to the viscoelastic behavior of the adhesive are higher too, as shown in Fig. 3.13.

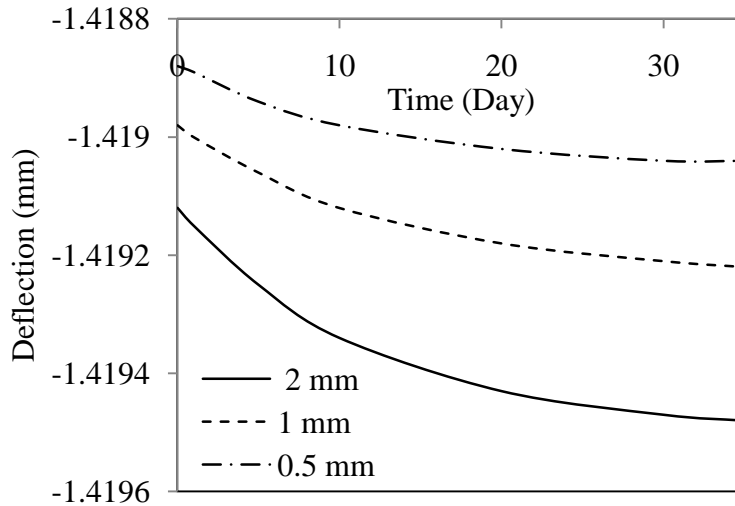


Fig.3.13. Deflection at the mid-span increasing with time.

3.2.6.2 Prestressed FRP-strengthened RC beam

In this section, the same beam considered in the above section is examined with a pretension load of 10 kN applied to the FRP plate. Figs. 3.14 and 3.15 show the interface stress redistributions in the adhesive layer with time. Similar trend as in the case without prestress can be observed in these two figures. The creep deformation of the adhesive layer actually alleviates the stress concentrations within the adhesive layer. Compared with the case without the prestress (Figs. 3.5 and 3.6), prestress applied to the FRP plate introduces higher stress concentration. The maximum interface shear and normal stresses in the prestressed case are more than twice as high as those in the un-prestressed case.

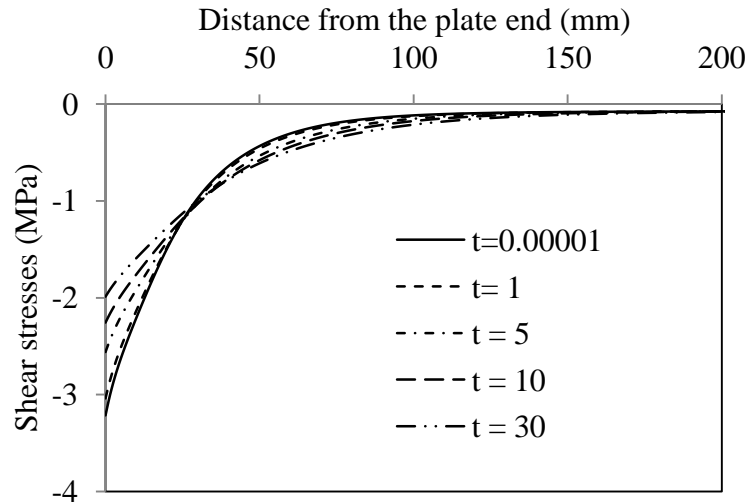


Fig.3.14. Redistribution of interface shear stress with time (day) in the prestressed FRP-strengthened RC beam.

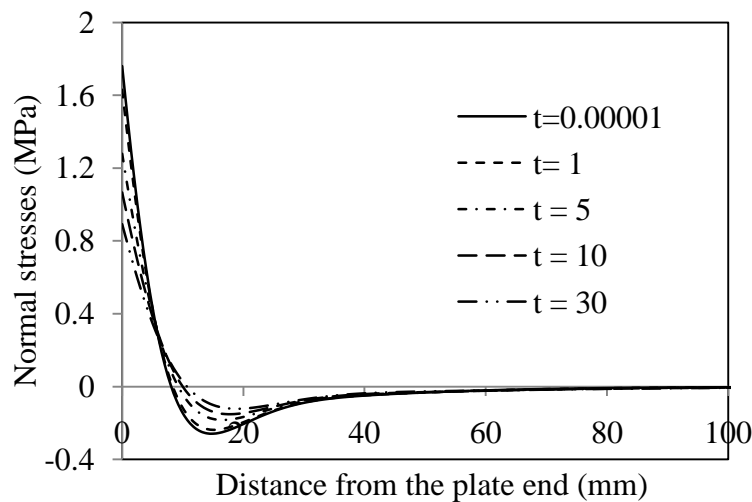


Fig.3.15. Redistribution of interface normal stress with time (day) in the prestressed FRP plate strengthened RC beam.

Fig. 3.16 shows the axial force of the FRP plate. Due to the pretension force, the axial force of the FRP plate is much higher than in the previous case without the pretension force (Fig. 3.9). Consequently, the moment in the RC beam is lower than in the case of without the pretension force (Fig. 3.10), as demonstrated by Fig. 3.17. Fig. 3.18 shows the creep deflection at

the middle span of the beam. Similar to the previous case (Fig. 3.13), higher instant deflection and creep deformation are observed for the thicker adhesive layer.

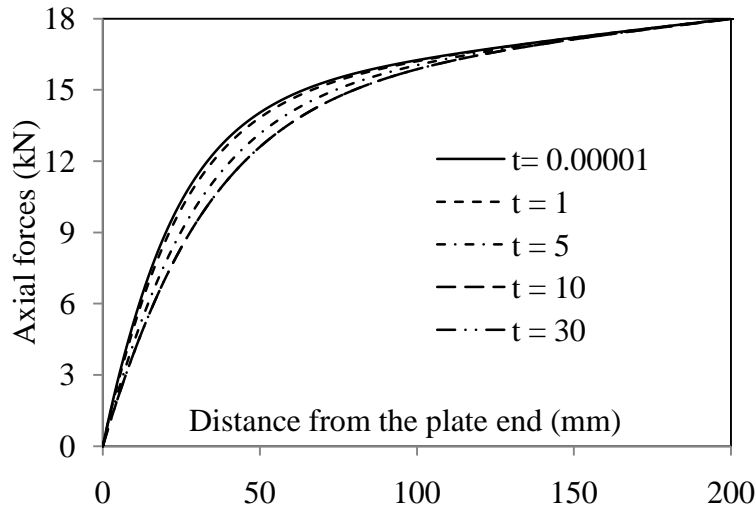


Fig. 3.16. Variation of the axial force in the prestressed FRP plate with time (day).

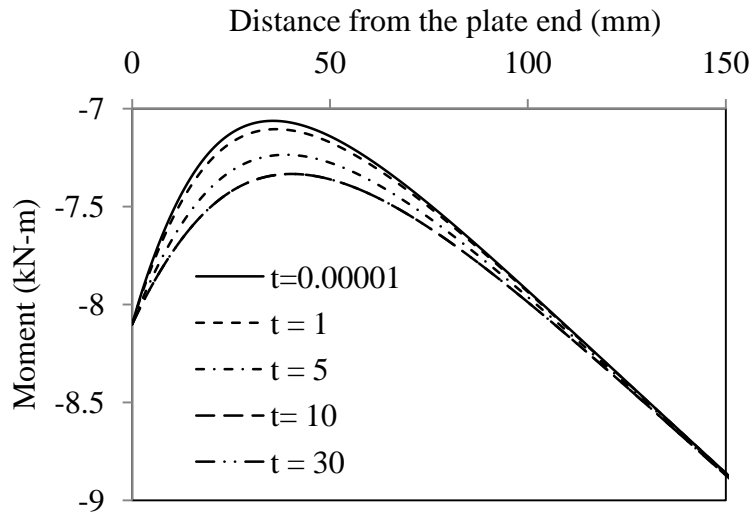


Fig.3.17. Variation of moment in RC beam with time (day)

Fig. 3.18 also clearly demonstrates the effect of the pretension force in reducing the deflection of the RC beam. Compared to the un-prestressed case, the instant deflection and creep deformation at the middle span for the prestressed case are lower than those in the case of without prestressing force (Fig. 3.13).

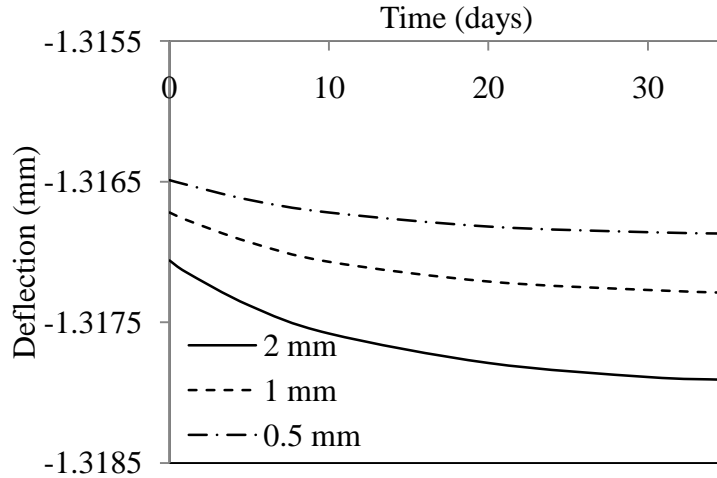


Fig.3.18. Deflection at the mid-span with time in the prestressed FRP-strengthened RC beam with time for different thicknesses of adhesive layer.

3.3. Viscoelastic model of an FRP-strengthened RC beam based on 3PEF model

The above viscoelastic interface stress solutions are based on the 2PEF model, which suffers two drawbacks as discussed in Chapter 2. To overcome these drawbacks, a viscoelastic analytical solution will be developed in this section based on the 3PEF model.

3.3.1. Bi-layer beam model for a prestressed FRP-strengthened RC beam

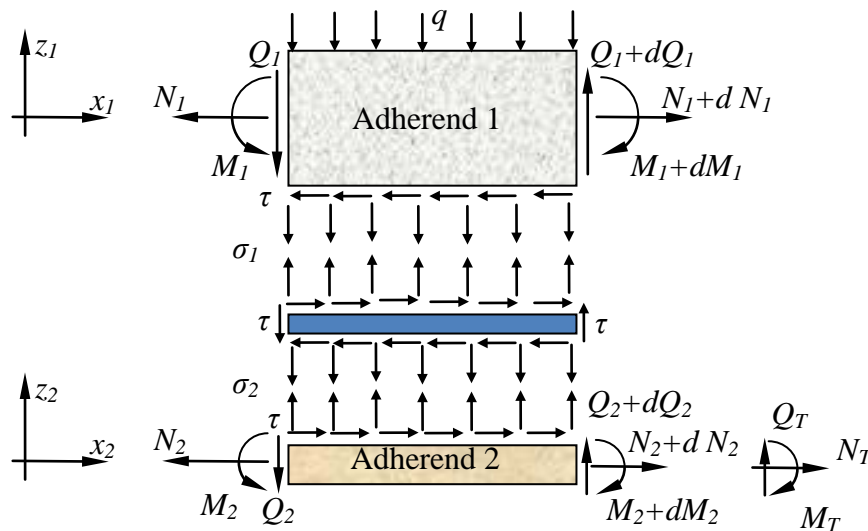


Fig. 3.19. Free body diagram of prestressed FRP-strengthened RC beam.

A prestressed FRP- strengthened RC beam can be modeled as a two-layer beam under general loading as shown in Fig. 3.1. The deformations, strains, and constitutive equations of the adherends are the same as in the 2PEF model given by Eqs. (3.1), (3.2), and (3.3), respectively.

Considering the infinitesimal free body diagram of FRP plate strengthened RC beam shown in Fig. 3.19, the following equilibrium equations can be established as,

$$\frac{\partial N_1(x,t)}{\partial x} = b\tau(x,t), \quad \frac{\partial M_1(x,t)}{\partial x} = Q_1(x,t) - \frac{h_1}{2}b\tau(x,t), \quad \frac{\partial Q_1(x,t)}{\partial x} = b\sigma_1(x,t) + bqH(t), \quad (3.48a)$$

$$\frac{\partial N_2(x,t)}{\partial x} = -b\tau(x,t), \quad \frac{\partial M_2(x,t)}{\partial x} = Q_2(x,t) - \frac{h_2}{2}b\tau(x,t), \quad \frac{\partial Q_2(x,t)}{\partial x} = -b\sigma_2(x,t), \quad (3.48b)$$

where $\tau(x,t)$ is the interface stress within the adhesive layer, which are assumed to be constant through the thickness of the adhesive layer. $\sigma_1(x,t)$ and $\sigma_2(x,t)$ are the interfacial normal stresses at the CA interface and AP interface, respectively. By combining the first and second equations of Eqs. (3.48a) and (3.48b), the following two equations can be derived,

$$Q_1(x,t) = \frac{\partial M_1(x,t)}{\partial x} + \frac{h_1}{2} \frac{\partial N_1(x,t)}{\partial x}, \quad (3.49a)$$

$$Q_2(x,t) = \frac{\partial M_2(x,t)}{\partial x} - \frac{h_2}{2} \frac{\partial N_2(x,t)}{\partial x}. \quad (3.49b)$$

3.3.2. 3PEF viscoelastic interface model

In this study, the 3PEF model proposed by Wang (2007) will be employed to model the viscoelastic behavior of the adhesive layer. As shown in Fig. 3.20, the deflection at the mid-plane of the adhesive layer is treated as an independent parameter, which is ignored in the conventional 2PEF model. It is assumed that the interface shear stress is constant through the thickness of adhesive layer, but interfacial normal stresses are different at two interfaces. Therefore, the average shear and normal strains within the adhesive layer can be established as (Wang, 2007),

$$\gamma_{xy}(x,t) = \left(u_1(x,t) - \frac{h_1}{2} \phi_1(x,t) - u_2(x,t) - \frac{h_2}{2} \phi_2(x,t) + u_0(x) \right) / h_0 + \frac{\partial w_a(x,t)}{\partial x}, \quad (3.50a)$$

$$\varepsilon_{y1}(x,t) = 2(w_1(x,t) - w_a(x,t)) / h_0, \quad (3.50b)$$

$$\varepsilon_{y2}(x,t) = 2(w_a(x,t) - w_2(x,t)) / h_0, \quad (3.50c)$$

$$\varepsilon_x(x,t) = \left(\frac{\partial u_1(x,t)}{\partial x} - \frac{h_1}{2} \frac{\partial \phi_1(x,t)}{\partial x} + \frac{\partial u_2(x,t)}{\partial x} + \frac{h_2}{2} \frac{\partial \phi_2(x,t)}{\partial x} - \frac{\partial u_0(x)}{\partial x} \right) / 2. \quad (3.50d)$$

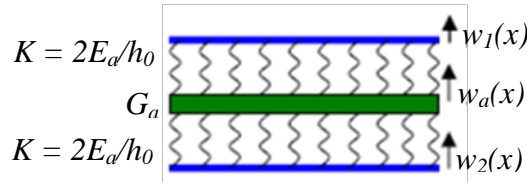


Fig. 3.20 Three-parameter elastic foundation model of the adhesive layer

To establish the viscoelastic constitutive equation of the adhesive layer, the strain tensors need to be decomposed into deviatoric components and volumetric strain components, which has elastic relationship with hydrostatic components of stress tensor for most viscoelastic materials under a hydrostatic stress state. For the plane stress condition, the volumetric strains and hydrostatic components of stress tensors can be defined as,

$$e_k = (\varepsilon_x + \varepsilon_{yk} + \varepsilon_z) / 3, \quad k = 1, 2. \quad (3.51a)$$

$$s_k = (\sigma_x + \sigma_{yk}) / 3, \quad k = 1, 2. \quad (3.51b)$$

where ε_{yk} and σ_{yk} represent the normal strains and stresses at different interfaces.

Therefore, the strain tensors of the adhesive layer can be decomposed as,

$$\begin{bmatrix} \varepsilon_x & \gamma_{xy}/2 & 0 \\ \gamma_{xy}/2 & \varepsilon_{yk} & 0 \\ 0 & 0 & \varepsilon_z \end{bmatrix} = \begin{bmatrix} e_k & 0 & 0 \\ 0 & e_k & 0 \\ 0 & 0 & e_k \end{bmatrix} + \begin{bmatrix} \varepsilon_x - e_k & \gamma_{xy}/2 & 0 \\ \gamma_{xy}/2 & \varepsilon_{yk} - e_k & 0 \\ 0 & 0 & \varepsilon_z - e_k \end{bmatrix}, \quad k = 1, 2. \quad (3.52a)$$

Similarly defining $\sigma_{yk} = \sigma_k$, $\tau_{xy} = \tau$, the stress tensors can be decomposed as,

$$\begin{bmatrix} \sigma_x & \tau & 0 \\ \tau & \sigma_k & 0 \\ 0 & 0 & 0 \end{bmatrix} = \begin{bmatrix} s_k & 0 & 0 \\ 0 & s_k & 0 \\ 0 & 0 & s_k \end{bmatrix} + \begin{bmatrix} \sigma_x - s_k & \tau & 0 \\ \tau & \sigma - s_k & 0 \\ 0 & 0 & -s_k \end{bmatrix}, \quad k = 1, 2. \quad (3.52b)$$

The linear isotropic viscoelastic behavior of the adhesive layer can be expressed by means of differential operators in the following forms,

$$P_1(s_{ij}) = Q_1(e_{ij}), \quad (i, j) = 1, 2, 3, \quad (3.53a)$$

$$P_2(s_k) = Q_2(e_k), \quad k = 1, 2, \quad (3.53b)$$

where e_{ij} and s_{ij} ($i, j = 1, 2, 3$) are the deviatoric components of strain and stress tensors. e_k and s_k are the volumetric strain and hydrostatic component of stress tensor, respectively. The SLS Model used in the 2PEF viscoelastic model as shown in Fig. 3.3 will be employed here to model the adhesive layer.

3.3.3. Governing equation based on 3PEF viscoelastic model

Plug the corresponding components of stress and strain tensor in Eqs. (3.51) and (3.52) into constitutive Eq. (3.53), the following equations can be established,

$$P_1(2\sigma_x - \sigma_k) = Q_1(2\varepsilon_x - \varepsilon_{yk} - \varepsilon_z), \quad k = 1, 2. \quad (3.54a)$$

$$P_1(2\sigma_k - \sigma_x) = Q_1(2\varepsilon_{yk} - \varepsilon_x - \varepsilon_z), \quad k = 1, 2. \quad (3.54b)$$

$$-P_1(\sigma_x + \sigma_k) = Q_1(2\varepsilon_z - \varepsilon_x - \varepsilon_{yk}), \quad k = 1, 2. \quad (3.54c)$$

$$P_1(\tau) = \frac{1}{2}Q_1(\gamma_{xy}), \quad k = 1, 2. \quad (3.54d)$$

$$P_2(\sigma_x + \sigma_k) = Q_2(\varepsilon_x + \varepsilon_{yk} + \varepsilon_z), \quad k = 1, 2. \quad (3.54e)$$

Noting that the three Eqs. 3.54 (a, b, c) are not independent, because equation (3.54b) can be obtained by adding (3.54a) to (3.54c). Therefore the equation (3.54b) will be neglected in the following derivation. The same viscoelastic materials properties as in the 2PEF model will be employed here.

Substituting Eq. (3.54e) into Eqs. (3.54a) and (3.54c) to eliminate ε_z yields,

$$\begin{aligned} & (2Q_1 + 3KP_1)(Q_1(2\varepsilon_x - \varepsilon_{yk}) - P_1(6K(\varepsilon_x + \varepsilon_{yk}) - 3\sigma_k)) \\ & - (6KP_1 + Q_1)(Q_1(\varepsilon_x + \varepsilon_{yk}) - 3KP_1(\varepsilon_x + \varepsilon_{yk})) = 0, \end{aligned} \quad k = 1, 2. \quad (3.55)$$

Substituting the expression of the differential operator (3.12) into (3.55) gives,

$$\left(a_{10} + a_{11} \frac{\partial}{\partial t} + a_{12} \frac{\partial^2}{\partial t^2} \right) \varepsilon_x + \left(b_{10} + b_{11} \frac{\partial}{\partial t} + b_{12} \frac{\partial^2}{\partial t^2} \right) \varepsilon_{yk} + \left(c_{10} + c_{11} \frac{\partial}{\partial t} + c_{12} \frac{\partial^2}{\partial t^2} \right) \sigma_k = 0, \quad (3.56)$$

where

$$a_{10} = 3b_1^2 - 9a_1b_1K, \quad a_{11} = 6b_1b_2 - 9b_1K - 9a_1b_2K, \quad a_{12} = 3b_2^2 - 9b_2K,$$

$$b_{10} = -3b_1^2 - 18a_1b_1K, \quad b_{11} = -6b_1b_2 - 18b_1K - 18a_1b_2K, \quad b_{12} = -3b_2^2 - 18b_2K,$$

$$c_{10} = 6a_1b_1 + 9a_1^2K, \quad c_{11} = 6b_1 + 6a_1b_2 + 18a_1K, \quad c_{12} = 6b_2 + 9K.$$

Substituting the strains Eq. (3.2) into Eq. (3.56) yields,

$$\begin{aligned} & \frac{1}{2} \left(a_{10} + a_{11} \frac{\partial}{\partial t} + a_{12} \frac{\partial^2}{\partial t^2} \right) \left(\frac{\partial u_1(x,t)}{\partial x} - \frac{h_1}{2} \frac{\partial \phi_1(x,t)}{\partial x} + \frac{\partial u_2(x,t)}{\partial x} + \frac{h_2}{2} \frac{\partial \phi_2(x,t)}{\partial x} - \frac{\partial u_0(x,t)}{\partial x} \right) \\ & + 2 \left(b_{10} + b_{11} \frac{\partial}{\partial t} + b_{12} \frac{\partial^2}{\partial t^2} \right) \left(\frac{w_1(x,t) - w_a(x,t)}{h_0} \right) + \left(c_{10} + c_{11} \frac{\partial}{\partial t} + c_{12} \frac{\partial^2}{\partial t^2} \right) \sigma_1(x,t) = 0, \end{aligned} \quad (3.57a)$$

$$\begin{aligned} & \frac{1}{2} \left(a_{10} + a_{11} \frac{\partial}{\partial t} + a_{12} \frac{\partial^2}{\partial t^2} \right) \left(\frac{\partial u_1(x,t)}{\partial x} - \frac{h_1}{2} \frac{\partial \phi_1(x,t)}{\partial x} + \frac{\partial u_2(x,t)}{\partial x} + \frac{h_2}{2} \frac{\partial \phi_2(x,t)}{\partial x} - \frac{\partial u_0(x,t)}{\partial x} \right) \\ & + 2 \left(b_{10} + b_{11} \frac{\partial}{\partial t} + b_{12} \frac{\partial^2}{\partial t^2} \right) \left(\frac{w_a(x,t) - w_2(x,t)}{h_0} \right) + \left(c_{10} + c_{11} \frac{\partial}{\partial t} + c_{12} \frac{\partial^2}{\partial t^2} \right) \sigma_2(x,t) = 0. \end{aligned} \quad (3.57b)$$

Differentiating on both sides of Eq. (3.57) twice and substituting constitutive Eq. (3.3)

into them give,

$$\begin{aligned}
& \left(a_{10} + a_{11} \frac{\partial}{\partial t} + a_{12} \frac{\partial^2}{\partial t^2} \right) \left(\frac{1}{2} \left(\frac{1}{C_1} - \frac{1}{C_2} - \frac{h_2}{2D_2} \left(\frac{h_1 + h_2}{2} + h_0 \right) \right) \frac{\partial^2 N_1(x,t)}{\partial x^2} \right. \\
& \quad \left. - \left(\frac{h_1}{4D_1} + \frac{h_2}{4D_2} \right) \frac{\partial^2 M_1(x,t)}{\partial x^2} + bqH(t) \frac{h_2}{4D_2} \right) \\
& + \frac{2}{h_0} \left(b_{10} + b_{11} \frac{\partial}{\partial t} + b_{12} \frac{\partial^2}{\partial t^2} \right) \left(\frac{1}{B_1} \frac{\partial^2 M_1(x,t)}{\partial x^2} + \frac{1}{B_1} \left(\frac{h_1}{2} + h_0 \right) \frac{\partial^2 N_1(x,t)}{\partial x^2} - \frac{M_1(x,t)}{D_1} - \frac{\partial^2 w_a(x,t)}{\partial x^2} \right) \quad (3.58a) \\
& + \frac{1}{b} \left(c_{10} + c_{11} \frac{\partial}{\partial t} + c_{12} \frac{\partial^2}{\partial t^2} \right) \left(\frac{\partial^4 M_1(x,t)}{\partial x^4} + \left(\frac{h_1}{2} + h_0 \right) \frac{\partial^4 N_1(x,t)}{\partial x^4} \right) = 0,
\end{aligned}$$

$$\begin{aligned}
& \left(a_{10} + a_{11} \frac{\partial}{\partial t} + a_{12} \frac{\partial^2}{\partial t^2} \right) \left(\left(\frac{1}{2C_1} - \frac{1}{2C_2} - \frac{h_2}{4D_2} \left(\frac{h_1 + h_2}{2} + h_0 \right) \right) \frac{\partial^2 N_1(x,t)}{\partial x^2} \right. \\
& \quad \left. - \left(\frac{h_1}{4D_1} + \frac{h_2}{4D_2} \right) \frac{\partial^2 M_1(x,t)}{\partial x^2} + bqH(t) \frac{h_2}{4D_2} \right) \\
& + \frac{2}{h_0} \left(b_{10} + b_{11} \frac{\partial}{\partial t} + b_{12} \frac{\partial^2}{\partial t^2} \right) \left(\frac{\partial^2 w_a(x,t)}{\partial x^2} + \frac{1}{B_2} \left(\frac{\partial^2 M_1(x,t)}{\partial x^2} + \left(\frac{h_1}{2} + h_0 \right) \frac{\partial^2 N_1(x,t)}{\partial x^2} - bqH(t) \right) \right. \\
& \quad \left. + \frac{1}{D_2} \left(M_T(x,t) - M_1(x,t) - N_1(x,t) \left(\frac{h_1 + h_2}{2} + h_0 \right) \right) \right) \quad (3.58b) \\
& + \frac{1}{b} \left(c_{10} + c_{11} \frac{\partial}{\partial t} + c_{12} \frac{\partial^2}{\partial t^2} \right) \left(\frac{\partial^4 M_1(x,t)}{\partial x^4} + \left(\frac{h_1}{2} + h_0 \right) \frac{\partial^4 N_1(x,t)}{\partial x^4} \right) = 0.
\end{aligned}$$

Substituting Eq. (3.50a) into (3.54d),

$$P_1(\tau, t) = \frac{1}{2} Q_1 \left\{ \left(u_1(x, t) - \frac{h_1}{2} \phi_1(x, t) - u_2(x, t) - \frac{h_2}{2} \phi_2(x, t) + u_0(x, t) \right) / h_0 + \frac{\partial w_a(x, t)}{\partial x} \right\}. \quad (3.59)$$

Differentiating on both sides of Eq. (3.59) twice and substituting constitutive Eq. (3.3)

into it yield,

$$P_1 \left(\frac{1}{b} \frac{\partial^2 N_1(x, t)}{\partial x^2} \right) = \frac{1}{2} Q_1 \left\{ \begin{aligned} & A_{90} N_1(x, t) + A_{100} M_1(x, t) + A_{9N} N_T(x, t) \\ & + A_{10M} M_T(x, t) + A_{N0} N_0(x, t) + \frac{\partial^2 w_a(x, t)}{\partial x^2} \end{aligned} \right\}, \quad (3.60)$$

where

$$A_{90} = \frac{1}{h_0} \left(\frac{1}{C_1} + \frac{1}{C_2} + \frac{h_2}{2} \frac{1}{D_2} \left(\frac{h_1 + h_2}{2} + h_0 \right) \right), \quad A_{100} = \frac{1}{h_0} \left(\frac{h_2}{2} \frac{1}{D_2} - \frac{h_1}{2} \frac{1}{D_1} \right), \quad A_{9N} = -\frac{1}{C_2 h_0},$$

$$A_{10M} = -\frac{h_2}{2} \frac{1}{D_2 h_0}, \quad A_{N0} = \frac{1}{C_2 h_0}.$$

Applying Laplace transform to equation (3.63),

$$\begin{aligned} \frac{\partial^2 K(x,s)}{\partial x^2} &= \frac{B_{60}(s)}{B_{5k}(s)} M_{1L}(x,s) + \frac{B_{50}(s)}{B_{5k}(s)} N_{1L}(x,s) + \frac{B_{52}(s)}{B_{5k}(s)} \frac{\partial^2 N_{1L}(x,s)}{\partial x^2} \\ &+ \frac{B_{6M}(s)}{B_{5k}(s)} M_{iL}(x,s) + \frac{B_{5N}(s)}{B_{5k}(s)} N_{iL}(x,s) + \frac{B_{N0}(s)}{B_{5k}(s)} \frac{N_0}{s}, \end{aligned} \quad (3.61)$$

where

$$B_{60}(s) = -\frac{A_{100}}{2}(b_1 + b_2 s), \quad B_{50}(s) = -\frac{A_{90}}{2}(b_1 + b_2 s), \quad B_{52}(s) = \frac{1}{b}(a_1 + s), \quad B_{5N}(s) = -\frac{A_{9N}}{2}(b_1 + b_2 s),$$

$$B_{6M}(s) = -\frac{A_{10M}}{2}(b_1 + b_2 s), \quad B_{N0}(s) = -\frac{A_{N0}}{2}(b_1 + b_2 s), \quad B_{5k}(s) = \frac{1}{2}(b_1 + b_2 s).$$

and $K(x, s)$, $M_{1L}(x, s)$ and $N_{1L}(x, s)$ are the Laplace transforms of $w_a(x, t)$, $N_I(x, t)$ and $M_I(x, t)$, respectively. $N_{iL}(x, s)$ and $M_{iL}(x, s)$ are the Laplace transform of $N_T(x, t)$ and $M_T(x, t)$.

Applying Laplace transform to Eq. (3.61) leads to,

$$\begin{aligned} B_{24}(s) \frac{\partial^4 M_{1L}(x,s)}{\partial x^4} + B_{14}(s) \frac{\partial^4 N_{1L}(x,s)}{\partial x^4} + B_{22}(s) \frac{\partial^2 M_{1L}(x,s)}{\partial x^2} + B_{12}(s) \frac{\partial^2 N_{1L}(x,s)}{\partial x^2} \\ + B_{20}(s) M_{1L}(x,s) + B_{1k}(s) \frac{\partial^2 K(x,s)}{\partial x^2} + B_{1q}(s) q = 0, \end{aligned} \quad (3.62a)$$

$$\begin{aligned} B_{44}(s) \frac{\partial^4 M_{iL}(x,s)}{\partial x^4} + B_{34}(s) \frac{\partial^4 N_{iL}(x,s)}{\partial x^4} + B_{42}(s) \frac{\partial^2 M_{iL}(x,s)}{\partial x^2} + B_{32}(s) \frac{\partial^2 N_{iL}(x,s)}{\partial x^2} \\ + B_{40}(s) M_{iL}(x,s) + B_{30}(s) N_{iL}(x,s) + B_{4M}(s) M_{iL}(x,s) + B_{3k}(s) \frac{\partial^2 K(x,s)}{\partial x^2} + B_{3q}(s) q = 0. \end{aligned} \quad (3.62b)$$

Substituting Eq. (3.61) into Eq. (3.62) gives,

$$\begin{aligned} \frac{\partial^4 M_{1L}(x,s)}{\partial x^4} + C_{11}(s) \frac{\partial^4 N_{1L}(x,s)}{\partial x^4} + C_{12}(s) \frac{\partial^2 N_{1L}(x,s)}{\partial x^2} + C_{13}(s) \frac{\partial^2 M_{1L}(x,s)}{\partial x^2} + C_{14}(s) N_{1L}(x,s) \\ + C_{15}(s) M_{1L}(x,s) = C_{16}(s) N_{iL}(x,s) + C_{17}(s) M_{iL}(x,s) + C_{18}(s) q + C_{19}(s) N_0, \end{aligned} \quad (3.63a)$$

$$\begin{aligned} & \frac{\partial^4 M_{1L}(x, s)}{\partial x^4} + D_{11}(s) \frac{\partial^4 N_{1L}(x, s)}{\partial x^4} + D_{12}(s) \frac{\partial^2 N_{1L}(x, s)}{\partial x^2} + D_{13}(s) \frac{\partial^2 M_{1L}(x, s)}{\partial x^2} + D_{14}(s) N_{1L}(x, s) \\ & + D_{15}(s) M_{1L}(x, s) = D_{16}(s) N_{1L}(x, s) + D_{17}(s) M_{1L}(x, s) + D_{18}(s) q + D_{19}(s) N_0. \end{aligned} \quad (3.63b)$$

The coefficients of equation (3.62) and (3.63) are listed in the appendix A.

Subtracting Eq. (3.63a) from Eq. (3.63b),

$$\begin{aligned} & \frac{\partial^2 M_{1L}(x, s)}{\partial x^2} = E_{11}(s) \frac{\partial^4 N_{1L}(x, s)}{\partial x^4} + E_{12}(s) \frac{\partial^2 N_{1L}(x, s)}{\partial x^2} + E_{13}(s) N_{1L}(x, s) \\ & + E_{14}(s) M_{1L}(x, s) + E_{15}(s) N_{1L}(x, s) + E_{16}(s) M_{1L}(x, s) + E_{17}(s) q + E_{18}(s) N_0, \end{aligned} \quad (3.64)$$

where

$$\begin{aligned} E_{11}(s) &= -\frac{D_{11}(s) - C_{11}(s)}{D_{13}(s) - C_{13}(s)}, \quad E_{12}(s) = -\frac{D_{12}(s) - C_{12}(s)}{D_{13}(s) - C_{13}(s)}, \quad E_{13}(s) = -\frac{D_{14}(s) - C_{14}(s)}{D_{13}(s) - C_{13}(s)}, \\ E_{14}(s) &= -\frac{D_{15}(s) - C_{15}(s)}{D_{13}(s) - C_{13}(s)}, \quad E_{15}(s) = \frac{D_{16}(s) - C_{16}(s)}{D_{13}(s) - C_{13}(s)}, \quad E_{16} = \frac{D_{17}(s) - C_{17}(s)}{D_{13}(s) - C_{13}(s)}, \\ E_{17}(s) &= \frac{D_{18}(s) - C_{18}(s)}{D_{13}(s) - C_{13}(s)}, \quad E_{18}(s) = \frac{D_{19}(s) - C_{19}(s)}{D_{13}(s) - C_{13}(s)}. \end{aligned}$$

Subtracting Eq. (3.63b) multiplied by $C_{13}(s)$ from Eq. (3.63a) multiplied by $B_{13}(s)$ and rearranging the results yields,

$$\begin{aligned} & \frac{\partial^4 M_{1L}(x, s)}{\partial x^4} = F_{11}(s) \frac{\partial^4 N_{1L}(x, s)}{\partial x^4} + F_{12}(s) \frac{\partial^2 N_{1L}(x, s)}{\partial x^2} + F_{13}(s) N_{1L}(x, s) + F_{14}(s) M_{1L}(x, s) \\ & + F_{15}(s) N_{1L}(x, s) + F_{16}(s) M_{1L}(x, s) + F_{17}(s) q + F_{18}(s) N_0, \end{aligned} \quad (3.65)$$

where

$$\begin{aligned} F_{11}(s) &= -\frac{C_{11}(s)D_{13}(s) - C_{13}(s)D_{11}(s)}{D_{13}(s) - C_{13}(s)}, \quad F_{12}(s) = -\frac{C_{12}(s)D_{13}(s) - C_{13}(s)D_{12}(s)}{D_{13}(s) - C_{13}(s)}, \\ F_{13}(s) &= -\frac{C_{14}(s)D_{13}(s) - C_{13}(s)D_{14}(s)}{D_{13}(s) - C_{13}(s)}, \quad F_{14} = -\frac{C_{15}(s)D_{13}(s) - C_{13}(s)D_{15}(s)}{D_{13}(s) - C_{13}(s)}, \\ F_{15}(s) &= \frac{C_{16}(s)D_{13}(s) - C_{13}(s)D_{16}(s)}{D_{13}(s) - C_{13}(s)}, \quad F_{16}(s) = \frac{C_{17}(s)D_{13}(s) - C_{13}(s)D_{17}(s)}{D_{13}(s) - C_{13}(s)}, \end{aligned}$$

$$F_{17}(s) = \frac{C_{18}(s)D_{13}(s) - C_{13}(s)D_{18}(s)}{D_{13}(s) - C_{13}(s)}, \quad F_{18}(s) = \frac{C_{19}(s)D_{13}(s) - C_{13}(s)D_{19}(s)}{D_{13}(s) - C_{13}(s)}.$$

Differentiating Eq. (3.64) twice and substituting the results into Eq. (3.65) give,

$$\begin{aligned} M_{1L}(x, s) = & G_{11}(s) \frac{\partial^6 N_{1L}(x, s)}{\partial x^6} + G_{12}(s) \frac{\partial^4 N_{1L}(x, s)}{\partial x^4} + G_{13}(s) \frac{\partial^2 N_{1L}(x, s)}{\partial x^2} \\ & + G_{14}(s) N_{1L}(x, s) + G_{15}(s) N_{1L}(x, s) + G_{16}(s) M_{1L}(x, s) + G_{17}(s) q + G_{18}(s) N_0, \end{aligned} \quad (3.66)$$

where

$$\begin{aligned} G_{11}(s) &= \frac{E_{11}(s)}{F_{14}(s) - E_{14}(s)^2}, \quad G_{12}(s) = \frac{E_{12}(s) + E_{14}(s)E_{11}(s) - F_{11}(s)}{F_{14}(s) - E_{14}(s)^2}, \\ G_{13}(s) &= \frac{E_{13}(s) + E_{14}(s)E_{12}(s) - F_{12}(s)}{F_{14}(s) - E_{14}(s)^2}, \quad G_{14}(s) = \frac{E_{14}(s)E_{13}(s) - F_{13}(s)}{F_{14}(s) - E_{14}(s)^2}, \\ G_{15}(s) &= \frac{E_{14}(s)E_{15}(s) - F_{15}(s)}{F_{14}(s) - E_{14}(s)^2}, \quad G_{16}(s) = \frac{E_{14}(s)E_{16}(s) - F_{16}(s)}{F_{14}(s) - E_{14}(s)^2}, \\ G_{17}(s) &= \frac{E_{14}(s)E_{17}(s) - F_{17}(s)}{F_{14}(s) - E_{14}(s)^2}, \quad G_{18}(s) = \frac{E_{14}(s)E_{18}(s) - F_{18}(s)}{F_{14}(s) - E_{14}(s)^2}. \end{aligned}$$

Substituting Eq. (3.66) into (3.64) and the governing equation can be obtained as,

$$\begin{aligned} H_{11}(s) \frac{\partial^8 N_{1L}(x, s)}{\partial x^8} + H_{12}(s) \frac{\partial^6 N_{1L}(x, s)}{\partial x^6} + H_{13}(s) \frac{\partial^4 N_{1L}(x, s)}{\partial x^4} + H_{14}(s) \frac{\partial^2 N_{1L}(x, s)}{\partial x^2} \\ + H_{15}(s) N_{1L}(x, s) + H_{16}(s) N_{1L}(x, s) + H_{17}(s) M_{1L} + H_{18}(s) q + H_{19}(s) N_0 = 0, \end{aligned} \quad (3.67)$$

where

$$\begin{aligned} H_{11}(s) &= G_{11}(s), \quad H_{12}(s) = G_{12}(s) - E_{14}(s)G_{11}(s), \quad H_{13}(s) = G_{13}(s) - E_{11}(s) - E_{14}(s)G_{12}(s), \\ H_{14}(s) &= G_{14}(s) - E_{12}(s) - E_{14}(s)G_{13}(s), \quad H_{15}(s) = -E_{13}(s) - E_{14}(s)G_{14}(s), \\ H_{16}(s) &= -E_{15}(s) - E_{14}(s)G_{15}(s), \quad H_{17}(s) = -E_{16}(s) - E_{14}(s)G_{16}(s), \quad H_{18}(s) = -E_{17}(s) - E_{14}(s)G_{17}(s), \\ H_{19}(s) &= -E_{18}(s) - E_{14}(s)G_{18}(s). \end{aligned}$$

The Laplace transform of the axial force in the RC beam can be solved from the governing equation (3.67) in the form as,

$$N_{1L}(x, s) = \sum_{i=1}^8 c_i(s) e^{R_i(s)x} + N_{1CL}(x, s), \quad (3.68)$$

where $R_i(s)$ ($i = 1, 2, \dots, 8$) are six roots of the characteristics equation of Eq. (3.68); $c_i(s)$ ($i = 1, 2, \dots, 8$) are coefficients to be determined by boundary conditions; and

$$N_{1CL}(x, s) = -\frac{H_{16}(s)}{H_{15}(s)} N_{1L}(x, s) - \frac{H_{17}(s)}{H_{15}(s)} M_{1L}(x, s) - \frac{H_{18}(s)}{H_{15}(s)} q - \frac{H_{19}(s)}{H_{15}(s)} N_0. \quad (3.69)$$

Inserting Eq. (3.69) into Eq. (3.66) gives,

$$M_{1L}(x, s) = \sum_{i=1}^8 c_i(s) \left(G_{11}(s) R_i^6(s) + G_{12}(s) R_i^4(s) + G_{13}(s) R_i^2(s) + G_{14}(s) \right) e^{R_i(s)x} + M_{1CL}(x, s), \quad (3.70)$$

where

$$\begin{aligned} M_{1CL}(x, s) = & G_{11}(s) \frac{\partial^6 N_{1CL}(x, s)}{\partial x^6} + G_{12}(s) \frac{\partial^4 N_{1CL}(x, s)}{\partial x^4} + G_{13}(s) \frac{\partial^2 N_{1CL}(x, s)}{\partial x^2} \\ & + G_{14}(s) N_{1CL}(x, s) + G_{15}(s) N_{1L}(x, s) + G_{16}(s) M_{1L}(x, s) + G_{17}(s) q + G_{18}(s) N_0. \end{aligned} \quad (3.71)$$

Substituting Eqs. (3.68) and (3.70) into Eq. (3.6) gives,

$$Q_{1L}(x, s) = \sum_{i=1}^8 \left(G_{11}(s) R_i^7(s) + G_{12}(s) R_i^5(s) + G_{13}(s) R_i^3(s) + \left(G_{14}(s) + \frac{h_1}{2} \right) R_i(s) \right) c_i(s) e^{R_i(s)x} + Q_{1CL}(x, s), \quad (3.72)$$

where

$$Q_{1CL}(x, s) = \frac{\partial M_{1CL}(x, s)}{\partial x} + \frac{h_1}{2} \frac{\partial N_{1CL}(x, s)}{\partial x}. \quad (3.73)$$

The Laplace transforms of interface shear and normal stresses are then obtained as

$$\tau_L(x, s) = \frac{1}{b} \left(\sum_{i=1}^8 c_i(s) R_i(s) e^{R_i(s)x} + \frac{\partial N_{1CL}(x, s)}{\partial x} \right). \quad (3.74)$$

$$\begin{aligned} \sigma_L(x, s) = & \frac{1}{b} \sum_{i=1}^8 \left(G_{11}(s) R_i^8(s) + G_{12}(s) R_i^6(s) + G_{13}(s) R_i^4(s) + \left(G_{14}(s) + \frac{h_1}{2} \right) R_i^2(s) \right) c_i(s) e^{R_i(s)x} \\ & + \frac{1}{b} \frac{\partial Q_{1CL}(x, s)}{\partial x} - \frac{q}{s}. \end{aligned} \quad (3.75)$$

For a simply supported beam shown in Fig.3.1, the following boundary conditions can be used to determine $c_i(s)$:

$$(1) N_1(-L,t)=0, \quad (2) Q_1(-L,t)=-bLqH(t), \quad (3) M_1(-L,t)=-b(L+a/2)aqH(t),$$

$$(4) N_1(L,t)=0, \quad (5) Q_1(L,t)=bLqH(t), \quad (6) M_1(L,t)=-b(L+a/2)aqH(t),$$

$$(7) \tau(-L,t)=0, \quad (8) \tau(L,t)=0,$$

where $H(t)$ is the Heaviside step function. It is assumed that the external forces are applied instantly and keep constant with time going.

Once the result forces, interface stresses, and their integrals are solved, the deflections and rotations of the RC beam, including strengthened portion and the portion without FRP plate can be expressed in the following forms,

$$\phi_3(x) = \int \frac{M_3(x)}{D_1} dx + C_{p1}, \quad \text{where } M_3(x) = bqH(t)x(x/2 - (L+a)). \quad (3.76a)$$

$$w_3(x) = \int \left(\frac{Q_3(x)}{B_1} - \phi_3(x) \right) dx + C_{p2}, \quad \text{where } Q_3(x) = -bqH(t)(L+a-x). \quad (3.76b)$$

$$w_1(x) = \int \left(\frac{Q_1(x)}{B_1} - \phi_1(x) \right) dx + C_{p4}, \quad \text{where } \phi_1(x) = \int \frac{M_1(x)}{D_1} dx + C_{p3}. \quad (3.76c)$$

$$\phi_4(x) = \int \frac{M_4(x)}{D_1} dx + C_{p5}, \quad \text{where } M_4(x) = -bq(a-x) \left(L + \frac{a+x}{2} \right). \quad (3.76d)$$

$$w_4(x) = \int \left(\frac{Q_4(x)}{B_1} - \phi_4(x) \right) dx + C_{p6}, \quad \text{where } Q_4(x) = bq(L+x). \quad (3.76e)$$

where subscript 3 and 4 represent the left and right portion of RC beam without FRP plate attached, respectively and C_{pi} are the unknowns.

Therefore the deflections and rotations can be solved by the following boundary conditions:

$$(7) w_3(0) = 0, \quad (8) w_4(a) = 0, \quad (9) w_3(a) = w_1(-L),$$

$$(10) \phi_3(a) = \phi_1(-L), \quad (11) w_4(0) = w_1(L), \quad (12) \phi_4(0) = \phi_1(L).$$

3.3.4. 3PEF viscoelastic solution of an FRP-strengthened RC beam

A simply supported beam under uniformly distributed load will be studied using present method. FEA results are employed to verify the correctness of present solutions considering the viscoelastic behavior of the adhesive layer. As shown in Fig. 3.1, a uniformly distributed load $q = 0.1 \text{ N/mm}^2$ is applied on the top of a simple supported strengthened beam. The distance from the support to the plate end is 300mm. The thickness of RC beam, adhesive layer and FRP plate are 300mm, 2mm and 4mm, respectively. The material properties are same as listed in Table 3.1. To obtain better accuracy, high order plane stress elements (CPS8) are employed to mesh the FRP strengthened simply supported RC beam. Due to the symmetry of the configuration, only half of the beam is modeled as shown in Fig. 3.4. Fine mesh is employed at the plate end. The smallest size of elements placed in the adhesive layer is 0.25mm, which is one fourth of the thickness of the adhesive layer. The viscoelastic behavior of the adhesive layer is implemented in a commercially FEA software ABAQUS through a user subroutine UMAT.

As shown in Figs. 3.21-3.23, the shear and normal stresses at the interface based on present 3PEF model agree with those from FEA very well except a small zone near the plane end, where stress concentrations exist. The normal stresses are extracted from the two bi-material interfaces (CA interface and PA interface). The shear stresses are extracted from the middle plane of the adhesive layer. The shear stresses based on the 3PEF model can satisfy the zero shear stress boundary conditions and yield good agreement with FEA results. Meanwhile, the normal stresses at CA interface are in tensile and those at PA interface are in compression. This feature is very important, because only tensile stresses can contribute to interface debonding.

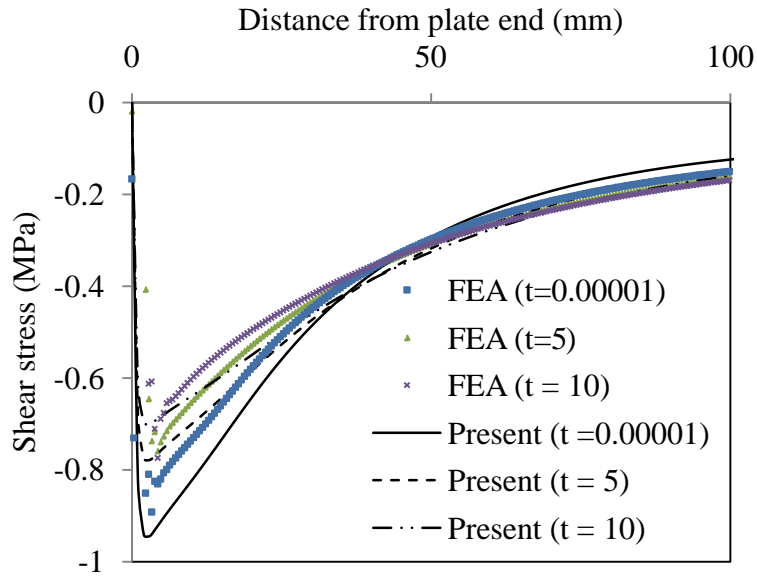


Fig. 3.21. Redistribution of interface shear stress with time (day).

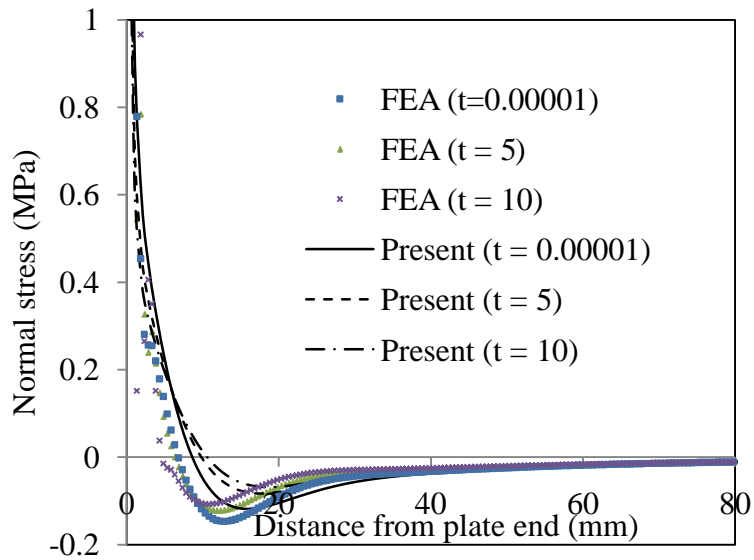


Fig. 3.22. Redistribution of normal stress along the CA interface with time (day).

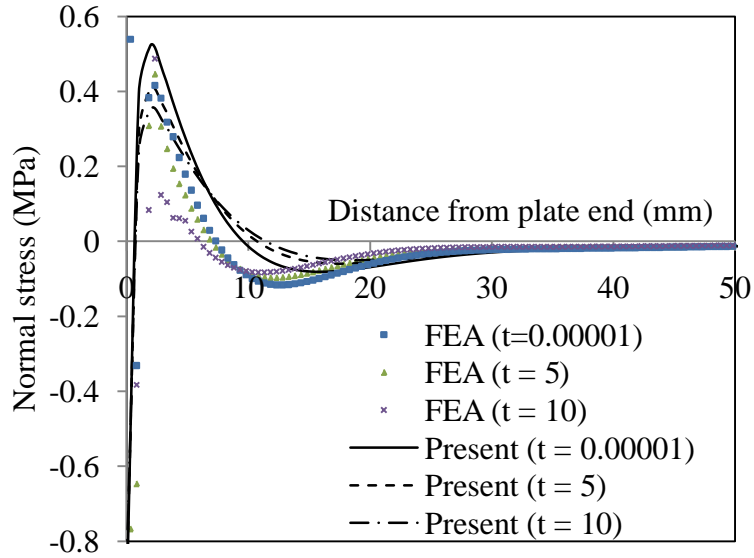


Fig. 3.23. Comparison of normal stress along the PA interface with time (day).

Figs. 3.24 ~ 3.26 show the interface shear and normal stresses redistributions after the uniformly distributed load is applied for 0.00001, 1, 5, 10 and 30 days. As shown in the figures, the stresses distributions become more uniform as time going. Therefore the most harmful situation is developed at the very beginning before stress relaxations take place.

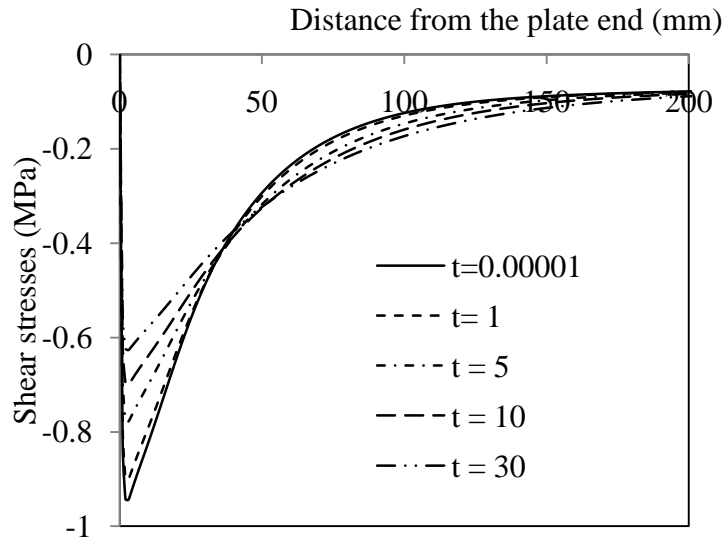


Fig. 3.24. Variation of shear stress distribution with time (day).

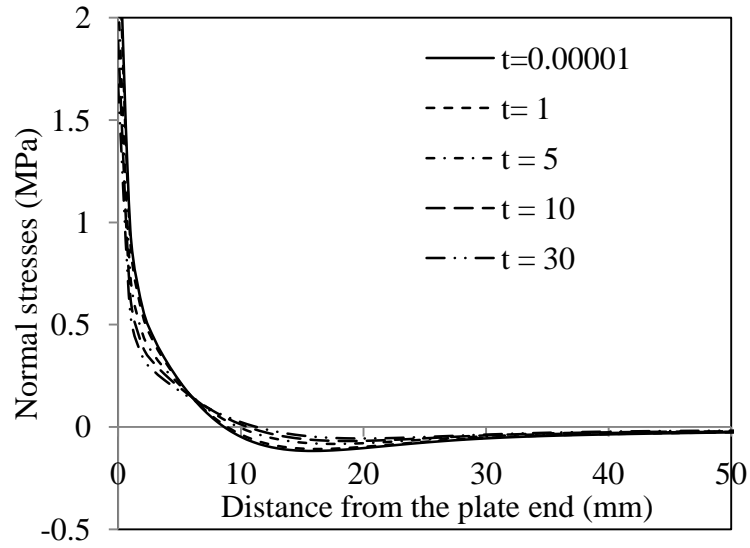


Fig. 3.25. Variation of normal stress at CA interface distribution with time (day).

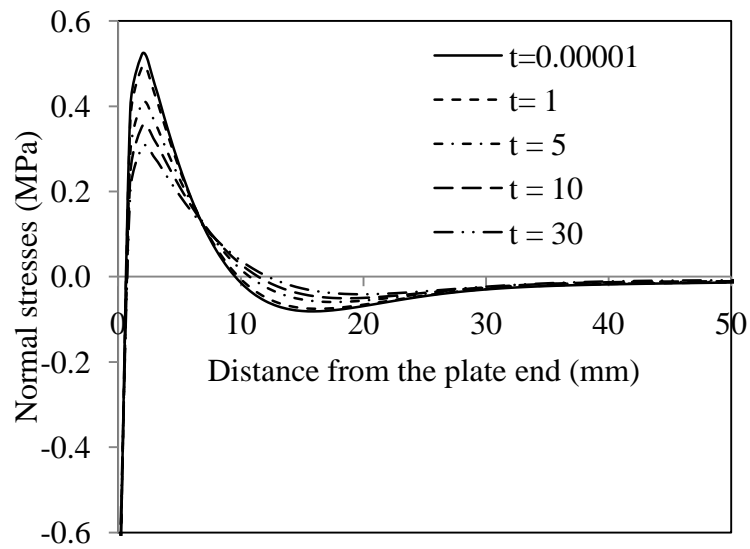


Fig. 3.26. Variation of normal stress at AP interface distribution with time (day).

Fig. 3.27 shows the increase of the deflection at the middle span of the simply supported RC beam under uniformly distributed load with variously thick adhesive layers. As shown in the Fig. 3.27, the deflections increase very fast in the first several days and become relatively stable after a certain time. Therefore the conventional method, which did not consider time effect, will underestimate the deflection in the long run.

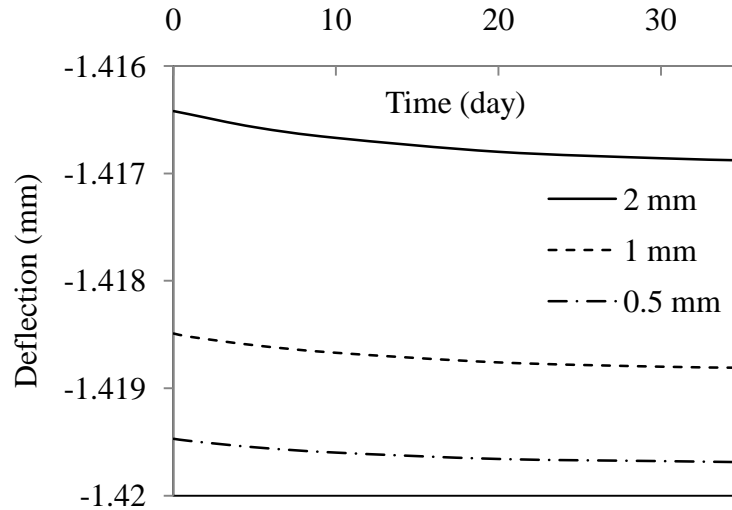


Fig.3.27. Deflections at the mid-span for different thicknesses of adhesive layer.

Fig.3.28 shows the variation of the axial force in the FRP plate near the plate end of the simply supported RC beam. As shown in the figure, the decrease of the axial force mainly focuses on a small zone near the plate end, which is induced by the redistribution of shear stresses. As shown in Fig.3.29, the increase of moment in the RC beam is also mainly near the plate end. This feature suggests the tradition method may underestimate the moment near the plate end.

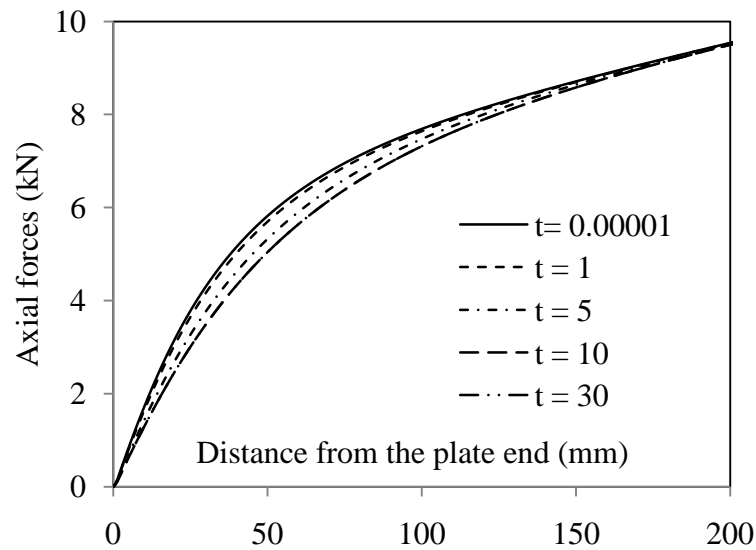


Fig.3.28. Change of axial force in the FRP plate with time (days).

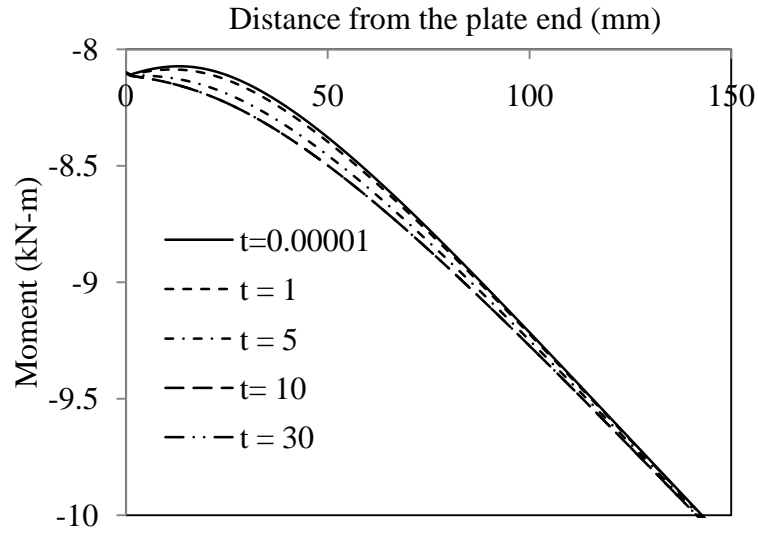


Fig.3.29. Change of moment in RC beam with time (day).

Similar trends are observed for the axial force in the FRP plate and the moment in RC beam as deflection at the middle span as shown in Figs. 3.30 and 3.31. The figures show the changes of axial forces and moments at 25mm away from the plate end.

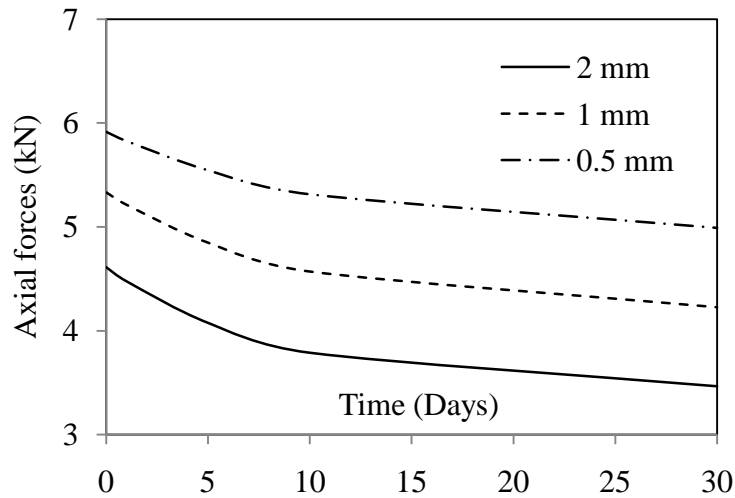


Fig. 3.30. Axial forces in FRP plate at 25mm away from plate end for different thicknesses of adhesive layer

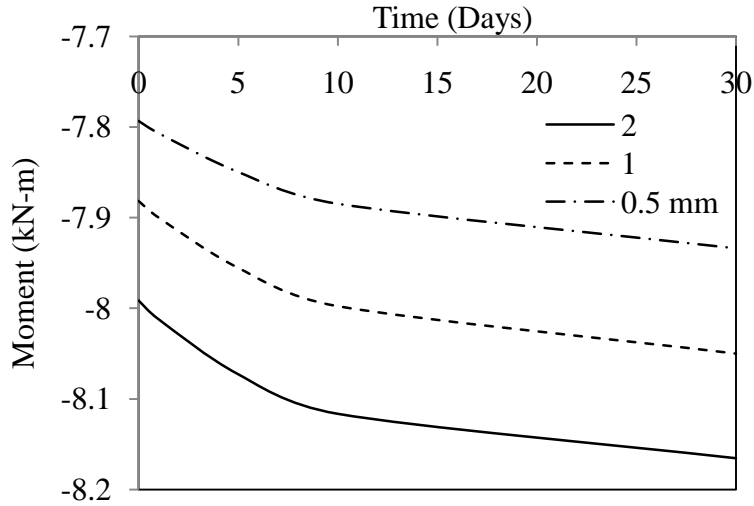


Fig.3.31. Moments in RC beam at 25mm away from plate end for different thicknesses of adhesive layer

3.3.5. 3PEF viscoelastic solution of a prestressed FRP-strengthened RC beam

In this section, a simply supported beam strengthened by a prestressed FRP plate will be studied using present method. The basic configuration is the same as in the last section, but a 10 kN pretension load is applied to the FRP plate. Figs. 3.32-3.34 show the interfacial stresses redistribution in the adhesive layer with time going.

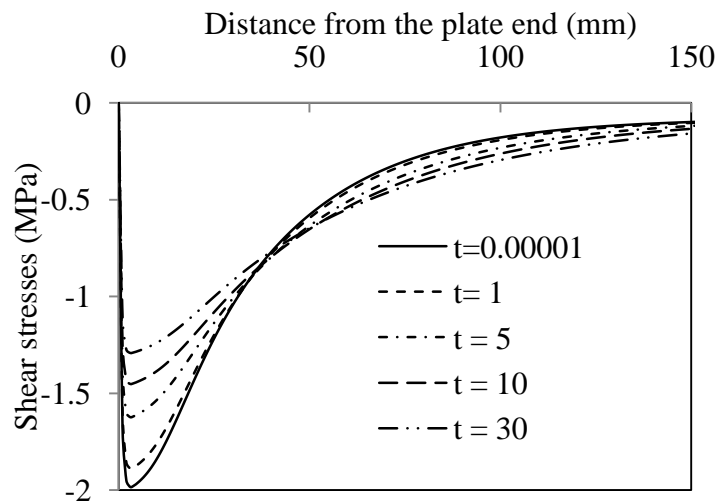


Fig.3.32. Variation of shear stress distribution of prestressed FRP-strengthened RC beam (days).

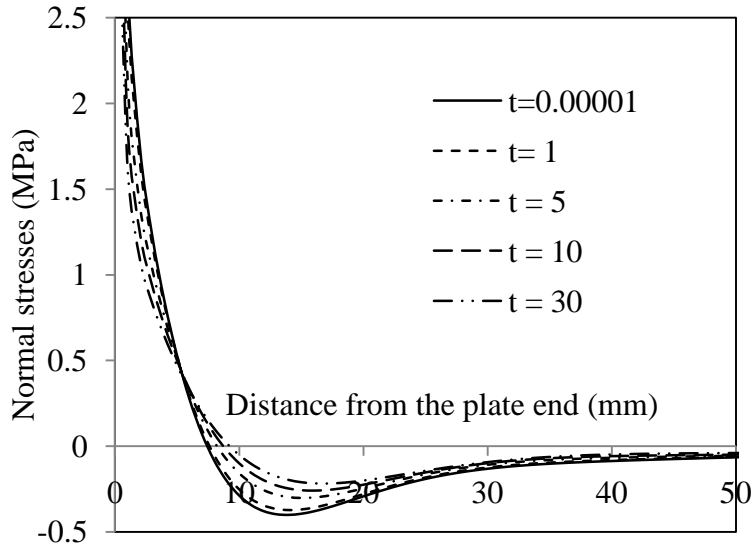


Fig.3.33. Variation of normal stress distribution of prestressed FRP-strengthened RC beam along the CA interface.

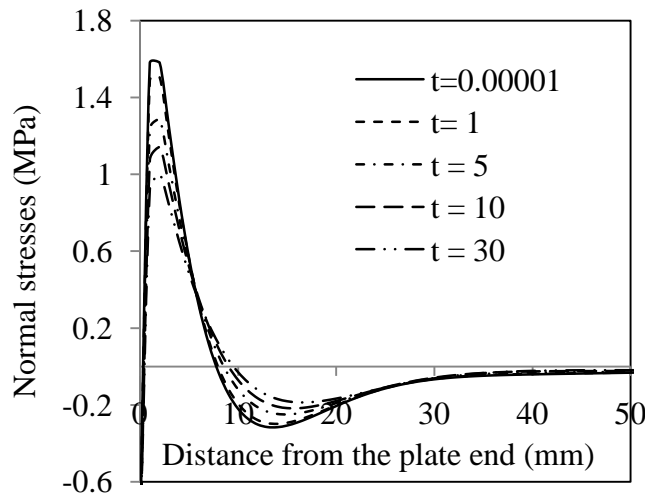


Fig.3.34. Variation of normal stress distribution of prestressed FRP-strengthened RC beam along the PA interface.

Compared to the interfacial shear and normal stresses of normal FRP-strengthened RC beam, the results of the prestressed FRP strengthened RC beam are higher. In this sense, debonding is more likely to occur in the prestressed FRP-strengthened RC structures. Similarly the axial forces in the FRP plate near the plate end of the simply supported RC beam are higher than

those of normal FRP-strengthened RC beam as shown in Fig. 3.35. However, the moment in the RC beam is lower than that of normal FRP-strengthened RC beam.

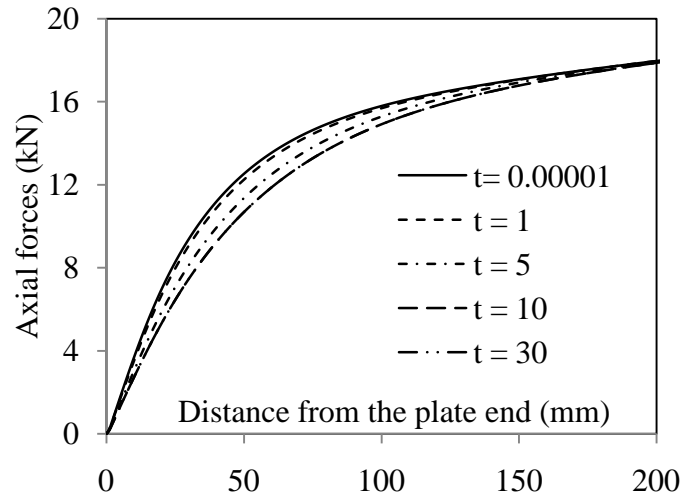


Fig.3.35. Variation of axial force in prestressed FRP plate with time (day).

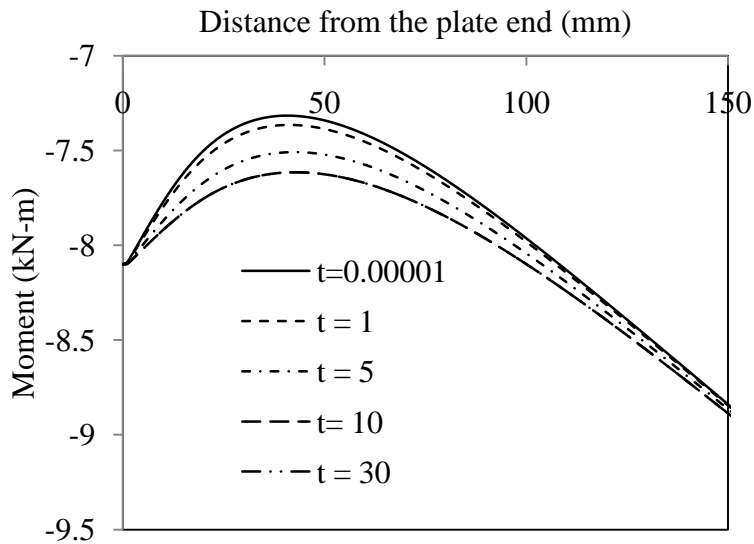


Fig.3.36. Variation of moment in prestressed FRP-strengthened RC beam with time (day).

Similar trends are observed for the axial forces in FRP plate and moments in RC beam as those of normal FRP strengthened RC beam. The magnitudes of the axial forces are higher than those without prestress and moments are lower than those without prestress.

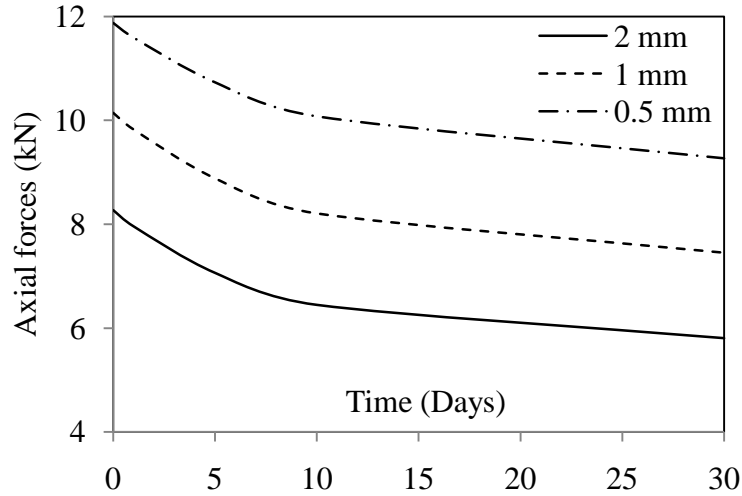


Fig.3.37. Axial forces variation in the FRP plate for different thicknesses of adhesive layer of prestressed FRP-strengthened RC beam (day).

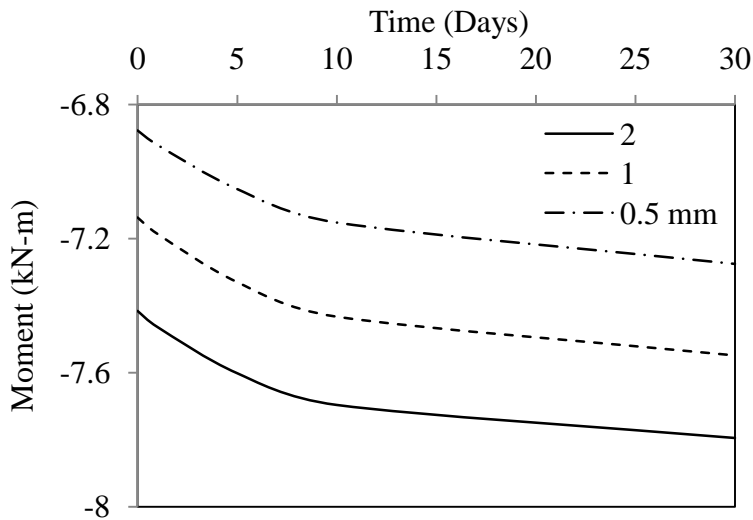


Fig.3.38. Change of moments in RC beam with time or different thicknesses of adhesive layer of prestressed FRP-strengthened RC beam (day).

Fig. 3.39 shows the increase of the deflection at the middle span of the simply supported RC beam under uniformly distributed load with various thick adhesive layers. As shown in the Fig.3. 39, the trends of the deflections are the same as those of the normal FRP-strengthened RC beam, but the magnitudes are much lower than those of normal FRP-strengthened RC beam.

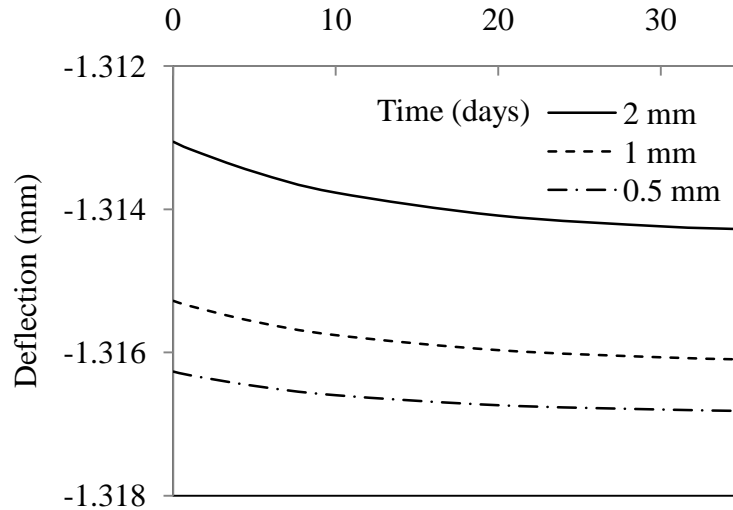


Fig. 3.39. Change of Deflection with time for different thicknesses of adhesive layer of prestressed FRP plated RC beam (day).

3.4. Conclusions

Viscoelastic analytical solutions are developed to investigate the relatively long-term behavior of the FRP-strengthened RC beams. The solutions model the adhesive layer as a viscoelastic material using the SLS model. Using the Laplace transform, the closed-form solutions of interface stresses, resultant forces, the deflection, and the rotation of the RC beam and the FRP plate are obtained in the Laplace transformed shape. An efficient numerical method, the Zakian's algorithm, is employed to conduct the inverse Laplace transform. These solutions also consider the prestressing force in the FRP plate. FEA using a subroutine UMAT is also conducted to verify the present analytical solution. Good agreement with FEA result has been achieved by the present analytical solutions. The redistributions of interfacial stresses, resultant beam forces, and relaxation deflection of the structure can be predicted by the present solution easily. The analytical solution developed in this study provides an efficient tool to evaluate the long-term behavior of the FRP-strengthened RC beams. However, since only the viscoelastic

behavior of adhesive layer is taken into consideration, these viscoelastic solutions are only valid to estimate the interface stress distributions and deformations in a “certain period”.

CHAPTER 4

LINEAR ELASTIC FRACTURE MECHANICS ANALYSIS OF THE FRP-STRENGTHEND CONCRETE BEAMS

4.1 Introduction

Usually, the FRP-concrete interface is usually not perfect, as assumed in previous chapters. Some small cracks can exist within this interface zone due to manufacturing quality or induced by intermediate cracks in the concrete substrate. Therefore, as another stage of the life cycle for the FRP strengthening system, the methods developed in previous chapters are not suitable any more. In this case, the integrity of the FRP-concrete interface should be assessed with linear elastic interface fracture mechanics (LEFM).

An existing LEFM solution of the FRP-concrete interface debonding was developed by Au and Büyüköztürk (2006) (referred as to “AB” in the following). Their proposed tri-layer interface fracture energy model is essentially a direct application of the classical interface fracture models in bi-layered beams (Hutchinson and Suo, 1990) to three-layered beams. Therefore, the shear forces were ignored in their expression of energy release rate (ERR), which could lead to underestimating of the ERRs if shear forces exist. Moreover, mode mixity of the interface debond is not available for the tri-layer model. To overcome the above two drawbacks in the existing solution, new interface fracture mechanics solutions considering the transverse shear effect and corresponding mode mixity are developed in this chapter.

4.2 A tri-layer crack tip element

Consider a delaminated FRP-strengthened concrete beam under general loading as shown in Fig. 4.1, where a crack lies at the interface between the adhesive layer and the concrete beam. The adhesive layer and FRP plate are modeled together as a composite beam I , and the concrete beam is modeled as beam 2. The length of the uncracked region L is relatively large compared to the thickness of the whole beam model, $h_1+h_0+h_2$, so the boundary condition's effect is negligible. This configuration essentially represents a crack tip element of a tri-layered beam, where the cracked and uncracked portions are joined, and to which the generic loads, previously determined by a global beam analysis, are applied.

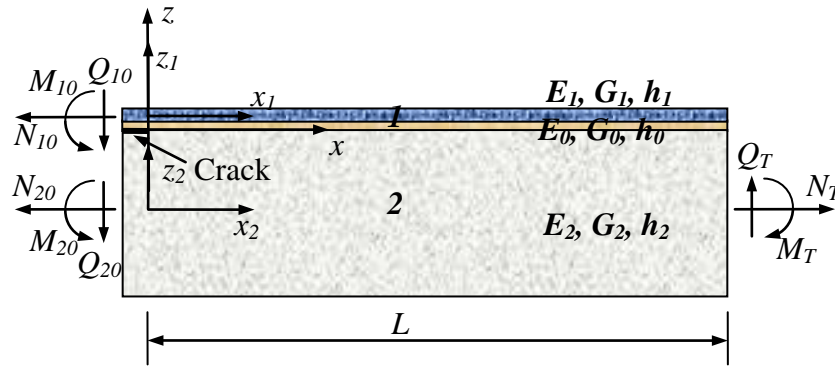


Fig.4.1. Crack tip element of FRP-strengthened concrete beam.

According to the Timoshenko's beam theory, the displacements of the concrete beam and the adhesive-FRP composite beam can be expressed as,

$$U_i(x_i, z_i) = u_i(x_i) + z_i \phi_i(x_i), \quad (4.2)$$

$$W_i(x_i, z_i) = w_i(x_i), \quad (4.3)$$

where subscript $i = 1, 2$, represent the beams I and 2 in Fig.4.1. u_i , w_i , and ϕ_i are the longitudinal displacement, transverse displacement, and rotation at the neutral axes of beam i , respectively.

The constitutive equations for beam i can be written as,

$$N_i = C_i \frac{du_i}{dx}, \quad Q_i = B_i \left(\phi_i + \frac{dw_i}{dx} \right), \quad M_i = D_i \frac{d\phi_i}{dx}, \quad (4.4)$$

where N_i , Q_i , and M_i are the resultant axial force, transverse shear force, and bending moment of beam i , respectively. C_i , B_i , and D_i are the axial, shear, and bending stiffness coefficients of the beam i , respectively, and given as below for the plain stress condition,

$$C_1 = b_1(E_1 h_1 + E_0 h_0), \quad C_2 = b_2 E_2 h_2, \quad B_1 = \kappa b_1 (G_1 h_1 + G_0 h_0), \quad B_2 = \kappa b_2 G_2 h_2, \\ D_1 = \frac{b_1}{3} \left(E_0 \left((h_0 + d)^3 - d^3 \right) + E_1 \left((h_1 - d)^3 + d^3 \right) \right), \quad D_2 = \frac{E_2 b_2 h_2^3}{12}, \quad (4.5)$$

where E_i , G_i ($i = 1, 2, 3$) are the longitude modulus and transverse shear modulus of the FRP plate, adhesive layer, and concrete beam, respectively; κ is the shear correction coefficient chosen as

5/6 in this study; $d = \frac{E_1 h_1^2 - E_0 h_0^2}{2(E_1 h_1 + E_0 h_0)}$ is the distance from the neutral axis of composite beam 1 to

the interface of the FRP plate and the adhesive layer; h_1 , h_0 , and h_2 are the thicknesses of the FRP plate, adhesive layer, and concrete beam; b_1 and b_2 are the widths of the composite beam 1 and concrete beam 2.

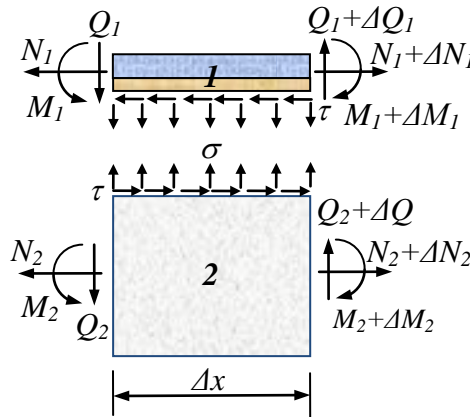


Fig.4.2. Free body diagram of the tri-layer beam model.

By using the free body diagram shown in Fig.4.2, the following equilibrium equations can be established as,

$$\frac{dN_1}{dx} = b\tau, \quad \frac{dQ_1}{dx} = b\sigma, \quad \frac{dM_1}{dx} = Q_1 - (h_0 + d)b\tau. \quad (4.6)$$

$$\frac{dN_2}{dx} = -b\tau, \quad \frac{dQ_2}{dx} = -b\sigma, \quad \frac{dM_2}{dx} = Q_2 - \frac{h_2}{2}b\tau. \quad (4.7)$$

Combing the first and third equations of Eqs. (4.6) and (4.7) yields,

$$Q_1 = \frac{dM_1}{dx} + (h_0 + d)\frac{dN_1}{dx}, \quad Q_2 = \frac{dM_2}{dx} - \frac{h_2}{2}\frac{dN_2}{dx}. \quad (4.8)$$

The overall equilibrium requires (Fig. 4.2),

$$N_T = N_1 + N_2 = N_{10} + N_{20}, \quad (4.9a)$$

$$Q_T = Q_1 + Q_2 = Q_{10} + Q_{20}, \quad (4.9b)$$

$$M_T = M_1 + M_2 + N_1\left(h_0 + d + \frac{h_2}{2}\right) = M_{10} + M_{20} + N_{10}\left(h_0 + d + \frac{h_2}{2}\right) + Q_T x, \quad (4.9c)$$

where N_{10} , N_{20} , Q_{10} , Q_{20} , M_{10} , and M_{20} are the applied axial force, transverse shear force, and bending moment, respectively, at the crack tip; N_T , Q_T , and M_T are the total applied resultant axial force, transverse shear force, and bending moment of the tri-layer beam system about the neutral axis of concrete beam.

4.3 Shear deformable joint model

According to the continuity conditions at the interface of crack tip, Qiao and Wang (2005) classified the joint models into three categories: rigid joint, semi-rigid joint, and flexible joint as shown in Fig.4.3. It has been proved that the semi-rigid joint model and flexible joint model can provide much better solutions than that of the rigid joint model, because those two models partially or fully include the crack tip deformations. The flexible joint model can estimate the ERR most accurately, but the solutions are much more complicated than those based on the semi-rigid joint model. Therefore, in this chapter both models are employed to calculate the ERRs and mode mixities of the delamination along the FRP-concrete interface.

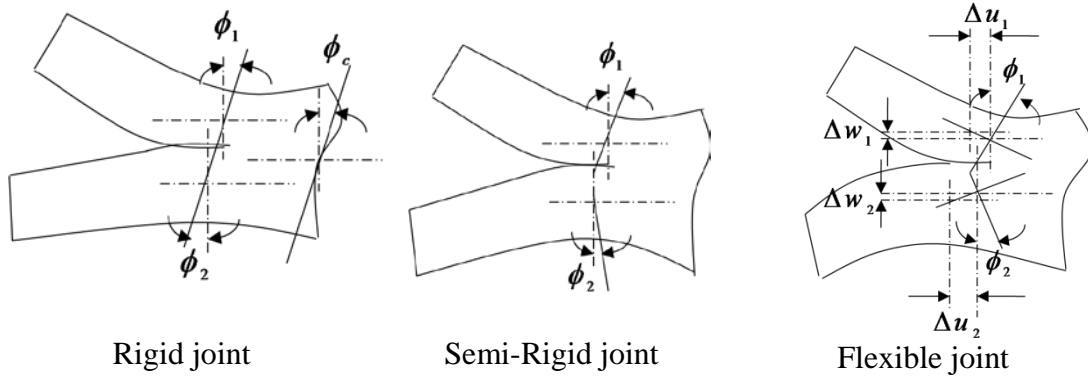


Fig.4.3. Crack tip elements for different joint models.

4.3.1. Semi-rigid joint model

At the interface of the beam 1 and 2, the displacement continuity requires:

$$u_1 - (h_0 + d)\phi_1 = u_2 + \frac{h_2}{2}\phi_2, \quad w_1 = w_2. \quad (4.10)$$

By differentiating the first equation of Eq. (4.10) and considering Eqs. (4.4) and (4.9), the moment in beam 1 can be expressed in term of axial force in beam 1 as,

$$M_1 = \frac{\eta}{\xi} N_1 - \frac{N_T}{\xi C_2} - \frac{h_2}{2\xi D_2} M_T, \quad (4.11)$$

where

$$\eta = \frac{1}{C_1} + \frac{1}{C_2} + \frac{h_2}{2D_2} \left(h_0 + d + \frac{h_2}{2} \right), \quad \xi = \frac{(h_0 + d)}{D_1} - \frac{h_2}{2D_2}. \quad (4.12)$$

Differentiating the second equation of Eq. (4.10) and considering Eqs. (4.4), (4.8), and (4.9) yield,

$$\left(\frac{1}{B_1} + \frac{1}{B_2} \right) \left(\frac{d^2 M_1}{dx^2} + (h_0 + d) \frac{d^2 N_1}{dx^2} \right) - \left(\frac{1}{D_1} + \frac{1}{D_2} \right) M_1 - \frac{1}{D_2} \left(h_0 + d + \frac{h_2}{2} \right) N_1 = -\frac{M_T}{D_2}. \quad (4.13)$$

Substituting Eq. (4.11) into (4.13), the governing equation is established as,

$$\left(\frac{1}{B_1} + \frac{1}{B_2} \right) \left(\eta + \frac{\xi h_1}{2} \right) \frac{d^2 N_1}{dx^2} - \left(\eta \left(\frac{1}{D_1} + \frac{1}{D_2} \right) + \frac{\xi}{D_2} \left(h_0 + d + \frac{h_2}{2} \right) \right) N_1 = -F(x), \quad (4.14)$$

where

$$F(x) = \left(\frac{\xi}{D_2} + \left(\frac{1}{D_1} + \frac{1}{D_2} \right) \frac{h_2}{2D_2} \right) M_T + \left(\frac{1}{D_1} + \frac{1}{D_2} \right) \frac{N_T}{C_2}. \quad (4.15)$$

Solving Eq. (4.14) gives the axial force of beam I as,

$$N_1(x) = ce^{-kx} + c_1 e^{kx} + N_{1c}, \quad (4.16)$$

where

$$N_{1c} = \frac{D_1 D_2 \xi + (D_1 + D_2) h_2 / 2}{D_2 (\eta (D_1 + D_2) - \xi D_1 (h_0 + d + h_2 / 2))} M_T + \frac{(D_1 + D_2)}{C_2 (\eta (D_1 + D_2) - \xi D_1 (h_0 + d + h_2 / 2))} N_T, \quad (4.17)$$

$$k^2 = \frac{B_1 B_2 (\eta (D_1 + D_2) + \xi D_1 (h_0 + d + h_2 / 2))}{D_1 D_2 (B_1 + B_2) (\eta + \xi (h_0 + d))}.$$

Since the length of the intact portion is relatively large, the second term in Eq. (4.16) can be neglected. Therefore the resultant forces in the composite beam I can be expressed as,

$$N_1 = ce^{-kx} + N_{1c}, \quad M_1 = \frac{\eta}{\xi} ce^{-kx} + M_{1c}, \quad Q_1 = -\left(\frac{\eta}{\xi} + h_0 + d \right) cke^{-kx} + Q_{1c}, \quad (4.18)$$

where

$$M_{1c} = \frac{\eta}{\xi} N_{1c} - \frac{N_T}{\xi C_2} - \frac{h_2}{2\xi D_2} M_T, \quad Q_{1c} = \frac{dM_{1c}}{dx} + (h_0 + d) \frac{dN_{1c}}{dx}. \quad (4.19)$$

Considering the overall equilibrium equations (4.9), we have,

$$N_2 = -ce^{-kx} + N_{2c}, \quad Q_2 = \left(\frac{\eta}{\xi} + h_0 + d \right) cke^{-kx} + Q_{2c}, \quad M_2 = -\left(\frac{\eta}{\xi} + \left(h_0 + d + \frac{h_2}{2} \right) \right) ce^{-kx} + M_{2c}, \quad (4.20)$$

where

$$N_{2c} = N_T - N_{1c}, \quad M_{2c} = M_T - M_{1c} - \left(h_0 + d + \frac{h_2}{2} \right) N_{1c}, \quad Q_{2c} = Q_T - Q_{1c}. \quad (4.21)$$

As shown in (Wang and Qiao, 2004a), there are a concentrated longitudinal force N_c and a concentrated peel force Q_c at the crack tip. Considering the equilibrium at the crack tip gives,

$$N_{10} = -N_c + N_1(0), \quad Q_{10} = -Q_c + Q_1(0), \quad M_{10} = -(h_0 + d)N_c + M_1(0). \quad (4.22)$$

Then, c , N_c and Q_c can be solved as,

$$c = \frac{(M + (h_0 + d)N)\xi}{\xi(h_0 + d) + \eta}, \quad N_c = \frac{(M\xi - N\eta)}{\xi(h_0 + d) + \eta}, \quad Q_c = -Q - k(M + (h_0 + d)N), \quad (4.23)$$

where

$$N = N_{10} - N_{1c}|_{x=0}, \quad Q = Q_{10} - Q_{1c}|_{x=0}, \quad M = M_{10} - M_{1c}|_{x=0}. \quad (4.24)$$

More details of the model can be found in (Wang and Qiao, 2004a). The above formulation of the FRP-strengthened concrete beam is referred to as the shear deformable beam theory in (Wang and Qiao, 2004a).

4.3.2. Flexible joint model

It has been demonstrated that the semi-rigid joint model under-evaluates the deformation at the crack tip. To fully capture the crack tip deformation, an interface deformable bi-layer beam theory (Qiao and Wang, 2004) can be employed here to calculate the crack tip deformation. In this theory, two interface compliances (Qiao and Wang, 2004), C_{si} and C_{ni} , were introduced to describe the deformations in the shear and normal directions along the interface under the shear and normal stresses, respectively. Similar to (Wang and Qiao, 2004a), the continuity conditions along the interface can be written as,

$$u_1 - (h_0 + d)\phi_1 - C_{s1}\tau = u_2 + \frac{h_2}{2}\phi_2 + C_{s2}\tau, \quad w_1 - C_{n1}\sigma = w_2 + C_{n2}\sigma. \quad (4.25)$$

A good estimation of these two compliances is given in (Wang and Qiao, 2004a) for bi-layered beams. However, this estimation cannot be simply applied to the problem shown in Fig. 4.3 because the thickness and modulus of the adhesive layer are much smaller than those of the FRP plate and concrete. Instead, we modify the interface compliance coefficients to incorporate the deformation of the soft adhesive layer as,

$$C_{n2} = \frac{h_0}{E_0} + \frac{h_1}{10E_1}, \quad C_{si} = \frac{h_0}{G_0} + \frac{h_1}{15G_1}. \quad (4.26)$$

Eq. (4.25) implies that the interface between two sub-layers is deformable under the interface stress. Therefore, it represents an improved tri-layer beam theory with deformable interface. By differentiating the first equation of Eq. (4.25) and considering Eqs. (4.4), (4.6), and (4.9), the moment in beam I can be expressed in term of axial force in beam I as,

$$M_1 = \frac{\eta}{\xi} N_1 - \frac{N_T}{\xi C_2} - \frac{h_2}{2\xi D_2} M_T - \frac{C_{s1} + C_{s2}}{b\xi} \frac{d^2 N_1}{dx^2}. \quad (4.27)$$

Differentiating the second equation of Eq. (4.25) and considering Eqs. (4.4), (4.6), (4.8), and (4.9) yield,

$$\begin{aligned} & \left(\frac{1}{B_1} + \frac{1}{B_2} \right) \left(\frac{d^2 M_1}{dx^2} + (h_0 + d) \frac{d^2 N_1}{dx^2} \right) - \frac{C_{n1} + C_{n2}}{b} \left(\frac{d^4 M_1}{dx^4} + (h_0 + d) \frac{d^4 N_1}{dx^4} \right) \\ & - \left(\frac{1}{D_1} + \frac{1}{D_2} \right) M_1 - \frac{1}{D_2} \left((h_0 + d) + \frac{h_2}{2} \right) N_1 = -\frac{M_T}{D_2}. \end{aligned} \quad (4.28)$$

Substituting Eq. (4.27) into (4.28), the governing equation is established as,

$$\frac{d^6 N_1(x)}{dx^6} + a_4 \frac{d^4 N_1(x)}{dx^4} + a_2 \frac{d^2 N_1(x)}{dx^2} + a_0 N_1(x) + a_M M_T + a_N N_T = 0, \quad (4.29)$$

where

$$a_4 = -b \left(K_s \left((h_0 + d)\xi + \eta \right) + K_n \left(\frac{1}{B_1} + \frac{1}{B_2} \right) \right),$$

$$a_2 = bK_n \left(bK_s \left(\frac{1}{B_1} + \frac{1}{B_2} \right) \left((h_0 + d)\xi + \eta \right) + \left(\frac{1}{D_1} + \frac{1}{D_2} \right) \right),$$

$$a_0 = -b^2 K_n K_s \left(\left(\frac{1}{D_1} + \frac{1}{D_2} \right) \eta + \frac{\xi}{D_2} \left(h_0 + d + \frac{h_2}{2} \right) \right), \quad a_N = b^2 K_n K_s \left(\frac{1}{D_1} + \frac{1}{D_2} \right) \frac{1}{C_2},$$

$$a_M = \frac{b^2 K_n K_s}{D_2} \left(\frac{h_2}{2} \left(\frac{1}{D_1} + \frac{1}{D_2} \right) + \xi \right), \quad K_s = \frac{1}{C_{s1} + C_{s2}}, \quad K_n = \frac{1}{C_{n1} + C_{n2}}. \quad (4.30)$$

The above governing equation can be solved by the characteristic equation:

$$x^6 + a^4 x^4 + a^2 x^2 + a_0 = 0. \quad (4.31)$$

The roots of Eq. (4.31) for the real material and geometry parameters can be expressed as:

(a) $\pm R_1$, $\pm R_2$ and $\pm R_3$, or (b) $\pm R_1$ and $\pm R_2 \pm iR_3$. Here R_1 , R_2 and R_3 are three real numbers.

Case (a) $\pm R_1$, $\pm R_2$ and $\pm R_3$:

The axial force N_I can be expressed as,

$$N_I = \sum_{i=1}^3 c_i e^{-R_i x} + \sum_{i=4}^6 c_i e^{R_i x} + N_{1c}, \quad (4.32)$$

where c_i ($i=1,2,\dots,6$) are the unknown coefficients, which can be solved by the boundary and continuity conditions. Similar to the semi-rigid joint, the terms with positive power can be neglected. So the resultant forces in the composite beam I can be given as,

$$N_I = \sum_{i=1}^3 c_i e^{-R_i x} + N_{1c}, \quad M_I = \sum_{i=1}^3 c_i S_i e^{-R_i x} + M_{1c}, \quad Q_I = \sum_{i=1}^3 c_i T_i e^{-R_i x} + Q_{1c}, \quad (4.33)$$

where

$$S_i = -\frac{R_i^2}{\xi} \frac{1}{bK_s} + \frac{\eta}{\xi}, \quad T_i = R_i \left(\frac{R_i^2}{\xi} \frac{1}{bK_x} - \frac{\eta}{\xi} - (h_0 + d) \right), \quad i = 1, 2, 3, \quad (4.34)$$

and

$$N_{1c} = -\frac{a_M}{a_0} M_T - \frac{a_N}{a_0} N_T, \quad M_{1c} = \frac{\eta}{\xi} N_{1c} - \frac{1}{\xi} \left(\frac{N_T}{C_2} + \frac{h_2}{2D_2} M_T \right), \quad Q_{1c} = \frac{dM_{1c}}{dx} + (h_0 + d) \frac{dN_{1c}}{dx}. \quad (4.35)$$

Considering the global equilibrium equation of Eq. (4.9), the resultant forces in the concrete beam 2, can be written as,

$$N_2 = -\sum_{i=1}^3 c_i e^{-R_i x} + N_{2c}, \quad M_2 = -\sum_{i=1}^3 \left(S_i + h_0 + d + \frac{h_2}{2} \right) c_i e^{-R_i x} + M_{2c}, \quad Q_2 = -\sum_{i=1}^3 c_i T_i e^{-R_i x} + Q_{2c}, \quad (4.36)$$

where

$$N_{2c} = N_T - N_{1c}, \quad Q_{2c} = Q_T - Q_{1c}, \quad M_{2c} = M_T - M_{1c} - \left(h_0 + d + \frac{h_2}{2} \right) N_{1c}. \quad (4.37)$$

Since no restraints are enforced on the displacements, there is no concentrated force at the crack tip (Qiao and Wang, 2004). The coefficients c_i ($i = 1, 2, 3$) can be obtain as,

$$\begin{pmatrix} c_1 \\ c_2 \\ c_3 \end{pmatrix} = \begin{pmatrix} c_{11} & c_{12} & c_{13} \\ c_{21} & c_{22} & c_{23} \\ c_{31} & c_{32} & c_{33} \end{pmatrix} \begin{pmatrix} N \\ M \\ Q \end{pmatrix} = \frac{1}{Y} \begin{pmatrix} S_3 T_2 - S_2 T_3 & T_3 - T_2 & S_2 - S_3 \\ S_1 T_3 - S_3 T_1 & T_1 - T_3 & S_3 - S_1 \\ S_2 T_1 - S_1 T_2 & T_2 - T_1 & S_1 - S_2 \end{pmatrix} \begin{pmatrix} N \\ M \\ Q \end{pmatrix}, \quad (4.38)$$

where

$$Y = S_2 T_1 - S_3 T_1 - S_1 T_2 + S_3 T_2 + S_1 T_3 - S_2 T_3, \quad (4.39)$$

and

$$N = N_{10} - N_{1c}|_{x=0}, \quad M = M_{10} - M_{1c}|_{x=0}, \quad Q = Q_{10} - Q_{1c}|_{x=0}. \quad (4.40)$$

Case (b) $\pm R_1$, and $\pm R_2 \pm i R_3$:

The axial force N_1 can be expressed as,

$$N_1 = c_1 e^{-R_1 x} + e^{-R_2 x} (c_2 \cos(R_3 x) + c_3 \sin(R_3 x)) + N_{1c}, \quad (4.41)$$

$$M_1 = c_1 S_1 e^{-R_1 x} + e^{-R_2 x} (c_2 (S_2 \cos(R_3 x) - S_3 \sin(R_3 x)) + c_3 (S_3 \cos(R_3 x) + S_2 \sin(R_3 x))) + M_{1c}, \quad (4.42)$$

$$Q_1 = c_1 T_1 e^{-R_1 x} + e^{-R_2 x} (c_2 (T_2 \cos(R_3 x) - T_3 \sin(R_3 x)) + c_3 (T_3 \cos(R_3 x) + T_2 \sin(R_3 x))) + Q_{1c}, \quad (4.43)$$

where

$$S_1 = -\frac{R_1^2}{\xi b K_s} + \frac{\eta}{\xi}, \quad S_2 = -\frac{R_2^2 - R_3^2}{\xi b K_s} + \frac{\eta}{\xi}, \quad S_3 = \frac{2R_2 R_3}{\xi b K_s}, \quad (4.44)$$

and

$$T_1 = -R_1 S_1 - (h_0 + d) R_1, \quad T_2 = -R_2 S_2 - S_3 R_3 - (h_0 + d) R_2, \quad T_3 = -R_2 S_3 + S_2 R_3 + (h_0 + d) R_3. \quad (4.45)$$

The coefficients c_i ($i = 1, 2, 3$) can be obtain as,

$$\begin{pmatrix} c_{11} & c_{12} & c_{13} \\ c_{21} & c_{22} & c_{23} \\ c_{31} & c_{32} & c_{33} \end{pmatrix} = \frac{1}{Y} \begin{pmatrix} S_3 T_2 - S_2 T_3 & T_3 & -S_3 \\ S_1 T_3 - S_3 T_1 & -T_3 & S_3 \\ S_2 T_1 - S_1 T_2 & T_2 - T_1 & S_1 - S_2 \end{pmatrix}, \quad (4.46)$$

where

$$Y = -S_3 T_1 + S_3 T_2 + S_1 T_3 - S_2 T_3. \quad (4.47)$$

4.4 Interfacial fracture parameters

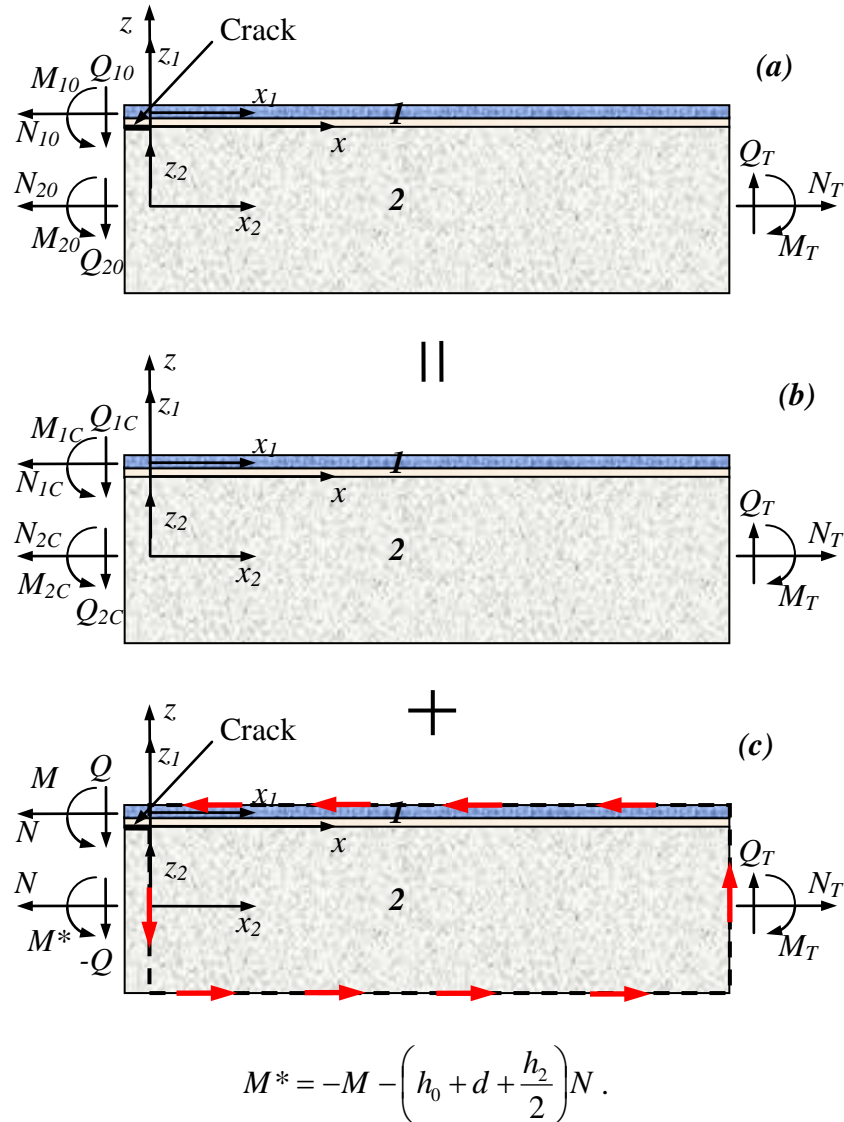


Fig.4.4. Calculation of energy release rate using the principle of superposition.

The delaminated FRP strengthened concrete beam can be obtained as the superposition of

two beams as shown in Fig. 4.4. Fig. 4.4 (a) is equivalent to the superposition of Fig. 4.4 (b) and (c). There is no crack in Fig. 4.4 (b). Therefore, forces applied to beams 1 and 2 can be obtained using composite beam theory as in Eqs. (4.17), (4.19), and (4.35).

The J-integral method is employed here to calculate the ERR at the crack tip. Since there is no crack in Fig. 4.4 (b), the J-integral of Fig. 4.4(b) is zero. Thus the total J-integral of Fig. 4.4(a) is equal to that of Fig. 4.4(c). Using the integration path shown in Fig. 4.4(c),

$$J = \frac{1}{2} \left(\frac{N_1^2}{C_1} + \frac{N_2^2}{C_2} + \frac{Q_1^2}{B_1} + \frac{Q_2^2}{B_2} + \frac{M_1^2}{D_1} + \frac{M_2^2}{D_2} - 2Q_1\phi_1 - 2Q_2\phi_2 \right) \Bigg|_{x=L}^{x=0}. \quad (4.48)$$

Eq. (4.48) can be rewritten as,

$$J = \frac{1}{2} \left(C_N N^2 + C_M M^2 + C_{MN} MN + \left(\frac{1}{B_1} + \frac{1}{B_2} \right) Q^2 - 2Q(\phi_1(0) - \phi_2(0)) \right), \quad (4.49)$$

where

$$C_N = \frac{1}{C_1} + \frac{1}{C_2} + \frac{(2(h_0 + d) + h_2)^2}{4D_2}, \quad C_M = \frac{1}{D_1} + \frac{1}{D_2}, \quad C_{MN} = \frac{2(h_0 + d) + h_2}{D_2}. \quad (4.50)$$

Eq. (4.50) clearly shows that the ERR depends on not only the three loading parameters but also the relative rotations at the crack tip.

In the classical solution of Suo and Hutchinson (1990), $\phi_1(0) = \phi_2(0)$, and therefore, the transverse shear force represented by the last term in Eq. (4.49) is ignored. In order to incorporate the transverse shear force into the ERR and its phase angle, the crack tip rotation must be properly estimated. If the semi-rigid joint model is used (Wang and Qiao, 2004a), the crack tip rotation of Fig. 4.4(c) can be given by,

$$\phi_1(0) = -\frac{\xi}{(h_0 + d)\xi + \eta} \frac{\eta}{D_2 k} ((h_0 + d)N + M),$$

$$\phi_2(0) = \frac{\xi}{(h_0 + d)\xi + \eta} \frac{\eta}{D_2 k} \left(\frac{\eta}{\xi} + (h_0 + d) + \frac{h_2}{2} \right) \left((h_0 + d)N + M \right). \quad (4.51)$$

If the flexible joint model (Qiao and Wang, 2004) is used, the rotations at the crack tip are obtained as,

$$\phi_1(0) = S_{21}N + S_{22}M + S_{23}Q, \quad \phi_2(0) = S_{51}N + S_{52}M + S_{53}Q, \quad (4.52)$$

where the coefficients S_{ij} ($i = 2, 5; j = 1, 2, 3$) are given in the appendix B. Eq. (4.51) requires a very simple calculation, but this calculation can underestimate the crack tip rotation (Qiao and Wang, 2005c). Eq. (4.52) can give a more accurate prediction of the crack tip rotation, but requires fairly complicated calculations.

Substituting the joint deformation model Eqs. (4.51) and (4.52) into Eq. (4.49) yields,

$$J = \frac{1}{2} \left(C_N N^2 + C_Q Q^2 + C_M M^2 + C_{MN} MN + C_{NQ} NQ + C_{MQ} MQ \right), \quad (4.53)$$

where

$$C_Q = \frac{1}{B_1} + \frac{1}{B_2}, \quad C_{NQ} = 2k \left(\frac{1}{B_1} + \frac{1}{B_2} \right) (h_0 + d), \quad C_{MQ} = 2k \left(\frac{1}{B_1} + \frac{1}{B_2} \right), \quad (\text{Semi-rigid joint}). \quad (4.54a)$$

$$C_Q = \frac{1}{B_1} + \frac{1}{B_2} + S_{23} - S_{53}, \quad C_{NQ} = S_{21} - S_{51}, \quad C_{MQ} = S_{22} - S_{52}, \quad (\text{Flexible joint}). \quad (4.54b)$$

Eq. (4.53) clearly shows that the transverse shear force is accounted for by “ Q ”. If all the terms with “ Q ” are ignored, Eq. (4.53) becomes identical to the existing AB’s solution (Au and Büyüköztürk, 2006). As illustrated by Qiao and Wang (2005c), the J-integral can be estimated more accurately by Eq. (4.54b) than Eq. (4.54a), because the rotation at the crack tip is fully included in Eq. (4.54b). However, Eq. (4.54a) is much simpler to calculate and easier to use. Therefore, both results are presented in this chapter.

The ERR can be related to the modulus of stress intensity factor (Suo, 1990) as,

$$G = \frac{H_{11}}{4 \cosh^2(\pi \varepsilon)} |K|^2. \quad (4.55)$$

Based on the dimensional consideration and linearity, the complex stress intensity factor K can be written in the form,

$$K = K_1 + iK_2 = \left(\sqrt{C_N} N - ie^{i\gamma_1} \sqrt{C_M} M - ie^{i\gamma_2} \sqrt{C_Q} Q \right) \frac{P}{\sqrt{2}} h_1^{-i\varepsilon} e^{i\omega}, \quad (4.56)$$

where ω is defined in the same manner as by Østergaard and Sørensen (2007) and

$$\varepsilon = \frac{1}{2\pi} \ln \left(\frac{1-\beta}{1+\beta} \right), \quad \beta = \left(\left[\sqrt{s_{11}s_{33}} + s_{13} \right]_2 - \left[\sqrt{s_{11}s_{33}} + s_{13} \right]_1 \right) / \sqrt{H_{11}H_{33}},$$

$$H_{11} = \left[2n\lambda^{\frac{1}{4}} \sqrt{s_{11}s_{33}} \right]_1 + \left[2n\lambda^{\frac{1}{4}} \sqrt{s_{11}s_{33}} \right]_2, \quad H_{33} = \left[2n\lambda^{\frac{1}{4}} \sqrt{s_{11}s_{33}} \right]_1 + \left[2n\lambda^{\frac{1}{4}} \sqrt{s_{11}s_{33}} \right]_2. \quad (4.57)$$

where β is the generalization of one of the Dundurs' parameters (Dundurs, 1969) for isotropic materials and ε is the bi-material constant. The subscripts "1" and "2" used outside the square brackets in the above expressions refer to the materials of beam 1 and 2, respectively. The non-dimensional parameters λ and n are given by,

$$\lambda = \frac{s_{11}}{s_{33}}, \quad n = \sqrt{\frac{1}{2}(1+\rho)}, \quad \rho = \frac{1}{2} \left(\frac{2s_{13} + s_{33}}{\sqrt{s_{11}s_{33}}} \right). \quad (4.58)$$

where s_{ij} are the material compliance defined in the conventional fashion.

It is convenient to use the combination $Kh_1^{i\varepsilon}$ as suggested by Rice (1988),

$$Kh_1^{i\varepsilon} = K_I + iK_{II} = |K| e^{i\psi}. \quad (4.59)$$

Then the individual stress intensity factors can be given by,

$$K_I = \frac{P}{\sqrt{2}} \left(\sqrt{C_N} N \cos(\omega) + \sqrt{C_M} M \sin(\omega + \gamma_1) + \sqrt{C_Q} Q \sin(\omega + \gamma_2) \right), \quad (4.60a)$$

$$K_{II} = \frac{P}{\sqrt{2}} \left(\sqrt{C_N} N \sin(\omega) - \sqrt{C_M} M \cos(\omega + \gamma_1) - \sqrt{C_Q} Q \cos(\omega + \gamma_2) \right). \quad (4.60b)$$

The phase angle “ ψ ” defined is given by,

$$\psi = \tan^{-1} \left(\frac{\sqrt{C_N} N \sin(\omega) - \sqrt{C_M} M \cos(\omega + \gamma_1) - \sqrt{C_Q} Q \cos(\omega + \gamma_2)}{\sqrt{C_N} N \cos(\omega) + \sqrt{C_M} M \sin(\omega + \gamma_1) + \sqrt{C_Q} Q \sin(\omega + \gamma_2)} \right), \quad (4.61)$$

where

$$\sin(\gamma_1) = \frac{C_{MN}}{2\sqrt{C_M C_N}}, \quad \sin(\gamma_2) = \frac{C_{NQ}}{2\sqrt{C_N C_Q}}. \quad (4.62)$$

It should be emphasized that the beam model does not have enough information to determine the ω in Eq. (4.61). Therefore, an extra continuum analysis such as FEA is needed to determine the angle ω in the same manner as Østergaard and Sørensen (2007).

4.5 Verifications of present LEFM solutions

To verify and demonstrate the enhanced accuracy of the new joint solutions, typical delaminated DCB specimens are analyzed using the existing model (Au and Büyüköztürk, 2006), the methods developed in this chapter, and the FEA method. The FEA results are used as the baseline of comparison. Commercially available finite element software, ANSYS 10.0, is used to perform the FEA. The FEA models are composed of the eight-node quadrilateral high order plane stress elements as shown in Fig.4.5. This element has compatible displacement interpolation functions and good ability to fit curved boundary. The modified CSD method (Davidson et al., 1995) is used to determine the ERRs and phase angles. In order to ensure the accuracy and stability of the ERR and its phase angle, the element size around the crack tip is selected as 0.01mm.

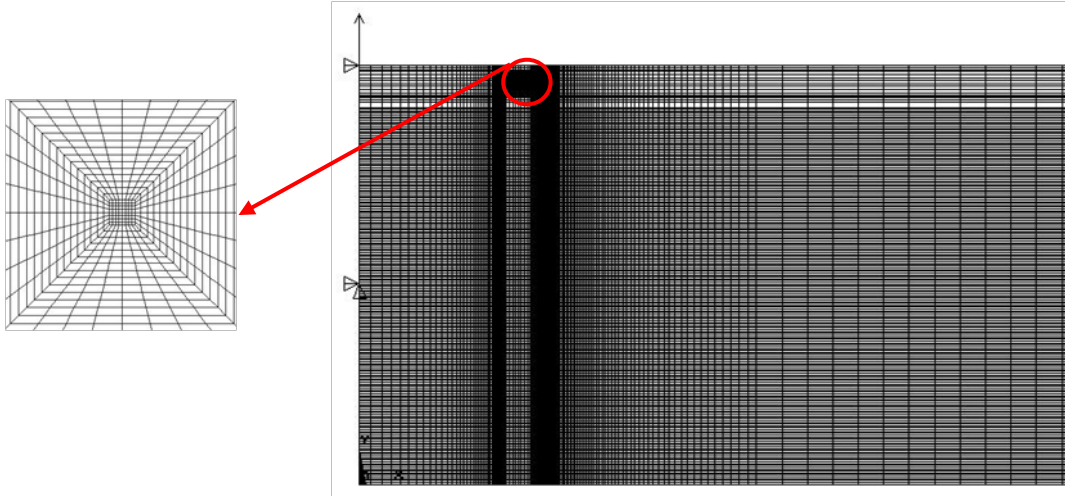


Fig.4.5. Finite element model of the FRP-strengthened concrete DCB specimen.

Analyses of the FRP-strengthened concrete DCB specimens (Fig.4.6) are conducted in this section. The Young's modulus and Poisson's ratios of the FRP plate, adhesive layer, and concrete specimens are $E_1 = 131$ GPa, $\nu_1 = 0.28$, $E_0 = 1.2$ GPa, $\nu_0 = 0.44$, $E_2 = 25$ GPa, $\nu_2 = 0.18$, respectively. The thicknesses of the FRP plate, adhesive layer, and concrete specimens are 1.4mm, 1.5mm, and 50.4mm. The crack lies along the interface between the concrete substrate and the adhesive layer as shown in Fig. 4.6.

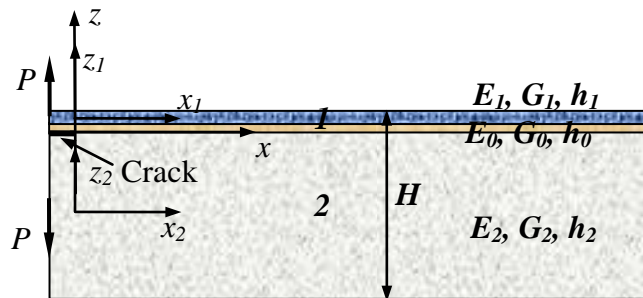


Fig. 4.6. FRP-strengthened concrete DCB specimen.

Results for the FRP-strengthened concrete DCB specimens with different crack lengths are presented in Fig. 4.7. Fig. 4.7 shows the ERRs predicted by different solutions. As expected, the two new joint models give better estimations of the ERRs than the existing solution. The

ERR solutions based on the semi-rigid joint model agree with the FEA results better than that of AB's method because shear deformation can be incorporated in this method. Because the crack length is much larger than the thickness of the FRP plate and adhesive layer, the contribution of shear force is not very significant in this case. However due to the existence of the soft adhesive layer, both the semi-rigid joint model and the AB's method cannot capture the local rotations at the crack tip accurately. This difficulty can be overcome by the flexible joint model by introducing the interface compliances. Therefore, the flexible joint model predicts much better solution than those of semi-rigid joint mode and AB's method.

Since on mode mixity solution is provided by the existing AB's solution, to demonstrate the effect of shear force in phase angle, a phase angle was obtained by ignoring the terms with shear force in Eq. (4.61). This phase angle is referred to as "solution without shear" in the figures. Fig.4.8 compares the phase angles obtained by all four methods. It can be seen that all but the solutions without shear force agree well with FEA results. This suggests that the DCB specimen is not a purely Mode I specimen if the crack is along the interface between the concrete and adhesive, which seems to contradict the common belief that DCB is a purely mode I specimen. In this figure, we can find that the phase angle increases with the crack length according to the new analytical solutions and FEA; while the solution without shear can't capture this feature. Because the transverse shear force is neglected in the solution without shear, the phase angle doesn't change with the length of crack, as shown in Figs. 4.8.

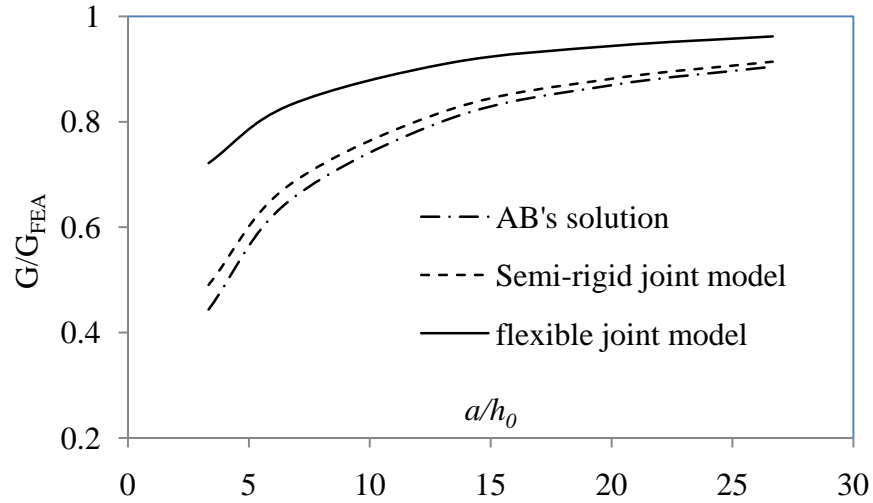


Fig.4.7. EERs versus crack lengths for a DCB specimen.

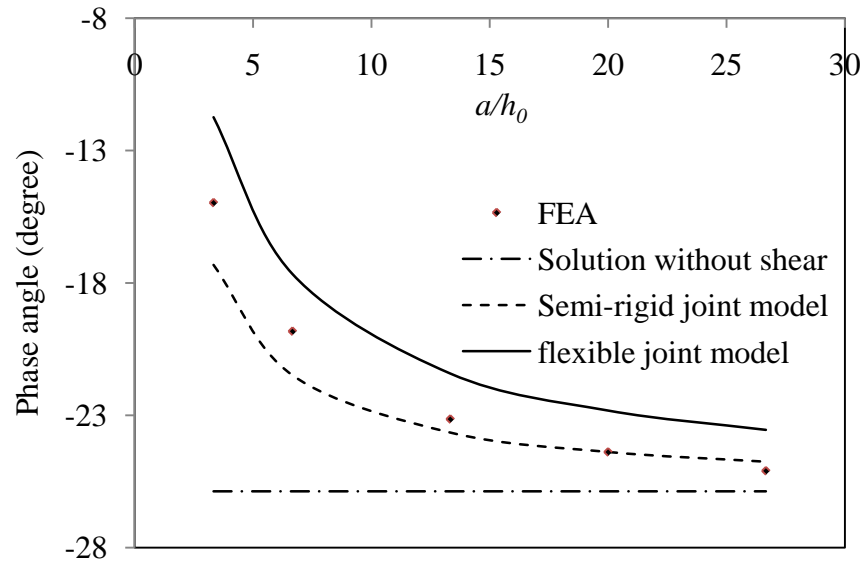


Fig.4.8. Phase angles versus crack lengths for a DCB specimen.

Fig. 4.9 compares the accuracy of three analytical solutions to predict the total ERRs for different thicknesses of the FRP plate. The total ERR calculated by analytical solutions are normalized by that of the FEA. It is easy to tell that the AB's model underestimates the total ERR considerably, especially when the FRP plate is thick. This is not surprising since the transverse shear force is not included in this model. By considering the transverse shear force, two new

analytical solutions, semi-rigid joint model and flexible joint model, predict the ERRs more accurately. Comparing these two new solutions, it can be seen that the flexible joint model is much more accurate than the semi-rigid joint model. This is because that the flexible joint model can capture more deformation at the crack tip of the FRP-concrete interface. All but the flexible joint model solutions underestimate the total ERRs when the FRP plate is thicker, which is caused by the approximate nature of the beam model. When the FRP plate is thinner, the beam model becomes more accurate to describe the deformation of the FRP-adhesive composite beam 1 and the concrete beam 2. As a result, the total ERRs obtained by the analytical solutions are more accurate for thin FRP plate, as shown in Fig. 4.9.

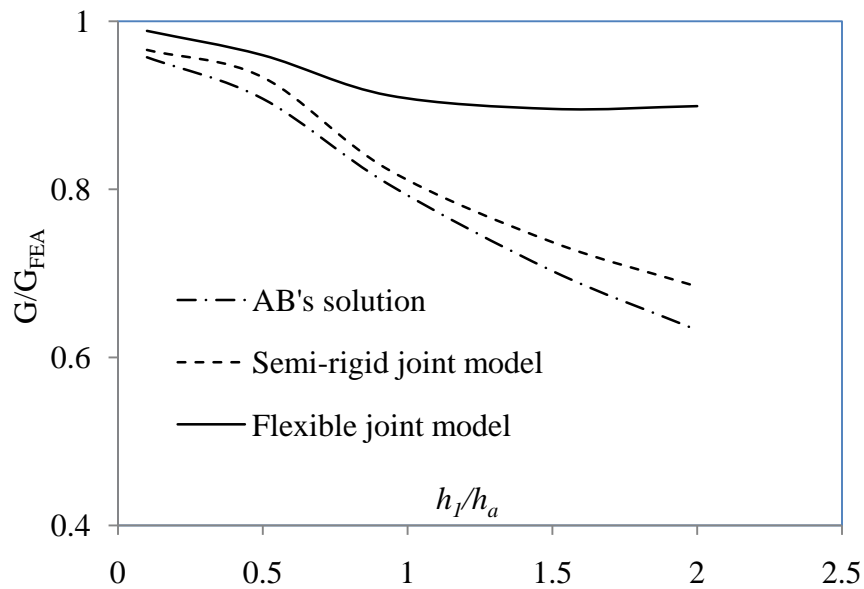


Fig.4.9. EERs versus thickness of the FRP plate for a DCB specimen.

Fig. 4.10 compares the phase angles obtained by all four methods. Overall, all four methods agree fairly well with each other. The solution without shear predicts the highest phase angle among all four methods, which is because that the transverse shear force is not included. Generally, the transverse shear force mainly introduces mode I energy release rate. By ignoring the effect of transverse shear force, the mode I component of the total ERR is underestimated and

the phase angle is overestimated. Both new analytical solutions in this study and the FEA account for the effect of the transverse shear force. As a result, their phase angles are lower. This figure also suggests that given all the other conditions are the same, the phase angle of the concrete-adhesive interface reduces with the thickness of the FRP plate.

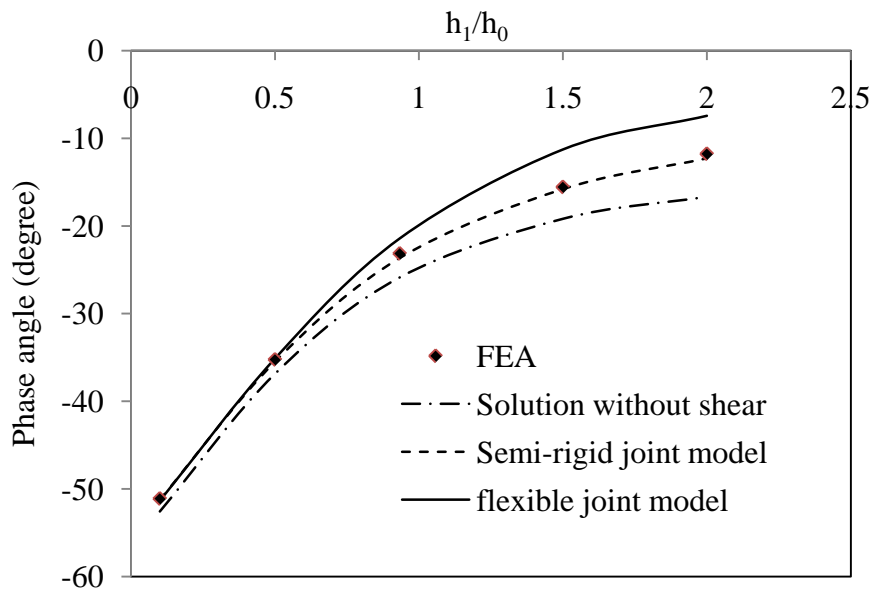


Fig.4.10. Phase angles versus thicknesses of the FRP plate for a DCB specimen.

4.6 Conclusions

In this study, the analytical solutions of total ERRs and their corresponding mode mixities have been obtained for the FRP-strengthened concrete specimen with a concrete/adhesive delamination. The effects of the transverse shear force, which cannot be included in the existing Au and Büyüköztürk (2006)'s solution, have been captured in these new solutions. This has been achieved through considering the crack tip deformations by two new joint deformation models, i.e., semi-rigid and flexible joint models. New terms related to the transverse shear force are introduced into the expressions of total ERR and its mode mixity, which directly indicate the effect of the transverse shear force on the concrete/adhesive delamination.

Calculations and comparisons of total ERRs and their phase angles for the typical DCB

specimens are conducted using the existing the AB's model, two new analytical solutions obtained in this chapter, and the FEA. It has been shown that three distinct accuracy levels of the solutions exist when compared to the FEA results. The existing AB's model gives the most approximate solutions of the ERRs and phase angles of the specimens since its neglecting of the deformation at the crack tip. The semi-rigid joint model accounts for the crack-tip deformation partially, and therefore, presents a better solution compared to the AB's model. The best accuracy is achieved by the flexible joint model since it accounts for the majority deformation at the crack tip. However, the expressions of flexible joint model are more complicated than those of the semi-rigid joint. In comparison to the existing AB's model, the solutions based on the semi-rigid and flexible joint models are in better agreements with the FEA results; therefore, they are more applicable for the concrete/adhesive delamination evaluation of the FRP-strengthened concrete specimens and data reduction analysis of the FRP-strengthened concrete specimens fracture experiments.

CHAPTER 5

ENVIRONMENT-ASSISTED SUBCRITICAL DEBONDING OF EPOXY-CONCRETE INTERFACE

5.1 Introduction

The integrity of the FRP-concrete interface with the cracks can be evaluated by the LEFM as discussed in the previous chapter. If the energy release rate at the crack tip is lower than a critical value, these small cracks will not grow if there is no environmental species. However, FRP-strengthened RC beams are usually exposed to aggressive environments during their whole service life. Under the synergistic effects of the service loads and environments species, these small cracks can grow slowly even the ERR at the crack tip is lower than the critical value.

A large body of testing results have shown that debond along the FRP-concrete interface is one of the most common failure modes of the FRP-strengthened concrete structures (Teng et al., 2003). However, a number of critical questions regarding the long-term durability of the FRP-concrete interface still remain unaddressed. The behavior of the FRP-concrete interface in aggressive environments is mainly examined through experimental studies (Chajes et al. 1995; Karbhari and Engineer, 1997; Green et al., 2000; Myers et al., 2001; Davalos et al., 2005; Wan et al., 2006; Au and Büyüköztürk, 2006; Ouyang and Wan, 2008). An inherent problem of all existing studies is that only the loads occurred at the time of catastrophic failure are measured. However, debond is, as pointed out by RILEM (Technical Committee FRP, 2003), “a gradual

process where slow growth of cracks occurs at the interface.” The cracks also grow slowly at lower loads compared to those associated with the critical conditions, such as the critical ERR. This slow crack growth is referred to as the subcritical crack growth, which is a long-term process of synergistic action of environments and mechanical loads. The catastrophic failure related to the critical crack is only the ending point of the slow crack growth process. Although some studies have shown that hydrolysis is the major effect on impairing the polymer/metal interfaces, there is no research has been conducted on the environment-assisted subcritical debond growth within the FRP-concrete interface. To understand the degradation mechanism of the interface debonding and gain the ability to accurately predict the long-term durability, it requires quantifying and appropriate analysis of the slow debond growth process. The current FRP research community seems unaware of the significant role of this slow debond growth, which could be a dominant mechanism for the failure of the FRP-concrete interface under service loads and aggressive environments. No study on it has ever been conducted or reported. To address this research gap in the long-term durability of the FRP-concrete interface and overcome the drawbacks in existing approaches, the environment-assisted subcritical debond growth within the FRP-concrete interface will be studied in details in this chapter using the wedge driving tests.

5.2 Environment-assisted subcritical cracking along the FRP-concrete interface

In the aggressive environments, cracks can propagate very slowly at driving forces below the critical value due to local chemical reactions at the crack tip. This slow crack growth in adhesive joints in aggressive environments is referred to as environment-assisted subcritical cracking (Wiederhorn, 1968; Maugis, 1985; Ritter and Conley, 1992; Gurumurthy et al., 2001; Singh et al., 2008) in corresponding to critical cracking when catastrophic failure occurs. To

illustrate the chemical reaction process, a schematic is shown in Fig.5.1.

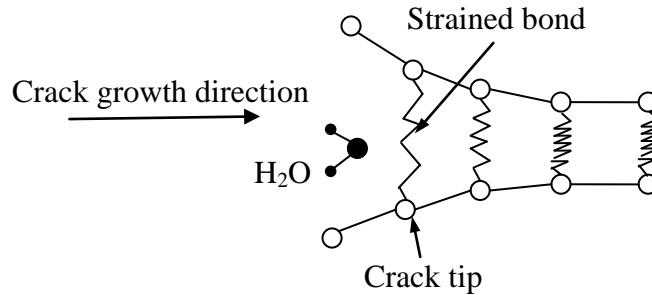


Fig.5.1. Reaction of water with a strained crack tip bond to propagate the crack at the driving forces below the critical fracture energy.

The subcritical crack growth behavior is usually described by the relationship of debond growth rate (da/dt) vs. driving energy release rate at the crack tip (G). A schematic illustration of such a curve is shown in Fig. 5.2. This curve consists of three crack growth regions and a threshold G_{th} . If the driving energy release rate G is less than G_{th} , subcritical cracking will not happen. In Region I, crack growth is so slow that the environmental species have enough time to transport to the crack tip to enable the environmental attack mechanism to occur readily. As a result, the crack growth rate is dependent on both the reaction rate and the mechanical load G . In Region II, the crack growth is faster so that the debond growth is controlled by the availability of the environmental species. As a result, the crack growth rate is almost independent of the mechanical load G . In Region III, crack growth is faster than the transportation rate of environmental species so that environmental species cannot reach the crack tip. Consequently, the crack growth rate is only dependent on G . Measurements in this region do not provide any information about the interaction of environmental species at the crack tip. Clearly, Region III describes critical crack growth in adhesive joint and the corresponding G is the critical ERR, G_c .

For the subcritical crack growth in Region I, existing studies on adhesive joints suggest that the G and da/dt can be fitting into a power-law expression (Johnsen et al., 2003),

$$da/dt = KG^n \exp(-Q/RT) \quad (5.1)$$

where K is a constant dependent on the materials and relative humidity; n is crack growth exponent. Because the subcritical debond is thermally activated, a temperature term also appears in Eq. (5.1), where Q is the apparent activation energy of the interface and R is the gas constant. It should be pointed out that Eq. (5.1) is not only valid for moisture-assisted subcritical debond growth, but also valid for creep-induced (Park et al., 2006) and cyclic fatigue load-induced (He and Hutchinson, 1989) subcritical crack growth. The crack growth exponent n is an important kinetic parameter of the environment-assisted debonding because its value reflects the reaction mechanism at the crack tip (Kinloch et al., 2007).

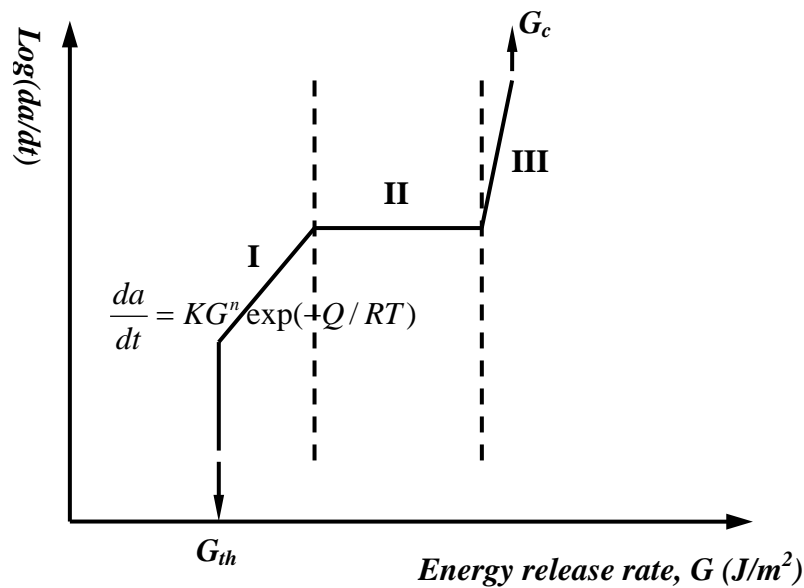


Fig.5.2. Crack growth velocity as a function the strain energy release rate.

5.3 Drawbacks of existing durability studies

Existing studies on the strength and durability of FRP-to-concrete interface in aggressive environments only focus on Region III. Region I and II are totally ignored. Since no environmental species can reach the crack tip in Region III, existing studies have to adopt a two-step approach. In first step, testing specimens are cured in designed accelerated environmental

conditions so that environmental species can reach the interface through diffusion and capillary actions. In second step, the residual strengths of the conditioned specimens are measured at catastrophic failure (Region III). This approach suffers a few obvious drawbacks:

- 1) The results of critical crack testing can be misleading when used to evaluate the long-term durability of the interface. As demonstrated in many studies (Diab and Wu, 2007; Singh et al., 2008), interface debond will shift from adhesive failure at slow growth rate, which is the case of under service loads, to cohesive failure at high growth rate, which is the case of catastrophic failure. Therefore, the catastrophic failure-based testing can lead to failure mode different from the real applications, in which the crack growth is very slow.
- 2) Interaction process between the environmental species and mechanical loads is lost. As a result, besides the ultimate strength, little information of the degradation mechanism of the interface due to environmental species attack can be obtained from the tests.
- 3) Testing results are specimen-dependent and an accurate relationship between the concentration of environmental species and the interface strength is difficult to obtain. Consequently, different authors reported different results. The transportation of environmental species depends on geometries and material properties of specimens. Some important properties related to transportation, such as diffusion coefficient of the adhesive-concrete interface, is difficult to measure. As a result, the concentration of environmental species along the FRP-concrete interface is difficult to control and predict during testing.
- 4) Environmental conditioning process usually takes a fairly long time.

5.4 Advantages of subcritical debonding test

To address the huge research gap in the long-term durability of the FRP-concrete interface and overcome the drawbacks in existing approaches, a systematical experimental study was conducted on the environment-assisted debond growth along the FPR-concrete interface under service loads in this chapter. The focus of this study was on subcritical crack growth (Region I and II) because our knowledge on it is virtually nonexistent and it provides a better way to study the long-term durability of the FRP-concrete interface for the following reasons:

- 1) The long-term durability of the FRP-concrete interface can be better characterized by subcritical crack testing because it closely simulates the failure occurring in the real-life application or service-life of the FRP-concrete interface. The change of debond locus occurred in catastrophic failure tests can be avoided.
- 2) Interaction with environmental species is allowed in subcritical crack testing because of slow crack growth rate. This can help us to understand the degradation mechanism, chemical kinetics, and other phenomena of the interface debond.
- 3) It takes much shorter time because the time-consuming process of conditioning specimens is unnecessary.
- 4) The transportation of environmental species is separated from the reaction at the crack tip in subcritical crack testing. Therefore, degradation rate of the interface induced by environmental species can be accurately quantified. Testing results are specimen-independent. A mechanism-based model can be developed to predict the degradation of the interface in aggressive environments. In existing studies, the transport of environmental species is always mixed with the reaction at the crack tip.

- 5) Ambiguity associated with bond strength due to competitive effects of concrete curing and long-term concrete strength gaining, can be reduced. This is because the debond locus is within the epoxy-concrete interphase zone and the long-term environmental conditioning is not needed.
- 6) A solid approach to predict service life of a interface can be developed based on the subcritical crack testing results.
- 7) Subcritical crack testing provides a far more useful indicator of interface quality than the ultimate interface bond strength and fracture toughness because the durability of the interface is generally more important than ultimate bond strength under harsh and changing environmental conditions. New knowledge to improve the durability of the interface can be obtained.

5.5 Research Scopes and Organization

Although there are many environment species which can induce adverse effects on the FRP-concrete interface, only water, deicing salt solution, and alkaline solution are considered in this study to keep this study tractable. Although the concrete, adhesive, and CFRP may play important roles in interface debond, the emphasis of this study is on gaining the fundamental knowledge, data, and mechanisms of the environment-assisted subcritical debond of the FRP-concrete interface. Therefore, their properties and geometries are fixed in this study. Other effects will be investigated in the future.

5.6 Materials and test specimens

A series of wedge driving tests were conducted in various environments to characterize the subcritical crack growth along the epoxy-concrete interface. The wedge driving test specimens were prepared with the epoxy layers constrained between the CFRP plates and the

concrete substrates. The test specimen size and structure are shown schematically in Fig. 5.3. The specimens will be inserted into a steel frame so that a steel wedge can be driven into the interface between the adhesive layer and concrete substrate. L_a is the total crack length from the edge of the specimen to the crack tip. a_c is the effective crack length, which is the distance from the contact point between the wedge and the FRP-epoxy layer to the crack tip. The width of the specimen is 2 in., which is the same as the width of the commercial available CFRP plate. The steel wedges were made according to the ASTM standard D3762-98, as shown in Fig. 5.4. The details of the concrete substrates, the CFRP plate, the bonding process, and testing procedures will be described in the following.

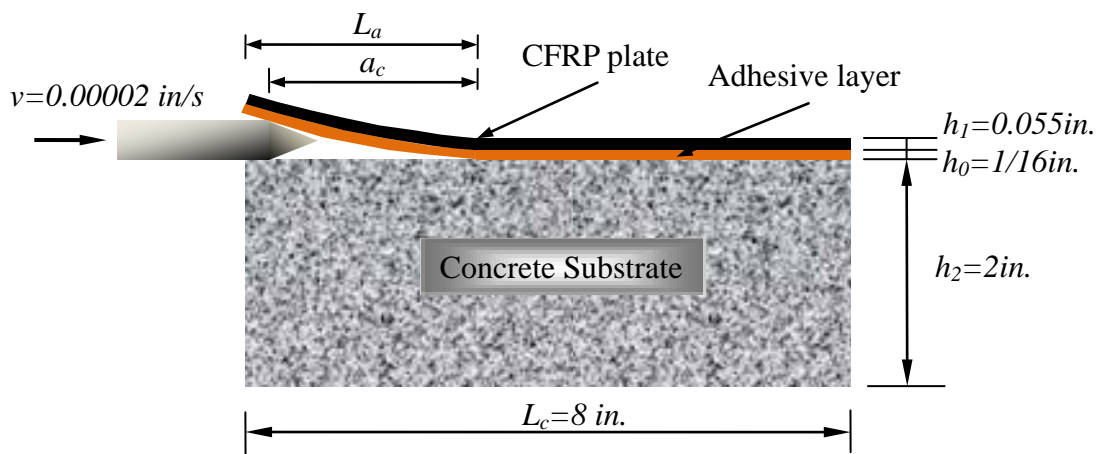


Fig.5.3. Wedge driving test configuration.

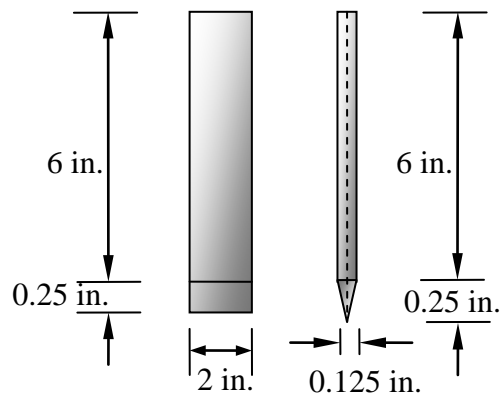


Fig.5.4. Wedge dimensions

5.6.1. Concrete substrates

To study the FRP-concrete interface cracking mechanism in the ambient condition, the tap water, the alkaline solution, and the deicing salt solution, three groups of different strength concrete specimens were casted in the laboratory using the aluminum models as shown in Fig. 5.5. The dimensions of the concrete substrates for the wedge driving tests in this study are $2 \times 2 \times 8$ in. Concrete specimens were mixed, casted, and cured following the standards ASTM C33 and ASTM C192. Totally, 60 normal density concrete specimens were casted by three batches as shown in Fig. 5.6. Three standard (6×12 in) cylinder specimens were casted each batch together with twenty specimens. After curing for 28 days in a water tank and drying in the laboratory for at least two months, the concrete specimens are ready to use. By conducting compressive strength tests on the standard cylinder specimens, the mean compressive strengths of these three groups' concrete are $2824.12psi$, $4238.83psi$, and $4880.75psi$, respectively. The modulus of elasticity of concrete substrates can be estimated by the following equation,

$$E_c = 57,000\sqrt{f'_c}, \quad (5.2)$$

where E_c is the modulus of elasticity of the concrete in lb/in^2 and f'_c is the specific 28-day compressive strength of the concrete in lb/in^2 .

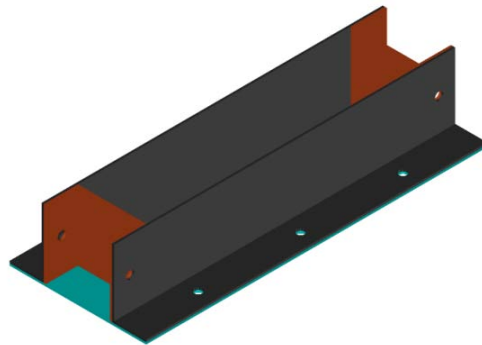


Fig.5.5. Aluminum models for concrete specimen making.



Fig.5.6. Concrete specimens and standard cylinder specimens prepared for experiment.

5.6.2. CFRP plates and structural adhesive

Commercially available CFRP plates were used to strengthen the concrete specimens. The CFRP composite was prepared by 700ksi, 33Msi carbon fiber, approximately 70% by weight in an epoxy resin matrix as reported by the manufacturer. The CFRP plates were manufactured in a controlled and consistent environment with guaranteed physical and mechanical properties. The CFRP plate with the dimensions of 0.055×2 in. was cut into 5.5 in. long strips. To allow better bonding with structural adhesive, one side of the FRP plates was sanded by the manufacturer. According to the technical sheet from manufacturer, the mean tensile strength and modulus of elasticity of the CFRP are 350 ksi and $1.9 \times 10^7 \text{ psi}$, respectively.

For the CFRP plates used in this experimental study, the recommended structural adhesive is Tyfo TC, which is a two-component adhesive based on a combination of epoxy resins and special filler. Tyfo TC is designed to bond the CFRP plates to the concrete substrates. According to the adhesive technical data sheet, the compressive strength, tensile strength, and tensile modulus of Tyfo TC are 4088 psi , 3285 psi , and $174,000 \text{ psi}$, respectively, after cured for seven days at room temperature.

5.6.3. Bonding CFRP plates onto the concrete substrates

As demonstrated in previous chapters, the most crucial part of the strengthening system is

the FRP-concrete interface. The structural adhesive has to be mixed and applied onto the FRP plates and concrete substrates properly to achieve good bond quality. Strict bonding procedures need to be followed as described below:

- 1) Sandblast the bonding surface of the concrete substrate carefully to remove the loose particles, expose coarse and fine aggregates, and create a roughened surface.
- 2) Clean the sandblasted concrete substrate surface with high pressure air. This surface should be dry and free of contaminations to ensure good bond between the structural adhesive and the concrete substrate.
- 3) Apply a layer of prime onto the concrete substrate to create a uniform base for the epoxy material and seal the concrete surface. This water-based epoxy primer is mixed using two equal parts of primer and hardener. The primer is applied onto the concrete surface using a short nap roller and cured for 24 hours.
- 4) Wipe the sanded side of the CFRP plate using white cloth and acetone to remove any excess residue from the CFRP plate until the cloth remains white after wiping.
- 5) Cover the bonding surface at one end of the concrete substrate with a Teflon foil to create a 0.125 in. pre-crack along the interface of the concrete substrate and epoxy layer.
- 6) Measure 100 parts of component A to 23.3 parts of component B by weight and pour component B into the bucket of component A. Mix thoroughly for five minutes with a low speed mixer until component B is thoroughly dispersed.
- 7) Place four plastic spacers at the four corners of the concrete surface to ensure the adhesive layer has a uniform thickness. Apply the structure adhesive onto the bonding surfaces with a towel to a nominal thickness of 1/16 in on both the concrete specimen and the CFRP plate.

- 8) Place the CFRP plate with adhesive onto the concrete specimens with the structural adhesive and press the CFRP plate with a hard rubber roller until the adhesive is forced out on both sides of the plates. Remove excess adhesive and make the glue line thickness equal to 1/16 in.
- 9) Apply proper pressure to the bonded specimens to ensure the maximum bonding strength is achieved. Cure the bonded specimens for two weeks.
- 10) Polish two sides of the specimens carefully to make sure no adhesive hinders the formation of the cracks.

5.7 Experimental set-up and research plan

The test system consists of a steel fixture for the FRP-concrete specimen, a MTS loading machine controlled by a computer, and a digital camera to monitor the crack growth as shown in Fig. 5.7. The wedge driving tests were conducted in various environmental exposures.

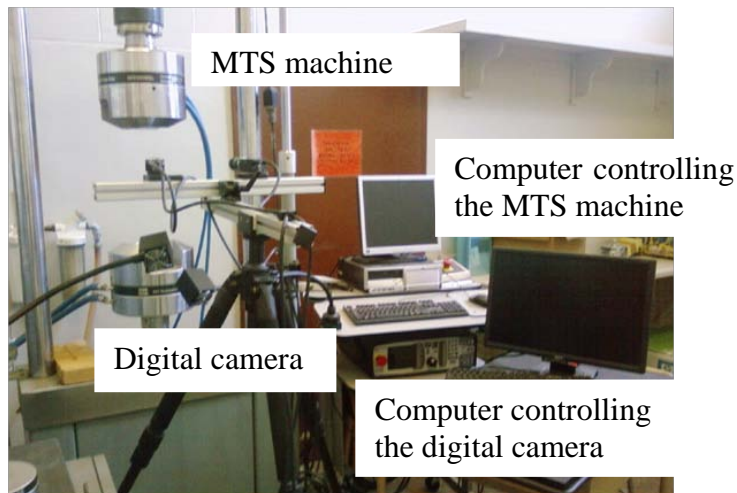


Fig.5.7. Experimental apparatus for the wedge driving tests.

5.7.1. Wedge driving tests

To conduct the wedge driving test in the ambient condition, the specimens were first placed in a home-made steel fixture and then mounted on the MTS loading machine as shown in

Fig.5.8. A 0.125 in. thick steel wedge was then inserted into the pre-crack between the epoxy and the concrete of the specimen at an intermediate speed (0.02 inch/second). After the thickest portion of the wedge reached the epoxy-concrete interface, the wedge was hold there for about one hour to reduce the instant effect of the high residue stress induced by the quick loading process. Then a computer-controlled electro-hydraulic MTS 810 material testing system was used to slowly drive the wedge into the crack at a very low speed (0.00002 in./s). To obtain the crack growth rate, the crack growth was monitored by a high resolution digital camera. The high-resolution images were taken around the crack tip zone every 10 seconds using the software of the DIC system. The length of the crack can be identified from these images.

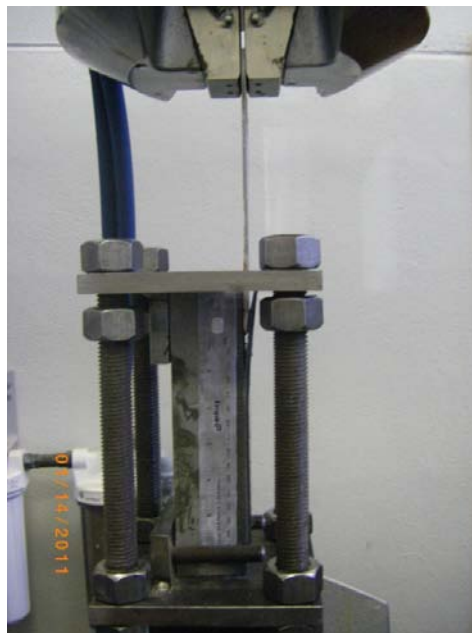


Fig. 5.8. Fixture of concrete specimen and test setup in ambient condition.

To investigate the environmental effects, a transparent glass vessel was used to enclose the whole specimen and the load fixture during the test (Fig.5.9). After filling this vessel with water or other aggressive chemical solutions, the FRP-concrete specimen was submerged in these fluids. In this way, we were able to apply both the mechanical forces and the environments

to the specimen. Compared to the FRP-epoxy layer, the concrete substrate is much stiffer. Therefore, the concrete block can be modeled as a rigid body. Then the driving ERR at the crack tip can be calculated as:

$$G = \frac{9D_c \Delta^2}{2ba_c^4} \quad (5.6)$$

where D_c is the bending stiffness of the FRP-epoxy composite layer; a_c is the effective crack length shown in Fig. 5.3; and Δ is the thickness of the wedge.

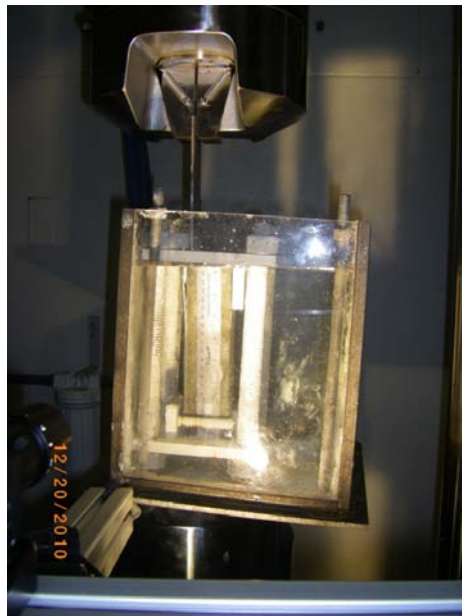


Fig.5.9. Wedge driving test set up in a transparent glass vessel.

5.7.2. Research experimental plan

Four typical environmental exposures were considered in this study, including the ambient condition, the tap water, the alkaline solution, and the deicing solution. As shown in table 5.1, three specimens were tested for each exposure. As a reference and control group, the subcritical debonding tests were conducted in the ambient condition first.

Table 5.1. Subcritical debonding test plan in different environmental exposures.

Group # \ Test conditions	Ambient condition	Tap water	Alkaline solution	Deicing salt solution
1	3	3	3	3
2	3	3	3	3
3	3	3	3	3

Water has been identified as the primary agent in the degradation process of adhesive bonds (Leung et al., 2004; Grace and Grace, 2005). Water molecules can permeate the adhesive or concrete and preferentially migrate to the interfacial region. These water molecules can reduce the bonding strength of adhesive/concrete interface through a displacement mechanism shown in Fig. 1.24 (Shimizu et al., 1999). To understand and quantify the role of water plays on the degradation of the adhesive-concrete interface, subcritical debond tests will be carried out in the water.

The subcritical debond tests were also conducted in the calcium chlorides solution to simulate the deleterious effect of the deicing salt agents used on the highways in wintry weather on the durability of the FRP-concrete interface. Saturated deicing salt solutions were used in this study to simulate the maximum deicing salt interface deterioration effect on the FRP-concrete interface. It has been shown that the deicing salt solutions can also cause blistering between the concrete and adhesive due to osmotic effects (Davalos et al., 2008). This study can also help to understand and quantify the synergistic effects of osmotic effects and moisture on the durability of the FRP-concrete interface.

The FRP-concrete interface can also be deteriorated by naturally occurred alkaline

solutions due to the presence of concrete pore water. These solutions have high PH value (as high as 13.5), which can attack the adhesive. To evaluate their effects on the durability of the epoxy-concrete interface, the subcritical debond tests were conducted in the sodium-hydroxide solutions with $PH = 13$.

5.8 Testing Results and discussions

Four groups of specimens were tested for different strength concrete substrates: the tests in the ambient environment, in tap water, alkaline solution, and deicing salt solution. The crack tips were identified through the high resolution images taken during the tests. Testing results for specimens exposed to the ambient environment are shown in Figs. 5.10 and 5.11. As shown in Fig.5.10, the interface debond grows very slowly and stably for the specimen tested at the slow driven rate for a fairly long time until a sudden jump of crack length is observed. This jump of crack length indicated that critical crack occurred. Fig. 5.10 shows that the energy release rate at the crack tip of the slow test specimen varies with the time. During the crack slowly growing period, the energy release rate is also slowly increasing until it reaches a maximum value where critical cracking occurs. Since this maximum value of energy release rate (2.59N/mm) triggered the critical crack, it is the fracture toughness of the interface. Figs.5.10 and 5.11 suggest that interface crack is slowly growing even though the ERR at the crack tip is well below the critical value. This phenomenon clearly confirms that subcritical crack growth exists between the epoxy and concrete interface. Similar subcritical cracking phenomenon can be observed in specimens testing in tap water, as shown in Figs.5.12 and 5.13. Compared with the previous case, it can be observed that the subcritical crack grows much faster in tap water than in ambient environment when the driving ERR is relatively low.

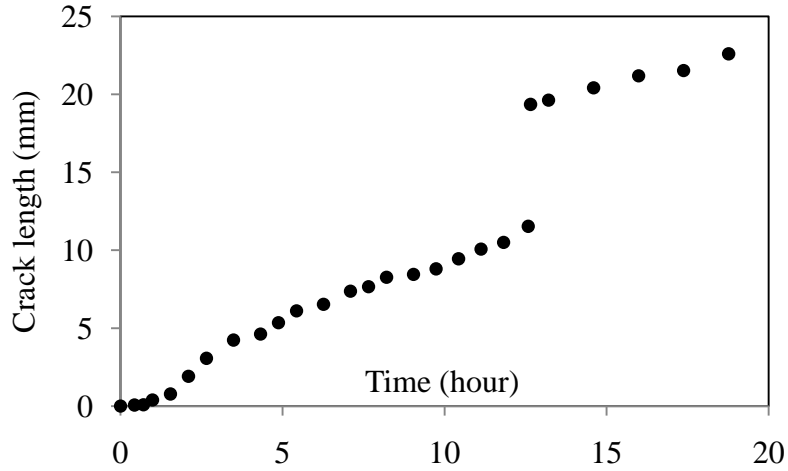


Fig.5.10. Crack growth with time in the ambient condition.

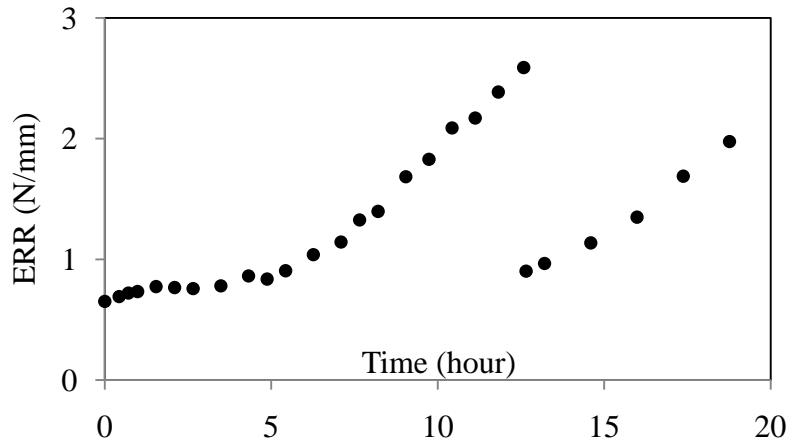


Fig.5.11. Variance of ERR with time in the ambient condition.

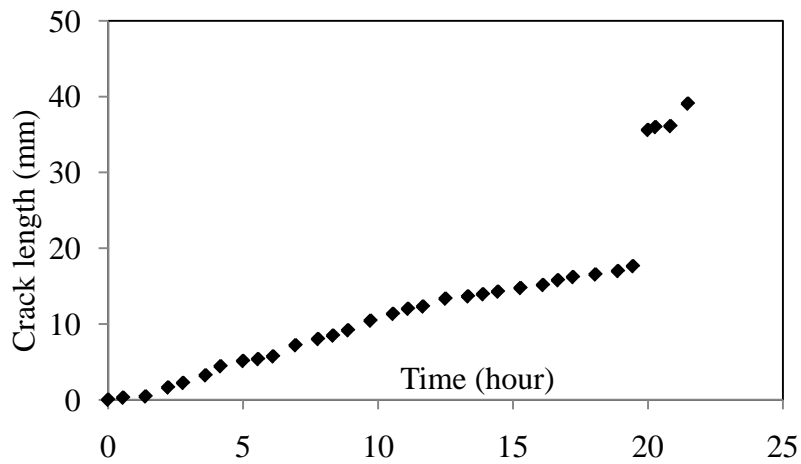


Fig.5.12. Crack growth with time in tap water

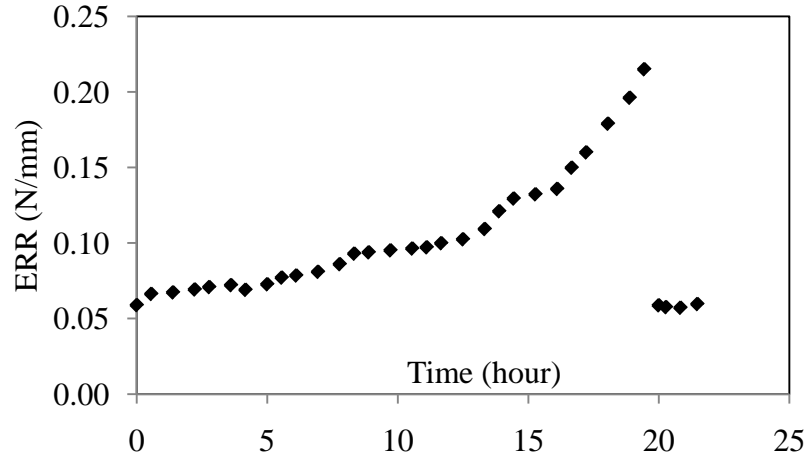


Fig.5.13. Variance of ERR with time in the tap water.

5.8.1. Effect of concrete substrate’s strength on subcritical debonding

In existing critical failure-based studies, the interface debonding occurs within a thin layer of the concrete substrate instead of along the FRP-concrete interface, so the FRP-concrete interface strength is related to the strength of the concrete substrate. To find out whether the substrate strength affects the subcritical cracking of epoxy-concrete interface, three different strengths of concrete were used to manufacture the testing specimens. The subcritical tests were conducted on these specimens in ambient condition, tap water, alkaline solution, and deicing salt solution, respectively. Testing results are presented in Figs. 5.14-5.17. In these figures, the strengths of the concrete substrate for group 1, 2, and 3 are 2824.12psi, 4238.83psi, and 4880.75psi, respectively. The experimental data shown in Figs. 5.14-5.17 clearly exhibits two distinct regions (Regions I and II). A noticeable experimental data scatter of crack growth velocity exists at the transition zone (in the red circle) from Region I to Region II. This phenomenon was also observed in previous studies (Ritter et al, 1998 and Kook and Dauskardt, 2002), and was referred to as a “stop-go” crack-growth process. It seems that the experimental results for concrete substrates with different strengths have the similar trends and no significant differences were observed among groups. The major differences for the tests in ambient

condition may be the value of the critical energy release rates, G_c . The G_c of group 1 with low strength concrete substrates is lower than those of other two groups.

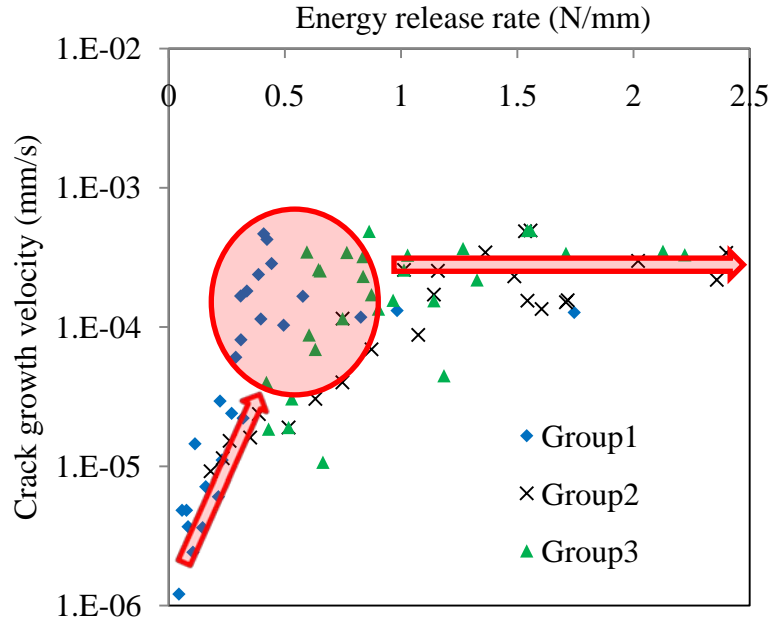


Fig.5.14. Comparison of subcritical crack growth velocity v (in log scale) as a function of the ERR in ambient condition for different concrete strength substrates.

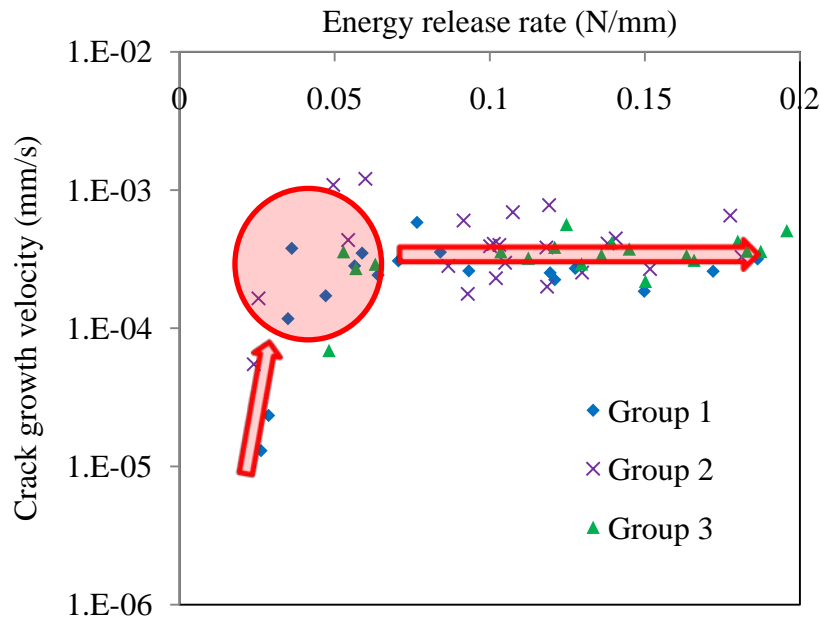


Fig.5.15. Comparison of subcritical crack growth velocity v (in log scale) as a function of the ERR in tap water for different concrete strength substrates.

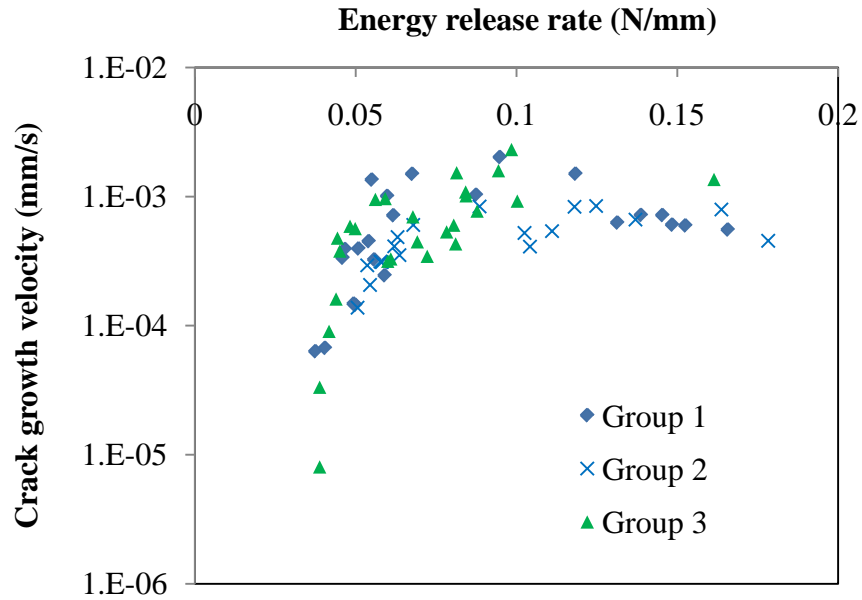


Fig.5.16. Comparison of subcritical crack growth velocity v (in log scale) as a function of the ERR in alkaline solution for different concrete strength substrates.

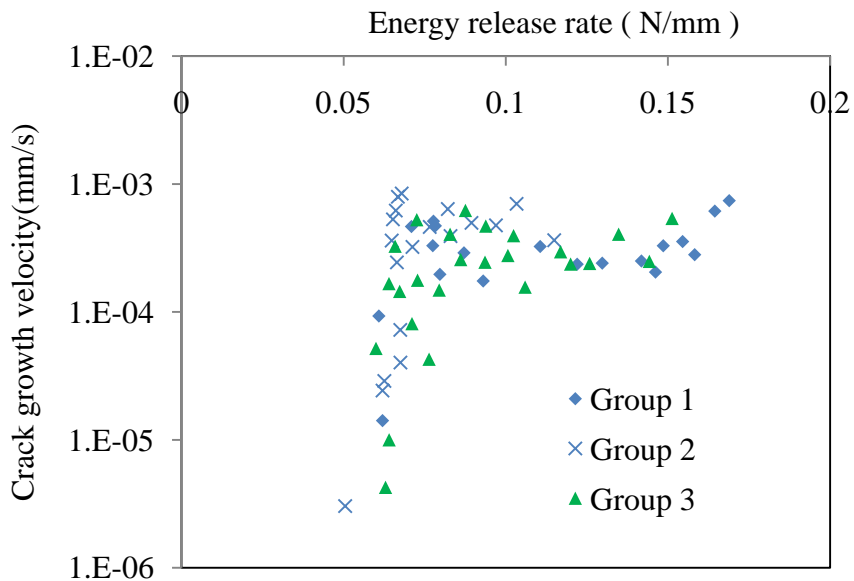


Fig.5.17. Comparison of subcritical crack growth velocity v (in log scale) as a function of the ERR in deicing salt solution for different concrete strength substrates.

5.8.2. Effect of aggressive environment on subcritical debonding

The results of subcritical debond tests in the ambient condition, the tap water, the alkaline solution, and the deicing salt solution are shown in Figs. 5.18-5.20, respectively. It can be seen

that the subcritical crack growths in tap water or solutions are much faster than that in ambient environment when the mechanical fracture driving energy is low. This difference is induced by the existence of water and solutions, which can displace the epoxy from the concrete. When tested in aggressive environments, much more liquid molecules are available at the crack tip than in the ambient environment. As a result, more epoxy chains can be displaced by the liquid molecules, leading to much faster subcritical debonding growth in these tests. This detrimental effect of water on the epoxy-concrete interface bond is demonstrated more clearly in Figs. 5.18-5.20. Figs. 5.18-5.20 compare the subcritical crack growth along the epoxy-concrete interface in the ambient environment, in the tap water, and the solutions.

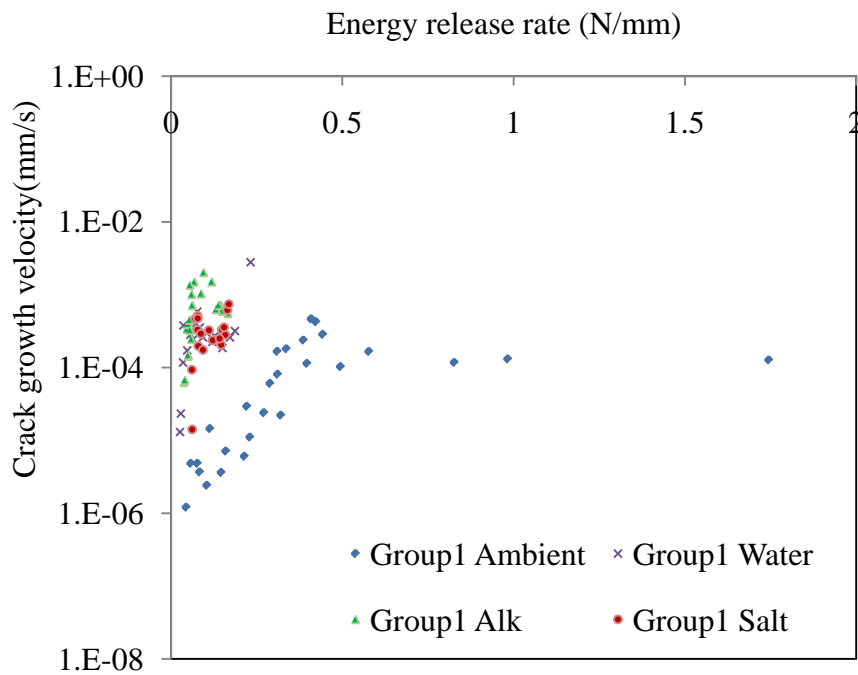


Fig.5.18. Comparison of the subcritical crack growth velocity v (in log scale) as a function of the ERR at the crack tip of group 1.

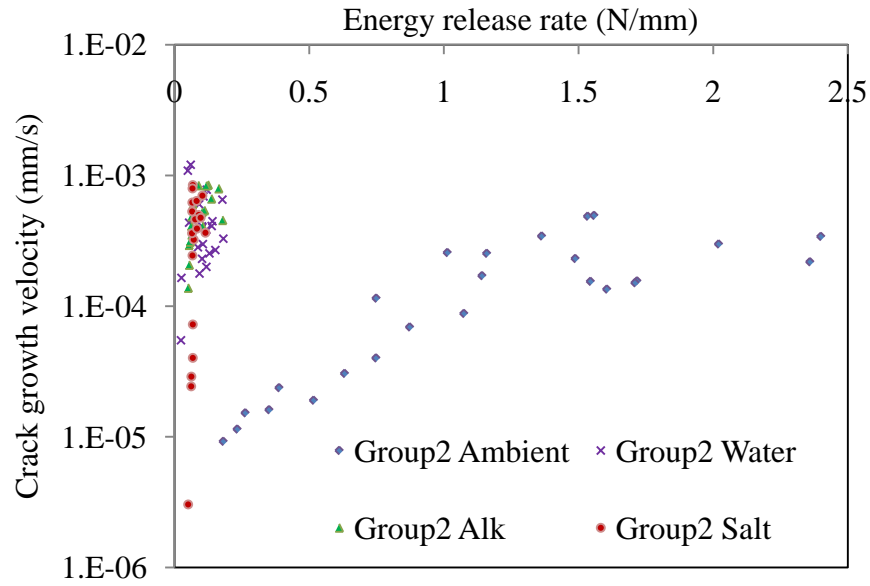


Fig.5.19. Comparison of the subcritical crack growth velocity v (in log scale) as a function of the ERR at the crack tip of group 2.

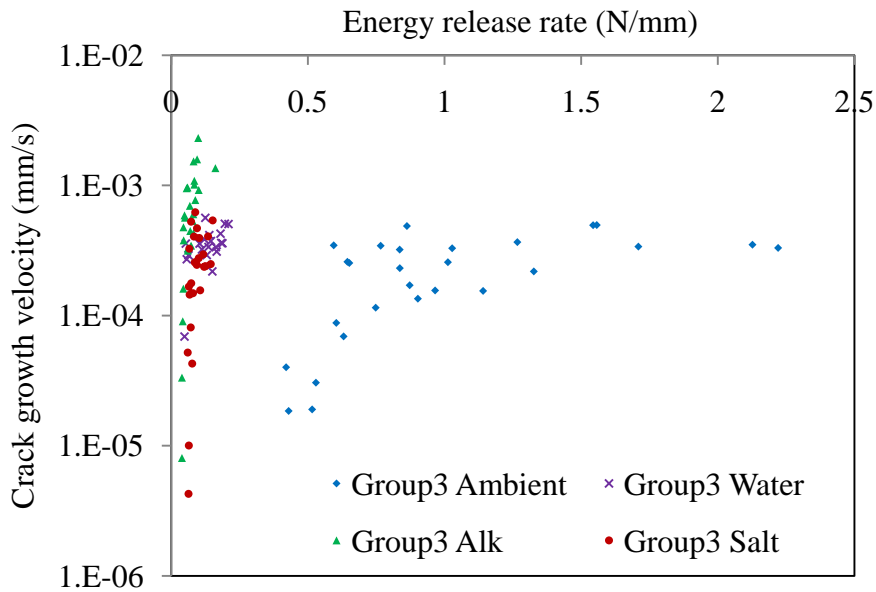


Fig.5.20. Comparison of the subcritical crack growth velocity v (in log scale) as a function of the ERR at the crack tip of group 3.

Fig. 5.21 compares the fracture surfaces of these tests. There is almost no concrete attached to the epoxy layer of specimens tested in aqueous conditions, indicating that debonding occurs along the epoxy-concrete interface. For the slow test in ambient environment, there is

very little concrete attached to the epoxy, suggesting that debonding is mainly adhesive failure along the epoxy-concrete interface. Much more concrete is attached to the epoxy in the fast loading region, suggesting that debonding is mainly cohesive failure within the concrete. In published testing results based on critical crack testing, debonding is usually occurred within the concrete because the strength of the concrete may be lower than that of the epoxy and the epoxy-concrete interface. For the test in the aqueous conditions, the specimens were submerged in the water and loaded at a very slow rate. There are sufficient water molecules available at the crack tip, which can substantially reduce the strength of the possible chemical bonds (hydrogen bonds) between the epoxy and concrete. As a result, the epoxy-concrete bond can be weaker than the adjacent concrete, leading to adhesive debonding along the epoxy-concrete interface. It has also been shown that the strength of the hydrogen bonds between the epoxy and the concrete increases with the loading rate (Namkanisorn et al, 2001). At the critical crack growth, the loading rate is so high that the strength of the bond between the epoxy and concrete can be higher than that of the concrete. As a result, debonding is occurred within the concrete, as shown in the fast loading region in Fig. 5.21. While in the subcritical crack growth, the loading rate is much lower. The strength of the bond between the epoxy and the concrete is lower than that of the concrete, leading to debonding along the epoxy concrete interface, as shown in Fig. 5.21.

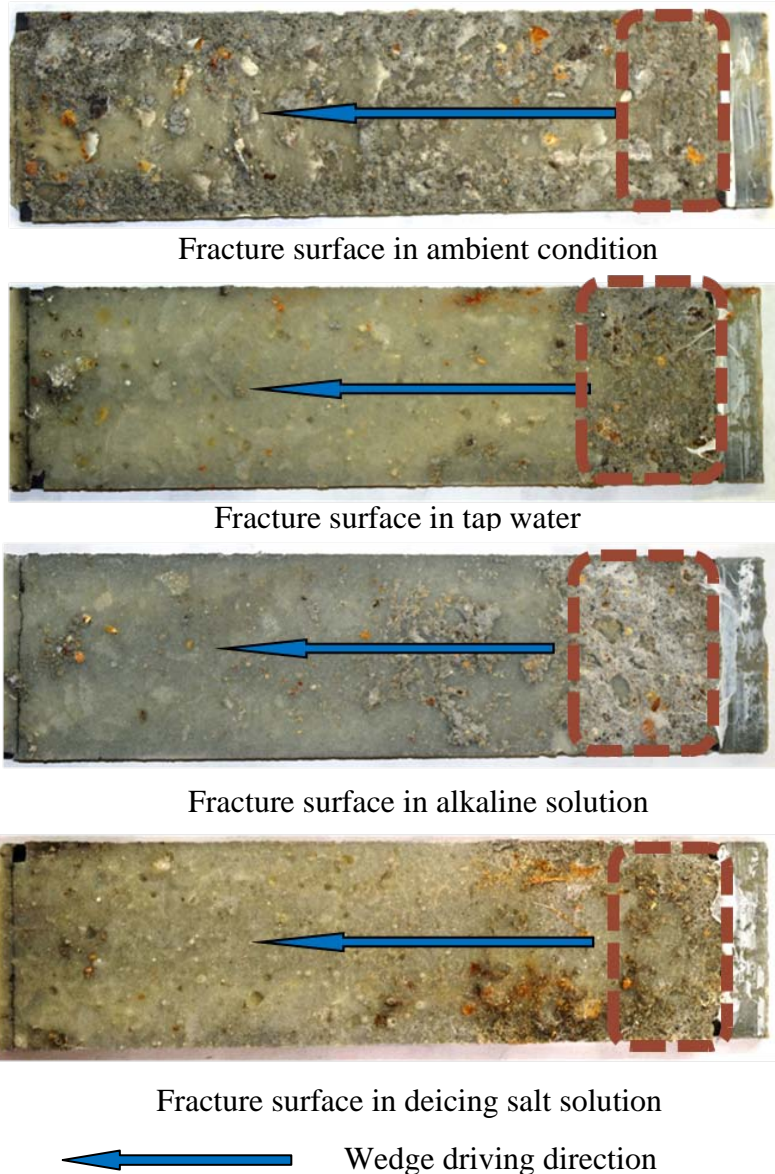


Fig.5.21. Interface fracture surfaces of wedge driving tests.

5.9 Conclusions

In this study, the subcritical crack growth along the epoxy-concrete interface was observed for the first time. It was found that the concrete substrates' strength does not have significant effect on the subcritical cracking growth except the critical energy release rate in the ambient condition. Water and other solutions can substantially reduce the energy release rate at the crack tip needed to drive the subcritical crack growth along the epoxy-concrete interface.

Under the same mechanical driving energy, water and other solutions can increase the subcritical debond growth rate along the epoxy-concrete interface by a few orders of magnitudes. Different failure modes were also observed in the subcritical debond process. The interface debonding changes from the cohesive failure within the concrete in critical cracking to the adhesive failure along the epoxy-concrete interface in the subcritical cracking.

CHAPTER 6

NONLINEAR FRACTURE MECHANICS OF FLEXURAL-SHEAR CRACK INDUCED DEBONDING OF FRP-STRENGTHENED CONCRETE BEAMS

6.1 Introduction

After a period of environment-assisted subcritical debond growth process, some of the cracks will approach their critical lengths. In such a situation, critical debonding will occur, leading to the premature failure of the strengthened structures. This crack propagation process cannot be assessed using the methods developed in previous chapters. Recent studies show a trend that nonlinear fracture mechanics have gained more popularity and been adopted by more and more researchers. Nonlinear fracture mechanics approach can avoid the difficulties arisen in LEFM (Triantafillou and Plevris, 1992; Täljsten, 1996, 1997a; Yuan et al., 2001; Wu et al., 2002; Yuan et al., 2004; Wang, 2006a, b; 2007a, b). Here, nonlinear fracture mechanics refers to using a nonlinear traction-separation law, rather than the linear one as assumed in the LEFM, to describe the stress-deformation behavior of the FRP-concrete interface. The application of a nonlinear traction-separation law is supported by many experimental evidences obtained in the last decade (Chajes et al., 1995, 1996; Bizindavyi and Neale, 1999; Dai et al., 2005; Yao et al., 2005). The shear traction-separation law of the FRP-concrete interface is generally referred to as bond stress-slip law in the literature. Generally, this nonlinear relationship consists of two stages: an initially elastic stage in which the interfacial stress increases with the slip until it reaches a maximum value, and a softening stage in which interfacial stress decreases with the slip. This

nonlinear relationship can be measured directly using a J-integral method as recently suggested by Wang (2007a). It should be pointed out that using a nonlinear bond stress-slip law in the analytical model, the debonding process is essentially approached through a CZM. All the nonlinear fracture models aforementioned are for the debonding of the FRP-concrete interface under mode II loading (Chajes et al., 1995, 1996; Ziraba et al., 1995; Bizindavyi and Neale, 1997, 1999; Täljsten, 1997; Yuan et al., 2004; Yao et al., 2005; Dai et al., 2005; Wang, 2006b, 2007a). This pure mode II debonding can only be induced at the locations of flexural cracks in concrete beams. At the plate end and the locations of flexural-shear concrete crack, as demonstrated by analytical solutions (Roberts and Haji-Kazemi, 1989; Malek et al., 1998; Jones et al., 1988), both the shear and peel stress (mixed-mode) concentrations exist along the interface. Therefore, neglecting the peeling stress leads to discrepancy on the fracture parameters measured by different specimens (Chen and Teng, 2001).

Intermediate crack induced debonding (IC debonding) is an ongoing research topic which attracts many researchers (Wu et al., 1997; Sebastian, 2001; Teng et al., 2003; Wang, 2006a,b; Liu et al., 2007; Smith and Gravina, 2007; Lu et al., 2007). By using a bilinear shear stress-slip law, Wang (2006a, b) established a CZM for the flexural crack induced debonding. This model unifies the debonding initiation and propagation into one model and interface stresses can be obtained in closed-form. However, the Wang's model is limited to one flexural crack. Recently, Liu et al. (2007) and Smith and Gravina (2007) modeled the IC debonding induced by multiple flexural cracks using the iteration approaches. All these studied are limited to flexural crack in which the debonding is in mode II. Very few studies have been conducted on the flexural-shear IC debonding because of its nature of mixed-mode. Besides a displacement jump in the axial direction, a transverse displacement jump is also induced by the flexural-shear crack, which

causes the interface under peeling and shear loading. Teng et al. (2003) noted this and believed that the peeling effect was a secondary factor in IC debonding. However, no rigorous analysis has been provided to verify their arguments. Niu et al. (2006) presented a finite element simulation of the diagonal-crack induced debonding of the FRP-concrete interface. Pan and Leung (2007) conducted a series of experimental studies of the FRP-concrete interface debonding under pulling/peeling effects. Wang (2007b) developed a mixed-mode CZM for the debonding of a FRP-concrete adhesive joint. By using this nonlinear fracture mechanics model, Wang (2007b) successfully simulated the mixed-mode debonding tests conducted by Pan and Leung (2007). By using the cohesive zone model, a unified description of the debonding initiation and progression can be developed, which is not possible by LEFM approach. The mode mixity of the debonding, which is difficult to obtain in the LEFM, can also be retrieved naturally. This nonlinear fracture mechanics approach is used in this study to simulate the mixed-mode interface debonding induced by a flexural-shear crack. Due to the difficulties in conducting mixed-mode debonding tests, the analytical results of this study provide valuable insights into the behavior of the flexural-shear IC debonding.

The chapter is arranged as follows. In the second section, an FRP strengthened reinforced concrete beam with a flexural-shear crack is modeled as two beams connected through the FRP-concrete interface. Closed-form solutions of the interface stresses and FRP force are obtained in this section. In the third section, as verifications, the closed-form solutions obtained in the second section are compared with the numerical solutions by FEA. In the fourth section, parametric studies are conducted to shed new lights on the flexural-shear IC debonding. Major findings of this study are summarized in the last section.

6.2 Mixed-mode CZM of the flexural-shear IC debonding

6.2.1 Bi-beam system

Consider a simply supported concrete beam externally strengthened by an FRP plate, as shown in Fig. 6.1(a). To simplify the analysis, only an flexural/shear crack existing at a random location of the RC beam is considered (to the left side of the mid-span in this study). In this study, only the FRP-concrete interface debonding is examined. Therefore, both the RC beam and FRP plate are modeled as linear elastic Euler-Bernoulli's beams (beam 1 and 2 in Fig. 6.2). This approach is widely used in debonding analysis by many researchers (Roberts and Haji-Kazemi, 1989; Malek et al., 1998; Smith and Teng, 2001; Rasheed and Pervaiz, 2002). Then, the constitutive laws for these two beams can be written as,

$$N_i = C_i \frac{du_i}{dx}, \quad M_i = -D_i \frac{d^2w_i}{dx^2}, \quad i = 1, 2, \quad (6.1)$$

where N_i and M_i are axial forces and bending moments of beam i ($i = 1, 2$), respectively; u_i and w_i are the axial and vertical displacements of beam i ($i = 1, 2$), respectively; C_i and D_i are axial and bending stiffnesses of beam i ($i = 1, 2$), respectively; and $C_i = E_i b_i h_i$, $D_i = E_i I_i$; E_i is the Young's modulus of beam i ($i = 1, 2$); b_i and h_i are the width and height of beam i ($i = 1, 2$); I_i is the moment of inertia of beam i .

Considering the free body diagram shown in Fig. 6.2, equilibrium equations can be written as,

$$\left\{ \begin{array}{l} \frac{dN_1}{dx} = b\tau \\ \frac{dQ_1}{dx} = -b\sigma \\ \frac{dM_1}{dx} = Q_1 + Y_1 b_2 \tau \end{array} \right., \quad \left\{ \begin{array}{l} \frac{dN_2}{dx} = -b\tau \\ \frac{dQ_2}{dx} = b\sigma \\ \frac{dM_2}{dx} = Q_2 + Y_2 b_2 \tau \end{array} \right. . \quad (6.2)$$

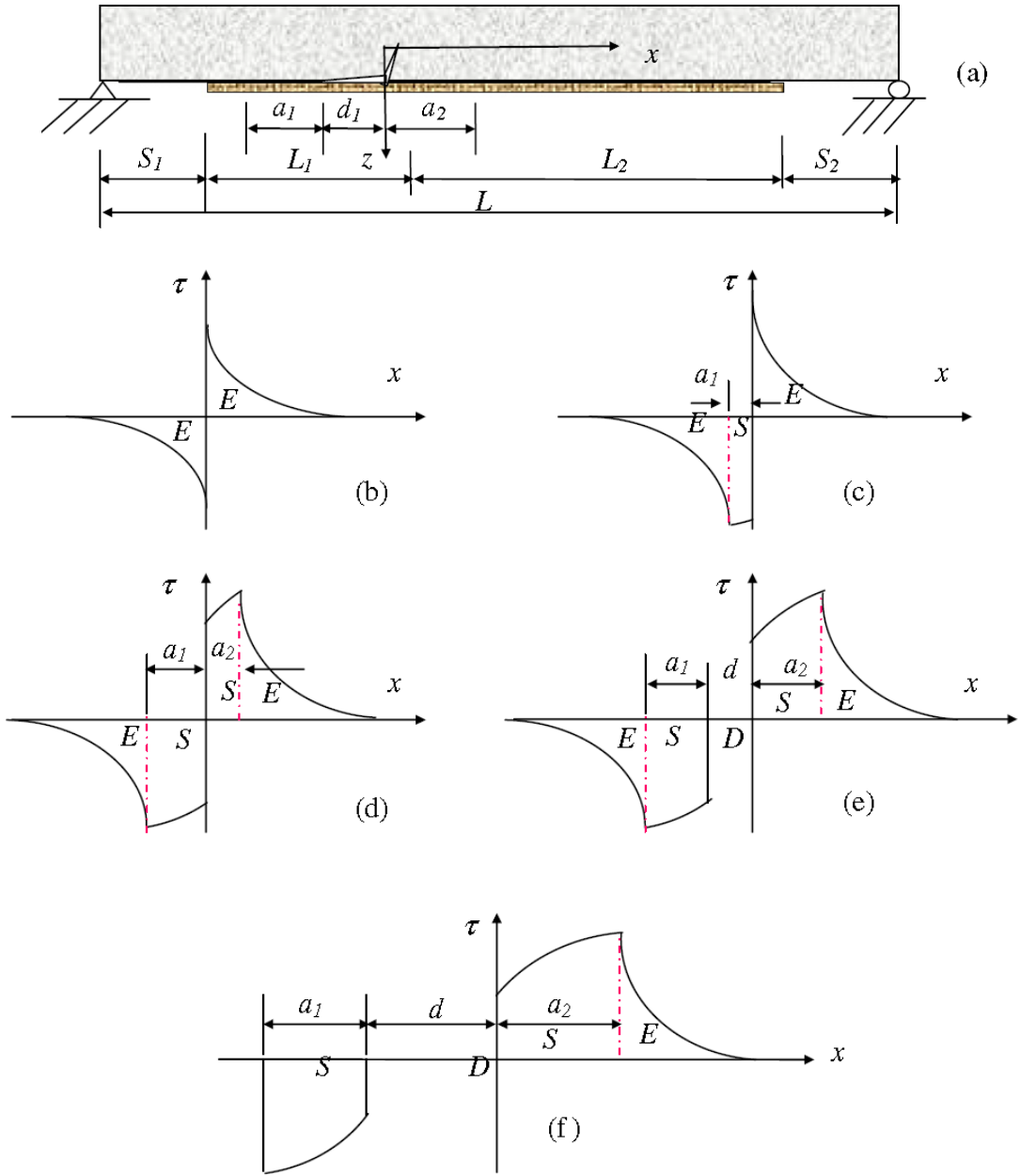


Fig.6.1. Flexural-shear crack induced debonding of an FRP-strengthened RC beam.

The overall equilibrium requires (Fig. 6.2),

$$N_1 + N_2 = N_T, \quad Q_1 + Q_2 = Q_T, \quad M_1 + M_2 + N_2(Y_1 + Y_2) = M_T, \quad (6.3)$$

where N_T , Q_T , and M_T are the resulting forces with respect to the neutral axis of the FRP plate. τ and σ are the interfacial shear and normal stress, respectively. Y_1 and Y_2 are the distances from the bottom of beam 1 and the top of beam 2 to their respective neutral axis.

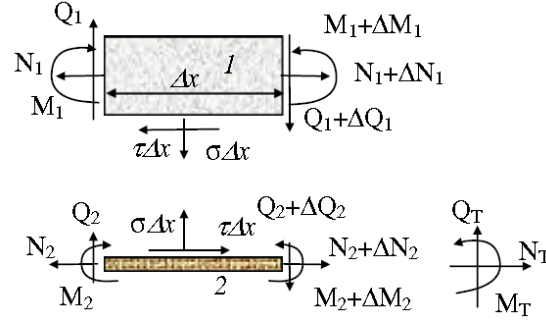


Fig.6.2. Free body diagram for equilibrium equation.

By using the coordinate system shown in Fig. 6.2, we can write the separations of the interface in the open and shear directions as,

$$\delta_n = w_2 - w_1, \quad (6.4)$$

$$\delta_t = u_1 - Y_1 \frac{dw_1}{dx} - u_2 - Y_2 \frac{dw_2}{dx}. \quad (6.5)$$

6.2.2 Mixed-mode nonlinear bond stress-slip model

As shown in Fig. 6.1(a), beam 2 (FRP plate/sheet) is bonded to beam 1 (concrete) through the FRP-concrete interface layer, which can be modeled as a large fracture processing zone with a nonlinear bond-slip law (Wang, 2006a). Extensive studies have been conducted on characterizing and modeling the shear (mode II) stress-separation (bond stress-slip) law along the FRP-concrete interface. Various nonlinear bond-slip laws have been proposed (Chajes et al., 1995, 1996; Täljsten, 1997; Wu and Yin, 2003; Yuan et al., 2004; Dai et al., 2005; Wang, 2007a,b). In these nonlinear shear stress-slip models, the shear stress increases initially as the bond-slip grows. When the bond-slip reaches certain value, the stress reaches its maximum and then decreases with the slip of the interface. Among them, bilinear law is the most popular one for its simplicity and good agreement with experiment observations (Yuan et al., 2004; Wang, 2006 a, b), and therefore, is also adopted in this study. As shown in Fig. 6.3(a), the bilinear bond stress-slip law consists of a linearly elastic branch for bond slip less than a particular value δ_I ,

and a linearly decreasing branch until complete delamination occurs. This law can be expressed by the following equations:

$$\tau = \begin{cases} 0 & \delta_t < -\delta_f \\ -\frac{\delta_f + \delta_t}{\delta_f - \delta_1} \tau_f & -\delta_f \leq \delta_t < -\delta_1 \\ \frac{\delta_t}{\delta_1} \tau_f & -\delta_1 \leq \delta_t < \delta_1 \\ \frac{\delta_f - \delta_t}{\delta_f - \delta_1} \tau_f & \delta_1 \leq \delta_t < \delta_f \\ 0 & \delta_f \leq \delta_t \end{cases} \quad (6.6)$$

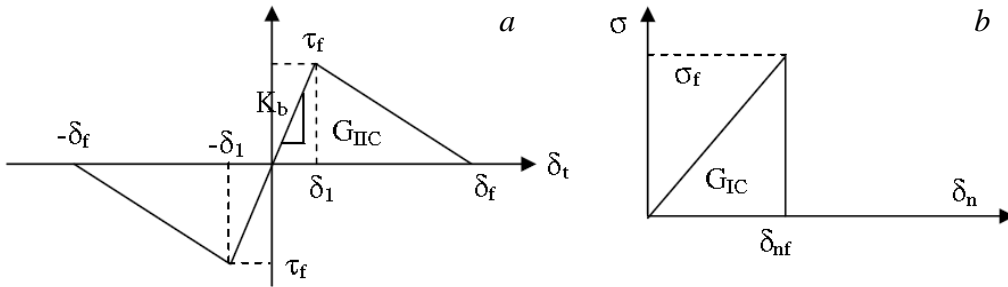


Fig.6.3. Traction-separation law used in this study: (a) Shear traction-separation law, (b) Normal traction-separation law.

From the point of view of CZM, such a nonlinear relationship given by Eq. (6.6) is a material property of the FRP-concrete interface. τ_f and δ_f are the shear strength and the separation slip of the interface, respectively; $K_b = \tau_f/\delta_1$ is the initial elastic stiffness of the FRP-concrete interface.

Very few studies have been conducted on characterizing the mode I traction-separation law of the FRP- concrete interface (Qiao and Xu, 2004; Dai et al., 2005). Existing modeling studies (Niu et al., 2006; Pan and Leung, 2007) used triangular model to approximate the open traction-separation law of the FRP-concrete interface. This model is also adopted in this study to simplify formulation (Fig. 6.3(b)). In Fig. 6.3(b), σ_f and δ_{nf} are the maximum normal stress and

open displacement of the FRP-concrete interface, respectively. Bond-slip law for normal stress simply reads,

$$\sigma_a = \begin{cases} 0 & \delta_n < -\delta_{nf} \\ \frac{\delta}{\delta_{nf}} \sigma_f & -\delta_{nf} \leq \delta_n < \delta_{nf} \\ 0 & \delta_{nf} \leq \delta_n \end{cases} \quad (6.7)$$

It should be pointed out that it is an open question on how the shear and open behaviors of the FRP-concrete interface couple due to very little experimental study has been carried out. For this reason, a mode-independent cohesive law is adopted in this study, which assumes the shear and opening traction-separation laws of the FRP-concrete interface are unrelated. Such an assumption was also used by Niu et al. (2006) in their finite element simulation.

The fracture energies of mode I and mode II of the interface, G_I and G_{II} , are given by the area below the traction-separation curves in Figs. 6.3(a) and (b):

$$G_I^f = \int_0^{\delta_{nf}} \sigma(\delta_n) d\delta_n, \quad G_{II}^f = \int_0^{\delta_{nf}} \tau(\delta_t) d\delta_t. \quad (6.8)$$

And the total fracture energy G_T of the interface reads:

$$G_T = G_I + G_{II}. \quad (6.9)$$

The mode mixity of the debonding can be described by the phase angle ψ , which is defined by:

$$\tan \psi = \sqrt{G_{II} / G_I}. \quad (6.10)$$

A simple linear debonding criterion (Hutchinson and Suo, 1992) is used in this study,

$$\frac{G_I}{G_{Ic}} + \frac{G_{II}}{G_{IIc}} = 1, \quad (6.11)$$

where G_{Ic} and G_{IIc} are the mode I and II fracture toughness of the interface, respectively, given by the area under the total traction-separation laws shown in Fig. 6.3. Full debonding occurs as soon as the fracture energies of mode I and II satisfy Eq. (6.11).

6.2.3 Spring model of flexural-shear crack

Displacement discontinuities in the axial and transverse directions at the bottom of the concrete beam, Δu and Δw shown in Fig. 6.4(a), can be induced by the opening and shearing of the flexural-shear crack. To capture the local flexibilities induced by the crack, a rotational and a transverse spring with infinitesimal thicknesses at the location of the flexural-shear crack is used, as shown in Fig. 6.4 (b). The rotational spring stiffness K_r , and transverse spring stiffness K_v , can be estimated by using linear elastic fracture mechanics approach (Paipetis and Dimarogonas, 1968). For the RC beam, however, it is difficult to obtain an explicit expression for these two stiffnesses. In such a case, a trial and error method proposed by Rabinovitch and Frostig (2001) is employed, which has been shown effective (Wang, 2006a,b). Then the local flexibilities read:

$$w'_1|_{x=0^-} - w'_1|_{x=0^+} = \frac{1}{K_r} M_1|_{x=0}, \quad (6.12a)$$

$$w_1|_{x=0^-} - w_1|_{x=0^+} = \frac{1}{K_v} Q_1|_{x=0}. \quad (6.12b)$$

Eq. (6.12b) represents the dowel effect created in the FRP plate across the base of the flexural-shear crack.

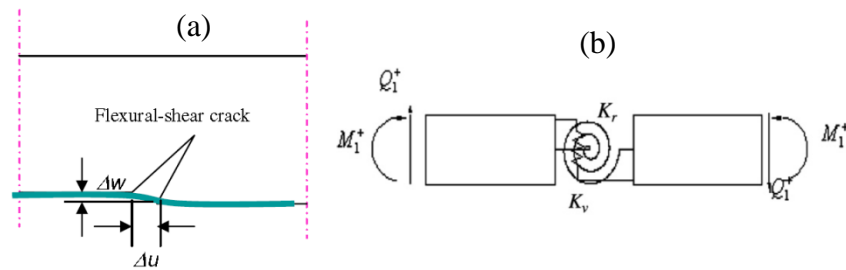


Fig.6.4. Spring model of the flexural-shear crack.

6.2.4 Analysis of the FRP-concrete interface debonding process

Under external loads, interfacial stresses are developed along the FRP-concrete interface. In Fig. 6.1(a), the whole FRP-concrete interface is divided into two portions by the flexural-shear crack. For the convenience of discussion, the portion of the interface to the left side of the crack is referred to as left interface and the other portion as right interface. Considering the traction-separation laws described in Eqs. (6.6) and (6.7), the debonding process of the beam can be described by the following different stages. (1) Elastic-Elastic (E-E) stage (Fig. 6.1(b)): due to the crack tip opening induced by the flexural-shear crack, there exist a finite slip and an opening between the FRP plate and the RC beam at the location of the crack. Stress concentrations are introduced at the vicinity of the crack. In this stage, both the maximum interfacial shear stress and normal stress are lower than their maximums and fracture energies do not satisfy Eq. (6.11). Therefore, both the left and right interfaces are in elastic stage. The interfacial shear stress distribution at this stage can be sketched as shown in Fig.6.1(b). (b) Elastic-Softening-Elastic (E-S-E) stage (Fig. 6.1(c)): if we increase the load, the maximum interfacial shear stress of the left interface (which is larger than the maximum shear stress of the right (Wang,2006b)) increases too and reaches shear strength τ_f while the maximum shear stress of the right interface is still below τ_f . (c) Elastic-Softening-Softening-Elastic (E-S-S-E) stage (Fig.6.1(d)): if load is increased further, part of the right interface also enters softening zone. Therefore, four zones exist along the interface, as shown in Fig. 6.1(d). (d) Elastic-Softening-Debonded-Softening-Elastic (E-S-D-S-E) stage (Fig. 6.1(e)): once Eq. (6.11) is satisfied due to the increasing of load, full debonding initiates and grows along the interface. Noting that the normal stress is tensile on the left interface and compressive on the right interface, full debonding only occurs on the left interface, as shown in Fig. 6.1(e). (e) Softening-Debonded-Softening-Elastic (S-D-S-E) stage (Fig. 6.1(f)):

once the debonding propagates near to the left end of the FRP plate, the interfacial slip of the whole left interface is greater than δ_l and thus no elastic zone exists on this side, as shown in Fig. 6.1(f). Due to the truncation of stress distribution at the plate end, the axial force transferred to the FRP plate through interface drops quickly in this stage with the development of debonding. As a result, the debonding propagates quickly and unstably in this stage until the FRP plate is fully separated from the RC beam. It should be pointed out that debonding only initiates and propagates along the left interface to the FRP plate end for the case shown in Fig. 6.1(a). This is because that the normal stress along the left interface is tensile which make considerable contribution to the debonding; while the normal stress along the right interface is compressive which makes no contribution to debonding. The one-side propagation of the debonding has been verified by many experimental studies (Garden et al., 1998; Rabinovitch and Frostig, 2003; Teng et al., 2003). The debonding stages outlined above may be not unique. For example, if the normal stress along the left side is very high due to the deflection jump caused by the flexural-shear crack (Fig. 6.4(a)), Eq. (6.11) can be satisfied even the maximum shear stress is still lower than τ_f . In such a case, an Elastic-Debonding stage of the left interface comes after the elastic stage. With the propagation of the debonding, the deflection jump can be accommodated more by the FRP plate and the contribution of the normal stress to the fracture energy reduces accordingly. In such a case, the shear stress and mode II fracture energy becomes the major driving force for the debonding. As a result, an Elastic-Softening-Debonding stage is formed after the Elastic-Debonding stage on the left interface.

To obtain the interface stresses and beam forces of the FRP-strengthened RC beam shown in Fig. 6.1(a), governing differential equations for three different zones are needed, i.e., elastic zone, softening zone, and fully debonded zone, as shown in Fig. 6.1. As demonstrated by

Wang (2007b), the governing equations for the elastic zone and softening zone can be derived as sixth order differential equations by using an approach similar to the 2PEF model of adhesively bonded joints (Wang, 2003). In this model, the normal and shear stresses are coupled, which complexes the solutions. To simplify the analysis, we adopt a widely used assumption which states that the FRP plate and concrete beam have the same curvature (Smith and Teng, 2001; Rasheed and Pervaiz, 2002), i.e.,

$$\frac{d^2 w_1}{dx^2} = \frac{d^2 w_2}{dx^2}. \quad (6.13)$$

By using the above assumption, the shear stress and normal stress can be decoupled (Wang, 2006a, b, 2007b). Consequently, we can derive the shear stresses first, based on which, the normal stress can then be obtained.

6.2.4.1 Shear stress along the interface

Elastic zone

By using the constitutive equation Eq. (6.1), equilibrium equation Eq. (6.2), interface compatibility Eq. (6.5), and bilinear law Eq. (6.6), the governing equation in this zone can be obtained as (Wang, 2006a, b),

$$\frac{d^2 \tau}{dx^2} = \frac{\tau_f}{\delta_1} \left(\frac{1}{C_1} + \frac{1}{C_2} + \frac{(Y_1 + Y_2)^2}{D_1 + D_2} \right) b \tau + \frac{\tau_f}{\delta_1} \frac{Y_1 + Y_2}{D_1 + D_2} \frac{dM_T}{dx}, \quad (6.14)$$

in which solution can be expressed as,

$$\tau = \Delta \tau + \tau_c, \quad (6.15)$$

where

$$\Delta \tau = \begin{cases} A_1 e^{-\lambda_1(x+a_1+d_1)} + B_1 e^{\lambda_1(x+a_1+d_1)} & x < -a_1 - d_1, \\ A_2 e^{-\lambda_1(x-a_2)} + B_2 e^{\lambda_1(x-a_2)} & x > a_2 \end{cases}, \quad (6.16a)$$

$$\tau_c = -C_\tau \frac{dM_T}{dx}, \quad (6.16b)$$

where

$$\lambda_1 = C_\lambda \sqrt{\frac{\tau_f}{\delta_1}}, \quad C_\lambda = \sqrt{b \left(\frac{1}{C_1} + \frac{1}{C_2} + \frac{(Y_1 + Y_2)^2}{D_1 + D_2} \right)}, \quad C_\tau = \frac{Y_1 + Y_2}{(D_1 + D_2) C_\lambda^2},$$

where a_1 and d_1 are the softening zone size and debonded zone size of the left interface, respectively. a_2 is the softening zone size of the right interface. $A_1, A_2, B_1,$ and B_2 are the coefficients to be determined by the boundary and continuity conditions presented later. Eq. (6.15) suggests that interfacial shear stress consists of two parts: (a) $\Delta\tau$ which is the stress concentration induced by the interfacial slip, and (b) τ_c which is the particular solution of Eq. (6.15) and essentially is the interfacial shear stress if the interfacial slip is neglected (i.e., FRP-concrete system is assumed as a fully composite beam).

Softening zone

In this zone, the governing equation becomes (Wang, 2006b),

$$\frac{d^2\tau}{dx^2} = \frac{-\tau_f}{\delta_f - \delta_1} \left(\frac{1}{C_1} + \frac{1}{C_2} + \frac{(Y_1 + Y_2)^2}{D_1 + D_2} \right) b\tau - \frac{\tau_f}{\delta_f - \delta_1} \frac{Y_1 + Y_2}{D_1 + D_2} \frac{dM_T}{dx}. \quad (6.17)$$

The solution of Eq. (6.17) can be expressed by Eq. (6.15) with the $\Delta\tau$ given by:

$$\Delta\tau = \begin{cases} C_1 \cos(\lambda_2(x + a_1 + d_1)) + D_1 \sin(\lambda_2(x + a_1 + d_1)), & x < -a_1 - d_1, \\ C_2 \cos(\lambda_2(x - a_2)) + D_2 \sin(\lambda_2(x - a_2)), & x > a_2, \end{cases} \quad (6.18)$$

where

$$\lambda_2^2 = \frac{\tau_f}{\delta_f - \delta_1} \left(\frac{1}{C_1} + \frac{1}{C_2} + \frac{(Y_1 + Y_2)^2}{D_1 + D_2} \right) = \frac{\delta_1}{\delta_f - \delta_1} \lambda_1^2. \quad (6.19)$$

Coefficients $C_1, D_1, C_2,$ and D_2 are to be determined by the boundary and continuity conditions given later.

Fully debonded zone

No contact between the FRP plate and RC beam, as shown in Fig. 6.5. Therefore, the shear stress within this zone is zero, i.e.,

$$\tau = 0. \quad (6.20)$$

Axial force of the FRP plate

The axial force of the FRP plate N_2 is given by,

$$N_2 = -\int_{-L_1}^x b_2 (\Delta\tau + \tau_c) dx = -\int_{-L_1-s_1}^x b_2 \tau_c dx + \int_{-L_1-s_1}^{-L_1} b_2 \tau_c dx - \int_{-L_1}^x b_2 \Delta\tau dx = N_{2c} + \Delta N_2, \quad (6.21a)$$

where

$$N_{2c} = \int_{-L_1-s_1}^x b_2 C_\tau \frac{dM_T}{dx} dx = b_2 C_\tau M_T, \quad (6.21b)$$

$$\Delta N_2 = -\int_{-L_1}^x b_2 \Delta\tau dx - b_2 C_\tau M_T \Big|_{x=-L_1}. \quad (6.21c)$$

Obviously, N_{2c} is the composite beam part of the axial force of the FRP plate and can also be obtained by treating FRP-concrete system as a fully composite beam. ΔN_2 is the part of the FRP axial forces induced by the bond slip and can be easily obtained by substituting shear stress solution into Eq. (6.21c). For the sake of brevity, the detailed expression of ΔN_2 is not presented here.

Boundary and continuity conditions

Assuming that the bond-length is sufficient large, the B_1 term and A_2 term in Eq. (6.16a) can be neglected (Wang and Qiao, 2004). At the joint of the elastic and softening zone, continuity conditions read,

$$\tau \Big|_{x=(-a_1-d_1)^-} = -\tau_f, \quad \tau \Big|_{x=(-a_1-d_1)^+} = -\tau_f, \quad \frac{d\tau}{dx} \Big|_{x=(-a_1-d_1)^+} = -\frac{\delta_1}{\delta_f - \delta_1} \frac{d\tau}{dx} \Big|_{x=(-a_1-d_1)^-}, \quad N_2 \Big|_{x=(-a_1-d_1)^-} = N_2 \Big|_{x=(-a_1-d_1)^+}, \quad (6.22a)$$

$$\tau|_{x=(a_2)^+} = \tau_f, \tau|_{x=(a_2)^-} = \tau_f, \frac{d\tau}{dx}|_{x=(a_2)^-} = -\frac{\delta_1}{\delta_f - \delta_1} \frac{d\tau}{dx}|_{x=(a_2)^+}, N_2|_{x=(a_2)^-} = N_2|_{x=(a_2)^+}. \quad (6.22b)$$

At the joint of softening zone and fully debonded zone, we have:

$$N_2|_{x=(-d_1)^-} = N_2|_{x=(-d_1)^+}. \quad (6.22c)$$

At the location of the flexural-shear crack, displacement continuity conditions require:

$$u_1|_{x=0^-} = u_1|_{x=0^+}, u_2|_{x=0^-} = u_2|_{x=0^+}, \frac{dw_2}{dx}|_{x=0^-} = \frac{dw_2}{dx}|_{x=0^+}. \quad (6.23a)$$

Therefore,

$$\delta|_{x=0^+} - \delta|_{x=0^-} = -Y_1 \left(\frac{dw_1}{dx}|_{x=0^+} - \frac{dw_1}{dx}|_{x=0^-} \right) = \frac{Y_1}{K_r} M_1|_{x=0}. \quad (6.23b)$$

The axial force of the FRP plate is also continuous at this location, i.e.,

$$N_2|_{x=0^-} = N_2|_{x=0^+}. \quad (6.23c)$$

Combining Eqs. (6.11) and (6.12b), the above boundary and continuity conditions can determine all the coefficients and a_1 , a_2 , and δ_1 . The above solutions describe the E-S-D-S-E stage of the debonding (Fig. 6.1(e)). For the other stages shown in Fig.6.1, we only need to solve for the existing zones on the interface. For example, for the E-E stage, we only need to consider Eq. (6.16) and continuity condition at the location of crack Eq. (6.23). The detailed analysis of each stage is not given here for the sake of brevity. More detailed information can be obtained from Wang (2006b).

6.2.4.2 Normal stress along the interface

Elastic and softening zone

As illustrated by Wang (2007b), the governing equation of the normal stress in both elastic and softening zones can be given by,

$$\frac{d^4\sigma}{dx^4} + K_n b_2 \left(\frac{1}{D_1} + \frac{1}{D_2} \right) \sigma = K_n b_2 \left(\frac{Y_1}{D_1} - \frac{Y_2}{D_2} \right) \frac{d\tau}{dx}. \quad (6.24)$$

The interfacial normal stress is then obtained as:

$$\sigma = e^{-\beta x} (E_{li} \cos(\beta x) + F_{li} \sin(\beta x)) + e^{\beta x} (G_{li} \cos(\beta x) + H_{li} \sin(\beta x)) + \sigma^* + \sigma_c, \quad (6.25)$$

where

$$\beta = \sqrt[4]{\frac{bK_n}{4} \left(\frac{1}{D_1} + \frac{1}{D_2} \right)}, \quad \sigma_c = \frac{bK_n}{4\beta^4} \left(\frac{Y_1}{D_1} - \frac{Y_2}{D_2} \right) C_\tau \frac{d^2 M_T}{dx^2}. \quad (6.26)$$

where σ^* is the particular solution of Eq. (6.24) corresponding to the term of τ and has different expressions at different zones.

$$\sigma^* = \frac{bK_n}{\beta^4 + \lambda_1^4} \left(\frac{Y_1}{D_1} - \frac{Y_2}{D_2} \right) \frac{d\Delta\tau}{dx}, \quad (\text{Elastic zone}). \quad (6.27)$$

$$\sigma^* = \frac{bK_n}{\beta^4 + \lambda_2^4} \left(\frac{Y_1}{D_1} - \frac{Y_2}{D_2} \right) \frac{d\Delta\tau}{dx}, \quad (\text{Softening zone}). \quad (6.28)$$

Coefficients E_{li} , G_{li} , F_{li} , and H_{li} for zone i in Eq. (6.25) are determined by the boundary and continuity conditions.

Debonded zone

In the debonded zone, the normal stress along the interface is zero. In order to obtain the continuity conditions needed to determine coefficients in the normal stress given by Eq. (6.25), the displacements of the FRP plate and RC beam in the debonded zone are needed. As shown in Fig. 6.5, the deflection of the RC beam can be written as:

$$-D_1 \frac{d^2 w_1}{dx^2} = M_1 \Big|_{x=-d_1} + Q_1 \Big|_{x=-d_1} (x + d_1). \quad (6.29)$$

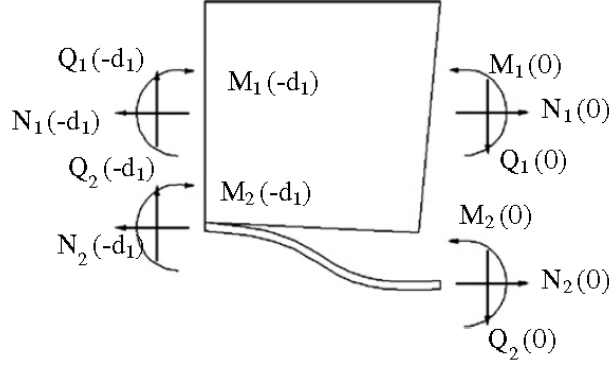


Fig.6.5. Free body diagram of the debonded zone.

Integrating both sides of Eq. (6.29) twice from $-d_1$ to x , the deflection of the concrete beam can be obtained as,

$$w_1 = -\frac{M_1|_{x=-d_1}}{D_1} \frac{(x+d_1)^2}{2} - \frac{Q_1|_{x=-d_1}}{D_1} \frac{(x+d_1)^3}{6} + w_1|_{x=-d_1} + w_1'|_{x=-d_1} (x+d_1). \quad (6.30)$$

Noting that the FRP plate is very thin, the geometrical nonlinearity should be taken into consideration in deriving its deflection. As shown in Fig. 6.5, the governing equation for the FRP plate reads:

$$-D_2 \frac{d^2 w_2}{dx^2} = M_2|_{x=-d_1} + Q_2|_{x=-d_1} (x+d_1) - N_2|_{x=-d_1} (w_2 - w_2|_{x=-d_1}). \quad (6.31)$$

Then the deflection of FRP plate can be solved as,

$$w_2 = c_1 \exp\left(\sqrt{\frac{N_2|_{x=-d_1}}{D_2}} x\right) + c_2 \exp\left(-\sqrt{\frac{N_2|_{x=-d_1}}{D_2}} x\right) + \left(\frac{M_2|_{x=-d_1} + Q_2|_{x=-d_1} (x+d_1)}{N_2|_{x=-d_1}} + w_2|_{x=-d_1}\right). \quad (6.32)$$

where

$$M_1|_{x=-d_1} = \frac{D_1}{D_1 + D_2} (M_T|_{x=-d_1} - (Y_1 + Y_2) N_2|_{x=-d_1}), \quad M_2|_{x=-d_1} = \frac{D_2}{D_1 + D_2} (M_T|_{x=-d_1} - (Y_1 + Y_2) N_2|_{x=-d_1}),$$

$$Q_1|_{x=-d_1} = \frac{D_1}{D_1 + D_2} \left(\frac{dM_T}{dx} \Big|_{x=-d_1} + b(Y_1 + Y_2) \tau|_{x=-d_1} \right) - Y_1 b \tau|_{x=-d_1}.$$

Boundary and continuity conditions

At the joint of elastic and softening zone at $x = -a_1 - d_1$,

$$\sigma \Big|_{x=(-a_1-d_1)^-} - \sigma \Big|_{x=(-a_1-d_1)^+} = K_n (w_2 - w_1) \Big|_{x=(-a_1-d_1)^-} - K_n (w_2 - w_1) \Big|_{x=(-a_1-d_1)^+} = 0, \quad (6.33)$$

$$\frac{d\sigma}{dx} \Big|_{x=(-a_1-d_1)^-} - \frac{d\sigma}{dx} \Big|_{x=(-a_1-d_1)^+} = K_n \left(\frac{dw_2}{dx} - \frac{dw_1}{dx} \right) \Big|_{x=(-a_1-d_1)^-} - K_n \left(\frac{dw_2}{dx} - \frac{dw_1}{dx} \right) \Big|_{x=(-a_1-d_1)^+} = 0, \quad (6.34)$$

$$\begin{aligned} \frac{d^2\sigma}{dx^2} \Big|_{x=(-a_1-d_1)^-} - \frac{d^2\sigma}{dx^2} \Big|_{x=(-a_1-d_1)^+} &= K_n \left(\frac{d^2w_2}{dx^2} - \frac{d^2w_1}{dx^2} \right) \Big|_{x=(-a_1-d_1)^-} - K_n \left(\frac{d^2w_2}{dx^2} - \frac{d^2w_1}{dx^2} \right) \Big|_{x=(-a_1-d_1)^+} \\ &= K_n \left(-\frac{M_2}{D_2} + \frac{M_1}{D_1} \right) \Big|_{x=(-a_1-d_1)^-} - K_n \left(-\frac{M_2}{D_2} + \frac{M_1}{D_1} \right) \Big|_{x=(-a_1-d_1)^+} = 0, \end{aligned} \quad (6.35)$$

$$\begin{aligned} \frac{d^3\sigma}{dx^3} \Big|_{x=(-a_1-d_1)^-} - \frac{d^3\sigma}{dx^3} \Big|_{x=(-a_1-d_1)^+} &= K_n \left(-\frac{1}{D_2} \frac{dM_2}{dx} + \frac{1}{D_1} \frac{dM_1}{dx} \right) \Big|_{x=(-a_1-d_1)^-} - K_n \left(-\frac{1}{D_2} \frac{dM_2}{dx} + \frac{1}{D_1} \frac{dM_1}{dx} \right) \Big|_{x=(-a_1-d_1)^+} \\ &= K_n \left(-\frac{Q_2 + Y_2 b \tau}{D_2} + \frac{Q_1 + Y_1 b \tau}{D_1} \right) \Big|_{x=(-a_1-d_1)^-} - K_n \left(-\frac{Q_2 + Y_2 b \tau}{D_2} + \frac{Q_1 + Y_1 b \tau}{D_1} \right) \Big|_{x=(-a_1-d_1)^+} = 0. \end{aligned} \quad (6.36)$$

Similarly, at $x = a_2$,

$$\sigma \Big|_{x=(a_2)^-} - \sigma \Big|_{x=(a_2)^+} = 0, \quad (6.37)$$

$$\frac{d\sigma}{dx} \Big|_{x=(a_2)^-} - \frac{d\sigma}{dx} \Big|_{x=(a_2)^+} = 0, \quad (6.38)$$

$$\frac{d^2\sigma}{dx^2} \Big|_{x=(a_2)^-} - \frac{d^2\sigma}{dx^2} \Big|_{x=(a_2)^+} = 0, \quad (6.39)$$

$$\frac{d^3\sigma}{dx^3} \Big|_{x=(a_2)^-} - \frac{d^3\sigma}{dx^3} \Big|_{x=(a_2)^+} = 0. \quad (6.40)$$

At the joint of softening zone and debonded zone $x = -d_1$, continuity conditions read,

$$(w_2 - w_1) \Big|_{x=(-d_1)^+} = (w_2 - w_1) \Big|_{x=(-d_1)^-} = \frac{\sigma \Big|_{x=(-d_1)^-}}{K_n}, \quad (6.41)$$

$$\left(\frac{dw_2}{dx} - \frac{dw_1}{dx} \right) \Big|_{x=(-d1)^+} = \left(\frac{dw_2}{dx} - \frac{dw_1}{dx} \right) \Big|_{x=(-d1)^-} = \frac{1}{K_n} \frac{d\sigma}{dx} \Big|_{x=(-d1)^-}, \quad (6.42)$$

$$\left(\frac{d^2w_2}{dx^2} - \frac{d^2w_1}{dx^2} \right) \Big|_{x=(-d1)^+} = \left(\frac{d^2w_2}{dx^2} - \frac{d^2w_1}{dx^2} \right) \Big|_{x=(-d1)^-} = \frac{1}{K_n} \frac{d^2\sigma}{dx^2} \Big|_{x=(-d1)^-}, \quad (6.43)$$

$$\left(\frac{d^3w_2}{dx^3} - \frac{d^3w_1}{dx^3} \right) \Big|_{x=(-d1)^+} - b \left(\frac{Y_2}{D_2} - \frac{Y_1}{D_1} \right) \tau \Big|_{x=(-d1)^-} = \frac{1}{K_n} \frac{d^3\sigma}{dx^3} \Big|_{x=(-d1)^-}. \quad (6.44)$$

At the location of the crack,

$$(w_2 - w_1) \Big|_{x=0^-} = (w_2 - w_1) \Big|_{x=0^+} + (w_1 \Big|_{x=0^+} - w_1 \Big|_{x=0^-}) = -\frac{Q_1 \Big|_{x=0}}{K_v} + \frac{\sigma \Big|_{x=0^+}}{K_n}, \quad (6.45)$$

$$\left(\frac{dw_2}{dx} - \frac{dw_1}{dx} \right) \Big|_{x=0^-} = \left(\frac{dw_2}{dx} - \frac{dw_1}{dx} \right) \Big|_{x=0^+} + \left(\frac{dw_1}{dx} \Big|_{x=0^+} - \frac{dw_1}{dx} \Big|_{x=0^-} \right) = -\frac{M_1 \Big|_{x=0}}{K_v} + \frac{1}{K_n} \frac{d\sigma}{dx} \Big|_{x=0^+}, \quad (6.46)$$

$$\left(\frac{d^2w_2}{dx^2} - \frac{d^2w_1}{dx^2} \right) \Big|_{x=0^-} = \left(\frac{d^2w_2}{dx^2} - \frac{d^2w_1}{dx^2} \right) \Big|_{x=0^+} - \left(\frac{M_1(x)}{D_1} - \frac{M_2(x)}{D_2} \right) \Big|_{x=0^+} + \left(\frac{M_1(x)}{D_1} - \frac{M_2(x)}{D_2} \right) \Big|_{x=0^-} = \frac{1}{K_n} \frac{d^2\sigma}{dx^2} \Big|_{x=0^+}, \quad (6.47)$$

$$\begin{aligned} \left(\frac{d^3w_2}{dx^3} - \frac{d^3w_1}{dx^3} \right) \Big|_{x=0^-} &= \left(\frac{d^3w_2}{dx^3} - \frac{d^3w_1}{dx^3} \right) \Big|_{x=0^+} - \left(-\frac{Q_2 + Y_2 b \tau}{D_2} + \frac{Q_1 + Y_1 b \tau}{D_1} \right) \Big|_{x=0^+} + \left(-\frac{Q_2}{D_2} + \frac{Q_1}{D_1} \right) \Big|_{x=0^-} \\ &= \frac{1}{K_n} \frac{d^2\sigma}{dx^2} \Big|_{x=0^+} - b \left(\frac{Y_1}{D_1} - \frac{Y_2}{D_2} \right) \tau \Big|_{x=0^+}. \end{aligned} \quad (6.48)$$

Assuming the FRP plate bond length is long enough, E_{li} and F_{li} of the left elastic zone and G_{li} and H_{li} of the right elastic zone can be chosen as zero. The rest coefficients can be determined by the continuity conditions Eqs. (6.37)-(6.48) and Eq. (6.11) for the E-S-D-S-E stage. For other stages, proper zones shown in Fig. 6.1 and the continuity conditions given above should be chosen accordingly.

6.3 Numerical verifications

To demonstrate the validity of the closed-form solution proposed in this chapter, finite element simulation is conducted for a simply supported beam under three point bending load P shown in Fig. 6.6. As shown in this figure, a flexural-shear crack exists to the left of the mid-span. The height of concrete beam h_1 is 150 mm; width b_1 is 100 mm; and the Young's modulus E_1 is 25 GPa. The FRP plate is bonded to the lower surface of the concrete beam, whose height h_2 is 0.11 mm, width b_2 is 100 mm, and Young's modulus E_2 is 230 GPa. The span of the beam is 1500 mm and the distance from the end of the plate to the end of the beam is 25 mm. The crack size and location are shown in Fig. 6.6. The parameters of the bi-linear shear stress-slip model are chosen as $K_b = 160 \text{ N/mm}^2$, $G_{If} = 0.5 \text{ N/mm}$, $\tau_f = 1.8 \text{ MPa}$. The parameters of the normal stress-separation law are chosen as: $K_t = 500 \text{ N/mm}^2$, $G_{If} = 0.1 \text{ N/mm}$.

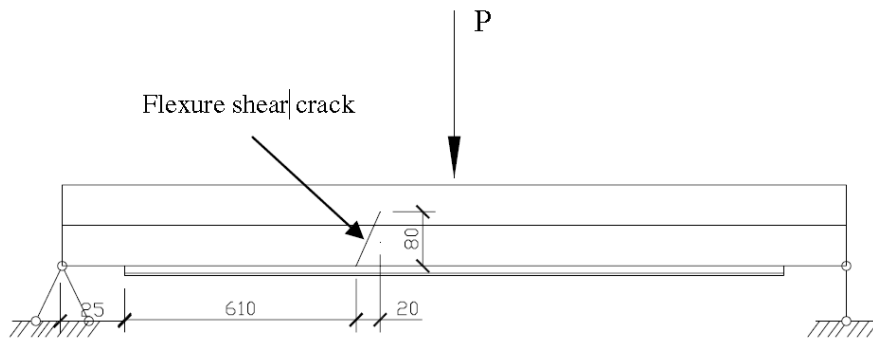


Fig.6.6. Simply supported FRP-strengthened RC beam with a flexural-shear crack.

Commercial finite element software ANSYS is employed to verify the accuracy of the prediction of these models. Eight nodes quadrilateral high order two-dimensional plane strain elements PLANE82 are used to mesh the structure, as shown in Fig. 6.7. This element provides more accurate results than mixed automatic meshes and tolerates irregular shapes without loss of too much accuracy. It has compatible displacement interpolation function and good curved boundary fitting ability. This capacity enables us to mesh the model more adaptable and obtain

more accurate results. As shown in Fig. 6.7, the vicinity of the flexural-shear crack is finely meshed. Nonlinear spring element COMBIN39 is used to model the traction-separation behavior of the interface in both the transverse and axial directions, as illustrated in Fig.6. 7.

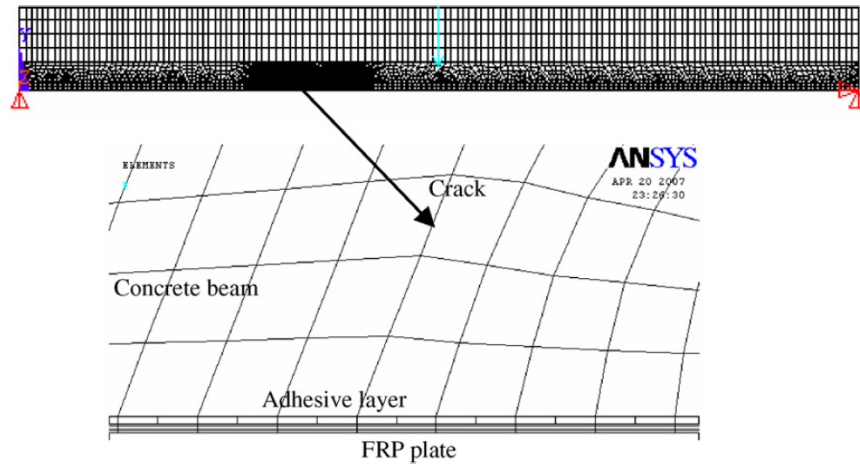


Fig.6.7. FEA model for the FRP-strengthened RC beam with a flexure-shear crack.

During the simulation, the concentrated load P is increased steadily so that the stress distributions along the interface of different stages can be obtained. Fig. 6.8 shows that good agreement with finite element analysis has been achieved by the present closed-form solutions for both the shear and normal stresses, especially on the left interface. The closed-form solutions deviate from the FEA results slightly on the right interface. This is caused by the approximation of the beam model itself. In the vicinity of the left side of the flexural-shear crack, the concrete beam has a wedge shape which can be captured exactly in finite element model. While in the closed-form analytical solution, this wedge shape is ignored and modeled as a rectangular beam. This deviation is not critical to the debonding simulation because debonding only occurs along the left interface.

Different debonding stages can be easily identified from Fig. 6.8. Line 1 of Fig. 6.8(a) and (b) presents the interfacial shear and normal stress distributions along the FRP-concrete interface when $P = 1.0$ kN, respectively. In this case, both the left and right interfaces are in

elastic stage, and the whole interface is in E-E stage. It can be observed that the normal stress is negative (compressive) along the right interface, while positive (tensile) along the left interface. The compressive normal stress does not contribute to the interface debonding. Therefore, the left interface is under mixed-mode loading; while the right interface is under pure mode II loading. Considering that the debonding is most difficult to occur under mode II loading, the flexural-shear crack induced debonding can only occur along the left interface for the case studied here.

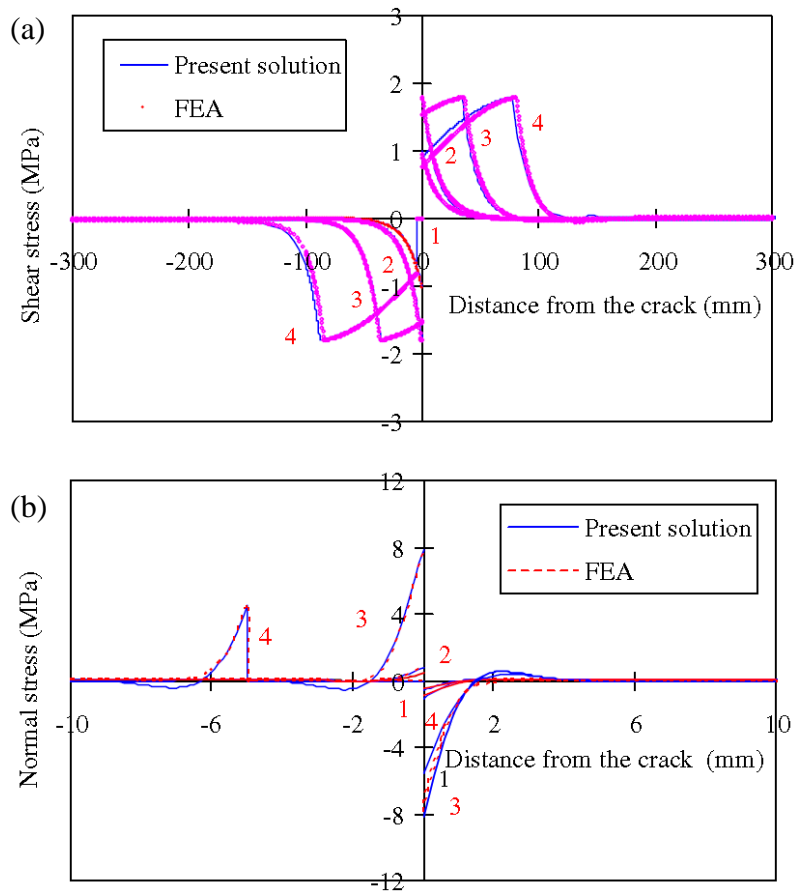


Fig. 6.8. Interface stress distributions at different debonding stages: (a) interfacial shear stress, (b) interfacial normal stress.

If P is increased to a certain range, the maximum of the shear stress is higher than the shear strength. In this case, the left interface enters Elastic-Softening stage (Wang, 2006b) while the right interface is still in the elastic stage. As demonstrated by Line 2 in Fig. 6.8, the whole interface enters E-S-E stage when $P = 1.95$ kN. If the applied load is $P = 9.0$ kN, both the left

and right interfaces enter Elastic-Softening stage as shown by the line 3 in Fig. 6.8. In this case, significant softening zones are developed along both the left and right interfaces, and the whole interface is in E-S-S-E stage. With the increase of load P , the energy release rate of the left interface increases too. Once Eq. (6.11) is satisfied, full debonding initiates and grows along the left interface, as demonstrated by line 4 in Fig. 6.8. In this case, the applied load $P = 24.4$ kN. A fully debonded zone of 5 mm is formed along the left interface. Unlike in the flexural IC debonding, the shear stress at the debonding tip is not zero as shown Fig. 6.8(a) because of the peeling effect induced by the transverse displacement at the location of the crack. It is interesting to see that the maximum normal stress in this stage is less than that in E-S-S-E stage, even though the applied load is much higher. This suggests that the right interface undergoes unloading after full debonding initiates. This is not surprising because more transverse displacement jump induced by the flexural-shear crack can be accommodated by longer debonded FRP plate. Fig. 6.8(a) also shows that the softening zone size on the right interface still increases after debonding initiating on the right interface. This is different from the flexural crack induced debonding, in which the right interface actually experiences unloading after debonding occurs along the left interface (Wang, 2006b). This is because the debonding along the left interface is in mixed-mode, not in mode II in the case of flexural crack induced debonding. Due to the contribution of peeling loading, debonding initiates along the left interface even though the maximum load transferring capacity of the interface has not been reached.

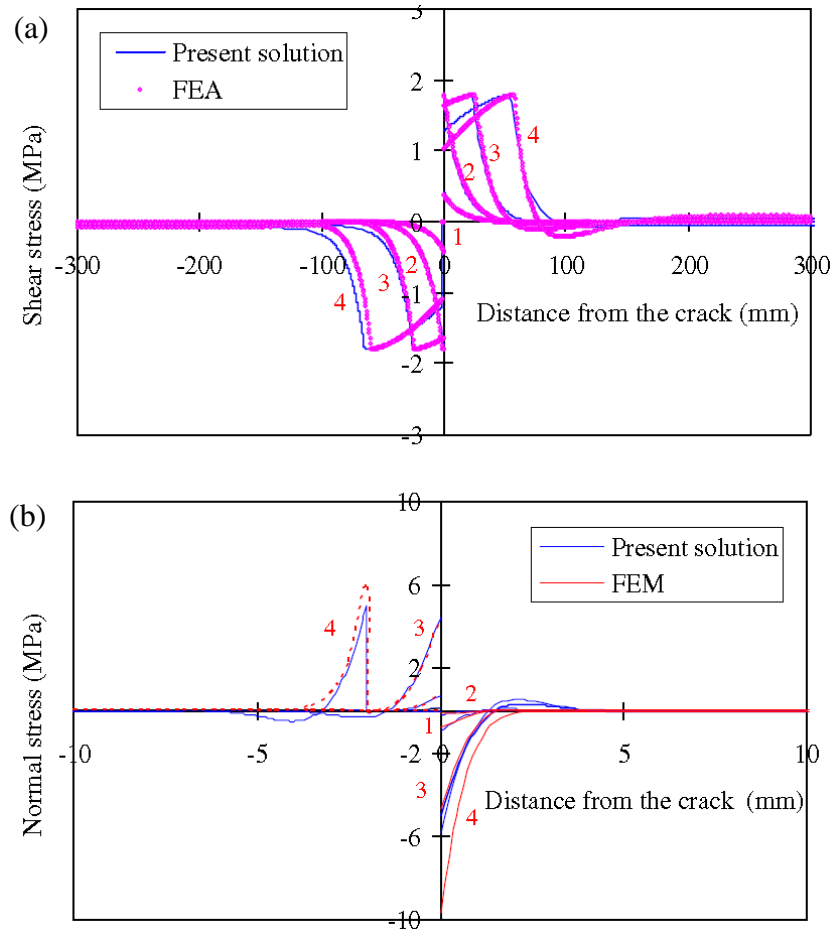
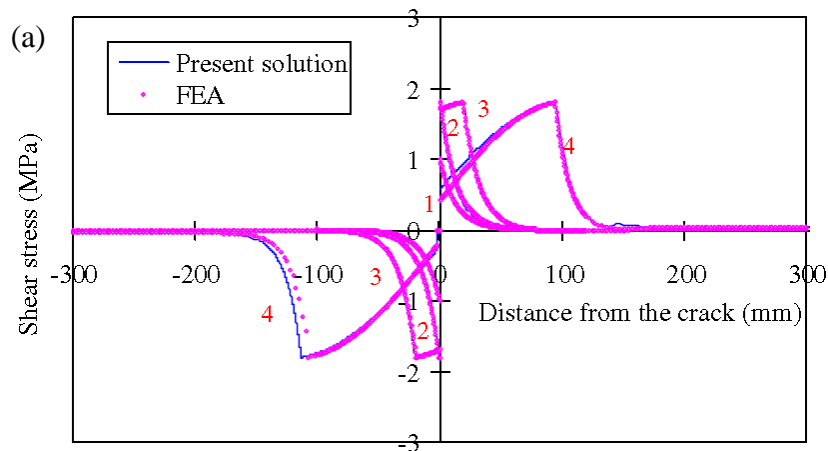


Fig. 6.9. Stress distributions at different debonding stages for small crack length: (a) interfacial shear stress, (b) interfacial normal stress

The accuracy of the current analytical models for flexural-shear cracks with different sizes and orientations are examined in Figs. 6.9 and 6.10. In Fig. 6.9, the crack size under examined is 1/4 of the one shown in Fig. 6.7 with all the other geometries the same as those used in Fig. 6.8. Fig. 6.9 shows that fairly good agreements between the present solutions and the FEA results are reached for both the shear and normal interface stresses. Similar to Fig. 6.8, four different debonding stages are presented in Fig. 6.9. Due to the much smaller crack size, the applied load P needs to be much higher to initiate and drive the interface debonding in this case. For example, $P = 4.7$ kN when the interface enters E-S-E stage and $P = 61$ KN when a 2 mm fully debonded zone is formed on the left interface. In Fig. 6.10, the crack under considered is

perpendicular to the axis of the concrete beam (i.e., flexural crack) with all other geometries the same as shown in Fig. 6.8. Once again, very good agreements with FEA results have been achieved by the present analytical solutions for both interface stresses. Four different debonding stages are presented in this figure. It can be found the both the shear and normal stresses near the debonding tip are very low compared with their counterparts of the flexural-shear cracks (Figs. 6.8 and 6.9). This suggests that the flexural crack induced debonding is mainly mode II controlled fracture process. It should be pointed out the Fig. 6.10 is slightly different from the solutions of flexural-crack induced debonding (Wang, 2006b) because the doweling effect of the FRP plate is considered in the present model (Eq. (6.12b)). Wang (2006b) established a CZM for flexural crack induced debonding in which the dowel effect of the FRP plate was ignored to simplify the analysis. Fig. 6.10 shows that such a simplification is reasonable. The above numerical results confirm that the present closed-form solution can be used with confidence to simulate flexural-crack induced debonding.



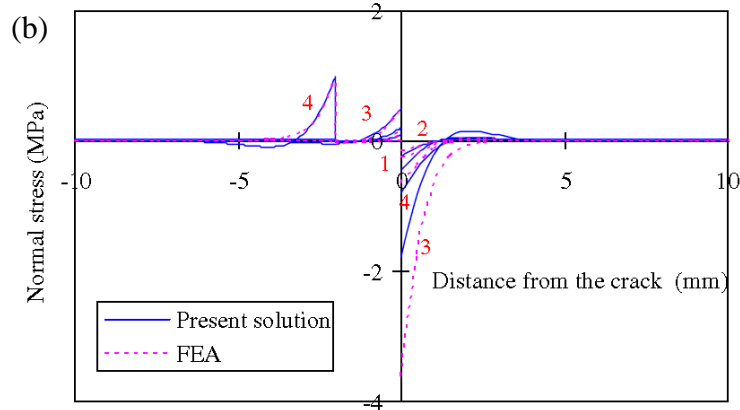


Fig.6.10. Stress distributions at different debonding stages for a flexural crack: (a) interfacial shear stress; (b) interfacial normal stress.

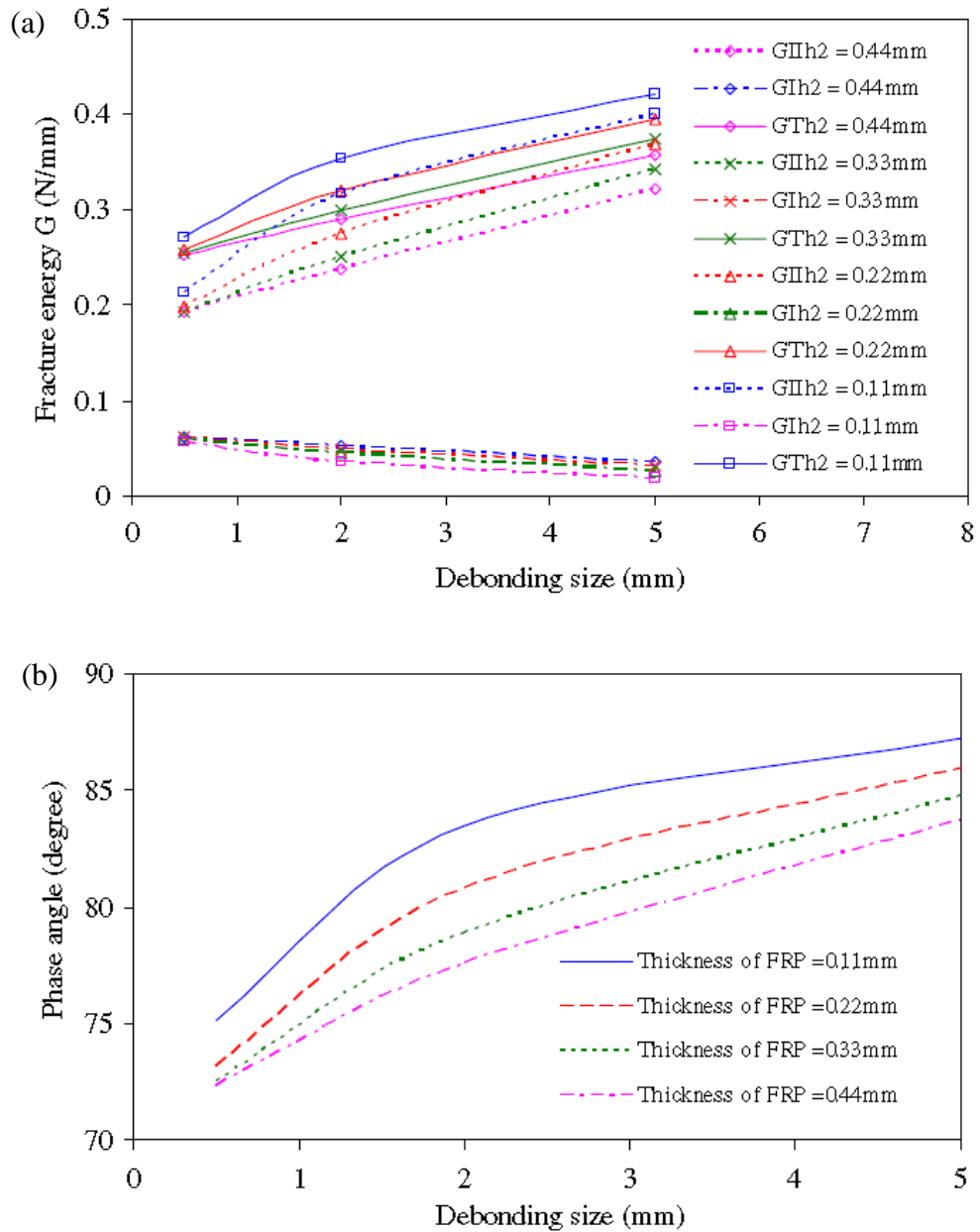
6.4 Parameter study and discussion

To shed more light on the flexural-shear crack induced debonding, parametric studies are conducted in this section. In the following calculations, all the data are the same as in the first case of the above section if not specified. The debonding features varying with the growth of the fully debonded zone size d_I is shown in Fig. 6.11. As shown in Fig. 6.11(a), the total fracture energy and its mode II component increase with d_I ; while the mode I fracture energy decreases with d_I . As a result, the phase angle of the debonding also varies with d_I , increasing from a smaller phase angle and approaching 90° (mode II) (Fig. 6.11(b)). This suggests that the peeling effect induced by the crack is more significant when the debonding zone size is small. However, this effect decreases with the propagation of debonding and becomes negligible when d_I is big enough. In that case, flexural-shear crack induced debonding can be treated approximately as pure mode II debonding. This phenomenon verifies the argument made by Teng et al. (2003). The trend of phase angle shown in Fig. 6.11(b) is in agreement with the experimental observations (Pan and Leung, 2007). Consequently, the maximum axial stress of the FRP plate increases with d_I as illustrated by Fig. 6.11(c). The upper limit of the maximum axial FRP stress should be given by pure mode II loading because debonding is most difficult to occur under

mode II loading. Fig. 6.11(c) shows that the applied load P needed to drive the debonding (refers to as debonding driving load thereafter) increases with debonding size d_I for the considered thickness of the FRP plate. This suggests that the debonding propagation is stable, which is a desirable feature for practical applications. It should be pointed out the above conclusions are based on the assumption that the flexural-shear crack does not grow within the RC beam. If the crack grows to larger size, the debonding driving force decreases, which can lead to the unstable propagation of the debonding. Fig. 6.11(c) also shows that the slope of the P - d_I curves decreases with the thickness of the FRP plate. It is possible that this slope becomes negative if the FRP plate is thick enough (Wang, 2006b). In such a case, the debonding is unstable. It is surprising to find that higher driving force is needed for thinner FRP plate when the debonding size is big enough as shown in Fig. 6.11(c). In other words, increasing the thickness of the FRP plate does not increase the debonding load P , which is contradictory to our intuition. This is because we assume the flexural-shear crack does not grow within the concrete beam. As shown in Fig. 6.11(d), smaller force is transferred to the thinner FRP plate. As a result, the bending moment applied to the concrete beam is higher and the chance for the crack to grow in the RC beam for thinner FRP plate is higher. Once crack grows in the concrete beam, debonding driving force P can be reduced significantly.

Fig. 6.12 examines the effect of the stiffness of the FRP plate on the FRP-concrete interface debonding. Different stiffness of the FRP plate is modeled by varying the thickness of the FRP plate. Fig. 6.12(a) shows that the total fracture energy and its mode II component decrease with the thickness of the FRP plate; while the mode I fracture energy increases. This is caused by the higher peeling interfacial stress induced by the stiffer FRP plate. With increasing mode I component in debonding, the mode II component of the fracture energy reduces

accordingly. As a result, the load efficiency of the FRP plate reduces as well, as demonstrated by Fig. 6.12(b), which shows that the maximum stress of the FRP plate decreases with the FRP thickness (Fig. 6.12(b)). Fig. 6.12(c) shows that the debonding driving force P increases when $d_l = 0.5$ mm, and decreases slightly when $d_l = 5$ mm with the FRP stiffness.



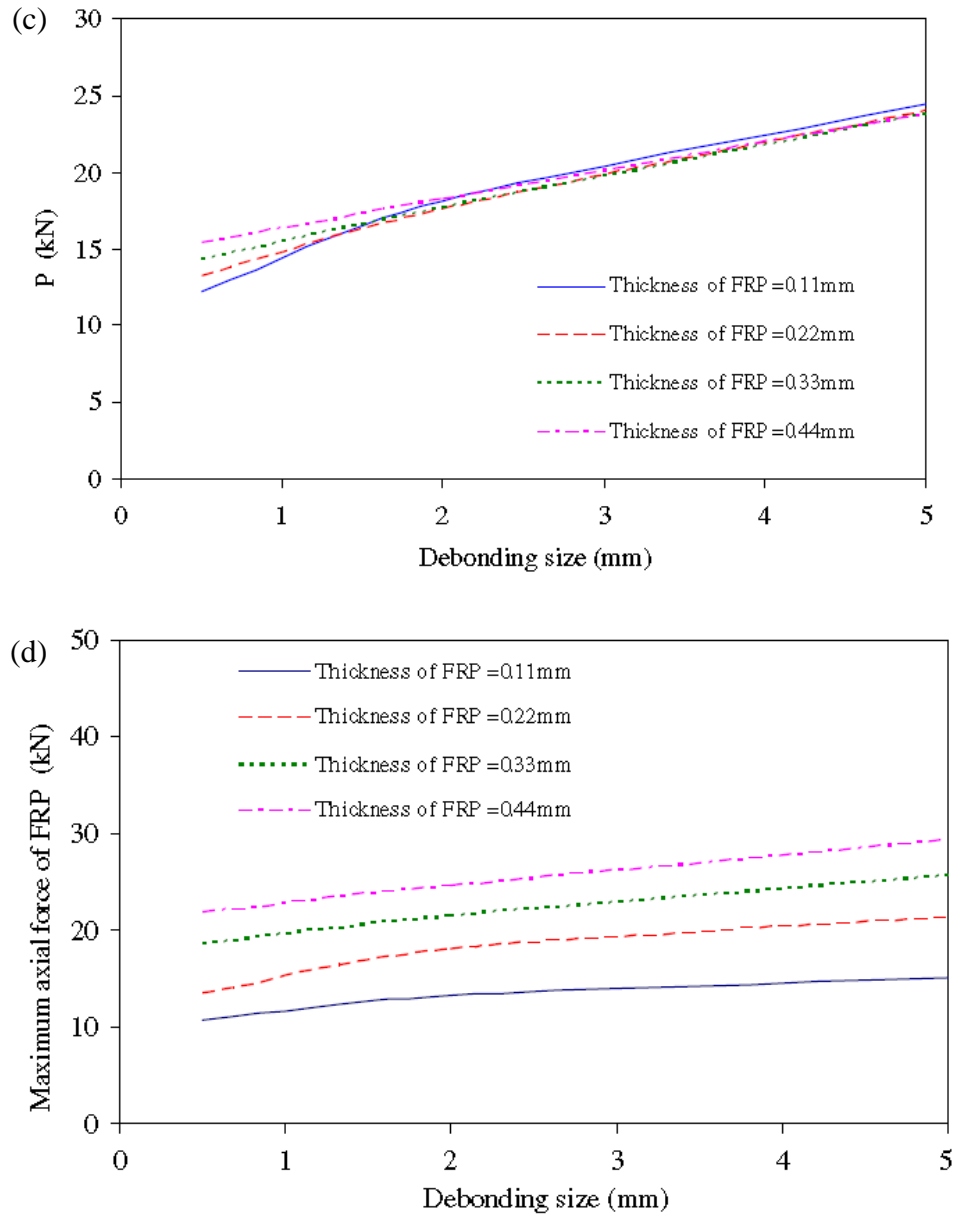


Fig. 6.11. Debonding propagation characteristics: (a) fracture energy; (b) mode mixity; (c) debonding driving force; (d) maximum axial force of the FRP plate.

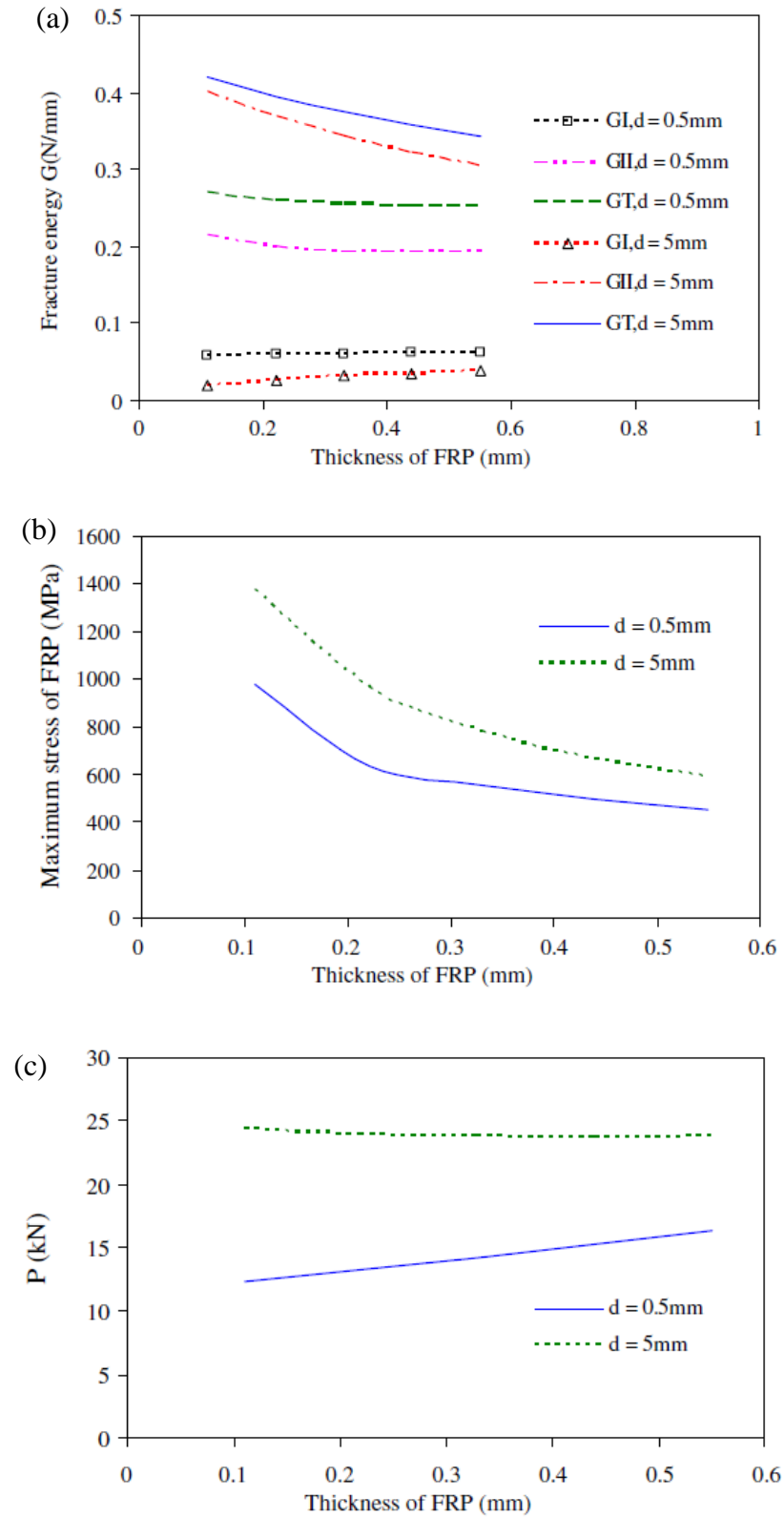
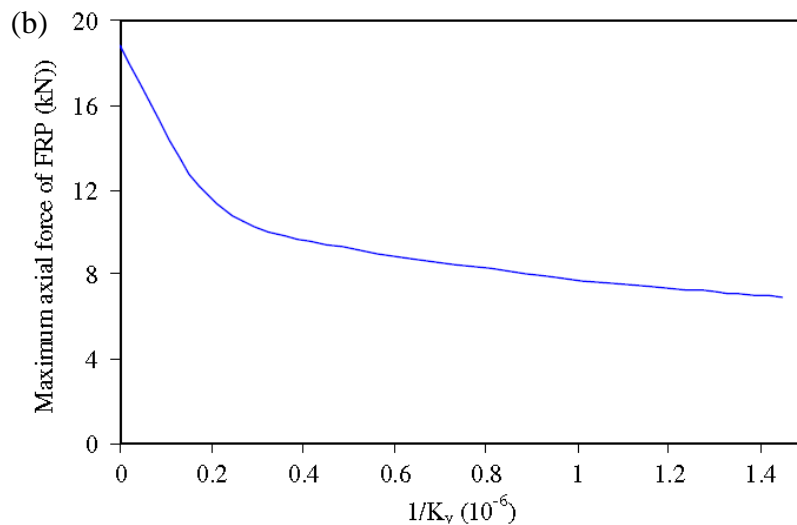
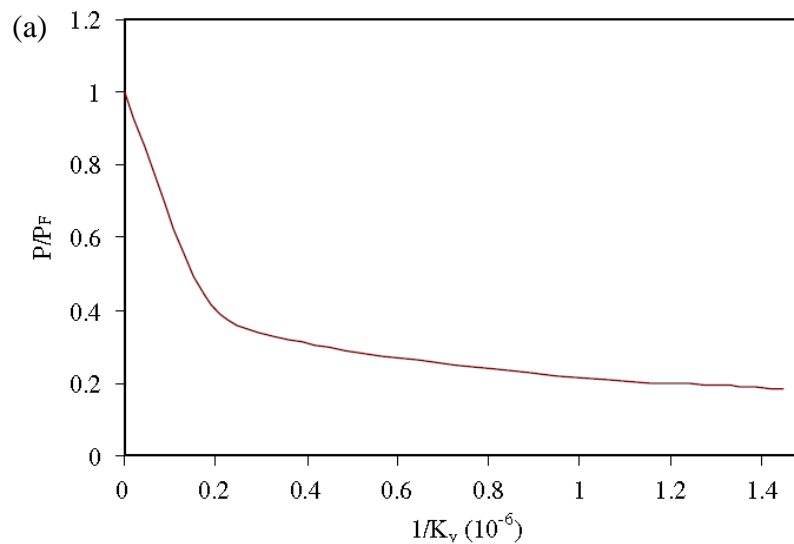


Fig.6.12. Effect of the FRP thickness on debonding: (a) fracture energy; (b) maximum stress of the FRP plate; (c) debonding driving force.

The effects the angle (with respect to the axis of the concrete beam) of the flexural-shear crack on the FRP-concrete interface debonding are examined in Fig. 6.13. In this figure, the height of the crack is fixed to be 80 mm and the width of it changes to simulate different angles (Fig. 6.6). Fig. 6.13(a) shows that P reaches its maximum P_F , which is the debonding force for flexural crack (crack angle is 90°). With the increase of $1/K_v$, debonding driving force P decreases quickly because larger mode I load is induced to the left interface. As a result, the load transferred to the FRP plate also decreases with $1/K_v$, as shown in Fig. 6.13(b). It can be observed that the peeling effect induced by the flexural-shear crack can reduce the debonding load and force transferring capacity of the interface significantly. This phenomenon can be explained by Fig. 6.13(c). This figure shows more mode II fracture energy can be induced by smaller K_v . As a result, the mode II and total fracture energy decreases accordingly because of debonding criterion Eq. (6.11). As shown in Fig. 6.13(d), the phase angle of the debonding reduces monotonically with $1/K_v$ from 89.4° (mode II-dominant) to as low as 45° when $K_v = 0.69 \times 10^6$. In this case, the debonding driving force P is as low as 20% of that of the flexural crack P_F . This suggests that the flexural-shear crack induced debonding is much easier to initiate than the flexural crack induced one due to significant peeling effect caused by the flexural-shear crack. This peeling effect decreases with the propagation of the debonding. As a result, both the debonding driving force P and maximum load transferred to the FRP plate increases with debonding, as shown in Fig. 6.11.

It should be pointed out that existing studies treated the flexural crack induced debonding as pure mode II debonding (Wang, 2006b, Smith and Gravina, 2007; Liu et al., 2007) because the dowel effect of the FRP plate was ignored in these analysis. This study accounts for the dowel effect by a transverse spring. Fig. 6.13(c) and (d) suggest that the mode I component of

the flexural crack induced debonding is negligible compared with the mode II component. However, both experimental study (Sebastian, 2001) and numerical analysis (Lu et al., 2007) suggest that secondary inclined cracks can be generated near the key flexural cracks in the concrete cover by the high shear stress concentration near the tip of the flexural crack. These secondary inclined cracks will induce peeling effect and the change the mode mixity of the interface debonding. As a result, the applied load needed to initiate the debonding is reduced. The peeling effect of the secondary inclined crack can also initiate the debonding on the right interface.



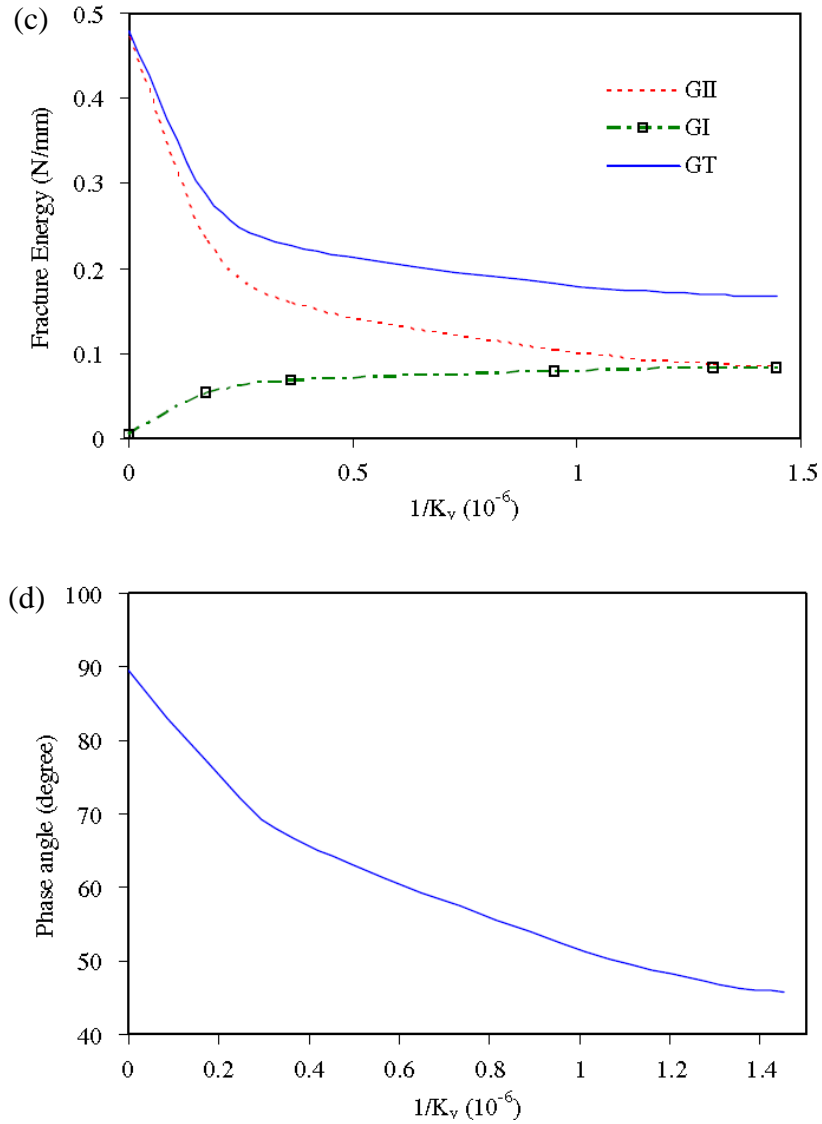


Fig. 6.13. Effect of the angle of the crack on debonding: (a) debonding driving force; (b) maximum axial force of the FRP plate; (c) fracture energy; (d) mode mixity.

6.5 Conclusions

In this study, a nonlinear fracture mechanics approach has been proposed to study the flexural-shear crack induced interface debonding of FRP strengthened concrete beams.

Displacement jumps in both the axial and transverse directions can be induced by a flexural-shear crack at the location of the crack. Therefore, the flexural-shear crack induced debonding is in mixed-mode. A mode-independent traction-separation law is adopted in this study to simulate

the shear and peeling behavior of the FRP-concrete interface. Closed-form solutions of the interfacial normal and shear stresses, and the axial force of the FRP plate are obtained for different debonding stages. The validation of this model is confirmed by excellent agreements achieved by the present solution with the numerical solution using finite element analysis. The peeling effect induced by the transverse displacement jump makes debonding much easier to initiate than in the case of flexural cracks. However, numerical example shows that this peeling effect on debonding reduces with the debonding progression. The mixed-mode debonding eventually turns into mode II debonding if the debonding size is big enough. The effects of the stiffness of the FRP plate on the FRP-concrete interface debonding are also studied. It has been also found that the peeling effect is more pronounced when the stiffness of the FRP plate is higher. The present nonlinear fracture mechanics model provides an effective and efficient analytical tool for flexural-shear crack induced debonding.

CHAPTER 7

CONCLUSIONS

This study proposes a life-cycle analytical framework on the integrity and long-term durability of the FRP-concrete interface through a combined analytical, numerical, and experimental approach. Several novel models have been established to achieve better understandings on the debonding mechanism of the FRP-concrete interface. The contributions of present dissertation can be summarized as:

1. An innovative 3PEF model has been established successfully to predict the interface stresses of the FRP-strengthened concrete beams. The salient features of the 3PEF model are as follows: 1) it can better predicts the tensile normal stress distribution trends along the CA interface and the compressive normal stress along the PA interface at the vicinity of the FRP plate end; 2) it satisfies all boundary conditions, including the zero shear stress at the free edge of the adhesive layer; 3) it is in explicit closed-form. Therefore, it can be easily implemented for analysis and design of the FRP-strengthened beams. The accuracy of the present model has been verified by its good agreements with FEA solutions. It should be pointed out that the present model can also be directly used to analyze general adhesively bonded joints.

2. Viscoelastic solutions of interface stresses within the adhesive layer have been developed based on the 2PEF and 3PEF models to study the long-term behavior of the FRP-strengthened RC beams. The SLS model is used to simulate the viscoelastic behavior of the adhesive layer. Prestressing force in the FRP plate is also considered in the models. FEA using a subroutine UMAT is conducted to verify the analytical solutions. Good agreements have been achieved by the analytical solutions and the FEA. The redistributions of interfacial stresses, resultant beam forces, and creep deflections of the strengthened beams can be predicted by the present solutions easily.

3. Improved analytical solutions of total ERR and its corresponding mode mixity have been obtained for the FRP-strengthened concrete specimen with debond along the adhesive-concrete interface. The effects of the transverse shear force, which cannot be included in the existing Au and Büyüköztürk (2006)'s solution, have been captured in these new solutions. This has been achieved through capturing the crack tip deformations by two new joint deformation models, i.e., semi-rigid and flexible joint models. Calculations and comparisons of total ERRs and their phase angles for the typical DCB specimens are conducted using the existing AB's model, two new analytical solutions, and the FEA. Better accuracies are achieved by the new solutions. Parametric studies also suggest that debonding along the epoxy-concrete interface subjected to opening loading is mixed mode, not pure mode I as assumed in many studies.

4. Subcritical crack growth along the epoxy-concrete interface was observed for the first time. It has been found that the interface crack can grow slowly even though the energy release rate is much lower than the corresponding fracture toughness. Water and other solutions can substantially increase the crack growth rate along the epoxy-concrete interface by a few orders of magnitudes. The concrete substrates' strengths have been found to have no significant effect on the subcritical cracking growth except the critical energy release rate in the ambient condition. Testing results also suggest that the interface debonding changes from the cohesive failure within the concrete in critical cracking to the adhesive failure along the epoxy-concrete interface in the subcritical cracking.

5. A nonlinear fracture mechanics method has been established to study the flexural-shear crack induced interface debonding of the FRP-strengthened concrete beams. Two mode-independent traction-separation laws are adopted in this study to simulate the shear and peeling behavior of the FRP-concrete interface. Closed-form solutions of the interfacial normal and shear stresses and the axial force of the FRP plate are obtained for different debonding stages. The validation of this model is confirmed by excellent agreements achieved by the present solution with the numerical solution using FEA. The peeling effect of the flexural-shear crack induced transverse displacement jump makes debonding much easier to initiate than in the case of flexural cracks. Numerical example shows that the peeling effect induced by a flexural-shear crack on debonding reduces with the debonding progression. The mixed-mode debonding eventually turns into mode II debonding if the debonding size is large enough. It has

been also found that the peeling effect is more pronounced when the stiffness of the FRP plate is higher. The present nonlinear fracture mechanics model provides an effective and efficient analysis tool for flexural-shear crack induced debonding.

REFERENCES

- Abdelouahed, T. (2006). Improved theoretical solution for interfacial stresses in concrete beams strengthened with FRP plate. *International Journal of Solids and Structures*, 43, 4154-4174.
- Agrawal, A., & Karlsson, A. (2006). Obtaining mode mixity for a bimaterial interface crack using the virtual crack closure technique. *International Journal of Fracture*, 141, 75-98.
- Ahmad, M., Subramaniam, K., & Ghosn, M. (2006). Experimental investigation and fracture analysis of debonding between concrete and FRP sheets. *Journal of Engineering Mechanics*, 132, 914-923.
- Al-Emrani, M., & Kliger, R. (2006). Analysis of interfacial shear stresses in beams strengthened with bonded prestressed laminates. *Composites Part B: Engineering*, 37, 265-272.
- Allman, D. (1977). A theory for elastic stress in adhesively bonded lap joints. *The Quarterly Journal of Mechanics and Applied Mathematics*, 30, 415-436.
- American Society of Civil Engineers (2009). Report card for America's infrastructure (2009 report card).
- Anderson, T. (2005). *Fracture Mechanics Fundamentals and Applications*. (Third Edition), Taylor & Francis, Boca Raton.
- Aprile, A., Spacone, E., & Limkatanyu, S. (2001). Role of bond in RC beams strengthened with steel and FRP plates. *Journal of Structural Engineering*, 127, 1445-1452.
- Ascione, F., Berardi, V., Feo, L., & Giordani, A. (2008). An experimental study on the long-term behavior of CFRP pultruded laminates suitable to concrete structures rehabilitation. *Composites Part B: Engineering*, 39, 1147-1150.
- Au, C., & Büyüköztürk, O. (2006). Debonding of FRP plated concrete: a tri-layer fracture treatment. *Engineering Fracture Mechanics*, 73, 348-365.
- Avramidis, I., & Morfidis, K. (2006). Bending of beams on three-parameter elastic foundation. *International Journal of Solids and Structures*, 43, 357-375.
- Barbato, M. (2009). Efficient finite element modelling of reinforced concrete beams retrofitted with fibre reinforced polymers. *Computers and Structures*, 87, 167-176.

- Barenblatt, G. (1962). The mathematical theory of equilibrium cracks in brittle fracture. *Advances in Applied Mechanics*, 7, 55-129.
- Barnes, R., & Mays, G. (1999). Fatigue Performance of Concrete Beams Strengthened with CFRP Plates. *Journal of Composites for Construction*, 3, 63-72.
- Berggreen, C. (2004). Damage Tolerance of Debonded Sandwich Structures. PhD Thesis, Department of Mechanical Engineering, Technical University of Denmark.
- Berggreen, C., Simonsen, B., & Borum, K. (2007). Experimental and numerical study of interface crack propagation in foam-cored sandwich beams. *Journal of Composite Materials*, 41, 493-520.
- Beuth, J. (1996). Separation of crack extension modes in orthotropic delamination models. *International Journal of Fracture*, 77, 305-321.
- Bizindavyi, L., & Neale, K. (1999). Transfer lengths and bond strengths for composites bonded to concrete. *Journal of Composites for Construction*, 3, 153-160.
- Bizindavyi, L., Neale, K., & Erki, M. (2003). Experimental investigation of bonded fiber reinforced polymer-concrete joints under cyclic loading. *Journal of Composites for Construction*, 7, 127-134.
- Bonacci, J. (1996). Strength, Failure Mode and Deformability of Concrete Beams Strengthened Externally with Advanced Composites. *Advanced Composite Materials in Bridges and Structures, Proceedings of the Second ACMBS International Conference, Montreal*, 419-426.
- Brinson, H. (1982). Viscoelastic constitutive modelling of adhesives, *Composites*, 13, 377-382.
- Brosens, K., & van Gemert, D. (1997). Anchoring stresses between concrete and carbon fibre reinforced laminates. *Non-Metallic (FRP) Reinforcement for Concrete Structure, Proc., 3rd Int. Symp., Japan Concrete Institute, Sapporo*, 1, 271-278.
- Buyle-Bodin, F., David, E., & Ragneau, E. (2002). Finite element modeling of flexural behavior of externally bonded CFRP RC structures. *Engineering Structures*, 24, 1423-1429.
- Büyüköztürk, O., & Hearing, B. (1998). Failure behavior of precracked concrete beams retrofitted with FRP. *Journal of Composites for Construction*, 2, 138-144.
- Camata, G., Spacone, E., & Zarnic, R. (2007). Experimental and nonlinear finite element studies of RC beams strengthened with FRP plates. *Composites Part B: Engineering*, 38, 277-288.
- Chajes, M., Finch, W., Januszka, T., & Thomson, T. (1996). Bond and Force Transfer of Composite-Material Plates Bonded to Concrete. *ACI Structural Journal*, 93, 209-217.
- Chajes, M., Januszka, T., Mertz, D., Thomson Jr., T., & Finch Jr., W. (1995). Shear strengthening of reinforced concrete beams using externally applied composite fabrics. *ACI Structural*

- Journal, 92, 295-303.
- Chajes, M., Thomson Jr., T., & Farschman, C. (1995). Durability of Concrete Beams Externally Reinforced with Composite Fabrics. *Construction and Building Materials*, 9, 141-148.
- Chan, M., & Williams, J. (1983). Slow stable crack growth in high density polyethylenes. *Polymer*, 24, 234-244
- Chandra, N., Li, H., Shet, C., & Ghonem, H. (2002). Some issues in the application of cohesive zone models for metal–ceramic interfaces. *International Journal of Solids and Structures*, 39, 2827-2855.
- Charalambides, P., & Zhang, W. (1995). An energy method for calculating the stress intensities in orthotropic bimaterial fracture. *International Journal of Fracture*, 76, 1573-2673.
- Chen, D., & Cheng, S. (1983). An analysis of adhesive-bonded single-lap joints. *Journal of applied mechanics*, 50, 109-115.
- Chen, J., & Teng, J. (2001). Anchorage strength models for FRP and plates bonded to concrete. *Journal of Structural Engineering*, 127, 784-791.
- Chen, J., Yang, Z., & Holt, G. (2001). FRP or steel plate-to-concrete bonded joints: effect of test methods on experimental bond strength. *Steel Composite Structure*, 1, 231-244.
- Chen, J., Yuan, H., & Teng, J. (2007). Debonding failure along a softening FRP-to-concrete interface between two adjacent cracks in concrete members. *Engineering Structures*, 29, 259-270.
- Chen, Y., Davalos, Ray J., & Kim, H. (2007). Accelerated aging tests for evaluations of durability performance of FRP reinforcing bars for concrete structures. *Composite Structures*, 78,101-111.
- Choi, K., Meshgin, P., & Reda Taha, M. (2007). Shear creep of epoxy at the concrete-FRP interfaces, *Composites Part B*, 38, 772–780.
- Choi, K., Reda Taha, M., Masia, M., Shrive, P., & Shrive, N. (2010). Numerical Investigation of Creep Effects on FRP-Strengthened RC Beams. *Journal of Composites for Construction*, 14, 812-822.
- Conolly, M. (1992). A substructuring approach to the fatigue modeling of polymeric matrix composite materials. *Cyclic deformation, fracture, and nondestructive evaluation of advanced materials*, 2, 265-277.
- Cooper, P., & Sawyer, J. (1979). A critical examination of stresses in an elastic single lap joint. NASA Report No. TP-1507.
- Corr, D., Accardi, M., Graham-Brady, L., & Shah, S. (2007). Digital image correlation analysis of interfacial debonding properties and fracture behavior in concrete. *Engineering Fracture*

- Mechanics, 74, 109-121.
- Crichton, S., Tomozawa, M., Hayden, J., Suratwala, T., & Campbell, J. (1999). Subcritical Crack Growth in a Phosphate Laser Glass. *Journal of the American Ceramic Society*, 82, 3097-3104.
- Dai, J., & Ueda, T. (2006). Local bond stress slip relations for FRP sheets-concrete interfaces. *Proc. Sixth Int. Symposium on FRP Reinforcement for Concrete Structures*, 1, 143-152.
- Dai, J., Ueda, T., & Sato, Y. (2005). Development of the nonlinear bond stress-slip model of fiber reinforced plastics sheet-concrete interfaces with a simple method. *Journal of Composites for Construction*, 9, 52-62.
- Dai, J., Ueda, T., & Sato, Y. (2006). Unified Analytical Approaches for Determining Shear Bond Characteristics of FRP-Concrete Interfaces through Pullout Tests. *Journal of Advanced Concrete Technology*, 4, 133-145.
- Dauskardt, R., Lane, M., Ma, Q., & Krishna, N. (1998). Adhesion and debonding of multi-layer thin film structures. *Engineering Fracture Mechanics*, 61, 141-162.
- Davalos, J., Kodkani, S., Ray, I., & Lin, C. (2008). Fracture evaluation of GFRP-concrete interfaces for freeze-thaw and wet-dry cycling. *Journal of Composite Materials*, 42, 1439-1466.
- Davidson, B., Hu, H., & Schapery, R. (1995). An analytical crack-tip element for layered elastic structures. *Journal of Applied Mechanics*, 62, 294-305.
- De Lorenzis, L., & Nanni, A. (2001). Characterization of FRP rods as near-surface mounted reinforcement. *Journal of Composites for Construction*, 5, 114-121.
- De Lorenzis, L., Teng, J., & Zhang, L. (2006). Interfacial stresses in curved members bonded with a thin plate. *International Journal of Solids and Structures*, 43, 7501-7517.
- Dean G. (2007). Modelling non-linear creep behaviour of an epoxy adhesive. *International Journal of Adhesion and Adhesives*, 27, 636-646.
- Delale, F., Erdogan, F., & Aydinoglu, M. (1981). Stress in adhesively bonded joints: a closed-form solution. *Journal of Composite Materials*, 15, 249-271.
- Diab, H., & Wu, Z. (2007). Nonlinear constitutive model for time-dependent behavior of FRP-concrete interface. *Composites Science and Technology*, 67, 2323-2333.
- Diab, H., & Wu, Z. (2008). A linear viscoelastic model for interfacial long-term behavior of FRP-concrete interface. *Composites Part B: Engineering*, 39, 722-730.
- Diab, H., Wu, Z., & Iwashita, K. (2009). Short and long term bond performance of prestressed FRP sheet anchorages. *Engineering Structure*, 31, 1241-1249.

- Dugdale, D. (1960). Yielding of steel sheets containing slits. *Journal of the Mechanics and Physics of Solids*, 8, 100-104.
- Dundurs, J. (1969). Mathematical theory of dislocations. *Journal of Applied Mechanics*, 36, 650-652.
- Dutta, P., & Hui, D. (1996). Low-temperature and freeze-thaw durability of thick composites. *Composites: Part B*, 27B, 371-379.
- El-Hacha, R., Wight, R., & Green, M. (2001). Prestressed fibre-reinforced polymer laminates for strengthening structures. *Progress in Structural Engineering and Materials*, 3, 111-121.
- Elmalich, D., & Rabinovitch, O. (2009). Masonry and monolithic circular arches strengthened with composite materials - a finite element model. *Computers and Structures*, 87, 521-533.
- Etter, F., Despetis, S., & Etienne, P. (2008). Sub-critical crack growth in some phosphate glasses. *Journal of Non-Crystalline Solids*, 354, 580-586.
- Fallah, A., Mohamed Ali, R., & Louca, L. (2008). Analytical–numerical study of interfacial stresses in plated beams subjected to pulse loading. *Engineering Structures*, 30, 856-869.
- Ferrier, E., & Hamelin, P. (1999). Influence of time–temperature loading on carbon epoxy reinforcement for concrete structure. *ACI publications SP-188-44*, 491-500.
- Ferrier, E., Michel, L., Jurkiewicz, B., & Hamelin, P. (2010). Creep behavior of adhesives used for external FRP strengthening of RC structures. *Construction and Building Materials*, 25, 461- 467.
- Freiman, S. (1974). Effect of Alcohols on Crack Propagation in Glass. *Journal of the American Ceramic Society*, 57, 350 - 353.
- Freiman, S., Wiederhorn, S., & Mecholsky, J. (2009). Environmentally enhanced fracture of glass: a historical perspective. *Journal of the American Ceramic Society*, 92, 1371-1382.
- Frostig, Y., & Baruch, M. (1996). Localized load effects in high-order bending of sandwich panels with flexible core. *Journal of Engineering Mechanics*, 122, 1069-1076
- Frostig, Y., & Shenhar, Y. (1995). High-order bending of sandwich beams with a transversely flexible core and unsymmetrical laminated composite skins. *Composites Engineering*, 5, 405-414.
- Frostig, Y. (1992). Behavior of delaminated sandwich beams with transversely flexible core-high order theory. *Composite Structures*, 20, 1-16.
- Frostig, Y. (1993). On stress concentration in the bending of sandwich beams with transversely flexible core. *Composite Structures*, 24, 161-169.
- Frostig, Y., & Baruch, M. (1990). Bending of sandwich beams with transversely flexible core.

AIAA Journal, 28, 523-530

- Frostig, Y., Thomsen, O., & Mortensen, F. (1999). Analysis of Adhesive Bonded Joints, square-end, and spew-fillet-high-order theory approach. *Journal of Engineering Mechanics*, 125, 1298-1307.
- Garden, H., Quantrill, R., Hollaway, L., Thorne, A., & Parke, G. (1998). An experimental study of the anchorage length of carbon fibre composite plates used to strengthen reinforced concrete beams. *Construction and Building Materials*, 12, 203-219.
- Gehrke, E., Ullner, Ch., & Hähnert, M. (1991). Fatigue Limit and Crack Arrest in Alkali-Containing Silicate Glasses. *Journal of Material Science*, 26, 5445–5455.
- Gemert, D. (1980). Force transfer in epoxy-bonded steel-concrete joints. *International Journal of Adhesion and Adhesives*, 12, 67-72.
- Giurgiutiu, V., Lyons, J., Petrou, M., Laub, D., & Whitley, S. (2001). Fracture mechanics testing of the bond between composite overlay and a concrete substrate. *Journal of Adhesion Science and Technology*, 15, 1351-1371.
- Goland, M., & Reissner, E. (1944). The Stresses in Cemented Joints. *Journal of Applied Mechanics*, 66, A17-A27.
- Goncalves, J, De Moura, M., & De Castro, P. (2002). A three-dimensional finite element model for stress analysis of adhesive joints. *International Journal of Adhesion and Adhesives*, 22, 357-365.
- Grace, N., & Grace M. (2005). Effect of repeated loading and long term humidity exposure on flexural response of CFRP strengthened concrete beams. *Proceedings of the International Symposium on Bonded behavior of FRP in Structures (BBFS 2005)*, Chen and Teng (eds), 539-546.
- Grace, N., & Singh, S. (2005). Durability evaluation of carbon fiber-reinforced polymer strengthened concrete beams: experimental study and design. *ACI Structural Journal*, 201, 40-53
- Green, M., Bisby, L., Beaudoin, Y., & Labossiere, P. (2000). Effect of freeze–thaw cycles on the bond durability between fibre reinforced polymer plate reinforcement and concrete. *Canadian Journal of Civil Engineering*, 27, 949-959.
- Gurumurthy, C., Kramer, E., & Hui, C. (2001). Water-assisted sub-critical crack growth along an interface between polyimide passivation and epoxy underfill. *International Journal of Fracture*, 109, 1-28.
- Harris, J., & Adams, R. (1984). Strength prediction of bonded single lap joints by non-linear finite element methods. *International Journal of Adhesion and Adhesives*, 4, 65-78.

- Hart-Smith, L. (1973). Adhesive-bonded single-lap joints. NASA., CR-112236.
- Hassan, T., & Rizkalla, S. (2003). Investigation of bond in concrete structures strengthened with near surface mounted carbon fiber reinforced polymer strips. *Journal of Composites for Construction*, 7, 248-257.
- He, M., & Hutchinson, J. (1989). Kinking of crack out of an interface. *Journal of Applied Mechanics*, 56, 270–278.
- Heffernan, P., & Erki, M. (2004). Fatigue behavior of reinforced concrete beams strengthened with carbon fiber reinforced plastic laminates. *Journal of Composites for Construction*, 8, 132-140.
- Hibino, Y., Sakaguchi, S., & Tajima, Y. (1984). Crack Growth in Silica Glass under Dynamic Loading. *Journal of the American Ceramic Society*, 67, 64–68.
- Hogan, C., & Knowles, J. (1983). Recent developments concerning Saint Venant's principle. *Advances in Applied Mechanics*, 23, 179-269.
- Horiguchi, T., & Saeki, N. (1997). Effect test method and quality of concrete on bond Strength of CFRP sheet. *Proceedings of Third International Symposium of Non-Metallic (FRP) Reinforcement for Concrete Structures*, 1, 265-270.
- Hutchinson, J., & Suo, Z. (1992). Mixed mode cracking in layered materials. *Advances in Applied Mechanics*, 29, 63-191.
- Hutchinson, J., Mear, M., & Rice, J. (1987). Crack paralleling an interface between dissimilar materials. *Journal of Applied Mechanics*, 54, 828-932.
- Irwin, G. (1957). Analysis of stresses and strains near the end of a crack traversing a plate. *Journal of Applied Mechanics*, 24, 361-364.
- Jerome, D., & Ross, C. (1997). Simulation of the dynamic response of concrete beams externally reinforced with carbon-fiber reinforced plastic. *Computers and Structures*, 64, 1129-1153.
- Johnsen, B., Olafsen, K., & Stori, A. (2003). Silanization of adhesively bonded aluminum alloy AA6060 with γ -glycidoxypropyltrimethoxysilane. II. Stability in degradation environments. *Journal of Adhesion Science and Technology*, 17, 1283-1298.
- Jones, K., Swamy, R., & Charif, A. (1988). Plate separation and anchorage of reinforced concrete beams strengthened by epoxy-bonded steel plates. *The Structural Engineer*, 66, 85-94.
- Kaplan, M. (1961). Crack Propagation and Fracture in the Concrete. *Journal of the American Concrete Institute*, 58, 591-609.
- Karbhari, V., & Engineer, M. (1996). Investigation of bond between concrete and composites: use of a peel test. *Journal of Reinforced Plastics and Composites*, 15, 208-227.

- Karbhari, V., & Engineer, M. (1997). Effect of environmental exposure on the external strengthening of concrete with composites-short term bond durability. *Journal of Reinforced Plastics and Composites*, 15, 1194-1216.
- Karbhari, V., & Zhao, L. (1998). Issues related to composite plating and environmental exposure effects on composite-concrete interface in external strengthening. *Composite Structures*, 40, 293-304.
- Karbhari, V., Chin, J., Hunston, D., Benmokrane, B., Juska, T., Morgan, R., Lesko, J., Sorathia, U., & Reynaud, D. (2003). Durability gap analysis for fiber-reinforced polymer composites in civil infrastructure. *Journal of Composites for Construction*, 3, 238-247.
- Karbhari, V., Zhao, L., Murphy, K., & Kabalnova, L. (1998). Environmental durability of glass reinforced composites-short term effects. 1st International Conference on Durability of Fiber Reinforced Polymer for Construction, Sherbrooke, Canada, 513-524.
- Kerr, A. (1965). A study of a new foundation model. *Acta Mechanica*, 1/2, 135-147.
- Kinloch, A. (1979). Interfacial Fracture Mechanical Aspects of Adhesive Bonded Joints — A Review. *Journal of Adhesion*, 10, 193-219.
- Kinloch, A., Korenberg, C., Tan, K., & Watts, J. (2007). Crack growth in structural adhesive joints in aqueous environments. *Journal of Material Science*, 42, 6353-6370.
- Ko, H., & Sato, Y. (2004). Analysis of FRP-strengthened RC members with varied sheet bond stress-slip models. *Journal of Advanced Concrete Technology*, 2, 317-326.
- Kobatake, Y., Kimura, K., & Ktsumata, H. (1993). A retrofitting method for reinforced concrete structures using carbon fibre. In: A. Nanni, Editor, *Fibre-reinforced-plastic (FRP) reinforcement for concrete structures: properties and applications*, Elsevier, Amsterdam, 435-450.
- Kook, S., & Dauskardt, R. (2002). Moisture-assisted subcritical debonding of a polymer/metal interface. *Journal of Applied Physics*, 91, 1293-1303.
- Korenberg, C., Kinloch, A., & Watts, J. (2004). Crack growth of structural adhesive joints in humid environments. *Journal of Adhesion*, 80, 169-201.
- Kotynia, R., Abdel Baky, H., Neale, K., & Ebead, U. (2008). Flexural strengthening of RC beams with externally bonded CFRP Systems: test results and 3D nonlinear FE analysis. *Journal of Composites for Construction*, 12, 190-202.
- Krausz, A. (1979). The theory of thermally activated processes in brittle stress corrosion cracking. *Engineering Fracture Mechanics*, 11, 33-42.
- Krueger, R. (2004). Virtual crack closure technique: history, approach, and applications. *Applied Mechanics Review*, 57, 109-143.

- Kurtz, S., & Balaguru, P. (2000). Postcrack creep of polymeric fiber-reinforced concrete in flexure. *Cement and Concrete Research*, 30, 183-190.
- Lau, K., Dutta, P., Zhou, L., & Hiu, D. (2001). Mechanics of bonds in an FRP bonded concrete beam. *Compos Part B: Engineering*, 32, 491-502.
- Lee, J., & Kim, H. (2005). Stress Analysis of Generally Asymmetric Single Lap Adhesively Bonded Joints. *Journal of Adhesion*, 81, 443-472.
- Leung, C. (2001). Delamination failure in concrete beams retrofitted with a bonded plate. *Journal of Materials in Civil Engineering*, 13, 106-113.
- Leung, S., Lam, D., Luo, S., & Wong, C. (2004). The role of water in delamination in electronic packages: degradation of interfacial adhesion. *Journal of Adhesion Science and Technology*, 18, 1103-1121.
- Li, G., & Pearl, L. (2001). Finite element and experimental studies on single-lap balanced joints in tension. *International Journal of Adhesion and Adhesives*, 21, 211-220.
- Liu, S., Oehlers, D., & Seracino, R. (2007). Study of intermediate crack debonding in adhesively plated beams. *Journal of Composites for Construction*, 11, 175-183.
- Liu, Z., & Zhu, B. (1994). Analytical solutions for R/C beams strengthened by externally bonded steel plates. *Journal of Tongji University*, 22, 21-26.
- Lorenzis, L., & Teng, J. (2006). Near-surface mounted FRP reinforcement: An emerging technique for strengthening structures. *Composite Part B: Engineering*, 38, 119-143.
- Lorenzis, L., Miller, B., & Nanni, A. (2001). Bond of fiber-reinforced polymer laminates to concrete. *ACI Materials Journal*, 98, 256-264.
- Lu, X., Teng, J., Ye, L., & Jiang, J. (2007). Intermediate crack debonding in FRP-strengthened RC beams: FE Analysis and strength model. *Journal of Composites for Construction*, 11, 161-174.
- Lubkin, J., & Reissner, E. (1958). Stress Distribution and Design Data for Adhesive Lap Joints between Circular Tubes. *Journal of Applied Mechanics*, 78, 1213-1221.
- Lucas F., Paulo J., Adams R., Wang A., & Spelt, J. (2009). Analytical models of adhesively bonded joints—Part I: Literature review. *International Journal of Adhesion and Adhesives*, 29, 319-330.
- Lucas F., Paulo J., Adams R., Wang A., & Spelt J. (2009). Analytical models of adhesively bonded joints—Part II: Comparative study. *International Journal of Adhesion and Adhesives*, 29, 331-341.
- Luo, Q., & Tong, L. (2004). Linear and higher order displacement theories for adhesively bonded lap joints. *International Journal of Solids and Structures*, 41, 6351-6381.

- Luo, Q., & Tong, L. (2007). Fully-coupled Nonlinear Analysis of Single Lap Adhesive Joints. *International Journal of Solids and Structures*, 44, 2349-2370.
- Lyons, J., Laub, D., Giurgiutiu, V., Petrou, M., & Salem, H. (2002). Effect of hygrothermal aging on the fracture of composite overlays on concrete. *Journal of Reinforced Plastics and Composites*, 21, 293-309.
- Maeda, T., Asano, Y., Sato, Y., Ueda, T., & Kakuta, Y. (1997). A Study on bond mechanism of carbon fiber sheet. *Proceedings of Third International Symposium of Non-Metallic (FRP) Reinforcement for Concrete Structures*, 1, 279-286.
- Malek, A., Saadatmanesh, H., & Ehsani, M. (1998). Prediction of failure load of R/C beams strengthened with FRP plate due to stress concentration at the plate end. *ACI Structural Journal*, 95, 42-52.
- Masoud, S., Soudki, K., & Topper, T. (2005). Postrepair Fatigue Performance of FRP-Repaired Corroded RC Beams: Experimental and Analytical Investigation. *Journal of Composites for Construction*, 9, 441-449.
- Matos, P., McMeeking, R., Charalambides, P., & Drory, M. (1989). A method for calculating stress intensities in bimaterial fracture. *International Journal of Fracture*, 40, 235-254.
- Maugis, D. (1985). Subcritical crack growth, surface energy, fracture toughness, stick-slip and embrittlement. *Journal of Materials Science*, 20, 3041-3073.
- Mazzotti, C., Savoia, M., & Ferracuti, B. (2008). An experimental study on delamination of FRP plates bonded to concrete. *Construction and Building Materials*, 22, 1409-1421.
- Meier, U., Deuring, M., Meier, H., & Schwegler, G. (1992). Strengthening of structures with CFRP laminates: Research and applications in Switzerland. *Advanced Composite Material in Bridges and Structures*. (Neale, K. and Labossiere, P., eds.) Canadian Society for Civil Engineers, Montreal, 2, 7-12.
- Meshgin, P., Choi K., & Reda Taha, M. (2009). Experimental and analytical investigations of creep of epoxy adhesive at the concrete-FRP interfaces, *International Journal of Adhesion and Adhesives*, 29, 56-66.
- Michalske, T., & Bunker, B. (1989). Effect of Surface Stress on Stress Corrosion of Silicate Glass. *Advances in Fracture Research*, 6, 3869-3901.
- Mirman, B., & Knecht, S. (1990). Creep strains in an elongated bond layer. *IEEE Transactions on Components Hybrids and Manufacturing Technology*, 13, 914-928.
- Mostovoy, S., & Ripling, E. (1971). The Fracture Toughness and Stress Corrosion Cracking Characteristics of an Adhesive. *Journal of Applied Polymer Science*, 15, 641-659.
- Mostovoy, S., & Ripling, E. (1972). Effect of temperature on the fracture toughness and stress

- corrosion cracking of adhesives. *Applied Polymer Symposium*, 395-408.
- Moutrille, M., Derrien, K., Baptiste, D., Balandraud, X., & Grédiac, M. (2009). Through-thickness strain field measurement in a composite/aluminium adhesive joint. *Composites Part A: Applied Science and Manufacturing*, 40, 985-996.
- Mukhopadhyaya, P., Swamy, R., & Lynsdale, C. (1998). Influence of aggressive exposure conditions on the behaviour of adhesive bonded concrete-GFRP joints. *Construction and Building Materials*, 12, 427-446.
- Mullins, G., Sen, R., & Spain, J. (1998). Testing of CFRP/Concrete Bond. *Second International Conference on Composites in Infrastructure*, 211-218.
- Myers, J., Murthy, S., & Micelli, F. (2001). Effect of combined environmental cycles on the bond of FRP sheets to concrete. *Proceedings - on Composites in Construction, Porto, Portugal*, 339-344.
- Nairn, J. (2006). On the calculation of ERRs for cracked laminates with residual stresses. *International Journal of Fracture*, 139, 267-293.
- Nakaba, K., Kanakubo, T., Furuta, T., & Yoshizawa, H. (2001). Bond behavior between Fiber-Reinforced Polymer laminates and concrete. *ACI Structural Journal*, 98, 359-367.
- Namkanisorn, A., Ghatak, A., Chaudhury, M., & Berry, D. (2001). A kinetic approach to study the hydrolytic stability of polymer-metal adhesion. *Journal of Adhesion Science and Technology*, 15, 1725-1745.
- Neale, K., Ebead, U., Abdel Baky, H., Elsayed, W., & Godat, A. (2005). Modeling of debonding phenomena in FRP-strengthened concrete beams and slabs. *Proceedings of the International Symposium on Bond Behaviour of FRP in Structures (BBFS 2005) Chen and Teng (eds)*, 45-54.
- Needleman, A. (1987). A continuum model for void nucleation by inclusion debonding. *Journal of Applied Mechanics*, 54, 525-531.
- Niu, H., Karbhari, V., & Wu, Z. (2006). Diagonal macro-crack induced debonding mechanisms in FRP rehabilitated concrete. *Composites Part B: Engineering*, 37, 627-641.
- Noor, A., Burton, W., & Bert, C. (1996). Computational models for sandwich panels and sheets. *Applied Mechanics Review*, 49, 155-159.
- Nordin, H., & Taljsten, B. (2006). Concrete beams strengthened with prestressed near surface mounted CFRP. *Journal of Composites for Construction*, 10, 60-68.
- O'Brien, E., Case, S., & Ward, T. (2005). Critical and subcritical adhesion measurements of a model epoxy coating exposed to moisture using the shaft-loaded blister test. *Journal of Adhesion*, 81, 41-48.

- Oplinger, D. (1991). A layered beam theory for single lap joints. Army Materials Technology Laboratory Report MTL TR91-23.
- Oplinger, D. (1994). Effects of adherent deflections in single-lap joints. *International Journal of Solids and Structures*, 31, 2565~87.
- Østergaard, R., & Sørensen, B. (2007). Interface crack in sandwich specimen. *International Journal of Fracture*, 143, 301-316.
- Ouyang, Z., & Wan, B. (2008). Modeling of Moisture Diffusion in FRP Strengthened Concrete Specimens. *Journal of Composites for Construction*, 12, 425-434.
- Paipetis, S., & Dimarogonas, A. (1968). *Analytical Methods in Rotor Dynamics*. Elsevier Applied Science, London.
- Pan, J., & Leung, C. (2007). Debonding along the FRP-concrete interface under combined pulling/peeling effects. *Engineering Fracture Mechanics*, 74, 132-150.
- Papakonstantinou, C., Petrou, M., & Harries, K. (2001). Fatigue behavior of beams strengthened with GFRP sheets. *Journal of Composites for Construction*, 5, 246-253.
- Park, S. (2004). Durability of adhesive joints between concrete and FRP reinforcement in aggressive environments. Ph.D. dissertation, The University of Texas at Austin.
- Park, S., Liechti, K., & Roy, S. (2006). A nonlinear viscoelastic fracture analysis of concrete/FRP delamination in aggressive environments. *International Journal of Fracture*, 142, 9-27.
- Parretti, R., & Nanni, A. (2004). Strengthening of RC members using near surface mounted FRP composites: design overview. *Advances in Structural Engineering*, 7, 469~483.
- Pellegrino, C., Tinazzi, D., & Modena, C. (2008). Experimental study on bond behavior between concrete and FRP reinforcement. *Journal of Composites for Construction*, 12, 180-189.
- Plevris, N., & Triantafillou, T. (1994). Time-dependent behavior of RC members strengthened with FRP laminates. *Journal of Structural Engineering*, 120, 1016-1042.
- Qiao, P., & Wang, J. (2004). Mechanics and fracture of crack-tip deformable bi-material interface. *International Journal of Solids and Structures*, 41, 7423-7444.
- Qiao, P., & Wang, J. (2005a). Novel joint deformation models and their application to delamination fracture analysis. *Composites Science and Technology*, 65, 1826-1839.
- Qiao, P., & Wang, J. (2005b). On the mechanics of composite sinusoidal honeycomb core. *ASCE Journal of Aerospace Engineering*, 18, 42-50.
- Qiao, P., & Wang, J. (2005c). Shear stiffness of composite honeycomb cores and efficiency of material. *Mechanics of Advanced Materials and Structures*, 12, 159-172.
- Qiao, P., & Xu, Y. (2004). Evaluation of the fracture energy of composite-concrete bonded

- interfaces using three-point bend tests. *Journal of Composites for Construction*, 8, 352-359.
- Quantrill, R., & Hollaway, L. (1998). The flexural rehabilitation of reinforced concrete beams by the use of prestressed advanced composite plates, *Composites Science and Technology*, 58, 1259-1275.
- Rabinovitch, O., & Frostig, Y. (2000). Closed-form high-order analysis of RC beams strengthened with FRP strips. *Journal of Composites for Construction*, 4, 65-74.
- Rabinovitch, O., & Frostig, Y. (2001). Delamination failure of RC beams strengthened with FRP strip - a closed-form high-order and fracture mechanics approach. *Journal of Engineering Mechanics*, 127, 852-861.
- Rabinovitch, O. (2008). Cohesive interface modeling of debonding failure in FRP strengthened beams. *Journal of Engineering Mechanics*, 134, 578-588
- Rahimi, H., & Hutchinson, A. (2001). Concrete beams strengthened with externally bonded frp plates. *Journal of Composites for Construction*, 5, 44-56.
- Raju, I., & Fichter, W. (1989). A finite-element alternating method for two dimensional mode I crack configurations. *Engineering Fracture Mechanics*, 33, 525-540.
- Raju, I., Shivakumar, K., & Crews, J. (1988). Three-dimensional elastic analysis of a composite double cantilever beam specimen. *AIAA Journal*, 26, 1493-1498.
- Rasheed, H., & Pervaiz, S. (2002). Bond slip analysis of fiber-reinforced polymer-strengthened beams. *Journal of Engineering Mechanics*, 128, 78-86.
- Rice, J., & Wang, J. (1989). Embrittlement of interfaces by solute segregation. *Materials Science and Engineering. A*, 107, 23-40.
- Rice, J. (1988). Elastic fracture mechanics concepts for interfacial cracks. *Journal of Applied Mechanics*, 55, 98-103.
- Ripling, E., Bersch, C., & Mostovoy, S. (1971). Stress Corrosion Cracking of Adhesive Joints. *Journal of Adhesion*, 3, 145-163.
- Ritchie, P., Thomas, D., Lu, L., & Connelly, G. (1991). External reinforcement of concrete beams using fiber reinforced plastics. *ACI Structural Journal*, 88, 490-500.
- Ritter, J., & Conley, K. (1992). Moisture-assisted crack propagation at polymer/glass interfaces. *International Journal of Adhesion and Adhesive*, 12, 245-250.
- Roberts, T., & Haji-Kazemi, H. (1989). Theoretical study of the behaviour of reinforced concrete beams strengthened by externally bounded steel plates. *Proceedings of the Institution of Civil Engineering (Part 2)*, 87, 39-55.
- Roberts, T. (1989a). Shear and normal stresses in adhesive joints. *Journal of Engineering*

- Mechanics, 115, 2460-2479.
- Roberts, T. (1989b). Approximate analysis of shear and normal stress concentrations in the adhesive layer of plated RC beams. *Structural Engineer*, 67, 228-233.
- Rybicki, E., & Kanninen, M. (1977). A finite element calculation of stress intensity factors by a modified crack closure integral. *Engineering Fracture Mechanics*, 9, 931-938.
- Saadatmanesh, H., & Ehsani, M. (1991). RC beams strengthened with GFRP plates. I: Experimental study. *Journal of Structural Engineering*, 117, 3417-3433.
- Savoia, M., Ferracuti B., & Mazzotti C. (2005). Long-term creep deformation of FRP-plated r/c tensile members. *Journal of Composites for Construction*, 9, 63-72.
- Schapery, R., & Davidson, B. (1990). Prediction of energy release rate for mixed-mode delamination using classical plate theory. *Applied Mechanics Review*, 43, S281-S287.
- Sebastian, W. (2001). Significance of midspan debonding failure in FRP-plated concrete beams. *Journal of Structural Engineering*, 127, 792-798.
- Seible, F., Priestley, M., Hegemier, G., & Innamorato, D. (1997). Seismic retrofit of RC columns with continuous carbon fiber jackets. *Journal of Composites for Construction*, 1, 52-62.
- Shahawy, M., & Beitelman, T. (1999). Static and Fatigue Performance of RC Beams Strengthened with CFRP Laminates. *Journal of Structural Engineering*, 125, 613-621.
- Sharif, A., Al-Sulaimani, G., Basunbul, I., Baluch, M., & Ghaleb, B. (1994). Strengthening of initially loaded reinforced concrete beams using FRP plates. *ACI Structural Journal*, 91, 160-168.
- Shimizu, S., Yanagimoto, T., & Sakai, M. (1999). Pyramidal indentation load-depth curve of viscoelastic materials. *Journal of Material Research*, 16, 4075-4086.
- Simmons, C., & Freiman, S. (1981). Effect of corrosion processes on subcritical crack-growth in glass. *Journal of the American Ceramic Society*, 64, 683-686.
- Singh, H., Wan, K., Dillard, J., Reboa, P., Smith, J., Chappell, E., & Sharan, A. (2008). Subcritical delamination in epoxy bonds to silicon and glass adherends: effect of temperature and preconditioning. *Journal of Adhesion*, 84, 619-637.
- Smith, S., & Gravina, R. (2007). Modeling debonding failure in FRP flexurally strengthened RC members using a local deformation model. *Journal of Composites for Construction*, 11, 184-191.
- Smith, S., & Teng, J. (2001). Interfacial Stresses in Plated Beams. *Engineering Structures*, 23, 857-871.
- Smith, S., & Teng, J. (2002). FRP-strengthened RC beams. I: Review of Debonding Strength

- Models. *Engineering Structures*, 24, 385-395.
- Spadea, G., Bencardino, F., & Swamy, R. (1998). Structural behavior of composite RC beams with externally bonded CFRP. *Journal of Composites for Construction*, 2, 132-137.
- Suo, X., & Valeta, M. (1998). Virtual crack extension in geometries under large displacements/rotations. *International Journal of Fracture*, 89, 309-331.
- Suo, Z., & Hutchinson J. (1990). Interface crack between two elastic layers. *International Journal of Fracture*, 43, 1-18.
- Suratwala, T., Steele, R., Wilke, G., Campbell, J., & Takeuchi, K. (2000). Effects of OH Content, Water Vapor Pressure, and Temperature on Sub-Critical Crack Growth in Phosphate Glass. *Journal of Non-Crystalline Solids*, 263, 213-227.
- Swamy, R., Jones, R., & Bloxham, J. (1986). Crack control of reinforced concrete beams through epoxy-bonded steel plates. *Adhesion between Polymers and Concrete, RILEM 86, 1986*, 542-555.
- Tada, H., Paris, P., & Irwin, G. (2000). *The stress analysis of cracks handbook (Third edition)*, ASME Press: Professional Engineering Publication: ASM International, New York.
- Taheri, F., & Zou, G. (2004). Treatment of Unsymmetric Adhesively Bonded Composite Sandwich Panels-To-Flange Joints. *Mechanics of Advanced Materials and Structures*, 11, 175-196.
- Täljsten, B. (1996). Strengthening of concrete prisms using the plate-bonding technique. *International journal of Fracture*, 82, 253-266.
- Täljsten, B. (1997a). Defining anchor lengths of steel and CFRP plates bonded to concrete. *International Journal of Adhesion*, 17, 319-327.
- Täljsten, B. (1997b). Strengthening of beams by plate bonding. *ASCE Journal of Materials in Civil Engineering*, 9, 206-12.
- Technical Committee FRP (2003). *FRP-concrete bond in structural strengthening and rehabilitation. RILEM.*
- Teng, J., Chen, J., Smith, S., & Lam, L. (2003a). Structures and Buildings. Behavior and strength of FRP-strengthened RC structures: a state-of-the-art review, 156, 51-62.
- Teng, J., Smith, S., Yao, J., & Chen, J. (2003b). Intermediate crack-induced debonding in RC beams and slabs. *Construction and Building Materials*, 17, 447-462.
- Teng, J., Zhang, J., & Smith, S. (2002). Interfacial stresses in reinforced concrete beams bonded with a soffit plate: A finite element study. *Construction and Building Materials*, 16, 1-14.
- Tilly, G. (2007). Fatigue of steel reinforcement bars in concrete: a review. *Fatigue and Fracture*

- of Engineering Materials and Structures, 2, 251-268.
- Tong, L. (1996). Bond strength for adhesive-bonded single-lap Joints. *Acta Mechanica*, 117, 101-113.
- Tonyali, K., & Brown, H. (1986). On the applicability of linear elastic fracture mechanics to environmental stress cracking of low-density polyethylene. *Journal of Materials Science*, 21, 3116-3124.
- Toutanji, H., & Gomez, W. (1997). Durability of concrete beams externally bonded with FRP sheets in aggressive environments. *Cement and Concrete Composites*, 19, 351-358.
- Triantafillou, T., & Deskovic, N. (1991). Innovative Prestressing with FRP Sheets: mechanics of short-term behavior *journal of engineering mechanics*, 117, 1652-1672.
- Triantafillou, T., & Plevris, N. (1992). Strengthening of RC beams with epoxy-bonded fiber-composite materials. *Materials and Structures*, 25, 201-211.
- Tsai, M., & Morton, J. (1994). An evaluation of analytical and numerical solutions to the single-lap joint. *International Journal of Solids and Structures*, 31, 2537~2563.
- Tsai, M., Oplinger, D., & Morton, J. (1998). Improved theoretical solutions for adhesive lap joints. *International Journal of Solids and Structures*, 35, 1163-1185.
- Vilnay, O. (1988). The analysis of reinforced concrete beams strengthened by epoxy bonded steel plates. *International Journal of Cement Composites and Lightweight Concrete*, 10, 73-78.
- Wan, B., Petrou, M., & Harries, K. (2006). The effect of the presence of water on the durability of bond between CFRP and concrete. *Journal of Reinforced Plastics and Composites*, 25, 875-890.
- Wan, B., Sutton, M., Petrou, M., Harries, K., & Li, N. (2004). Investigation of bond between fiber reinforced polymer and concrete undergoing global mixed mode I/II loading. *Journal of Engineering Mechanics*, 130, 1467-1475.
- Wang, J., & Qiao, P. (2004a). Interface fracture between two shear deformable elastic layers. *Journal of the Mechanics and Physics of Solids*, 52, 891-905.
- Wang, J., & Qiao, P. (2004b). On the energy release rate and mode mixity in delaminated shear deformable composite plates. *International Journal of Solids and Structures*, 41, 2757-2779.
- Wang, J., & Qiao, P. (2004c). Novel beam analysis of end notched flexure specimen for mode-II fracture. *Engineering Fracture Mechanics*, 71, 219-231.
- Wang, J., & Zhang, C. (2007a). Delamination in elastic shear deformable circular layers. *Composites Science and Technology*, 67, 3323-3330.

- Wang, J., & Zhang, C. (2007b). Nonlinear fracture mechanics of flexural-shear crack induced debonding of FRP strengthened concrete beams. *International Journal of Solids and Structures*, 45, 2916-2936.
- Wang, J., & Zhang, C. (2009). Three-parameter, elastic foundation model for analysis of adhesively bonded joints. *International Journal of Adhesion and Adhesives*, 29, 495-502.
- Wang, J. (2003). Mechanics and fracture of hybrid material interface bond, Ph.D. Thesis, Department of Civil Engineering, The University of Akron, OH.
- Wang, J. (2006a). Debonding of FRP-plated reinforced concrete beam, a bond-slip analysis. I. Theoretical formulation. *International Journal of Solids and Structures*, 43, 6649-6664.
- Wang, J. (2006b). Cohesive zone model of intermediate crack-induced debonding of FRP-plated concrete beam. *International Journal of Solids and Structures*, 43, 6630-6648.
- Wang, J. (2007a). Cohesive zone model of FRP-concrete interface debonding under mixed-mode loading. *International Journal of Solids and Structures*, 44, 6551-6568.
- Wang, J. (2007b). Cohesive-bridging zone model of FRP-concrete interface debonding. *Engineering Fracture Mechanics*, 74, 2643-2658.
- Wang, J. (2007c). Cohesive zone model of FRP-concrete interface debonding under mixed-mode loading. *International Journal of Solids and Structures*, 44, 6551-6568.
- Wiederhorn, S., & Bolz, L. (1970). Stress corrosion and static fatigue of glass. *Journal of the American Ceramic Society*, 53, 543-548.
- Wiederhorn, S. (1968). Moisture assisted crack growth in ceramics, *International Journal of Fracture*, 4, 171-177.
- Wiederhorn, S., Freiman, S., Fuller Jr., E., & Simmons, C. (1982). Effects of water and other dielectrics on crack growth. *Journal of Materials Science*, 17, 3460-3478.
- Wight, R., Green, M., & Erki, M. (2001). Prestressed FRP sheets for poststrengthening reinforced concrete beams. *Journal of Composites for Construction*, 5, 214-220.
- Williams, D. (1973). A new criterion for failure of materials by environmental-induced cracking. *International Journal of Fracture*, 9, 63-73.
- Wooley, G., & Carver, D. (1971). Stress concentration factors for bonded lap joints. *Journal of Aircraft*, 8, 817-820.
- Wu, Z., & Niu, H. (2000). Study on Debonding Failure Load of RC Beams Strengthened with FRP Sheets. *Journal of Structural Engineering A*, 46A, 1431-1441.
- Wu, Z., & Yin, J. (2003). Fracture behaviors of FRP-strengthened concrete structures. *Engineering Fracture Mechanics*, 70, 1339-1355.

- Wu, Z., Matsuzaki, T., & Tanabe, K. (1997). Interface crack propagation in FRP-strengthened concrete structures. In: Proceedings of the Third International Symposium. Non-Metallic (FRP) Reinforcement for Concrete Structures. Sapporo, Japan, 319-326.
- Wu, Z., Yuan, H., & Niu, H. (2002). Stress Transfer and Fracture Propagation in Different Kinds of Adhesive Joints. *Journal of Engineering Mechanics*, 128, 562-573.
- Xue, W., Tan, Y., & Zeng, L. (2010). Flexural response predictions of reinforced concrete beams strengthened with prestressed CFRP plates, *Composite Structures*, 92,612-622.
- Yang, J., Teng, J., & Chen, J. (2004). Interfacial stresses in soffit-plated reinforced concrete beams. *Proceedings of the Institution of Civil Engineering, Structures and Buildings*, 157, 77- 89.
- Yao, J., Teng, J., & Chen, J. (2005). Experimental study on FRP-to-concrete bond joints. *Composites Part B: Engineering*, 36, 99-113.
- Yuan, H., Teng, J., Seracino, R., Wu, Z., & Yao, J. (2004). Full-range behavior of FRP-to-concrete bonded joints. *Engineering Structures*, 26, 553-565.
- Yuan, H., Wu, Z., & Yoshizawa, H. (2001). Theoretical solutions on interfacial stress transfer of externally bonded steel/composite laminates. *JSCE Journal of Structural Mechanics and Earthquake Engineering*, 18, 27-39.
- Zakian, V. (1969). Numerical inversion of Laplace transform. *Electronic Letters*, 3, 120-121.
- Zakian, V. (1970a). Rational approximation to transform function matrix of distributed system. *Electronic Letters*, 6, 474-476.
- Zakian, V. (1970b). Optimization of numerical inversion of Laplace transform. *Electronic Letters*, 6, 677-679.
- Ziraba, Y., Baluch, M., Basunbul, A., Azad, A., Al-Sulaimani, G., & Sharif, I. (1995). Combined experimental-numerical approach to characterization of steel-glue-concrete interface. *Materials and Structures*, 28, 518-525.
- Zou, G., Shahin, K., & Taheri, F. (2004). An analytical solution for the analysis of symmetric composite adhesively bonded joints. *Composite Structures*, 65, 499-510.

APPENDIX A

The coefficients of the equations (3.62) and (3.63):

$$B_{20}(s) = -\frac{1}{D_1 h_0} (b_{10} + b_{11}s + b_{12}s^2),$$

$$B_{22}(s) = \frac{1}{B_1 h_0} (b_{10} + b_{11}s + b_{12}s^2) - \frac{1}{4} \left(\frac{h_1}{D_1} + \frac{h_2}{D_2} \right) (a_{10} + a_{11}s + a_{12}s^2),$$

$$B_{12}(s) = \frac{h_1}{2B_1 h_0} (b_{10} + b_{11}s + b_{12}s^2) + \frac{1}{8} \left(\frac{4}{C_1} - \frac{4}{C_2} - \frac{2h_2}{D_2} \left(\frac{h_1 + h_2}{2} + h_0 \right) \right) (a_{10} + a_{11}s + a_{12}s^2),$$

$$B_{24}(s) = \frac{1}{b} (c_{10} + c_{11}s + c_{12}s^2), \quad B_{14}(s) = \frac{h_1}{2b} (c_{10} + c_{11}s + c_{12}s^2),$$

$$B_{1k}(s) = -\frac{1}{h_0} (b_{10} + b_{11}s + b_{12}s^2),$$

$$B_{1q}(s) = \frac{bh_2}{4D_2 s} (a_{10} + a_{11}s + a_{12}s^2), \quad B_{40}(s) = -\frac{1}{D_2 h_0} (b_{10} + b_{11}s + b_{12}s^2),$$

$$B_{30}(s) = -\frac{1}{D_2 h_0} \left(\frac{h_1 + h_2}{2} + h_0 \right) (b_{10} + b_{11}s + b_{12}s^2),$$

$$B_{42}(s) = \frac{1}{B_2 h_0} (b_{10} + b_{11}s + b_{12}s^2) - \frac{1}{4} \left(\frac{h_1}{D_1} + \frac{h_2}{D_2} \right) (a_{10} + a_{11}s + a_{12}s^2),$$

$$B_{32}(s) = \frac{1}{B_2 h_0} \left(\frac{h_1}{2} + h_0 \right) (b_{10} + b_{11}s + b_{12}s^2) + \frac{1}{4} \left(\frac{2}{C_1} - \frac{2}{C_2} - \frac{h_2}{D_2} \left(\frac{h_1 + h_2}{2} + h_0 \right) \right) (a_{10} + a_{11}s + a_{12}s^2),$$

$$B_{44}(s) = \frac{1}{b} (c_{10} + c_{11}s + c_{12}s^2), \quad B_{34}(s) = \frac{1}{b} \left(\frac{h_1}{2} + h_0 \right) (c_{10} + c_{11}s + c_{12}s^2),$$

$$B_{4M}(s) = \frac{1}{D_2 h_0} (b_{10} + b_{11}s + b_{12}s^2), \quad B_{3k}(s) = \frac{1}{h_0} (b_{10} + b_{11}s + b_{12}s^2),$$

$$B_{3q}(s) = -\frac{2b}{B_2 h_0 s} (b_{10} + b_{11}s + b_{12}s^2) + \frac{bh_2}{4D_2 s} (a_{10} + a_{11}s + a_{12}s^2),$$

$$C_{11}(s) = \frac{B_{14}(s)}{B_{24}(s)}, \quad C_{12}(s) = \frac{1}{B_{24}(s)} \left(B_{12}(s) + \frac{B_{1k}(s)B_{52}(s)}{B_{5k}(s)} \right), \quad C_{13}(s) = \frac{B_{22}(s)}{B_{24}(s)},$$

$$C_{14}(s) = \frac{B_{1k}(s)B_{50}(s)}{B_{5k}(s)B_{24}(s)}, \quad C_{15}(s) = \frac{1}{B_{24}(s)} \left(B_{20}(s) + \frac{B_{1k}(s)B_{60}(s)}{B_{5k}(s)} \right), \quad C_{16}(s) = -\frac{B_{1k}(s)B_{5N}(s)}{B_{5k}(s)B_{24}(s)},$$

$$C_{17}(s) = -\frac{B_{1k}(s)B_{6M}(s)}{B_{24}(s)B_{5k}(s)}, \quad C_{18}(s) = -\frac{B_{1q}(s)}{B_{24}(s)}, \quad C_{19}(s) = -\frac{B_{1k}(s)B_{N0}(s)}{B_{24}(s)B_{5k}(s)s},$$

$$D_{11}(s) = \frac{B_{34}(s)}{B_{44}(s)}, \quad D_{12}(s) = \frac{1}{B_{44}(s)} \left(B_{32}(s) + \frac{B_{3k}(s)B_{52}(s)}{B_{5k}(s)} \right), \quad D_{13}(s) = \frac{B_{42}(s)}{B_{24}(s)},$$

$$D_{14}(s) = \frac{1}{B_{44}(s)} \left(B_{30}(s) + \frac{B_{3k}(s)B_{50}(s)}{B_{5k}(s)} \right), \quad D_{15}(s) = \frac{1}{B_{44}(s)} \left(B_{40}(s) + \frac{B_{3k}(s)B_{60}(s)}{B_{5k}(s)} \right),$$

$$D_{16}(s) = -\frac{B_{3k}(s)B_{5N}(s)}{B_{5k}(s)B_{44}(s)}, \quad D_{17}(s) = -\frac{1}{B_{44}(s)} \left(B_{4M}(s) + \frac{B_{3k}(s)B_{6M}(s)}{B_{5k}(s)} \right), \quad D_{18}(s) = -\frac{B_{3q}(s)}{B_{44}(s)},$$

$$D_{19}(s) = -\frac{B_{3k}(s)B_{N0}(s)}{B_{44}(s)B_{5k}(s)s}.$$

APPENDIX B

Deformation of Crack tip:

Case (a): The characteristic equation of Eq. (4.31) with roots of $\pm R_1$, $\pm R_2$, and $\pm R_3$,

$$S_{1i} = \frac{1}{A_1} \left(\frac{c_{1i}}{R_1} + \frac{c_{2i}}{R_2} + \frac{c_{3i}}{R_3} \right), i = 1, 2, 3.$$

$$S_{2i} = \frac{1}{D_1} \left(\frac{c_{1i}S_1}{R_1} + \frac{c_{2i}S_2}{R_2} + \frac{c_{3i}S_3}{R_3} \right), i = 1, 2, 3.$$

$$S_{3i} = \left(\left(\frac{S_1}{D_1R_1^2} + \frac{T_1}{B_1R_1} \right) c_{1i} + \left(\frac{S_2}{D_1R_2^2} + \frac{T_2}{B_1R_2} \right) c_{2i} + \left(\frac{S_3}{D_1R_3^2} + \frac{T_3}{B_1R_3} \right) c_{3i} \right), i = 1, 2, 3.$$

$$S_{4i} = -\frac{1}{A_2} \left(\frac{c_{1i}}{R_1} + \frac{c_{2i}}{R_2} + \frac{c_{3i}}{R_3} \right), i = 1, 2, 3.$$

$$S_{5i} = -\frac{1}{D_2} \left(\frac{c_{1i}S_1}{R_1} + \frac{c_{2i}S_2}{R_2} + \frac{c_{3i}S_3}{R_3} \right) - \frac{h_2 + 2h_0 + 2d}{2D_2} \left(\frac{c_{1i}}{R_1} + \frac{c_{2i}}{R_2} + \frac{c_{3i}}{R_3} \right), i = 1, 2, 3.$$

$$S_{6i} = - \left(\frac{\frac{h_2}{2} + h_0 + d + S_1}{D_1R_1^2} + \frac{T_1}{B_1R_1} \right) c_{1i} - \left(\frac{\frac{h_2}{2} + h_0 + d + S_2}{D_1R_2^2} + \frac{T_2}{B_1R_2} \right) c_{2i} - \left(\frac{\frac{h_2}{2} + h_0 + d + S_3}{D_1R_3^2} + \frac{T_3}{B_1R_3} \right) c_{3i},$$

$$i = 1, 2, 3.$$

(B4.1)

Case (b): The characteristic equation of Eq. (4.31) with roots of $\pm R_1$ and $\pm R_2 \pm iR_3$

$$S_{1i} = \frac{1}{A_1} \left(\frac{c_{1i}}{R_1} + \frac{c_{2i}R_2}{R_2^2 + R_3^2} + \frac{c_{3i}R_3}{R_2^2 + R_3^2} \right), i = 1, 2, 3.$$

$$S_{2i} = \frac{1}{D_1} \left(\frac{c_{1i}S_1}{R_1} + \frac{c_{2i}(R_2S_2 + R_3S_3)}{R_2^2 + R_3^2} + \frac{c_{3i}(R_2S_3 + R_3S_2)}{R_2^2 + R_3^2} \right), i = 1, 2, 3.$$

$$S_{3i} = \left(\frac{S_1}{D_1R_1^2} + \frac{T_1}{B_1R_1} \right) c_{1i} + \left(\frac{S_2(R_2^2 - R_3^2) + 2R_2R_3S_3}{D_1(R_2^2 + R_3^2)^2} + \frac{T_2R_2 + T_3R_3}{B_1(R_2^2 + R_3^2)} \right) c_{2i} \\ + \left(\frac{S_3(R_2^2 - R_3^2) + 2R_2R_3S_2}{D_1(R_2^2 + R_3^2)^2} + \frac{T_2R_3 + T_3R_2}{B_1(R_2^2 + R_3^2)} \right) c_{3i}, i = 1, 2, 3.$$

$$S_{4i} = -\frac{1}{A_2} \left(\frac{c_{1i}}{R_1} + \frac{c_{2i}R_2}{R_2^2 + R_3^2} + \frac{c_{3i}R_3}{R_2^2 + R_3^2} \right), i = 1, 2, 3.$$

$$S_{5i} = -\left(\frac{c_{1i}(h_1/2 + h_0 + d + S_1)}{D_2R_1} + \frac{c_{2i}((h_1/2 + h_0 + d + S_2)R_2 + R_3S_3)}{D_2(R_2^2 + R_3^2)} + \frac{c_{3i}((h_1/2 + h_0 + d + S_3)R_3 + R_2S_3)}{D_2(R_2^2 + R_3^2)} \right) \\ , i = 1, 2, 3.$$

$$S_{6i} = -\left(\frac{h_1/2 + h_0 + d + S_1}{D_1R_1^2} + \frac{T_1}{B_1R_1} \right) c_{1i} - \left(\frac{(h_1/2 + h_0 + d + S_2)(R_2^2 - R_3^2) + 2R_2R_3S_3}{D_1(R_2^2 + R_3^2)^2} - \frac{T_2R_2 + T_3R_3}{B_1(R_2^2 + R_3^2)} \right) c_{2i} \\ - \left(\frac{S_3(R_2^2 - R_3^2) + 2R_2R_3(h_1/2 + h_0 + d + S_2)}{D_1(R_2^2 + R_3^2)^2} - \frac{T_2R_3 + T_3R_2}{B_1(R_2^2 + R_3^2)} \right) c_{3i} \\ , i = 1, 2, 3. \tag{B4.2}$$